The hydrodynamics of an eco-innovative sediment reuse project in the Rotterdam Waterway

Gaining insight into the physics and the predictive capability of two operational hydrodynamic models

M.E.G. Geraeds

Port of Rotterdam

TU Delft

The hydrodynamics of an eco-innovative sediment reuse project in the Rotterdam Waterway

Gaining insight into the physics and the predictive capability of two operational hydrodynamic models

by

M.E.G. (Marlein) Geraeds

in partial fulfilment of the requirements for the degree of

Master of Science

in

Hydraulic Engineering
Faculty of Civil Engineering and Geosciences
Department of Hydraulic Engineering
Section of Environmental Fluid Mechanics

at the Delft University of Technology,
to be defended publicly on Monday, June 8, 2020 at 10:00.

Student number:	4219465	
Project duration:	July 1, 2019 – June 8, 2020	
Thesis committee:	Prof. Dr. Ir. J. D. Pietrzak,	Delft University of Technology
	Ir. L. Hulsen,	Port of Rotterdam
	Dr. A. Kirichek,	Deltares
	Dr. C. Chassagne,	Delft University of Technology
	Dr. Ir. S. de Vries,	Delft University of Technology

An electronic version of this thesis is available at http://repository.tudelft.nl/.

(Image courtesy of the Port of Rotterdam Mediabank)

TU Delft

Port of Rotterdam

Abstract

Phenomena like sea level rise, global warming and erosion together contribute to increasing flood risk in vulnerable coastal areas. As this flood risk increases, initiatives to mitigate the effects of climate change in the coastal zone are also increasingly sought. During recent years, the view that these measures should be circular has gained significant momentum. In line with this, the idea that sediment should not be treated as waste, but as a valuable product in a circular economy has been widely accepted. Within this theme, the *sediment uses as resources in circular and in territorial economies* (SURICATES) was created to develop and execute eco-innovative solutions for the reuse of sediments in Western Europe. As a part of SURICATES, over the course of a nine week pilot, a total of 500 tonnes of sediment was reallocated in a designated area in the Rotterdam Waterway, with the expectation that this sediment would be transported out of the Rhine-Meuse estuary into the North Sea.

The SURICATES project is one of the first real large-scale efforts to reuse sediment for economic as well as ecosystem services. Effective implementation of the SURICATES project, however, requires a thorough understanding of the governing physical processes impacting the distribution of the deposited sediment locally. Furthermore, to assess the feasibility of similar future applications, efficient modelling of the pilot project is necessary.

The work presented here aims to elucidate the hydrodynamic processes that are governing in the Rotterdam Waterway, within the framework of the SURICATES pilot project, and assess the reproducibility of these processes by (two) predictive models that are currently operational at the Port of Rotterdam.

A special 6-hour monitoring survey was set up to measure salinities, velocities, temperature, and suspended particulate matter (SPM) along a transect crossing the reallocation location. In combination with a literature review, this dataset provides the basis for research into the predictive capabilities of two currently operational hydrodynamic models. Analysis of this dataset reveals the dominant terms in the momentum balance, the influence of Coriolis, the occurrence of internal waves, and the effect that all these mechanisms may have on the SPM distribution around the reallocation location. When the system dynamics are elucidated, the model performance of the two hydrodynamic models is assessed—both quantitatively and qualitatively. It is also investigated whether phase shifts are introduced in the models.

It is found that the primary hydrodynamic processes in the Rotterdam Waterway are related to the barotropic tidal asymmetry imposed at the river mouth, the tidal excursion of the salt wedge, baroclinic exchange flow processes, and turbulence damping at the pycnocline. Turbulence damping at the pycnocline generally poses an upper limit to the (re)distribution of SPM over the water column, although field data suggests that this damping may not be sufficient to counteract diffusion processes locally. This effect occurs under certain forcing conditions and during low water slack. Furthermore, an internal Froude number analysis provides evidence for the possible generation of internal waves in one of the river's bends.

The evaluated models, however, are not capable of reproducing all of these hydrodynamic processes adequately. Although both models adequately reproduce water levels and the vertical velocity structure, both models have difficulties predicting the pycnocline height. Additionally, it is found that both models introduce a small phase shift in the velocity and salinity prediction.

The research presented here is a contribution to the understanding of the governing hydrodynamic processes in the Rotterdam Waterway, and the effect that (in)accurate modelling of these processes may have on future studies. Recommendations following from this research could improve future modelling practices.

Preface

This master thesis, as it lies before you, marks the end of my time as a student at Delft University of Technology. It fulfils the final requirement in order to receive my Master of Science degree in Hydraulic Engineering, with a specialisation in Environmental Fluid Mechanics. The project was funded by the Port of Rotterdam in the context of the *sediment uses as resources in circular and in territorial economies* (SURICATES) pilot project, and was also largely executed at the Port of Rotterdam office.

The last year of my master was a whirlwind in the most positive sense of the word. I'm incredibly grateful for all the opportunities that I was given; from a fantastic internship, an experience abroad, and a published paper, to the cherry on top—the research presented here. I could have never imagined that I would meet so many interesting people and learn so much in so little time.

Of course, this work would not have been realised if it weren't for the support of others. Therefore, I'd like to take this opportunity to express my gratitude to the people that guided me through the process.

First off, I'd like to thank my committee members. I want to thank my daily supervisor Lambèr Hulsen, for the many meaningful conversations, his endless knowledge on the subject of hydrodynamic modelling, and his unequivocal devotion to helping me when necessary. I want to thank dr. Alex Kirichek, dr. ir. Claire Chassagne, and dr. ir. Sierd de Vries, for all of their valuable feedback and expertise-specific views on the project. And lastly, my expressions of gratitude go out to Prof. dr. Julie Pietrzak for chairing my M.Sc. thesis committee, sharing her inspiring amount of knowledge, and for believing in my capabilities.

Additionally, I want to thank all of my colleagues at the Port of Rotterdam; for all of the sparring sessions, coffee breaks, and the opportunity to work in an inspiring working environment. A special mention here goes out to Daan Deckers, my fellow graduate student—I'm very grateful that we could help each other throughout the project.

I'd like to end this word of thanks on a personal note, by thanking my family and friends. Thank you for keeping me sane and distracting me from work. And last, but definitely not least, thank you Xander; thank you for making me laugh and dragging me out of the house for distraction walks—I don't know how I would've coped without you.

I look back on an incredibly interesting chapter of my life, and a great overall experience. Enjoy reading!

M.E.G. Geraeds
Rotterdam, May 2020

Contents

List of Symbols

Latin symbols

ρ_{air}	Air density	[kg m^{-3}]
h_k	Layer thickness in a σ-grid	[m]
S	Salinity	[PSU]
T	In-situ temperature	[$^\circ$ C]
U_*	Scale for the bottom friction velocity	[m s^{-1}]
u_*	Bottom friction velocity	[m s^{-1}]
c	(Total) wave phase speed	[-]
C_0	Linear wave phase speed	[-]
C_D	Drag coefficient	[-]
c_E	External wave phase speed	[-]
c_I	Internal wave phase speed	[-]
c_s	Sound velocity	[-]
d	Index of agreement	[-]
D_T	Vertical eddy diffusivity	[-]
f	Coriolis parameter	[-]
Fr	Froude number	[-]
Fr_V	Vertical Froude number	[-]
G	Greenwich phase lag	[-]
g	Gravitational constant	[-]
H	Total water depth	[-]
N	Brunt-Vaïsalä frequency	[-]
R_E	External Rossby radius of deformation	[-]
R_I	Internal Rossby radius of deformation	[-]
Ri_B	Bulk Richardson number	[-]
Ri_f	Flux Richardson number	[-]
Ri_g	Richardson gradient number	[-]
Ri_x	Horizontal Richardson number	[-]
S	Vertical shear	[-]
Si	Simpson number	[-]
U	Horizontal along-channel background flow velocity	[-]
u	(Total) horizontal along-channel velocity	[-]
Un	Unsteadiness parameter	[-]
V	Horizontal cross-channel background flow velocity	[-]
v	(Total) horizontal cross-channel velocity	[-]
W	Background vertical velocity	[-]
w	(Total) vertical velocity	[-]
w_s	Vertical sediment fall velocity	[-]

Greek symbols

α^Θ	Thermal expansion coefficient w.r.t. the conservative temperature	[K^{-1}]
β	Latitudinal variation of the Coriolis parameter	[rad s^{-1} m]
β^Θ	Saline contraction coefficient w.r.t. the conservative temperature	[kg g^{-1}]
χ	Phase of complex oscillation	[rad s^{-1}]
ϵ	Dissipation rate of turbulent kinetic energy	[m^2 s^{-3}]
η	Water level elevation	[m]
κ	Von Kármán constant	[-]
λ_O	Ozmidov length scale	[m]
ν_T	Vertical turbulent eddy viscosity	[m^2 s^{-1}]
$\nu_{t,s}$	Turbulent viscosity affected by salinity stratification	[m^2 s^{-1}]
Ω	Earth rotation rate	[s^{-1}]
ω	Angular frequency	[rad s^{-1}]
Φ	Modal structure of the vertical velocity	[-]
Θ	Conservative temperature	[$^\circ$ C]
θ	Latitude	[rad]
θ	Potential temperature	[$^\circ$ C]
ρ	Density	[kg m^{-3}]
ρ^Θ	Potential density	[kg m^{-3}]
ρ_0	Reference density of water	[kg m^{-3}]

List of Abbreviations

ADCP	Acoustic doppler current profiler
ADI	Alternating Direction Implicit
ASIPS	Advection and strain induced periodic stratification (de Boer *et al.*, 2008)
BRGM	Bureau de Recherches Géologiques et Minières
CTD	Conductivity, temperature, depth
ETM	Estuarine turbidity maximum
GEP	General eigenvalue problem
GPS	Global positioning system
HLES	Horizontal large eddy simulation
HWS	High water slack
IRLS	Iteratively-reweighted least squares
KdV	Korteweg-de Vries
LWS	Low water slack
MAE	Mean absolute error
OBS	Optical backscatter
PCA	Principle component analysis
PoR	Port of Rotterdam
QEP	Quadratic eigenvalue problem
RD	Rijksdriehoek
RMSE	Root mean square error
ROFI	Region of freshwater influence (Simpson *et al.*, 1993)
SEP	Standard eigenvalue problem
SIMONA	SImulatie MOdellen NAtte waterstaat
SIPS	Strain induced periodic stratification
SPM	Suspended particulate matter
SURICATES	Sediment uses as resources in circular and in territorial economies
SVP	Sound Velocity Profiler
SWAN	Simulating WAves Nearshore
TEOS-10	Thermodynamic equation of seawater 2010
UNESCO	United Nations Educational, Scientific and Cultural Organization

List of Figures

List of Tables

Chapter 1

Introduction

1.1 Context

The complex and unpredictable effects of climate change are felt all around the world. Sea level rise, global warming and erosion together contribute to the increasing flood risk in vulnerable coastal areas. To be able to combat this ever-increasing flood risk brought about by climate change, circular mitigation measures that take into account the resilience of the complete estuarine system are of paramount importance. In line with this, the view that sediment should not be treated as waste, but can be a valuable product in a more efficient circular economy, has increasingly been accepted. Coastal habitat creation in particular is considered to be a good opportunity for the beneficial reuse of sediment. Coastal habitats such as mudflats, salt marshes and shingle ridges are not only important for the survival of increasingly endangered species, but they double as defences against coastal flooding by reducing storm surge impact.

The European Union has several programmes set in place to increase transnational cooperation between member countries to add an extra 'European dimension' to regional development. Amongst these transnational programmes is the Interreg North-West Europe programme, which focuses on three main themes: innovation, low carbon economy, and resource and materials efficiency. Within the latter theme, the Interreg North-West Europe programme funds projects to accelerate the transition to a circular economy model (Interreg NWE, 2019). Within this theme falls the so-called *sediment uses as resources in circular and in territorial economies* (SURICATES) project.

The scope of the SURICATES project is two-fold. Firstly, the programme aims to develop new methods to optimise the social, economic and environmental costs and proceeds of eco-innovative solutions for the reuse of sediments in ports and waterways. Secondly, the programme aims to execute several of these innovative solutions, providing guidelines for reapplication based on long term impact evaluation (Port of Rotterdam, 2018). In the pilot implementation, sediment is used as raw material for four solutions that make up the SURICATES project (Interreg NWE, 2018).

One of these pilot projects has been executed in The Netherlands, and is under the supervision of the *Port of Rotterdam* (PoR) and Rijkswaterstaat in cooperation with Deltares and *Bureau de Recherches Géologiques et Minièrès* (BRGM) (Port of Rotterdam, 2018). During this 9-week pilot project executed in 2019, a total of 500 tonnes of dredged sediment were deposited in The Rotterdam Waterway near Maassluis during ebb tide (*see* Fig. 1.1). The aim of the project is to decrease dredging costs and contribute to accretion of the "Groene Poort Zuid", a tidal park located on the southern river bank of Rotterdam Waterway, on the Rozenburg headland. This tidal park, along with several other tidal parks that will be realised on the river banks of The Rotterdam Waterway, contributes to the flood resilience of the Rhine estuary by enlarging its natural foreshore. The dredged sediment is expected to be transported with the tide to eventually flow out of the estuary into the North Sea, whilst partly accreting on the tidal park's river banks. Furthermore, the SURICATES project is expected to reduce dredging costs by decreasing the sailing distance of dredging vessels.

1.2 Problem statement

The SURICATES project is one of the first real large-scale efforts to reuse sediment for economic as well as ecosystem services. If the current initiative is able to live up to its expectations, it has the potential

to be the leading example project for other eco-innovative pilot projects incorporating dredged sediment. However, to be able to assess whether the pilot project executed in the Rotterdam Waterway will be suitable for application in other (similar) estuarine systems, efficient modelling of the pilot project is necessary. Furthermore, efficient predictive modelling of the pilot project could increase project efficiency through the optimisation of the sediment reallocation location.

Earlier studies by de Nijs *et al.* (De Nijs and Pietrzak, 2012; de Nijs and Pietrzak, 2012; de Nijs *et al.*, 2009, 2010a,b) executed in the Rotterdam Waterway have aimed to obtain a better general understanding of estuarine SPM trapping, SPM transport and sedimentation processes, and their relation to harbour siltation. Since it is widely assumed that the exchange of SPM is proportional to the total exchange of water (Langendoen, 1992), several of the papers in the series by de Nijs *et al.* have focused on better understanding the internal flow structure and the evolution of the salt wedge within the Rotterdam Waterway. Modelling studies executed within the framework of de Nijs *et al.*'s research have indicated the need for accurate modelling of the governing hydrodynamic processes and the salt wedge dynamics specifically, since SPM concentrations in the Rotterdam Waterway are closely related to the tidal and subtidal excursions of the salt wedge and the associated *estuarine turbidity maximum* (ETM).

Accordingly, in order to be able to effectively model the SURICATES pilot project, it is crucial that the hydrodynamics within the Rotterdam Waterway are well understood and can besides be modelled well. Although the previous studies executed by de Nijs *et al.* already provide general insight to the governing hydrodynamic processes in the Rotterdam Waterway, their insights are based on the lay-out and bathymetry of the Rotterdam Waterway in the year 2006. Since 2006, however, several drastic man-made changes have been realised in the Rotterdam Waterway and its side branches, such as the construction of the Tweede

Figure 1.1: Overview of the Rotterdam Harbour area and the approximate sediment reallocation location used in the SURICATES pilot project. Reallocation location is indicated with the boat icon. Map obtained via OpenStreetMap (OpenStreetMap contributors, 2017), adapted by the author.

Maasvlakte and the deepening of the Nieuwe Waterweg. Although these measures have inevitably induced changes in the overall workings of the Rhine-Meuse estuarine system, similar research into the internal flow structure has not been executed since.

Part of these knowledge gaps need to be filled in order to be able to assess whether currently operational computational models are able to sufficiently predict the effectiveness of novel eco-innovative projects, such as the SURICATES pilot project, in the changed system. The research presented in this thesis therefore aims to fill the necessary knowledge gaps and assess the predictive capability of two different hydrodynamic models.

1.3 Research objectives

The SURICATES pilot project executed in The Rotterdam Waterway is one of the first eco-innovative solutions implementing the reuse of dredged sediment for river bank nourishing and habitat creation. Effective implementation of this pilot project could provide a basis for new eco-friendly dredging strategies in the Port of Rotterdam and significantly decrease dredging costs, provided that the measure does not impact the sedimentation rates in the harbour.

Effective implementation of the SURICATES project, however, requires a thorough understanding of the governing physical processes impacting the distribution of the deposited sediment locally. The most important physical processes are inevitably related to the hydrodynamics in the Rotterdam Waterway and the larger Rhine-Meuse estuarine system. Furthermore, to ensure optimisation and reproducibility of the project, knowledge gaps in currently available predictive models need to be identified and investigated. These two factors, together, motivate the initiation of this research, which covers the following main research objective:

Elucidate the hydrodynamic processes in the Rotterdam Waterway within the framework of the SURICATES pilot project, and assess the reproducibility of these processes by currently operational 3D hydrodynamic models at the Port of Rotterdam, based on the results of a recent monitoring survey.

In support of achieving this research objective, a main research question is formulated:

What are the governing hydrodynamic processes relevant within the scope of the SURICATES pilot project, and how well can these processes be reproduced by the currently operational (3D) numerical models used in the Port of Rotterdam?

To further explicate this main research question, two research sub-questions are formulated. These are stated below, accompanied by their corresponding research objectives.

1. *What are the primary hydrodynamic processes occurring in the Rotterdam Waterway and in the larger Rhine-Meuse estuarine system?*

   (a) Study existing literature on the hydrodynamic processes occurring in estuarine systems;

   (b) Study the results of a previous study by de Nijs *et al.* (2009, 2010a,b) to elucidate the governing hydrodynamic processes in the Rotterdam Waterway specifically.

2. *What are the governing hydrodynamic processes near the SURICATES reallocation location, and how may these influence the distribution of SPM?*

   (a) Set up, conduct, and analyse a monitoring survey completed during the execution phase of the SURICATES pilot project to determine whether the hydrodynamic processes found in literature by de Nijs *et al.* (2009, 2010a,b) are still governing;

(b) Analyse the results of Siltprofiler measurements and ADCP backscatter data around the SURICATES reallocation location from the monitoring survey, and assess how the previously uncovered hydrodynamic processes may have influenced these results.

3. *How accurately can two currently operational 3D numerical models reproduce the hydrodynamics of a monitoring survey conducted in the Rotterdam Waterway during the SURICATES pilot project?*

   (a) Determine the phase shifts introduced in predicting the water level and salinities by both models;

   (b) Determine correlation parameters to quantitatively assess the predictive capability of both models;

   (c) Quantitatively assess the capability of both hydrodynamic models to reproduce salinity and water level time series from fixed measuring stations;

   (d) Quantitatively assess the capability of both hydrodynamic models to reproduce measured water levels, salinities, pycnocline height and velocities measured during the new monitoring survey.

4. *What are the key parameters that impact the predictive capability of the currently operational 3D numerical models used by the Port of Rotterdam?*

   (a) Quantitatively compare output from the two different hydrodynamic models with each other;

   (b) Give recommendations about parameters that may improve model performance.

1.4 Scope of the research

Although this thesis is executed with the main focus on the SURICATES pilot project, it does not cover all of the complexities relevant for the project. Therefore, this thesis is the first part of a series of theses—each focusing on different aspects that contribute to the understanding and reproducibility of the SURICATES project in the future. Since a thorough understanding and correct modelling of the hydrodynamics is essential before the dynamics of suspended sediment processes can be understood and modelled well, the scope of this specific thesis is restricted to understanding the hydrodynamics first. For this, a monitoring survey that was conducted during the execution phase of the SURICATES pilot project is examined and modelled. To lay a foundation for the understanding of the SPM dynamics under the specific conditions of the monitoring survey considered here, this thesis also shortly introduces and discusses the outcome of the SPM measurements, although SPM is not modelled. Later theses will build upon the knowledge gained from this research, and will elaborate more on understanding and modelling of the complex interactions between SPM and the hydrodynamics. The scope of this study is specified in the list presented below.

1. The study considers a monitoring survey conducted on August 13th, 2019, during the execution phase of the SURICATES pilot project. On this specific day, no dredged SPM was reallocated. The survey was set up for this study specifically, and is therefore optimised—within practical limits and based on knowledge available beforehand—for the data analysis presented in Chapter 6. To be able to use the results of this thesis in future research on the SURICATES pilot project, the monitoring survey also shortly addresses SPM measurements obtained using two different instruments. Besides the brief coverage of the topic in the data analysis, SPM will not be modelled in this thesis—SPM modelling specifically will be the subject of another thesis in the series.

2. The models that are used for the predictive capability tests are two models that are currently operational at the Port of Rotterdam. They are documented well, are kept up-to-date, and they have been validated extensively under different boundary conditions in previous years. The two models that are evaluated are the NSC-Fine model, primarily used for salinity-related calculations, and the NSC-Coarse model, which is mainly used for SPM-related modelling studies. The reason for re-evaluating them here, is that they have mainly been evaluated on their performance at fixed measuring stations in the past, and, unfortunately, there are no fixed salinity stations along the part of the Rotterdam

Waterway that is most relevant for the SURICATES pilot project. Furthermore, locally occurring hydrodynamic processes may be relevant within the scope of the SURICATES pilot project, which motivates the choice to evaluate the hydrodynamic models' performance locally—using the results of the monitoring survey—and over the vertical as well.

3. One of the main goals of this thesis is *evaluating* the currently used hydrodynamic models, which means that recommendations are the outcome of the evaluation presented in this thesis. Extensive sensitivity analyses into the tunable parameters, aimed at *optimising* the models, are therefore outside the scope of this thesis.

1.5 Approach and thesis outline

This thesis is structured into four different parts that each serve its own purpose. The structure of each part, and the chapters that it contains, are discussed here.

Part I focuses on a system analysis by a literature study. It contains two separate chapters, the contents of which are discussed below:

Chapter 2: Literature study on estuarine hydrodynamics
This chapter focuses on providing the necessary theory on the hydrodynamic processes occurring in estuarine systems and the Rhine-Meuse estuarine system specifically. The general hydrodynamic processes are discussed based on the subdivision of the processes into large-scale and small-scale processes, after which the interaction and coupling of these processes within the Rhine-Meuse estuarine system, specifically, is explained.

Chapter 3: Literature study on estuarine sediment dynamics
A short introduction into the subject of estuarine sediment dynamics, as a basis for the interpretation of the results of SPM measurements in the Rotterdam Waterway, is given in this chapter. The set-up of this chapter is similar to the set-up of Chapter 2—general large and small-scale sediment dynamic processes are covered first, after which it is elaborated which of these processes occur and interact within the Rotterdam Waterway specifically.

Part II focuses on discussing the methods used to answer the remaining research questions. It therefore elaborates on the set-up of a monitoring survey, along with the pre-processing and post-processing steps, as well as the set-up of the hydrodynamic models that are assessed in this study.

Chapter 4: Data analysis set-up
This chapter explains the set-up of a monitoring survey conducted on August 13th, 2019, which is used as the basis of a data analysis presented in this study. This chapter also covers the pre-processing and post-processing steps that are taken to obtain interpretable results.

Chapter 5: Model set-up(s)
The theoretical background behind the modelling study as well as the general set-up of the considered hydrodynamic models is covered in Chapter 5. Typical model parameters such as boundary conditions, initial conditions and vertical and horizontal grid resolution are mentioned here.

Part III essentially encompasses the core of the research, presenting the results of the data analysis and the modelling study.

Chapter 6: Data analysis results
This chapter aims to close knowledge gaps by presenting the results of the monitoring survey dataset analysis. The results obtained using the methodology presented in Chapter 4 are discussed and linked to similar earlier work by de Nijs *et al.* where possible.

Chapter 7: Modelling study results
Chapter 7 elaborates on the results of the modelling effort, by discussing the model output qualitatively. Parallels are sought between the model output of the modelling study presented here and similar preceding modelling studies.

Chapter 8: Comparative model validity study
This chapter elaborates on the predictive capabilities of the two considered models, by calculating the correlation between model output and measurements. The models are also compared to each other.

Part IV covers a discussion of the research in a general sense and the concluding remarks.

Chapter 9: Discussion
This chapter critically reflects on the research and the validity of the results in a general sense. This chapter provides the basis for the following chapter.

Chapter 10: Conclusions and recommendations
In the last chapter of this report, Chapter 10, conclusions to the defined research (sub)questions are formulated. In addition, the points brought forward in Chapter 9 are assimilated into recommendations, which are subsequently discussed.

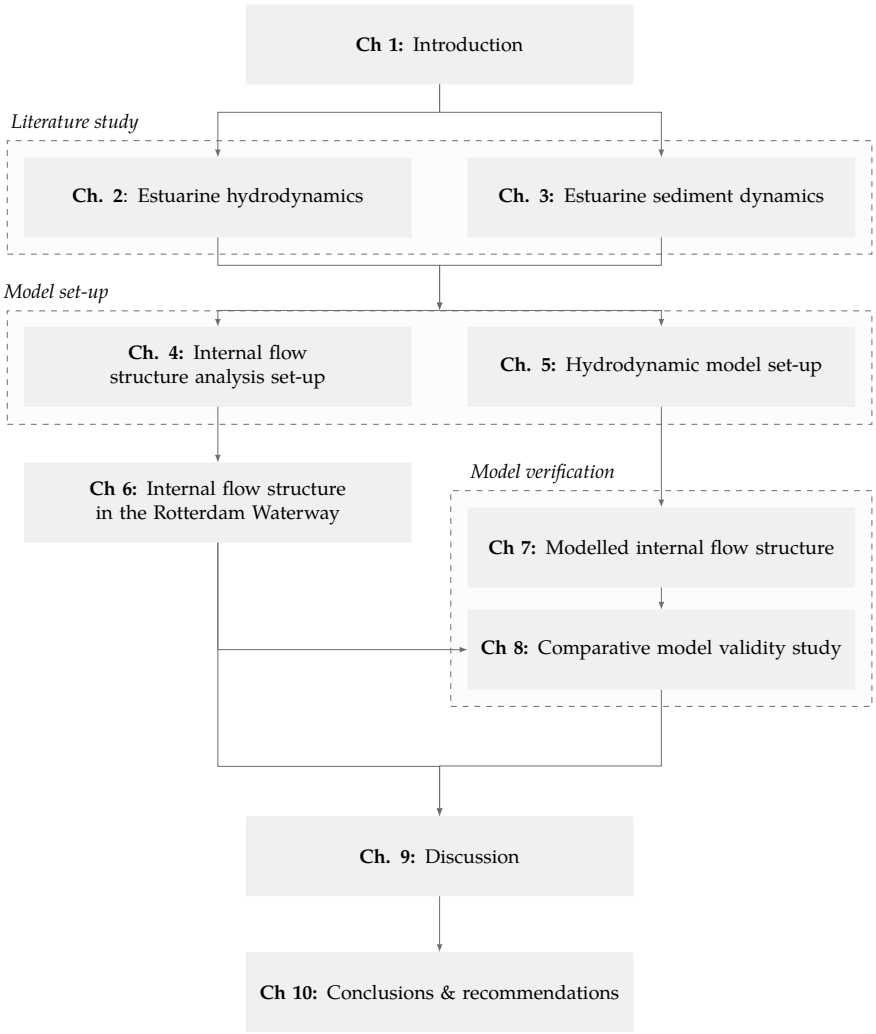

Figure 1.2: Overview of thesis outline (simplified).

Part I

SYSTEM ANALYSIS

This part elaborates on a *literature study* that aims to clarify the system dynamics. The knowledge obtained from this literature study provides a good basis for the understanding and interpretation of the rest of this study, and additionally answers one of the key research questions.

Chapter 2

Estuarine hydrodynamics

The physical processes that are known to dominate estuarine environments are the residual circulation, tidal velocity and mixing asymmetry, and freshwater inflow (de Nijs *et al.*, 2010b). Since estuarine systems are very dynamic, a thorough understanding of the flow structure in a specific estuarine system requires understanding of the competition and interaction between each of these governing processes. Section 2.1 aims to give a global understanding of the large-scale physical processes that occur in estuarine systems, after which Section 2.2 will cover some small-scale hydrodynamic processes in estuarine systems that may be relevant in the framework of the SURICATES project. Hereafter, Section 2.3 will consider how these processes together determine the dynamics of the flow in the Rotterdam Waterway specifically. Lastly, Section 2.4 summarises the findings of this chapter, thereby answering the first research question.

2.1 Large-scale hydrodynamics

2.1.1 Estuarine circulation

An often used and broadly defined definition of an estuary is "*any embayment of the coast in which buoyancy forcing alters the fluid density from that of the adjoining ocean*" (Geyer and MacCready, 2014). Under this definition, the range of estuary types is extensive, as are the classification methods (Valle-Levinson, 2012). A river or multiple rivers is the most common source of buoyancy for an estuary, although heating, evaporation, or freezing and melting of ice may also be a source of buoyancy. The competition between the horizontal density gradient induced by the buoyancy forcing and turbulent mixing caused by tidal currents and wind leads to a circulation pattern, which is the subject of many studies.

Although many studies have investigated the circulation in tidal estuaries over the last half century (Burchard and Hetland, 2010; Schulz, 2014; Schulz *et al.*, 2015; Simpson *et al.*, 1990, 1993, and references therein), the driving mechanisms are still not fully understood. In the beginning, the classic gravitational circulation was only taken into account, which is now referred to as the classical estuarine circulation. Later, Simpson *et al.* (1990) added the stratifying and destratifying effect of *strain induced periodic stratification* (SIPS). Once the feedback mechanism between SIPS and tidal straining was described by Jay and Musiak (1994), the circulation resulting from this tidal asymmetry was called the tidal straining circulation. Burchard *et al.* (2011) later described the effect of lateral differential advection on the residual longitudinal circulation, which they called the advectively driven circulation. The individual contributions of the advectively driven circulation, the gravitational circulation, and the tidal straining circulation under different forcing conditions were also investigated by Burchard *et al.* (2011), who found that most major contributors to longitudinal estuarine circulation seem to roughly scale with the Simpson number, and that the relative influence of the advectively driven circulation scales with decreasing stratification.

All of the above mentioned aspects and terms, including their effect on the estuarine circulation, are discussed in the following sections.

Gravitational circulation

Gravitational circulation is a physical phenomenon that occurs in (partially) stratified environments, and is believed to be the dominant contribution to the estuarine circulation in many estuaries. In such envi-

ronments, pressure differences are induced by changes in the height of the free surface and the horizontal pressure gradient along the axis of the estuary. The former contribution to the pressure distribution is the barotropic pressure gradient and the latter is referred to as the baroclinic pressure gradient. A longitudinal density decrease in the landward direction due to a decrease in salinity induces an up-estuary baroclinic pressure gradient force. Since the barotropic pressure gradient is constant over the vertical, the combined effect of these pressure gradients drives an up-estuary bottom flow and a down-estuary surface flow. This resulting circulation flow is called the gravitational circulation.

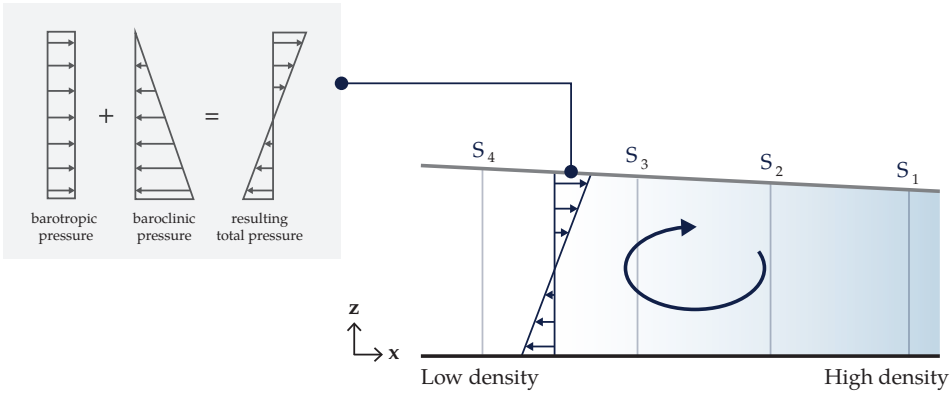

Figure 2.1: Figure explaining gravitational circulation and the contributions of the baroclinic and barotropic pressure to the total pressure leading to the gravitational circulation. S_1 to S_4 indicate the isohalines. Adapted from Pietrzak (2015).

Baroclinic exchange flows

Under the influence of gravity, fluids with different densities will be subject to different pressures. In estuaries, the freshwater input from rivers induces substantial horizontal density gradients. To get to an equilibrium situation, an adjustment process is set into action in which lighter water is advected over heavier water (Gill, 1982). This flow type is called *baroclinic exchange flow*. This adjustment process is the same as the adjustment process that would occur in a well-mixed external flow case if the gravitational acceleration were reduced with a factor $(\rho_2 - \rho_1)/\rho_2$ to a value g', which is called the *reduced gravity*. In many studies concerning estuaries, this exchange flow is synonymous with the estuarine circulation (Geyer and Ralston, 2012; Geyer and MacCready, 2014, and many others).

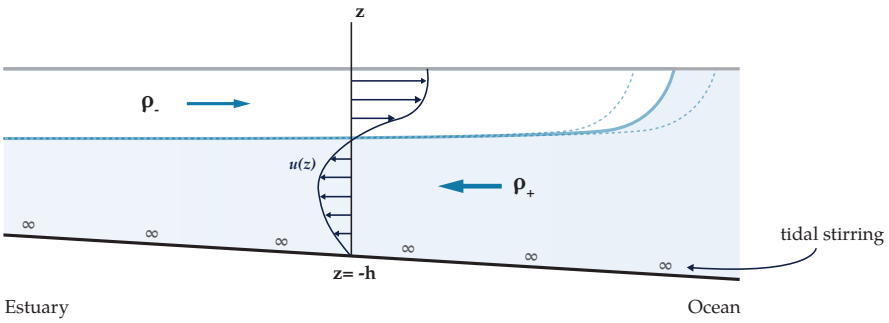

Figure 2.2: Schematic of a stratified estuary maintained by freshwater input in competition with bottom stirring. Baroclinic flows are superimposed upon the gravitational circulation to move lighter water offshore and heavier water onshore. Blue depicts saltier water and white depicts fresh water. Adapted from Pietrzak (2015) and Simpson *et al.* (1990).

Differential advection

In open channel flows, depth-averaged along-channel tidal currents tend to be strongest in the thalweg, the deepest location of a channel cross-section. On the sides, where the channel is more narrow, the depth-averaged along-channel tidal currents are weaker. This effect is called differential advection (Lerczak and Geyer, 2004). Because of this lateral shear, advection of the along-channel density gradient induces a cross-channel density gradient. This lateral baroclinic pressure gradient in turn leads to a pressure gradient, which drives a lateral flow.

It is evident that the sign of the lateral shear during flood is the opposite of the sign of the lateral shear during ebb. The residual currents at the surface would therefore be convergent during flood, leading to downwelling in the thalweg, and divergent during ebb, leading to upwelling in the thalweg. In stratified estuarine channels specifically, the lateral flow induced by the lateral density gradient tilts isopycnals, setting up an adverse lateral baroclinic pressure gradient. This baroclinic pressure gradient then tends to suppress the lateral circulation. Therefore, in such estuaries the differential advection that accelerates the lateral flow opposes the effect of the tilting isopycnals, which tend to decelerate the lateral flow (Lerczak and Geyer, 2004).

Tidal straining

tidal straining was first described by Simpson *et al.* (1990), who observed marked semi-diurnal oscillations in the stability of the stratification in Liverpool Bay. If one assumes that the flow velocity over the vertical follows a perfect logarithmic profile, the absolute velocity increases with distance from the bottom. This leads to a differential advection of fresher water over more saline water. On ebb tide, stratification is promoted through this differential displacement of lighter fresher water over denser saline water, which distorts the isohalines and leads to a more stable structure. Tidal stress at the bottom and wind stress at the surface will tend to transform the salinity structure into a two-layer profile with a distinct halocline. During flood tide however, this process is reversed. Tidal stirring accelerates the breakdown of the stratification and instabilities will form, leading to a more uniform salinity profile. These instabilities will form when the instantaneous local gradient Richardson number falls below the critical value of $^1/_4$ (*see* Appendix D.2.1). Therefore, tidal straining generates fluctuations in the vertical stratification at the tidal frequency.

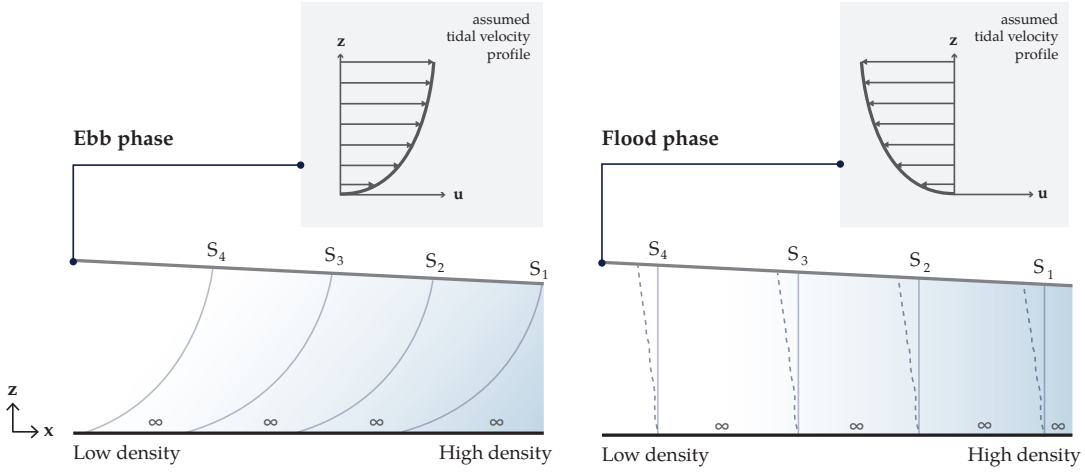

Figure 2.3: Schematic of tidal straining in the case of an assumed logarithmic velocity profile. (**Left**) Stratification of the estuary induced by the shear on the ebb. S_1 to S_4 represent the isohalines. (**Right**) Vertical isohalines, situation at the end of flood tide. Further convective processes may lead to an unstable situation (dashed lines). Adapted from Pietrzak (2015) and Simpson *et al.* (1990).

Strain induced periodic stratification

The process of tidal straining gives rise to a semi-diurnal (re-)stratification pattern, a process that Simpson *et al.* (1990) called SIPS. Jay and Musiak (1994) later described the feedback mechanism of SIPS on the tidal currents. Stratification during ebb decreases the eddy viscosity (see also Section 2.2), and thus allows stronger shear, which generates surface-enhanced ebb currents. Conversely, the more uniform salinity profile apparent during flood leads to an increased eddy viscosity and thus prohibits strong shear. This in turn gives rise to bottom-enhanced flood currents.

Besides the effect of tidal straining, multiple other processes contribute to the estuarine circulation. To make the distinction between these processes clearer, Schulz *et al.* (2015) proposed to call this longitudinal SIPS *primary strain-induced periodic stratification* (1SIPS), and additionally suggested calling lateral and vertical straining *secondary strain-induced periodic stratification* (2SIPS) and *tertiary strain-induced periodic stratification* (3SIPS) respectively. In narrow channels, such as the Rotterdam Waterway, 2SIPS is the dominant stratifying term.

Transverse circulation

Besides the processes of tidal straining and gravitational circulation, which take place along the longitudinal axis of an estuary, a transverse circulation is also present in estuaries. Although the cross-channel currents associated with this process are typically only 10% of the size of the along-channel tidal currents, they can play a critical role in the dynamics of estuaries. Lerczak and Geyer (2004) first described the effect of lateral circulation with a model study of an idealised stratified estuary. They found that lateral salinity gradients were consistent with the forcing provided by the differential advection, but the effect of transverse circulation is decreasing with increasing stratification. In the model with the strongest stratification, only one hour after maximum flood, a weak lateral circulation was apparent in the bottom half of the water column and downwelling at the thalweg was observed. From this it was deduced that the lateral straining process is more important during stronger mixing conditions than during ebb, which is in contrast with the effect of SIPS.

Schulz *et al.* (2015) later researched the effect of the depth-to-width ratio on the effect of transverse circulation in stratified estuaries. The model study by Schulz *et al.* encompassed three typical channels: a wide, medium and narrow channel, characterised based on their depth-to-width ratio $\alpha = H_{\max}/W$. The bathymetry of each of the channels was modelled as parabolic. In both cases of the medium channel and the narrow channel, strong stratification persists in the centre of the channel throughout the flood and ebb phase. Lowest salinities are found in the thalweg, in the upper half of the cross-section. The ebb-oriented transverse circulation created during ebb enhances stratification, just like the flood-oriented transverse circulation enhances stratification during flood. In the narrow channel, the steeper slope of the banks induces larger lateral longitudinal velocity and salinity gradients than occur in the case of the medium channel. Therefore, the transverse circulation is stronger. In combination with the smaller channel width, this leads to faster straining of the salinity field, which was already observed just after slack after flood and slack after ebb.

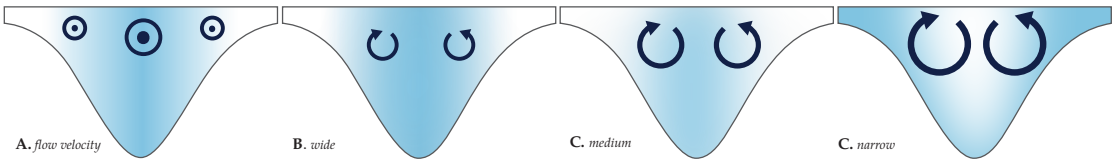

Figure 2.4: Schematic indicating the phenomenon of transverse or secondary straining. Figure is oriented down-estuary. (**A**) Laterally differential longitudinal advection, indicated by the dark blue arrowheads. Salinity distribution is indicated in blue, and the deeper blue indicates a higher salinity. (**B**), (**C**), (**D**): transverse circulation and strained salinity field in wide, medium and narrow estuary channels at slack after flood, respectively. Adapted from Schulz *et al.* (2015).

Concerning the effect of the depth-to-width ratio on the estuarine circulation, it was found that in wide channels, the estuarine circulation was relatively weak. The tidal straining contribution to the estuarine circulation was dominant, followed by the gravitational circulation. In medium channels, the total estu-

arine circulation reached a maximum. The tidal straining contribution primarily contributed to this peak, although the advectively driven contribution and the gravitational circulation also contributed. At a certain depth to width ratio, the tidal straining contribution started to decrease again, and even fell below zero, implying that the tidal straining contribution opposed the classical estuarine circulation.

Besides these transverse flow phenomena caused by baroclinity, there may be local transverse circulation phenomena in channel bends. Due to the centripetal force, the flow is pushed outwards in a channel bend, after which, following from continuity, an inwards directed return flow over the bed occurs. This effect is reversed when the flow direction is reversed under the influence of the tide.

2.1.2 Current-wave interactions

In coastal areas, waves and currents interact with each other in multiple ways. Waves do not only affect currents, but currents also affect waves. Waves affect currents by influencing the surface stress and bottom friction, as well as by introducing radiation stress and Stokes' drift (Holthuijsen, 2007; Wolf *et al.*, 2012). The latter components contribute to the mean flow and lead to wave set-up and set-down. Conversely, currents affect waves by altering wave propagation, by influencing bottom friction (through modification of the wave friction factor) and by inducing changes in wind input and dissipation. The combined effect of waves and currents results in a net velocity distribution that is important for the determination of sediment transport. Waves are furthermore of importance for momentum and energy transfer, since the net balance between wave growth and dissipation is the main mechanism for this transfer (Wolf *et al.*, 2012).

2.1.3 Salt wedge dynamics

At the mouth of an estuary, different strengths of river outflow can lead to different regimes of hydraulic transition caused by expansion. Farmer (1986) described three distinct regimes in the case of flow over an obstacle that are also applicable in highly stratified estuarine environments (Nihoul and Ronday, 1975). The flow is subcritical early in the ebb tide in the estuary, but transitions to supercritical at the mouth with a thin seaward-spreading plume. Later on in the ebb tide, as the tide accelerates, the upper layer deepens in the estuary but remains subcritical. When at a certain point during the tide the outflow velocity exceeds the critical Froude number everywhere in the estuary, a frontal regime at the mouth is re-established. A critical Froude number of $Fr = 1$ is the controlling parameter for front formation, under the condition that the the upper (fresher) layer occupies the entire water column.

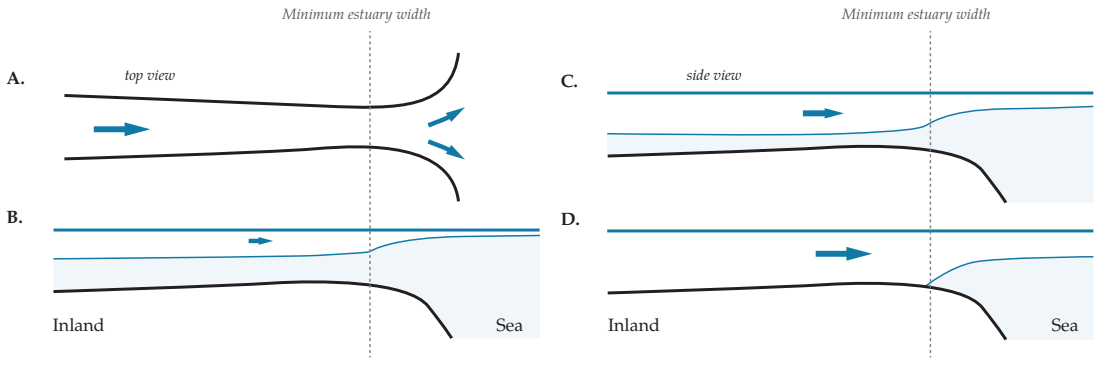

Figure 2.5: Schematic representation of the plume lift-off regime for varying river outflow strength. (A) Top view of a generic estuary, the dashed line indicating the narrowest point of the estuary. **(B)**, **(C)** and **(D)** Different structures of the salt wedge under increasing outflow condition. In **(B)** and **(C)**, the flow in the estuary is subcritical, whereas in **(D)**, the flow is supercritical. Adapted from Farmer (1986) and Nihoul and Ronday (1975).

2.2 Small-scale hydrodynamics

2.2.1 Turbulence

Turbulence is generated in flows where energy can be transferred from the mean motion to the turbulent fluctuations. Turbulent fluctuations induce turbulent shear stresses if a velocity gradient is present, which together provide the conditions for energy transfer. The covariances of the velocity fluctuations can be interpreted as a stress tensor, which is called the *Reynolds stress*.

Turbulent motions are three-dimensional motions characterised by so-called 'eddies', that may have a range of characteristic length scales. Since the largest length scales are the most energetic, these dominate the mixing and transport processes (Stacey *et al.*, 2012). Energy is transferred from the largest length scales to smaller scales until the molecular viscosity is able to dissipate the energy into heat at the smallest length scales. This process of transfer of energy is oftentimes referred to as the energy cascade.

The turbulent shear stress, or Reynolds stress, can also be considered analogously to the viscous shear stress, providing the eddy viscosity ν_T [m^2 s^{-1}] as a parameterisation of the eddy momentum flux. The eddy viscosity can be regarded as a product of a velocity and a length scale, giving a unit of m^2 s^{-1}. In estuarine regions subject to periodically stratified conditions, the magnitude of the eddy viscosity varies strongly over the tidal cycle. Shears are weaker during flood tides than during ebb tide due to increased mixing, and at the end of ebb tides, there is a distinct reversal of shear (Geyer and MacCready, 2014). An illustration of the evolvement of the eddy viscosity during the course of a tidal cycle is shown in Fig. 2.6.

2.2.2 Turbulence damping

Under influence of stratification, either by salinity of suspended sediment, turbulence is suppressed. Richardson (1920) first described the effect of turbulence damping in the context of an atmosphere. In a vertically stratified environment, the vertical buoyancy gradient induced by the vertical density difference stabilises turbulent exchange. This effectively means that when turbulent motions act on a two-layer flow, heavy particles are displaced from the bottom layer through turbulent motions into the lighter fluid layer, where buoyancy effects act on the heavier fluid particle to bring the fluid particle back to its initial equilibrium position. The same applies for lighter particles that are transported to the heavier fluid through turbulent motions. This effectively dampens the turbulent motions, which is referred to as turbulence damping. Stratification therefore poses an upper limit to the turbulent length scales. This limit is called the Ozmidov length scale (Stacey *et al.*, 2012).

2.3 Hydrodynamics of the Rhine-Meuse estuarine system

2.3.1 Dynamics of the North Sea

The Rotterdam Waterway is the artificial mouth of the river Rhine, which discharges into the shallow North Sea. The North Sea is a continental shelf sea of the North Atlantic Ocean, located on the Northwest European shelf. The physical state of the North Sea is essentially determined by the adjacent Atlantic Ocean and the European continent, the latter through freshwater supply and the input of suspended and dissolved matter (Quante and Colijin, 2016).

The North Sea can be divided into different regions based on the processes that dictate the physical environment. The density structure of the central part of the North Sea is determined by heating and cooling, which leads to the northern North Sea being vertically stratified in summer, and vertically mixed in winter. Conversely, strong tides keep the North Sea vertically mixed throughout the year along the western and southern parts, with the exception of the regions that are influenced by freshwater river discharge (Quante and Colijin, 2016). These distinctly different regions are schematically indicated in Figure 2.7.

The geometry of the North Sea basin gives rise to three amphidromic points. The tide penetrates the North Sea basin from the Atlantic, propagating cyclonically through the basin as a confined Kelvin wave. Interactions of the tide with wind forcing and the topography of the North Sea lead to residual currents, which circulate the water through the North Sea basin. Most of the water in the North Sea enters from the North,

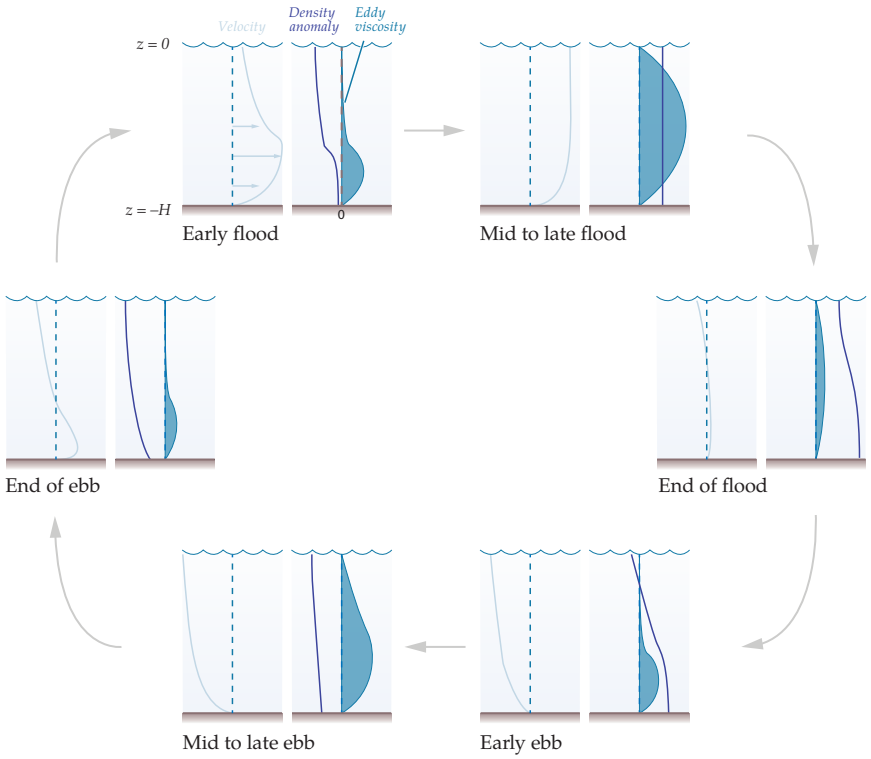

Figure 2.6: Illustration of the velocity, density anomaly and eddy viscosity profiles as they evolve throughout a tidal cycle for a partially stratified estuary. During flood tide, the water column is completely destratified, giving rise to strong mixing. At the end of flood tide, a slightly stratified profile appears, owing to lateral straining. During ebb tide, however, a strong shear develops as a result of the suppression of turbulence over the pycnocline originating from the straining of the horizontal density gradient. This increasing stratification during ebb tide results from along-channel straining. Adapted from Geyer and MacCready (2014).

and is circulated through the shallow sea on the timescale of a year (Rodhe, 2004). South-westerly winds drive a predominantly north-eastward directed flow along the Dutch coast, although persistent atypical wind forcing may induce large deviations from this typical flow pattern. The wind field also contributes to the distribution of the salinity field, both through forcing of the horizontal circulation and through the provision of kinetic energy for turbulent mixing (van der Giessen *et al.*, 1990).

2.3.2 Dynamics of the Rhine ROFI

Wherever significant amounts of buoyancy, supplied by freshwater runoff from rivers, flow out into coastal seas and oceans, they form a so-called *region of freshwater influence (Simpson* et al., *1993)* (ROFI). These river plumes can maintain their cross-shelf structure up to hundreds of kilometres out at sea, where the influence of the Earth's rotation tends to deflect the outflowing current anti-cyclonically. Changes in the amount of run-off and the intensity of tidal stirring induce alternating mixing conditions in these ROFIs. The physical regime is thus distinctly different from other parts of the shelf seas, where heating and cooling provide the predominant exchange of buoyancy.

The Rhine ROFI, a consequence of the outflowing waters of the Rhine river, extends on average 20 km along the Dutch coast, occasionally extending to a distance almost 40 km offshore (De Boer *et al.*, 2006; Simpson *et al.*, 1993; Visser *et al.*, 1994). Within the Rhine ROFI, there is a residual northward flow and the stratification is established by a competition between wind, waves and tidal mixing. Research by Simpson *et al.* (1993) established that there are two distinct timescales that determine the water column structure, one fortnightly, and the other semi-diurnal. The fortnightly time scale is controlled by tidal mixing and mixing by wind, which leads to well-mixed conditions during spring tides and storms. The semi-diurnal time scale on the other hand is related to the interactions between the 3D density structure and the tidal

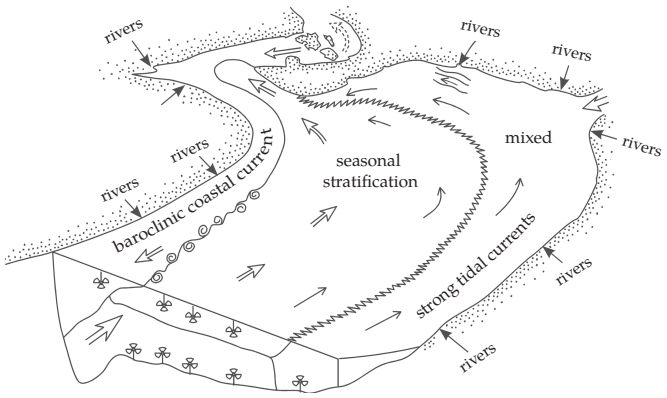

Figure 2.7: Schematic of the three main physical processes that occur in the shallow North Sea. Three different regions can be distinguished; a region where a strong baroclinic coastal current is found, a region that is seasonally stratified, and a mixed region. Adapted from Rodhe (2004).

velocity shear. Simpson and Souza (1995) first identified that this cross-shore tidal velocity shear induces an interaction pattern between the tide and the 3D density field in the Rhine ROFI, which in turn induces an alternating advection pattern of fresh coastal waters. This process had previously been labelled by Simpson *et al.* (1990) as tidal straining.

The process of tidal straining gives rise to a semi-diurnal SIPS signal in the Rhine ROFI. In the Rhine ROFI specifically, not only SIPS is important for the evolution of the stratification, but the along-shore advection is also dominant. This leads to the concept of *advection and strain induced periodic stratification (de Boer* et al., *2008)* (ASIPS).

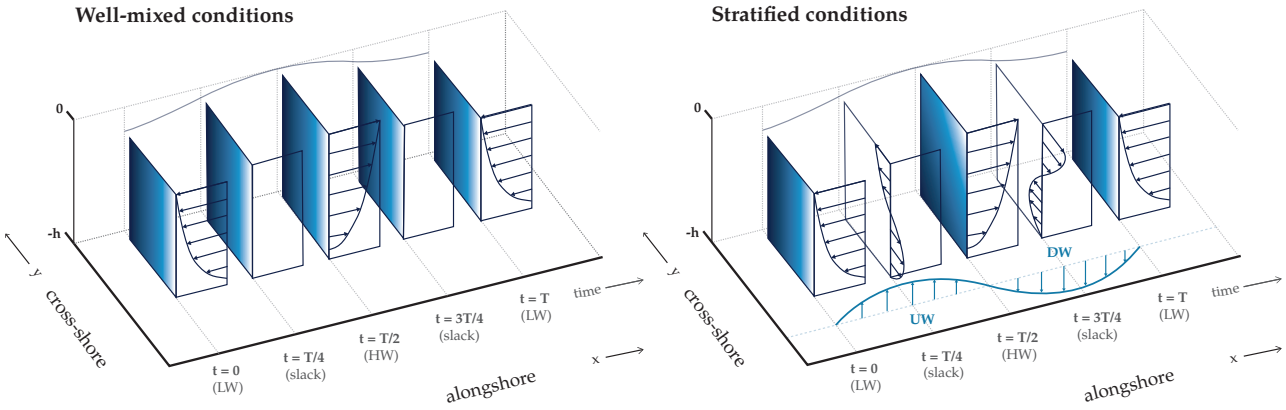

Figure 2.8: Overview of currents and stratification in a ROFI. **(A)** Well-mixed conditions prevail in the Rhine ROFI. There is no interaction between the alongshore ebb and flood velocities and the average cross-shore density gradients. **(B)** Stratified conditions prevail in the Rhine ROFI. Tidal straining (Simpson *et al.*, 1990) occurs due to interaction between the cross-shore velocity shear and the average cross-shore density gradients. The resulting cross-shore currents lead to coastal upwelling and downwelling, indicated by UW and DW respectively. Adapted from de Boer (2009).

During spring tide conditions, the Rhine ROFI is well-mixed over the vertical, which is referred to as the *bottom-advected* state. During reduced neap tide mixing levels, the ROFI is allowed to stratify, a state which is also known as *surface-advected* (Yankovsky and Chapman, 1997). During stratified conditions of the Rhine ROFI, cross-shore currents lead to coastal upwelling and downwelling (de Boer *et al.*, 2009).

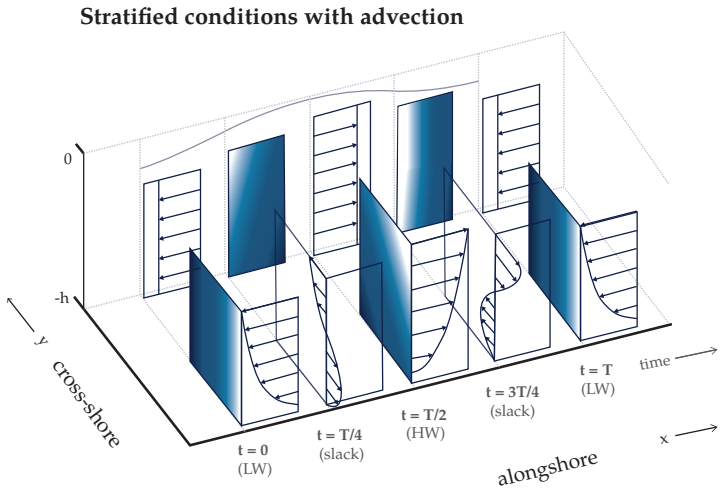

Figure 2.9: Overview of currents and stratification in the Rhine ROFI under stratified conditions. In the site-specific configuration, the effect of tidal straining is combined with along-shore advection. Cross-shore straining alone establishes maximum stratification at high water ($T/2$), whereas the along-shore straining and advection operate together to establish maximum stratification at slack ($3T/4$). Adapted from de Boer (2009).

2.3.3 Flow structure in the Rotterdam Waterway

Estuary classification

Estuaries are transitions between rivers and seas, where there is a constant exchange between a tide-driven saltwater flux and a freshwater flux that flushes the saltwater back (Savenije, 2008). The Rotterdam Waterway can be classified as a meso-tidal estuary, which has a tidal range between two and four meter (de Nijs *et al.*, 2005; Savenije, 2008). In the Rotterdam Waterway—and in estuaries in general—the competition between turbulent mixing and stratifying processes due to barotropic and baroclinic forcing determines the estuarine salt balance and the resulting stratification, and furthermore has important implications or the transport of SPM.

Tidal structure

Harmonic analysis presented in de Nijs *et al.* (2010b) indicates that the tidal wave has characteristics of both progressive and standing waves as it progresses upestuary. This shift is ascribed to the large number of harbour basins lining the New Meuse. Furthermore, the measurements presented in de Nijs *et al.* (2010a) show that the tidal wave is already deformed before it enters the Rotterdam Waterway, which is ascribed to the shallowness and interaction with topography in the coastal zone. Harmonic analysis also indicated that the phase differences between water levels related to the M_2 and M_4 tidal constituents is such that the tide rises faster than it falls, which means that a barotropic tidal asymmetry is present in the Rotterdam Waterway. In combination with the effect of the regulated freshwater discharge at Lobith, this barotropic tidal asymmetry causes a larger ebb than flood duration. This tidal asymmetry is clearly illustrated by Figure 2.10, which is reconstructed from time series measurements in the Rotterdam Waterway in 2006 (de Nijs *et al.*, 2010a).

Research by de Nijs *et al.* (2010b) shows that close to the harbour mouth, this barotropic tidal asymmetry leads to ebb dominance in the upper part of the water column, whereas flood dominance occurs in the lower part of the water column. Higher up-estuary however, the freshwater discharge dominates over the effects of the barotropic tidal asymmetry, and measurements indicate a larger ebb period than flood period over the entire vertical.

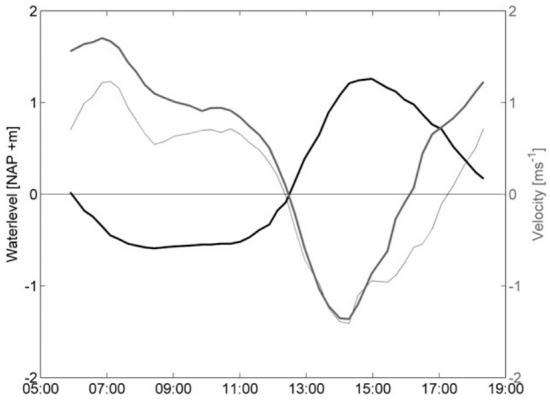

Figure 2.10: Figure indicating the occurrence of tidal asymmetry in the Rotterdam Waterway. Indicated are a time series of water level (black) and two velocity time series at 2.5 m above bed (dashed grey) and at 12.5 m above bed (thick grey) as measured during a survey conducted on 11 April 2006. Image taken from de Nijs *et al.* (2010a).

Internal flow structure

Within the Rotterdam Waterway, the barotropic tidal asymmetry imposed at the mouth governs the advection of the salt wedge (de Nijs *et al.*, 2010a). This barotropic asymmetry influences the internal flow structure and causes asymmetries therein. In combination with the phenomenon of turbulence damping as described by Geyer (1993) at the pycnocline, the barotropic advection of the salt wedge results in the formation of exchange flows driven by the along-channel baroclinic pressure gradient, and mid-depth jets. Tidal asymmetries in turbulent mixing, stratification and pycnocline height also develop as a consequence of this barotropic tidal asymmetry.

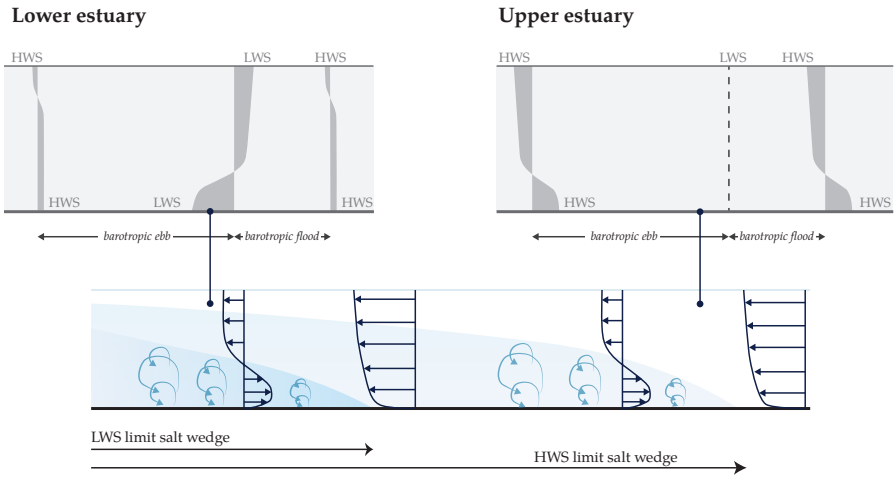

Figure 2.11: Relationship between the tidal advection of the salt wedge and the evolution of the internal baroclinic structure in the Rotterdam Waterway. Adapted from de Nijs *et al.* (2010a).

The largest baroclinic pressure gradients are measured at the head of the salt wedge, like is typically the case. At the limit of saltwater intrusion, a baroclinically driven exchange-type flow is superimposed on the barotropically driven tidal flow, which governs the vertical distribution of the along-channel flow around slack water. These superimposed baroclinic effects lead to near-bed flow convergence and divergence in the upper part of the water column through the retardation of flow reversal. Maximal velocities are observed at the pycnocline during flood, which indicates a distinct decoupling of brackish and saltwater and local turbulence dampings (de Nijs *et al.*, 2010a). The internal shear induced by the maximal velocities results in additional advective transport from the pycnocline towards regions of lower momentum. Furthermore, velocity measurements presented in de Nijs *et al.* (2010b) indicate that bed-generated turbulence is mainly

confined to the region below the pycnocline.

As was mentioned in Subsection 2.2, the values of the Reynolds stress are an indicator for the amount of turbulence present. In the Rotterdam Waterway, the maximal Reynolds stress value is lower during ebb than during flood, and occurs somewhat higher above the bed. This is a result of the fact that the baroclinic pressure gradient opposes the barotropic pressure gradient during ebb, whereas it reinforces the baroclinic pressure gradient during flood. It was observed by de Nijs *et al.* (2010b) that the pycnocline position in the water column controls the distribution of the turbulent viscosity.

Salt wedge structure

In the Rotterdam Waterway, the salt wedge structure remains stable during the tidal cycle. The salt wedge structure that is apparent in the Rotterdam Waterway is displaced some 16 km back and forth by the tide at the dominant semidiurnal time scale (de Nijs *et al.*, 2010b). The periods with pronounced exchange flow-type shear are short, since they are limited to the periods around slack water, which in turn limits interfacial mixing. Due to the limited amounts of mixing at the pycnocline, the salt wedge structure does not break down during a tidal cycle, and advection likely controls changes in the vertical salinity structure at a particular location (de Nijs *et al.*, 2010b). Especially during ebb and flood advection periods, the growth rate of the pycnocline height is primarily governed by advection effects (de Nijs *et al.*, 2010a).

2.4 Summary

In estuaries, a competition between the horizontal density gradient and turbulent mixing leads to a well-known circulation pattern that is the subject of many studies—the estuarine circulation. The driving mechanisms of this circulation pattern, however, are still not fully understood, and vary from estuary to estuary.

The Rotterdam Waterway can be classified as a meso-tidal estuary with a tidal range between two and four meters (de Nijs *et al.*, 2005; Savenije, 2008). A competition between turbulent mixing and stratifying processes as a result of baroclinic and barotropic forcing determines the estuarine salt balance.

The barotropic tidal asymmetry imposed at the mouth of the Rotterdam Waterway governs the advection of the salt wedge, which is stable throughout the tidal cycle. The barotropic asymmetry of the tide has important implications for the internal flow structure in the Rotterdam Waterway, and causes asymmetries therein. Because of this, the ebb tide duration is longer than the flood tide duration. Close to the river mouth, the effect of tidal asymmetry is visible as flood dominance in the lower part of the water column and ebb dominance in the upper part of the water column. Farther upestuary, however, the effect of the freshwater discharge is higher than the effect of the barotropic tidal asymmetry, leading to a larger ebb period than flood period over the entire vertical.

At the limit of saltwater intrusion, baroclinically driven exchange flows are superimposed on the barotropically driven flow. The effect of these exchange-type processes is mainly felt during flow reversal, where it leads to near-bed flow convergence and near-surface flow divergence.

Chapter 3

Estuarine sediment dynamics

This chapter covers the main relevant sediment dynamic processes that can occur in estuarine environments such as the Rotterdam Waterway. This chapter has a different set-up than was used in Chapter 2; here, use is made of a more bottom-up approach by first discussing the small-scale cohesive sediment dynamics before discussing the relevant large-scale cohesive sediment dynamics. First, Section 3.1 goes further in-depth about the small-scale sediment dynamic processes that may be relevant in the context of the SURICATES project. Next, Section 3.2 covers the large-scale sediment dynamic processes. With large-scale sediment dynamics we refer to the processes governing large-scale SPM fluxes in estuarine systems. Lastly, Section 3.3 describes how these large-scale and small-scale processes contribute to sedimentation in the Rotterdam Waterway and its surrounding harbour basins. A summary of the most relevant processes and their interplay in the Rotterdam Waterway is given at the end of this chapter.

3.1 Small-scale cohesive sediment dynamics

To be able to understand the large-scale processes, it is crucial to understand the interactions occurring at the micro-scale. The processes that are of key importance are the vertical processes occurring in the water column, the processes in and on the bed, and the exchange of sediments between the bed and the water column. An overview of the main processes governing fine sediment dynamics, and the competition between these processes, are depicted in Figure 3.1.

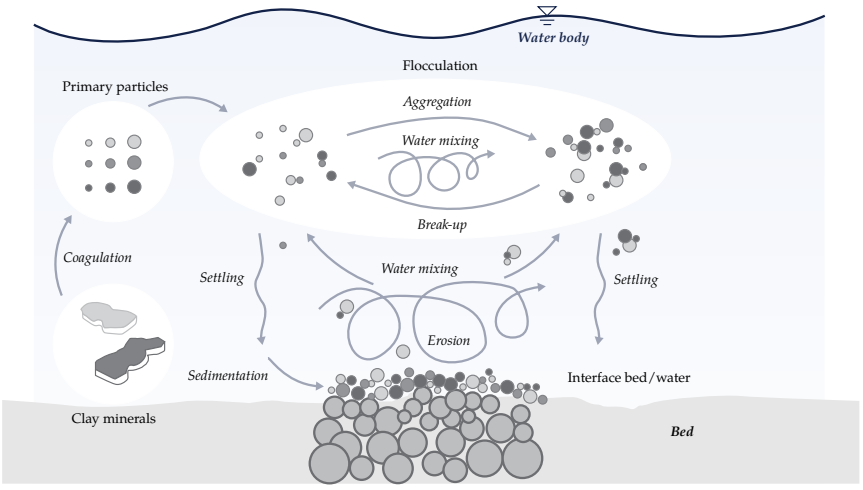

Figure 3.1: Overview of the main small-scale sediment processes that are of influence on fine sediments. Adapted from Maggi (2005).

3.1.1 Coagulation

Cohesive sediment is made up of predominantly clayey particulate matter. Cohesive sediment, sometimes referred to as mud, materialises as a mixture of a mixture of many different elements and particles—

organic and non-organic compounds, silt, sand, water, and gas (Maggi, 2005; Winterwerp, 2011). The components of mud can therefore be seen as minuscule ecosystems, filled with different kinds of bacteria, viruses and algae. The exact composition of cohesive sediment may vary; it is even found in Winterwerp and van Kesteren (2004b) that seasonal effects may affect the composition of these sediments. The smallest—solid—constituents of cohesive sediment are clay particles, which are largely responsible for the cohesion properties. Organic bounds may also contribute to cohesion. Clay particles, in turn, are made up of small board-shaped particles (clay minerals) that may coagulate into larger primary particles. Usually, the minerals that make up these particles are connected face-to-face; although edge-to-edge or face-to-edge connections are also possible, the face-to-face connection gives the particles high resilience.

Once these primary particles are formed, they may subsequently be exposed to the process of aggregation, under the influence of which larger aggregates are formed (flocs).

3.1.2 Flocculation processes

Flocs are formed through *aggregation* and *breakup*, the net effect of which is called *flocculation*. Aggregation and break-up are examples of flocculation processes (Maggi, 2005). Both of these processes are briefly discussed below.

Aggregation

The collision amongst particles is the most influential mechanism contributing to the aggregation of particles. In turn, the collision of particles is dependent on the intensity of the turbulent motions and gravity. Collision itself, however, does not inherently induce aggregation; the collision efficiency, usually expressed as an empirical coefficient, is used to express the likelihood of aggregation. Aggregation of flocs is impacted by several factors that may increase the collision frequency of individual flocs; turbulent diffusion, differential settling, and Brownian motion (Winterwerp and van Kesteren, 2004b). Differential settling entails the effect that larger flocs take over smaller flocs because of their larger settling velocity. However, the chances of a smaller particle colliding with a larger particle are small because the trajectory of the smaller particle is deflected around the trajectory of the larger particle. In estuarine environments, the effect of Brownian motion and differential settling on the aggregation of particles are likely negligible (Winterwerp, 2002).

Break-up

Besides contributing to aggregation of particles, turbulent motions may also induce the break-up of particles when particles are not able to resist the shear stresses brought about by the turbulent motions. Another process that may bring about break-up—or *disaggregation*—is due to the collision of particles with each other (Maggi, 2005). The former process is usually described using a *linear* break-up frequency, while the latter is described using a *non-linear* break-up frequency (Maggi, 2005).

3.1.3 Settling and sedimentation

After flocs are formed, they may "fall"; they *settle*. A universal settling velocity of cohesive sediments does not exist. The settling velocity of cohesive sediments is not only dependent on flocculation and hindered settling, but it is also not a unique parameter, since the settling velocity is actually characterised by an often bimodal distribution (Winterwerp, 2011). Therefore, the settling velocity is often determined from floc size distributions using Stokes' law or determined empirically for the calibration of numerical models. After these flocs have settled accumulated they may *sediment*, which means that they become a part of the bed layer.

3.1.4 Erosion and entrainment

If the rate of shear has reached certain magnitude, light aggregates that have become a part of the bed layer are lifted up from the interface between the bed and the water column; this process is called *erosion*. In the natural environment, erosion occurs under the action of shear stresses imposed at the bed-water interface

by waves and currents (Mathew and Winterwerp, 2017). Four different modes of erosion can be discerned. In increasing order of magnitude of shear stress responsible, these are floc erosion, surface erosion, mass erosion and liquefaction (Winterwerp and van Kesteren, 2004a).

Floc erosion is referred to as the process in which part of the flocs of a fine sediment are individually disrupted at the bed surface, which erodes individual flocs. This process is continuous and although floc erosion rates are commonly not very large, the continuous nature of the process may greatly add to the overall erosion process. *Surface erosion* is a so-called drained failure process, that occurs when the top of the bed liquefies. This liquefaction can either be induced by swelling of the top of the bed, or of a result of hydrodynamic pressure fluctuations induced by e.g. wave and current induced bed shear stress. This process is referred to as 'drained' because the material is able to adapt to the fluid forcing before it is eroded. Conversely, *mass erosion* is an undrained failure process, that principally occurs under the action of turbulent flow over an irregular bed. The process of mass erosion is brought about when external stresses exceed the undrained shear stress of the bed (Winterwerp and van Kesteren, 2004a). Lastly, total liquefaction of the bed may occur due to cyclical loading of the bed. This type of erosion may also be referred to as *undrained bulk erosion*. The process of liquefaction is still not well understood, since the history of loading of the bed also plays a role in this process.

3.2 Large-scale cohesive sediment dynamics

3.2.1 Estuarine Turbidity Maximum (ETM)

A distinct feature of many estuaries is an ETM, which is an SPM balance on the freshwater-saltwater interface that is maintained by landward directed transport processes against the tidally averaged seaward discharge (de Nijs and Pietrzak, 2012). An ETM is formed through trapping of SPM at the tip of the salt wedge through turbulence damping at the pycnocline, a mechanism that was first described by Geyer (1993). Near the pycnocline, salt stratification reduces the turbulent diffusion locally, causing a reduction in the amount of sediment that can be carried by the flow. This leads to local trapping of SPM beneath the pycnocline. This mechanism was recently extended by de Nijs *et al.* (2010b) to a relatively narrow salt wedge estuary that is strongly forced by a barotropic tide, as is the case in the Rotterdam Waterway.

3.3 Sediment dynamics in the Rotterdam Waterway

3.3.1 Sediment characteristics

Fine sediments may originate from several different sources. In general, three different sources are distinguished in the estuarine environment. Fine sediments can be of fluvial origin, can be of marine origin or can be autochthonous. Sediments from different origin may exhibit different soil mechanical and hydrodynamic behaviour.

Tracer analysis indicated that in the harbours lining the Rotterdam Waterway, predominantly SPM of fluvial origin is dredged (de Nijs *et al.*, 2010b), although in the Maasmond and the harbour basins close to the Maasmond (Maasvlakte and Europoort harbour) mainly sediments of marine origin are found (de Nijs and Pietrzak, 2012; Spanhoff and Verlaan, 2000). These marine sediments are likely advected into the harbour basins by tidal currents and fluid mud processes (Spanhoff and Verlaan, 2000). These near-bed suspensions rarely make it into the Rotterdam Waterway, since the large depth difference between the Maasmond area and the Rotterdam Waterway prevent them from propagating further land inward (de Nijs *et al.*, 2010b).

Furthermore, the Rotterdam Waterway itself does not function as a complete fluvial SPM trap. Sediment balances presented in de Nijs *et al.* (2010b) indicated that the annual influx of SPM into the Rotterdam Waterway exceeds the siltation rates in the channels and harbours lining the Rotterdam Waterway. Approximately 50% of the annual fluvial SPM influx is able to leave the Rotterdam Waterway through the junction with the New Meuse through excursions of the salt wedge. The harbour basins, however, do function as a complete fluvial SPM trap, which leads to very distinct transitions between the Rotterdam Waterway and the harbour basins lining the Rotterdam Waterway. The Rotterdam Waterway has a sandy bed, whereas the harbour basin beds are predominantly muddy.

3.3.2 ETM formation

ETM formation in the Rotterdam Waterway is closely related to the phenomenon of turbulence damping (Geyer, 1993), through which SPM is trapped underneath the pycnocline (de Nijs *et al.*, 2010b). As was mentioned in Subsection 2.3.3, the baroclinic pressure gradient and the damping of turbulence at the pycnocline combined induce vertical velocity shear during ebb tide, which encourages differential advection of SPM over the salt wedge while retarding near-bed currents. This effect leads to near-bed velocity and transport gradients that are directed into the salt wedge during ebb, which induces horizontal trapping. The exchange flows caused by the baroclinic pressure gradient at the head of the salt wedge drive near-bed convergence of transports and relative motion between salt and freshwater layers. Both these processes contribute to SPM trapping and thus to ETM formation. The barotropic asymmetry of the tide imposed at the mouth establishes a time scale on the advection of the salt wedge, and thus to the advection of the ETM.

A relatively large amount of fluvial SPM is constantly supplied to the ETM, which keeps the ETM maintained even when the marine SPM supply is limited. However, if the saline water persistently passes the junction of Rotterdam Waterway-Old Meuse for periods exceeding the tidal period, the ETM and the corresponding longitudinal salinity front break up in patches. This may lead to temporary local salinity-induced trapping of SPM, indicating temporary multiple ETMs in the Port of Rotterdam (de Nijs *et al.*, 2009).

3.3.3 SPM concentrations

SPM concentrations in the Rotterdam Waterway vary throughout the tidal cycle, although background concentrations remain relatively low. The SPM concentration also decreases seaward. All of the sediment that is settling on the bed at slack water is kept in suspension during the ebb-flood advection periods, which means that deposition before slack and entrainment after slack are approximately equal. This is the case for both slack tides, at *high water slack* (HWS) and *low water slack* (LWS).

The magnitude of SPM concentration is regulated by a complex interplay between the absence of supply of SPM at the bed, advection of the salt wedge and the dynamics of SPM within the associated ETM. The dynamic processes within the ETM that are relevant include the deposition, resuspension and the exchange between ETM and adjacent harbour basins. The limited bed-based supply of SPM is mainly related to the exchange mechanisms between ETM and harbour basins as well as to the associated dredging operations (de Nijs *et al.*, 2010b).

3.3.4 Flocculation

Even though a permanent salt wedge is present in the Rotterdam Waterway (de Nijs *et al.*, 2010a), there is no evidence of salt-induced flocculation processes occurring (Eisma *et al.*, 1980). It has been hypothesised that the effect of salt-induced flocculation on the contact of fresh river water with the salty sea water is reduced due to the pollution of the Rhine river with sea salt (Eisma *et al.*, 1980). Flocculation processes in high energy estuaries, such as the Rotterdam Waterway, are mostly regulated by SPM concentration and shear rate (de Nijs *et al.*, 2010b).

Observations by Eisma *et al.* (1980, 1991) and van Leussen (1994) showed a gradual seaward increase in the percentage of fine floc aggregates and a decrease of the percentage of macroflocs near the surface. These observations are in line with observations by De Nijs and Pietrzak (2011), which indicated the production of turbulence in the region of high shear rates around the pycnocline. This may imply that the turbulence generated locally breaks up fragile macroflocs.

3.3.5 Harbour siltation

Research by de Nijs *et al.* (2005), conducted at the entrance of the Botlek Harbour, showed that salinity-induced density gradients are the dominant mechanism that causes high siltation rates in the Botlek Harbour. The Botlek harbour is located at the salt intrusion limit, which leads to tidal filling and emptying by baroclinically driven exchange processes. The ETM is an advective phenomenon that determines the avail-

ability of SPM that can be exchanged with the harbours lining the Rotterdam Waterway, and the saltwater intrusion length is one of the key parameters controlling the SPM trapping probability. The trapping efficiency of the Rotterdam Waterway and the availability of SPM in front of the harbour mouths is determined by this saltwater intrusion length, as was showed by de Nijs *et al.* (2010b). In turn, the saltwater intrusion length is determined by the forcing conditions imposed at the boundaries and the hydrodynamic history.

3.4 Summary

To be able to interpret the results of SPM measurements, this chapter introduces some general terms and definitions concerning estuarine sediment dynamics. We constrict ourselves to understanding the behaviour of cohesive sediments—also sometimes referred to as *mud*.

Cohesive sediment is made up of predominantly clayey particulate matter, although it is rather a mixture of organic and non-organic compounds, silt, sand, water, and gas. The main small-scale processes that may influence the composition of cohesive sediments—that are discussed here—are flocculation processes, such as aggregation and break-up, settling, sedimentation, and erosion.

There is no evidence of salt-induced flocculation processes occurring in the Rotterdam Waterway, specifically. It is hypothesised that amount of salt-induced flocculation is reduced due to the pollution of the Rhine river with sea salt, which causes flocculation farther upestuary.

On a larger scale, cohesive sediments may be trapped in an estuarine turbidity maximum (ETM), which is essentially a balance of SPM that is formed at the interface between freshwater and saltwater. Such an ETM is maintained by the competition between landward directed transport processes and the tidally averaged seaward discharge.

In the Rotterdam Waterway, specifically, ETM formation is closely related to the phenomenon of *turbulence damping* at the pycnocline (*see* Chapter 2). The ETM is formed by the near-bed convergence of transports at the limit of saltwater intrusion as a result of exchange flows caused by the baroclinic pressure gradient at the head of the salt wedge. If the salt wedge persistently passes the junction Rotterdam Waterway-Old Meuse, the longitudinal salinity front—and with it, the associated ETM—breaks up into multiple smaller ETMs. Furthermore, outside of the ETM region, SPM concentrations generally remain low, but do vary throughout the tidal cycle. SPM is kept in suspension during the ebb-flood advection periods, and settles during LWS and HWS.
Harbour siltation is also closely related to the ETM in the Rotterdam Waterway. The harbour basins located at the salt intrusion limit are filled and emptied throughout the tidal cycle as a consequence of baroclinically driven exchange flows. The SPM transported at the salt intrusion limit—in the ETM—may be exchanged with the harbour basins as a result of such exchange flows.

Part II

DATA ANALYSIS & MODEL SET-UP

This part considers the *methodology* used to answer the posed research questions. The approach taken to answering these questions is discussed here, leading to a sound basis for the synthesis of results.

Chapter 4

Internal flow structure analysis

This chapter is mainly dedicated to the introduction of the used dataset, pre- and postprocessing methods, and the analyses used to derive what processes govern the hydrodynamics in the New Waterway. Section 4.1 introduces the survey set-up, the hydrodynamic conditions during the survey, and the instruments used. Section 4.2 covers the pre- and post processing methods used on the dataset. Then, Section 4.3 summarises all parameters considered in the analysis of the dataset, after which Section 4.4 lastly covers the calculation of all considered parameters.

4.1 Dataset(s)

The harbour authority, in combination with Rijkswaterstaat, has multiple monitoring systems set in place to ensure the continuation of all harbour activities. These monitoring systems consist of fixed sensors measuring several flow characteristics, such as height of tide, temperature, pressure, wind, tidal stream, waves or salinity. The sensors either line the Rotterdam Waterway or are located in harbour basins, and may also be positioned at different heights at the same geographical location. Furthermore, incidental along-channel measurements are done when commissioned by the harbour authority under special circumstances, e.g. when critical weather conditions persist or when specific research is being executed.

In order to obtain a better understanding of the (interplay between) the governing hydrodynamic processes and their effect on the dispersion and trapping of SPM in the Rotterdam Waterway, several boat surveys have been executed during the course of the SURICATES pilot project. One of these boat surveys has been made available for analysis in this thesis. This survey was specifically executed with the aim to acquire insight into the internal flow structure and hydrodynamics.

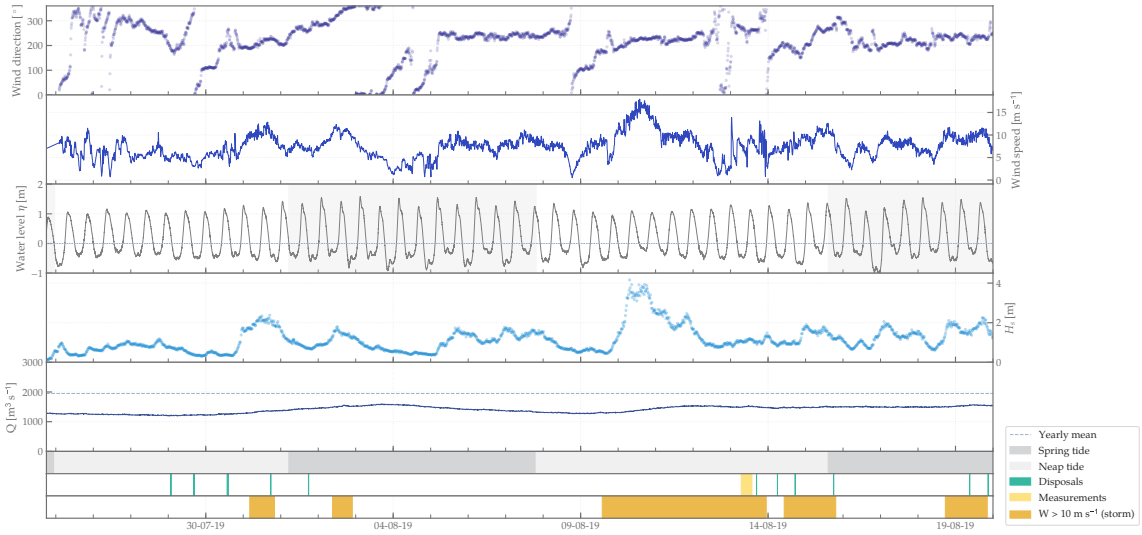

Figure 4.1: Plots of water level at Hoek van Holland, discharges at Lobith and wind conditions at Noorderpier in the weeks prior to and after the August 13th measurement campaign. Several durations are highlighted; disposal durations, measurement campaigns, storm conditions, and the spring-neap tidal cycle.

Figure 4.2: Overview maps of the Port of Rotterdam, the study area of this research. (**A**) Overview map of a larger part of the Rhine-Meuse estuary. (**B**) Zoom view of the study area of this thesis, including the New Waterway, New Meuse, and Old Meuse. Indicated in this figure are the measurement locations of the incidental along-channel salinity and velocity measurements conducted on August 13th, 2019, as well as the fixed salinity and water level measuring stations.

4.1.1 Internal flow structure survey

Survey set-up and hydrodynamic conditions

A special 7-h boat survey was carried out on August 13th, 2019, from 06:57 UTC to 13:29 UTC, at times of relatively low discharges. The Rhine discharge at the day of the survey was approximately 1500 m^3s^{-1}, whereas the average annual discharge at Lobith in 2019 was equal to approximately 1960 m^3s^{-1}. In the weeks preceding the measurements, the discharge at Lobith fluctuated between 1200 m^3s^{-1} and 1550 m^3s^{-1} (see Fig. 4.1). The mean water level at Hoek van Holland fluctuated between -0.48 m NAP and +1.11 m NAP during the survey, which is representative of a situation of moderate tidal conditions (not at neap or at spring tide).

The mean wind speed during the two weeks preceding the survey was 7.64 m s^{-1} and the average wind direction was at an angle of 209.88°. Although the wind field had a general relatively uniform shape, distinct outliers are also visible. On the day of the survey itself, the average wind speed was 7.44 m s^{-1} and the average wind direction was 266.08°. The wind field was largely uniform during the survey, as can be seen from Fig. 4.1.

For the survey, a boat navigated the Rotterdam Waterway along a track starting at Botlek harbour and ending at Hoek van Holland. Botlek harbour was chosen as a starting point so that the boat would travel with the salt wedge as much as possible. This style of measurements corresponds to a Lagrangian description, as presented in research by de Nijs *et al.* (2005, 2010b). The boat navigated the track three times in total, starting and ending at Botlek harbour.

CTD measurements were conducted at specific sites along the longitudinal axis of the Rotterdam Waterway. These sites were chosen such that they were spaced 1 km apart (equidistantly) within a 5-km range around the approximate SURICATES reallocation location. The geographical measurement locations logged by the

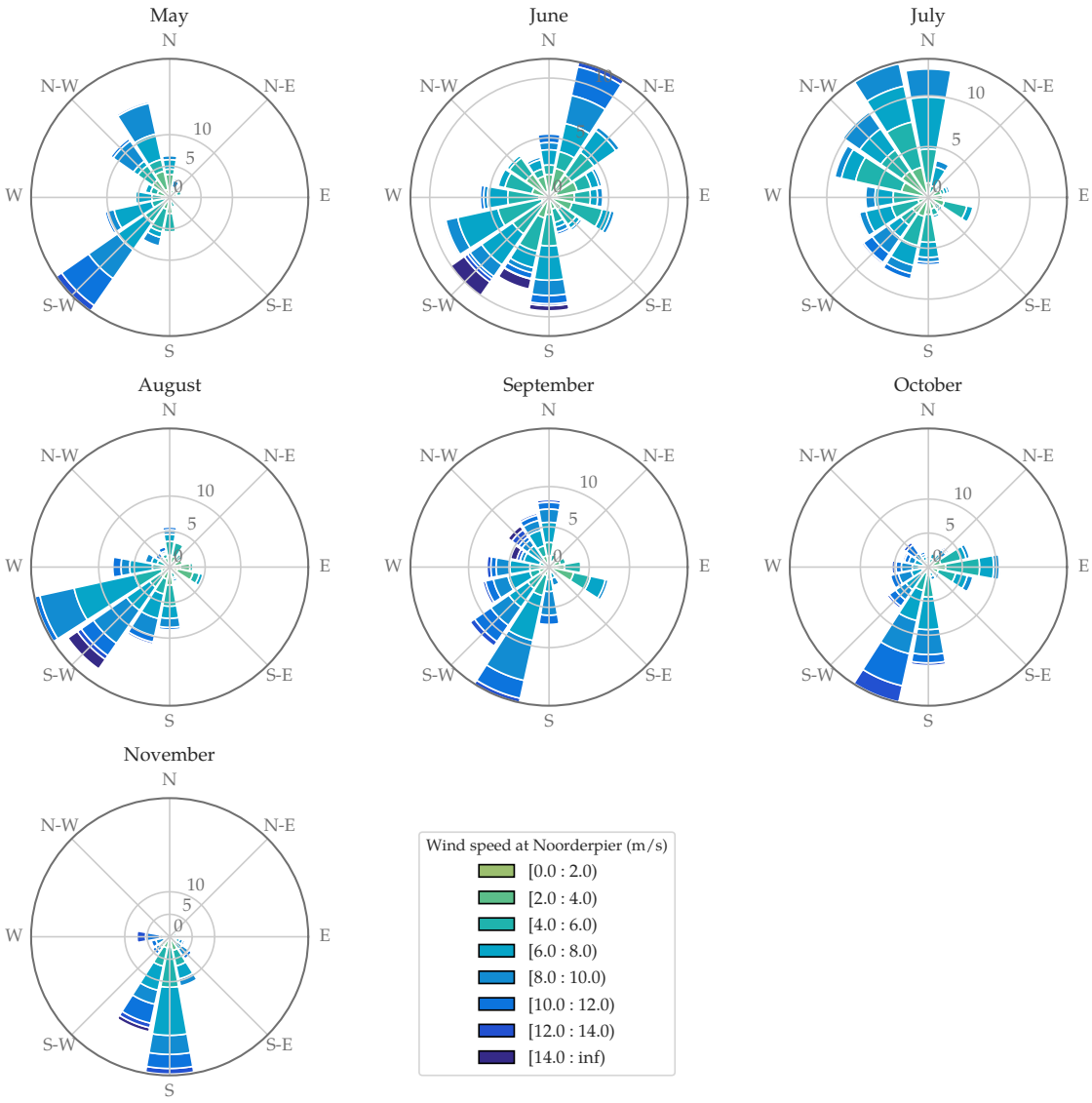

Figure 4.3: Wind roses depicting the wind conditions per month, for the months May 2019 to November 2019. Different colours indicate bins of different wind speed.

boat during the survey are indicated in Fig. 4.2B. Whilst navigating between these measurement locations, an ADCP was used to obtain along-channel velocity profiles. Additional measurements were done on the Rotterdam Waterway channel axis near Hoek van Holland, to serve as comparative measurements for the data obtained from the fixed measuring station at Hoek van Holland.

Instruments and procedures

Siltprofiler turbidity measurements Because the SPM concentration range in estuarine environments is very large, conventional turbidity instrument packages are often not very reliable (de Nijs *et al.*, 2010b). Such instrument packages often also lack a high (enough) vertical resolution, which in turn affects the capability to detect pycnoclines and lutoclines. The Siltprofiler is a measuring device developed by Deltares (formerly Delft Hydraulics) in combination with Ravensrodd Consultants, Ltd., and is equipped with several high-frequency turbidity sensors that are able to sample at high frequencies of 80-100 Hz (de Nijs *et al.*, 2010b).

Five different sensors are mounted on the Siltprofiler: one CTD (including Chlorphyll sensor), one sound velocity profiler, two turbidity sensors, or OBS sensors, and a transmission probe for the high-

est SPM concentrations. Moreover, three Niskin water samplers, each with a volume of 1.8 litre are mounted on the Siltprofiler (Borst and Vellinga, 2013), which can be used to calibrate the Siltprofiler. The Siltprofiler was last calibrated on May 17th, 2019, with four silt samples obtained from the Eemhaven.

The working principle of the two turbidity OBS sensors is based on the detection of scattered infrared light by particles. The OBS consists of an infrared emitting diode and four detecting photodiodes, between which information is exchanged. Because the amount of scattering is determined by parameters such as the composition, size and shape of the measured particles, the OBS sensors have to be calibrated. Each of the three turbidity sensors mounted on the Siltprofiler covers a separate measuring range. The $0 - 0.04$ g l^{-1} range and the $0.04 - 0.165$ g l^{-1} measuring range are covered by Seapoint OBS sensors, and the highest SPM concentrations are measured using a transmission probe. The Siltprofiler is deployed freefalling, after which it is hauled up again. The sensor data are transmitted after the Siltprofiler resurfaces by use of wireless Bluetooth transmission (de Nijs *et al.*, 2010b).

Conductivity, Temperature, Depth The CTD sensor is a CastAway CTD with a sampling rate of 5 Hz, manufactured by Sontek (SonTek, San Diego, USA; http://www.sontek.com). The salinity and temperature accuracy stated by the manufacturer are 1.1 PSS and 0.05°C respectively. Latitude and longitude information is acquired before and after deployment, which is used to calculate the average deployment position.

Sound velocity profiler The sound velocity profiler mounted to the frame is a Valeport SWiFT *Sound Velocity Profiler* (SVP) (Valeport Ltd., Totnes, United Kingdom; https://www.valeport.co.uk). This SVP covers a range of 1375-1900 m s^{-1}, has a resolution of 0.001 m s^{-1} and the manufacturer states an accuracy of $\pm$0.02 m s^{-1}.

Boat-mounted ADCP measurements ADCP data were gathered using a boat-mounted 600 kHz Workhorse ADCP by Teledyne RD Instruments (Teledyne Technologies International Corp., Thousand Oaks, USA; http://www.teledynemarine.com/rdi/). This two-beam ADCP was mounted to the boat at an angle of 34.57 degrees. The ADCP was active during the entire monitoring survey: both when stationary at locations 1014-1024, and whilst navigating between subsequent locations. Because this specific ADCP only has two beams, vertical velocities were not recorded.

For these measurements, an ensemble time of 5 seconds, 10 water pings per ensemble and a depth bin size of 0.5 m were used. The depth range was set to 60 bins. With these settings, an average of 60 velocity profiles between each of the measuring locations were obtained, each with a depth range of approximately 12.5 m. The blanking distance of these measurements amounted to 44 cm. The ADCP was also measuring during CTD measurements, which yielded velocity time records of 5-10 minutes. On average, these time records contain 100 ensembles.

Besides the application of ADCPs to measure velocities, they can also be used for the estimation of SPM concentrations (Deines, 1999). To do so, the acoustic backscatter strength is used. The ADCP's emitted sound pulse is scattered by SPM present in the water column, changing the amount of energy in the sound pulse. By comparing the emitted acoustic energy with the retrieved acoustic energy, the ADCP is able to relate the change in energy to the amount of scattering. After a scaling procedure using the speed of sound in water, sound propagation characteristic and the scattering strength, a relationship between the amount of backscatter and the SPM characteristics can be determined. Several studies have elaborated on finding suitable relationships (Hoitink and Hoekstra, 2005; Park and Lee, 2016, and references therein), finding that ADCPs with 0.3-2.4 MHz frequencies are in many cases sufficiently able to estimate SPM concentrations from backscatter data.

4.2 Data processing

4.2.1 Pre-processing of raw data

Both the CTD and ADCP sensors used during the measurement campaigns create output files with raw data. This raw data is still erratic, and needs to be processed before it can be used for further computa-

tions. The data is therefore processed following a multi-step processing routine carried out by the Port of Rotterdam. Following these steps, data is obtained at different levels of processing. For the CTD sensors, the levels at which data are stored are:

Level 0: Original raw data per sensor. These entail the directly measured quantities of conductivity, temperature, pressure and sensor settings;

Level 1: Raw data is processed to remove spikes (low-pass filtered), down and upcasts are combined into vertical bins based on pressure and averaged into a single value, data in the air is eliminated by calculating the rate of change of pressure versus time, and pressure is corrected for the atmospheric pressure. Furthermore, the specific conductivity, salinity, sound speed, density and depth are derived;

Level 2: The down and upcasts are combined in one profile using an algorithm that takes a weighted average of the down and upcasts based on their fall velocity. Upcasts are more heavily weighted near the surface and downcasts are more heavily weighted near the bottom, reducing the effects of air bubbles at the surface and turbulence near the bottom (Son, 2012). The files are then saved as `.csv` files.

For the boat-mounted ADCP sensors, the pre-processing levels are:

Level 0: Original raw data per sensor. These entail the directly measured quantities of the beams and external data such as the *global positioning system* (GPS) data, speed of the vessel, course of the vessel, and the heave, pitch and roll variables of the vessel.

Level 1: Data is processed using the program 'VISEA DAS', where data is checked for consistency and ensembles are averaged over 10 ensembles.

Level 2: Output from the 'VISEA DAS' program is processed in the program 'VISEA DPS'. All remaining irregularities are removed. Files are saved as `.type2` files.

4.2.2 Principal component analysis (PCA)

To obtain the principal velocities, i.e. the velocity along the x-axis in an along-channel coordinate system, the measured velocities need to be transformed from a North-West local coordinate system to an along-channel versus cross-channel coordinate system. To do so, it is assumed that the velocity variance is largest in the direction of the channel axis. Under this assumption, the along-channel direction can be found by performing a PCA.

PCA is a dimensionality reduction method that is most often used to transform a large set of variables into a smaller set of variables whilst retaining most of the information of the large set. PCA can be applied for data analytics and machine learning applications, but is also often used for oceanographic analysis purposes (Pauthenet, 2018; Preisendorfer, 1988; Thomson and Emery, 2014). It may also be used to identify clusters in large datasets. PCA reduces the dimensionality of the large dataset by geometrically projecting data onto a lower-dimensional space. This lower-dimensional space is based on the direction along which the data varies the most, or in other words, where the variance is largest.

Figure 4.4 qualitatively shows the steps in a PCA.

Algebraically, the PCA starts after normalisation of the data, i.e. after subtracting the mean of each of the columns in the original data so the mean of each column becomes zero. The resulting data matrix is called $\mathbf{X}$, which is *centered* and of size $n \times p$, where n is the number of samples and p is the number of variables (dimensions). The *covariance matrix* $\mathbf{C}$ is then defined as:

$$\mathbf{C} = \frac{1}{(n-1)}\mathbf{X}^{\mathrm{T}}\mathbf{X} \tag{4.1}$$

Principal component analysis

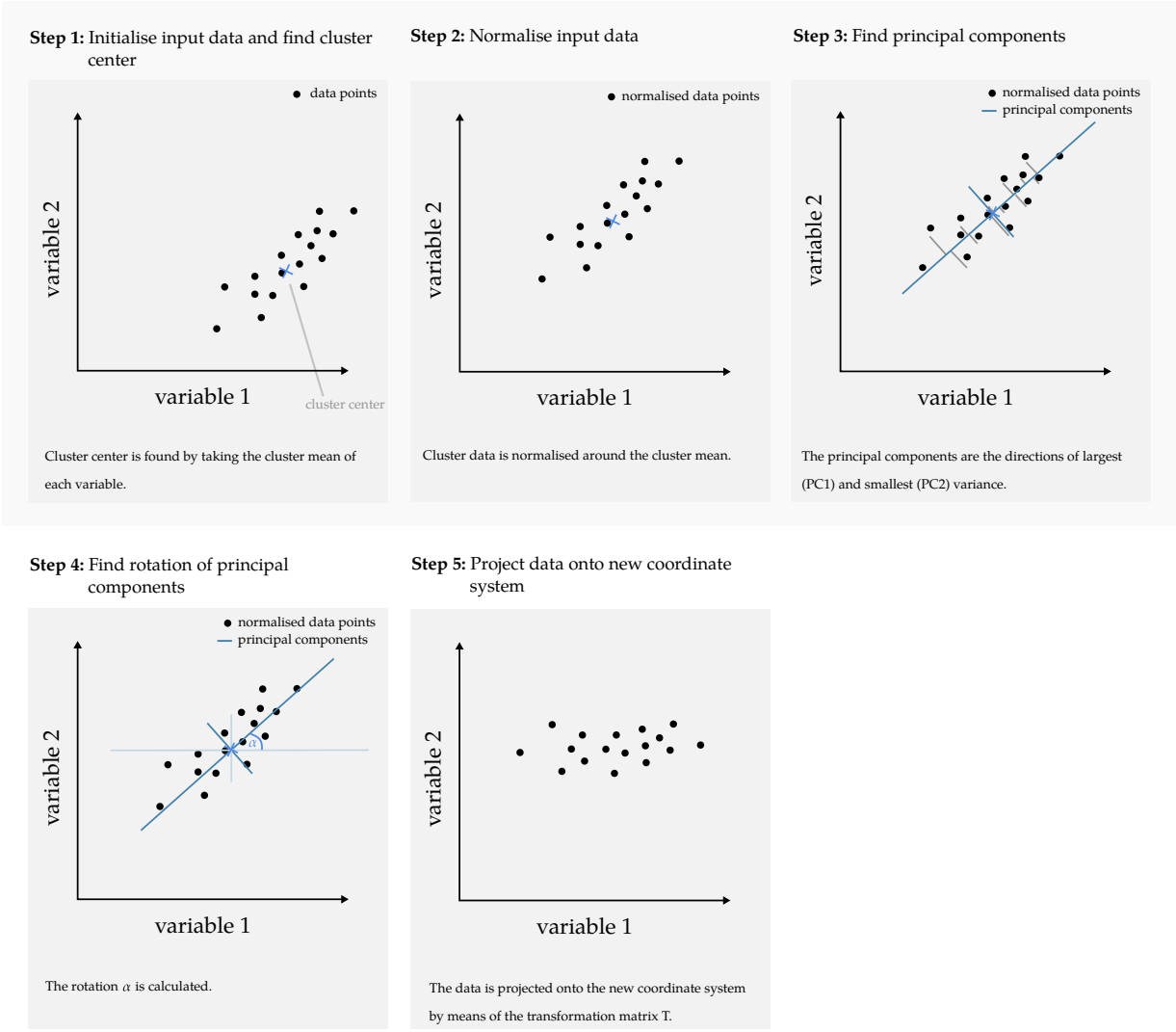

Figure 4.4: Step-by-step of the data processing steps to obtain the principal velocities. The first three steps are part of the PCA, whereas steps 4-5 are necessary to transform the data from a North-East coordinate system to an along-channel coordinate system.

Where $\mathbf{C}$ is a *symmetric* matrix of shape $p \times p$. Since it is symmetric, the matrix can be diagonalised. This is done as follows:

$$\mathbf{C} = \mathbf{V}\mathbf{L}\mathbf{V}^{\mathrm{T}} \tag{4.2}$$

in which $\mathbf{V}$ is the matrix of eigenvectors and $\mathbf{L}$ is a diagonal matrix containing all eigenvalues λ_i along the diagonal. These eigenvectors are the *principal components*, the directions of largest and smallest covariance.

Lastly, the data is transformed by a rotation of axes. The coordinates of the data points in the new, along-channel, coordinate system are calculated using the following transformation matrix T:

$$T = \begin{bmatrix} \cos(\alpha) & \sin(\alpha) \\ -\sin(\alpha) & \cos(\alpha) \end{bmatrix} \tag{4.3}$$

The data is then transformed by doing:

$$\begin{bmatrix} v_1' \\ v_2' \end{bmatrix} = T \begin{bmatrix} v_1 \\ v_2 \end{bmatrix} = \begin{bmatrix} \cos(\alpha) & \sin(\alpha) \\ -\sin(\alpha) & \cos(\alpha) \end{bmatrix} \begin{bmatrix} v_1 \\ v_2 \end{bmatrix} \tag{4.4}$$

Where v_1 and v_2 are the original variables and v_1' and v_2' are the variables in the new, along-channel coordinate system. The rotation of the axes is indicated with α.

In this new along-channel coordinate system, the flood direction (upestuary) is taken as positive, starting at the Hoek van Holland station location, and the z-coordinate is taken positive upwards from the water surface. These conventions are illustrated by Fig. 4.5.

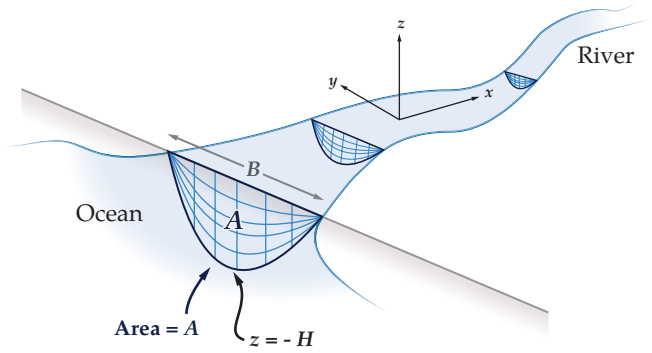

Figure 4.5: Overview of along-channel coordinate system conventions used in all of the computations in this thesis. The upstream direction is taken as the positive x-axis, the positive y-axis is taken positive perpendicular to the positive x-axis, and the positive z-axis is taken upwards from the water surface. Figure adapted from Geyer and MacCready (2014).

4.2.3 Interpolation

Data obtained with the boat-mounted ADCP and the CTD measurements were recorded separately and at different depths. Also, the GPS logger of the equipment logged the device location in different coordinate systems: the location logger of the ADCP used the *Rijksdriehoek* (RD) or Parisian coordinate system, whereas the CTD profiler used the regular geographic coordinate system. The RD-coordinates were converted to longitudes and latitudes using a coordinate transformation.

To obtain a complete time versus depth record, the ADCP data were matched to the CTD data by matching the CTD data to the nearest ADCP profile using a nearest-neighbour algorithm, based on timestamp only. To obtain velocities at the same depths as the CTD measurements, the ADCP data was simply linearly interpolated over the vertical. To make overview figures for the Richardson gradient numbers, a slightly different approach was taken. For this, the data were gridded onto the same 100×100 grid. This was done because the spatial data density of the ADCP is much higher than the spatial data density of the CTD, and only interpolating the matched ADCP data to the CTD verticals would result in a loss of information.

4.2.4 Extrapolation

Since the calculation of the total Reynolds shear stress over the water column (*see* Section 4.4.3) requires integration over the entire water column, the velocity profiles must be extrapolated to cover the velocity data near the surface (blanking distance) and the bed (side lobe effect). To cover the data missing due to side lobe effects, the velocity was extrapolated using a parabolic fit, based on the velocity in the deepest profiling point, that curves to zero at the bottom. To obtain the velocity data near the surface, the shear was extrapolated using a parabolic fit that matched the shear in the top bin and curved toward zero shear at the surface, as is done in Geyer *et al.* (2000). This way, the velocity profile abides the zero surface shear restriction at the surface and the no slip condition at the bottom.

Besides the calculation of the total Reynolds shear stress over the water column, the extrapolated values of the velocity profiles are only used in the determination of the Richardson gradient number Ri_g.

4.2.5 Filtering

As a last step, a uniform 2D spatial filter (3 by 3 block weighted) is used to smooth the data. This is in line with previous research conducted in the Rotterdam Waterway (de Nijs *et al.*, 2009, 2010a,b). The workings of such a uniform filter are more clearly demonstrated by the schematic depicted in Fig. 4.6.

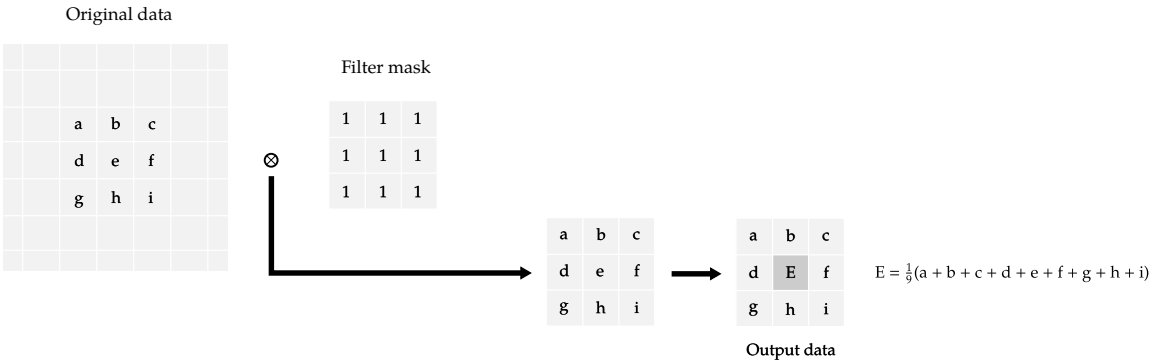

Figure 4.6: Illustration showing the effect of a 3 by 3 two dimensional uniform filter on 2-dimensional data. The uniform filter takes the average of all values a through i to calculate the new value of e, E.

4.3 Overview considered parameters

Several parameters are assessed with the aim to elucidate the internal flow structure in the Rotterdam Waterway. All these parameters are evaluated within a Lagrangian reference frame, based on the moving-boat measurements conducted on August 13th 2019. The different flow parameters that are assessed can be subdivided into the following groups:

- **Stratification parameters:** Amongst the stratification parameters are the salinity distribution over the vertical $S(z)$ and the pycnocline height h_p. The salinity parameters are closely connected to the stability parameters, since the salinity distribution largely determines the density distribution, which in turn determines the squared buoyancy frequency distribution. The stratification parameters also directly influence the SPM distribution through processes such as turbulence damping at the pycnocline (Geyer, 1993). The calculation method the pycnocline height is discussed in Section 4.4.1.

- **Stability parameters:** The stability parameters to be considered are the squared buoyancy frequency $N^2(z)$ over the vertical and the Richardson gradient number $Ri_g(z)$ over the vertical. The squared buoyancy frequency is the oscillation frequency that a particle is displaced with when moved from a certain density to another density, and can be used to say something about the static stability of a water column. Additionally, the Richardson gradient number is a dimensionless number that can be used to assess the dynamic stability of a water column, through relating the squared buoyancy frequency to the shear. The methods and scheme used to calculate these parameters is elaborated in Section 4.4.2.

- **Momentum balance terms:** The terms in a simplified along-channel momentum balance are estimated, giving insight into the dominant forcing mechanisms in the Rotterdam Waterway. The estimated terms are the local acceleration, the advective acceleration, the barotropic pressure gradient and the baroclinic pressure gradient. These terms are estimated for different times during the tidal cycle, based on an Eulerian control volume confined between CTD measuring locations. The specific grid and used method are explained in Section 4.4.3. Summing these terms, an estimate for the turbulent Reynolds stresses can be obtained following the reasoning presented in de Nijs *et al.* (2010a,b).

- **The Rossby radius of deformation:** Both the internal and external Rossby radius of deformation are calculated for each of the measuring locations of the survey. The Internal Rossby radius of deformation is a measure for the importance of Coriolis in stratified flows, and is calculated from the internal wave propagation speed. Different methods for calculating this wave speed are considered in Section 4.4.4.
- **The internal Froude number:** To assess whether internal waves occur in the Rotterdam Waterway, the internal Froude number is calculated from the internal wave speed, the mean flow velocity and the velocity in the upper layer of the flow, following the definition presented in work by Platell (2019). The internal Froude number is then used to determine whether internal waves can be generated.

Furthermore, since the advection of the salt wedge is known to be related to the competition between the barotropic forcing by the tide and the Rhine discharge from previous work by de Nijs *et al.* (2009, 2010a,b), a harmonic analysis of the water level signal was done at Hoek van Holland and at Maassluis.

All abovementioned parameters influence the SPM concentrations in the Waterway. The SPM concentrations measured using the Siltprofiler are therefore also analysed and possibly coupled to the occurring internal flow processes. An overview of all assessed parameters, and their mutual dependencies, is shown in Fig. 4.7.

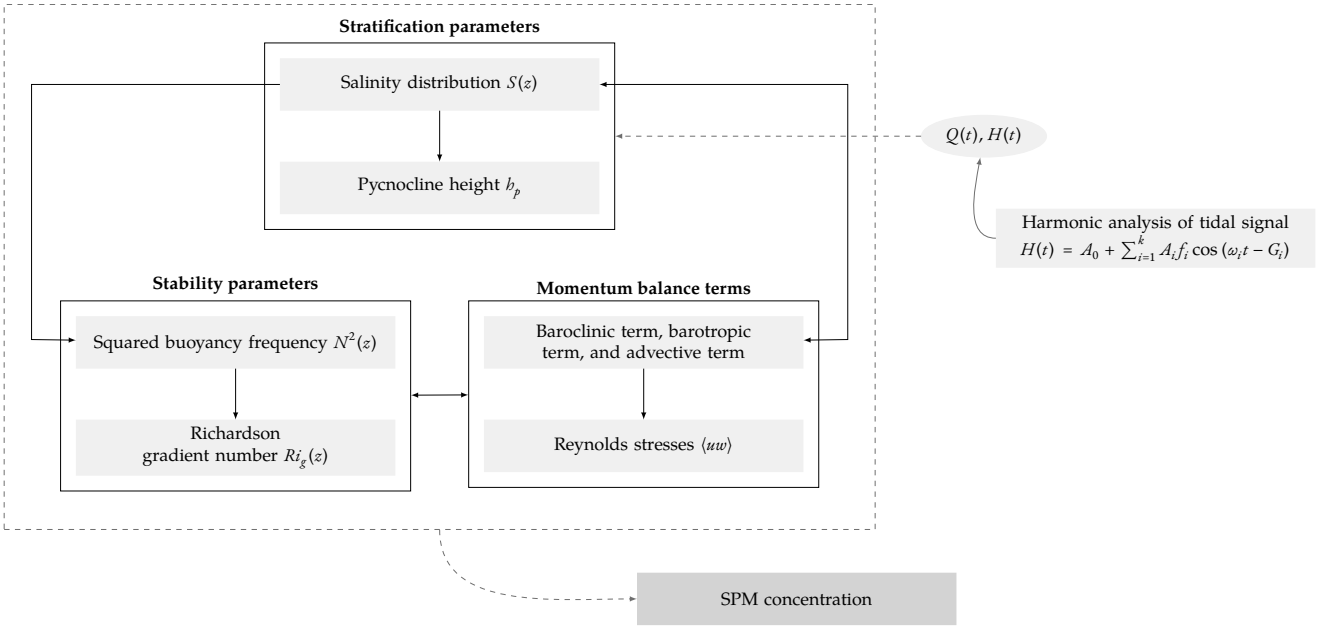

Figure 4.7: Overview of the parameters considered in the presented data analysis and their mutual (inter)dependence. Indicated are the different parameter groups (stability, stratification and turbulence parameters).

4.4 Methodology

4.4.1 Pycnocline height

By calculating the pycnocline height, the time evolution of the pycnocline can be better visualised. In this thesis, a very plain definition has been adopted for the pycnocline height for reasons of simplicity. The pycnocline height h_p [m] is the height at which the stratification is largest, or in other words, where the absolute density gradient is maximal. This height can be calculated for every measured CTD vertical. In equation form, it can be represented as:

$$h_p = h|_{\left|\frac{\partial \rho}{\partial z}\right|_{max}} \tag{4.5}$$

where h is the depth, and $\left|\frac{\partial \rho}{\partial z}\right|_{max}$ is the maximum absolute density gradient.

4.4.2 Stability parameters

Brunt-Vaïsalä frequency

The buoyancy frequency or Brunt-Vaïsalä frequency N is the frequency at which a water particle with a certain density will start to oscillate when displaced to an environment with another density. In terms of water density and sound speed it is defined as:

$$N^2(z) = -\frac{g}{\rho}\frac{\partial \rho}{\partial z} - \frac{g^2}{c_s^2} \tag{4.6}$$

The latter term containing the sound speed can be neglected, since the sound speed is so large that the latter term tends to zero (Chelton *et al.*, 1998). The negative sign in the definition of the buoyancy frequency is associated with the definition of z, which is usually taken relative to the water level ($z = 0$) and then decreases downwards away from the water level.

Density must increase with depth in order for the water column to be stable. Therefore, if $\partial\rho/\partial z$ becomes negative, instabilities start to develop in the water column. In such a case, the square of the buoyancy frequency becomes negative as well, $N^2 < 0$. There are several known numerical methods that produce good results in estimating N^2 from field data. The following paragraphs elaborate on several of these methods.

Potential density method

The *potential density method* for calculating the squared buoyancy frequency $N^2(z)$ is widely used in oceanographic research. The potential density method is implemented in the *thermodynamic equation of seawater 2010* (TEOS-10) functions as used by *United Nations Educational, Scientific and Cultural Organization* (UNESCO), and is widely accepted in the field. Using this method, two seawater parcels separated by a small vertical distance Δz are displaced adiabatically and without exchange of matter to an average pressure. The difference in density of the two parcels after this change in pressure is then calculated, which essentially means that the potential densities of the two parcels are then compared at the same pressure (IOC SCOR, 2010). This can be expressed in an equation as follows:

$$N^2 = g\left(\alpha^{\Theta}\Theta_z - \beta^{\Theta}S_{A_z}\right) \approx -\frac{g}{\rho}\frac{\Delta\rho^{\Theta}}{\Delta z} \tag{4.7}$$

where Θ_z [°C] is the conservative temperature and $\Delta\rho^{\Theta}$ is the difference between the potential densities of the two parcels, with the average of the two original pressures of the parcels as reference pressure. α^{Θ} and β^{Θ} are the thermal expansion coefficient and the saline contraction coefficient with respect to the conservative temperature, respectively.

Neutral density method

Chelton *et al.* (1998) set out the differences between several of these methods, amongst which the *neutral density method*, the *potential density method* and the *forward first difference method*. According to Chelton *et al.*, the neutral density method performs best in large ocean basins. Using this method, the squared buoyancy frequency $N^2(z)$ is estimated by centered first differences of the in-situ density, which is adiabatically adjusted to the midpoint between standard depths:

$$N^2(z_{k+1/2}) = -\frac{g}{\rho_0}\left[\frac{\rho(z_k \rightarrow z_{k+1/2}) - \rho(z_{k+1} \rightarrow z_{k+1/2})}{z_k - z_{k+1}}\right] \tag{4.8}$$

In this equation, $\rho(z_{k+1} \rightarrow z_{k+1/2})$ is a shorthand notation for the density that a water parcel at depth z_{k+1} has when moved adiabatically to the shallower midpoint depth $z_{k+1/2}$.

Centered differences method

Studies by van Gastel and Pelegrí (2004) and King *et al.* (2012) later suggest, however, that simpler methods also provide sufficient estimates for the buoyancy frequency. In the case of the August 13th survey, CTD data is obtained at a high spatial resolution over the vertical, and since the Rotterdam Waterway is relatively

shallow, large density differences between subsequent depths are therefore not expected. To calculate the buoyancy frequency profiles from the CTD data obtained from the Nieuwe Waterweg on August 13th, it was therefore chosen to omit complicated schemes and calculate the buoyancy frequency profiles using a simple centered scheme like King *et al.* (2012) suggests. For a point at depth z, the Brunt-Vaïsalä frequency is then calculated taking:

$$N_z^2 = g^2 \left(\frac{\rho_{z+1} - \rho_{z-1}}{z_{z+1} - z_{z-1}} - \frac{1}{c_{s,z}} \right) \qquad 1 < \mathrm{z} < \mathrm{Z} \tag{4.9}$$

To also obtain values for $N^2(z)$ at the endpoints, the first order forward differences and backward differences methods are used for these points:

$$N_z^2 = g^2 \begin{cases} \dfrac{\rho_{z+1} - \rho_z}{z_{z+1} - z_z} - \dfrac{1}{c_{s,\,z}} & \mathrm{z} = 1 \\ \dfrac{\rho_z - \rho_{z-1}}{z_z - z_{z-1}} - \dfrac{1}{c_{s,\,z}} & \mathrm{z} = \mathrm{Z} \end{cases} \tag{4.10}$$

Richardson gradient number Ri_g

The *gradient Richardson number* Ri_g is a dimensionless number that is oftentimes used as a parameter to indicate the onset of instabilities and convective overturning. It is the square of the Brunt-Vaïsalä frequency divided by the velocity shear over the vertical squared (Geyer, 1993; Pietrzak, 2015; van Gastel and Pelegrí, 2004):

$$Ri_g = -\frac{\frac{g}{\rho_0}\frac{\partial \rho}{\partial z}}{\left(\frac{\partial u}{\partial z}\right)^2 + \left(\frac{\partial v}{\partial z}\right)^2} = \frac{N^2}{\left(\frac{\partial u}{\partial z}\right)^2 + \left(\frac{\partial v}{\partial z}\right)^2} \tag{4.11}$$

where u is the primary velocity component and v is the secondary velocity component. The denominator in this definition of Ri_g may also be referred to as the *vertical shear* (van Gastel and Pelegrí, 2004):

$$S = \left[\left(\frac{\partial u}{\partial z} \right)^2 + \left(\frac{\partial v}{\partial z} \right)^2 \right]^{1/2} \tag{4.12}$$

The velocity gradients are also calculated using a second order central difference scheme, combined with backward differences at the largest depth and forward differences at the shallowest depth. This is done as follows for depth a point at depth z:

$$\left.\frac{\partial u}{\partial z}\right|_z \approx \begin{cases} \dfrac{u_{z+1} - u_z}{z_{z+1} - z_z} = \dfrac{u_{z+1} - u_z}{\Delta z} & \mathrm{z} = 1 \\ \dfrac{u_{z+1} - u_{z-1}}{z_{z+1} - z_{z-1}} = \dfrac{u_{z+1} - u_{z-1}}{2\Delta z} & 1 < \mathrm{z} < \mathrm{Z} \\ \dfrac{u_z - u_{z-1}}{z_z - z_{z-1}} = \dfrac{u_z - u_{z-1}}{\Delta z} & \mathrm{z} = \mathrm{Z} \end{cases} \tag{4.13}$$

$$\left.\frac{\partial v}{\partial z}\right|_z \approx \begin{cases} \dfrac{v_{z+1} - v_z}{z_{z+1} - z_z} = \dfrac{v_{z+1} - v_z}{\Delta z} & \mathrm{z} = 1 \\ \dfrac{v_{z+1} - v_{z-1}}{z_{z+1} - z_{z-1}} = \dfrac{v_{z+1} - v_{z-1}}{2\Delta z} & 1 < \mathrm{z} < \mathrm{Z} \\ \dfrac{v_z - v_{z-1}}{z_z - z_{z-1}} = \dfrac{v_z - v_{z-1}}{\Delta z} & \mathrm{z} = \mathrm{Z} \end{cases} \tag{4.14}$$

where Δz [m] is the depth difference between two subsequent velocity measurements over the vertical, u [m s^{-1}] is the along-channel velocity, v [m s^{-1}] is the velocity perpendicular to the along-channel velocity and Z [m] is the total depth.

Thus, the gradient Richardson number may also be expressed in terms of the buoyancy equation and the vertical shear:

$$Ri_g = \frac{N^2}{S^2} \tag{4.15}$$

In estuaries, the gradient Richardson number is typically between 0.5 and 10, although values outside of this range can also be encountered. Large values of the Richardson gradient number indicate very stable conditions, whereas low values may indicate dynamic instability. In the case that $N^2(z) < 0$, the value of Ri_g is generally not of interest, because a low value of $N^2(z)$ already indicates the onset of instabilities. However, low values of the squared Brunt-Vaïsalä frequency only indicate low static stability, whereas low Ri_g indicates *dynamic instability* since dynamic stability also depends on the vertical shear (van Gastel and Pelegrí, 2004). Typically, the criterion for flow stability is defined as $Ri_g > \frac{1}{4}$.

4.4.3 Momentum balance terms

Estimation of the separate terms in the momentum balance gives insight into which processes are dominant during what part of the tidal cycle. Based on the assumption of uniformity of the flow in the along-channel direction (*see* App. A), it is sufficient to estimate the terms in a simplified along-channel momentum balance, as was previously shown in work by de Nijs (2012); de Nijs *et al.* (2010b). The momentum balance that is used for this analysis therefore only considers the along-channel terms, under the assumption of gradient type turbulent transport. This balance reads:

$$\underbrace{\frac{\partial u}{\partial t}}_{1} + \underbrace{u\frac{\partial u}{\partial x}}_{2} + \underbrace{g\frac{\partial \eta}{\partial x}}_{3} + \underbrace{\int_{z=z*}^{\eta} \frac{g}{\rho_0}\frac{\partial \rho}{\partial x} dz}_{4} + \underbrace{\frac{\partial}{\partial x}\langle uu \rangle}_{5} + \underbrace{\frac{\partial}{\partial z}\langle uw \rangle}_{6} \tag{4.16}$$

In this equation, u [m s^{-1}] is the along-channel velocity, or in other words, the primary velocity component, η is the water level, ρ [kg m^{-3}] is the in-situ density, $\rho_0 = 1000$ kg m^{-3} is the reference density of water, and $\langle uu \rangle$ and $\langle uw \rangle$ [m^2 s^{-2}] are the Reynolds normal stress and shear stress, respectively. For consistency, the upestuary direction is taken as positive, leading to positive values of u during flood.

Because the measurements were taken in a Lagrangian reference frame, the determination of each of the separate terms in the simplified momentum balance is done for each measuring location, based on an Eulerian control volume between subsequent locations. Using this approach, a momentum balance is obtained for only a part of the tidal period. This method is not completely in line with previously conducted research by de Nijs *et al.* (2010a,b) and Geyer *et al.* (2000), which use stationary measurements in combination with the assumption of gradient-type transport. However, the method used here is a necessity as a consequence of the measuring approach taken during the survey on August 13th, and is believed to give sufficient insight into the dominant processes nonetheless. The errors introduced by the method are discussed later on in this section.

The following subsections elaborate on the determination of each of the different terms in the momentum balance.

Local acceleration

The first term in the momentum balance (*see* Equation (4.16)) is the local acceleration term. This term is determined for all depths at which the ADCP has recorded velocity data, for each point x_n at which a CTD vertical was recorded. In earlier work by de Nijs *et al.* (2010a,b), this term is neglected.

It is possible to match ADCP verticals to CTD verticals directly, because the ADCP kept recording whilst the CTD verticals were taken. This recording therefore gives a stationary record of a velocity signal. Because these ADCP time series are as long as the CTD measurement protocol duration, these time series are between five and ten minutes long. These stationary time series record multiple ensembles, which are

ensemble-averaged over the total recording to give a mean along-channel velocity profile. Finally, these mean velocity profiles are used for the calculation of the advective acceleration term.

In the center points, the derivative of the along-channel velocity gradient in the along-channel direction is calculated by means of centered differences between the times at which the CTD verticals were recorded at the previous and following location, $t_{x_{n-1}}$ and $t_{x_{n+1}}$ respectively. These times are determined by the CTD device directly, and are equal to the starting time plus half of the duration of the recording. First order difference schemes are used at the endpoints. This can be summarised by the following scheme:

$$\left.\frac{\partial u}{\partial t}\right|_n \approx \begin{cases} \dfrac{u_{n+1}-u_n}{t_{x_{n+1}}-t_{x_n}} & \text{n = 1} \\ \dfrac{u_{n+1}-u_{n-1}}{t_{x_{n+1}}-t_{x_{n-1}}} & \text{1 < n < N} \\ \dfrac{u_n-u_{n-1}}{t_{x_n}-t_{x_{n-1}}} & \text{n = N} \end{cases} \tag{4.17}$$

Because of the nature of the ADCP recording, the depth bins are equal for each vertical. The total depth at subsequent measuring locations, however, is not equal. This means that recordings may have different depth ranges. Because the velocity profiles are not extrapolated for the analysis of the separate terms, the maximum depth of the mean velocity profile at x_n is equal to the maximum depth of the shallowest profile x_{n-1} or x_{n-1} (*see* Fig. 4.8).

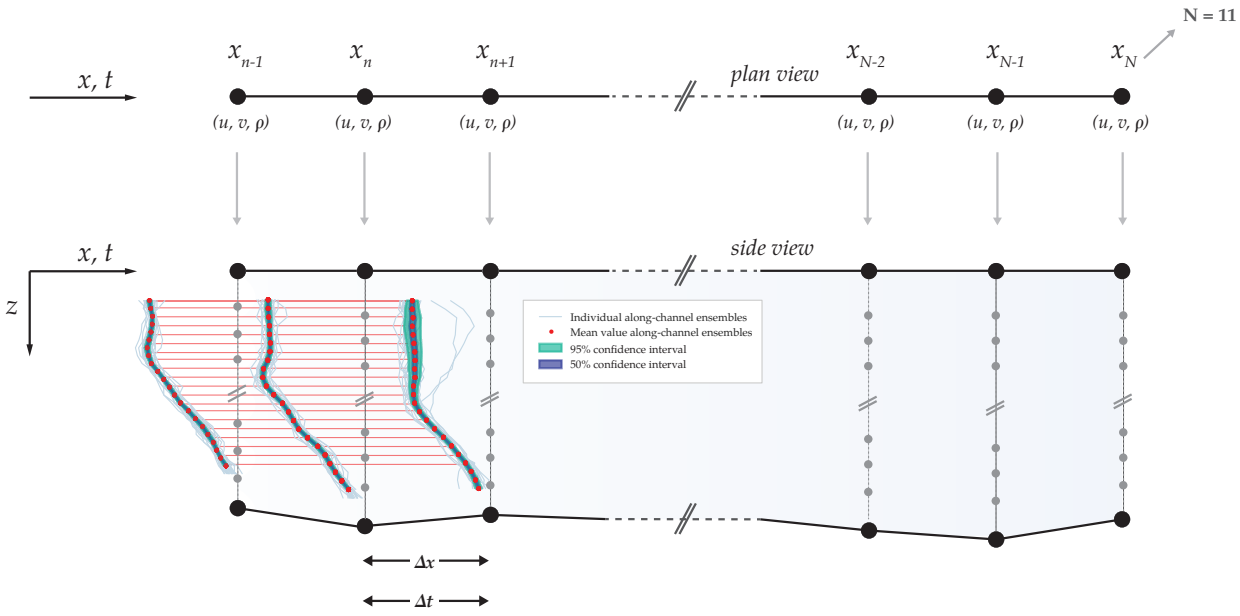

Figure 4.8: Schematic showing the grid and method used to calculate the derivative of the along-channel velocity in the along-channel direction and the local acceleration. The derivative is calculated using centered differences in the center points and first order forward and backward differences at the starting point and end point, respectively. Schematic shows calculation method for the derivative at point x_n. Method is the same at each depth z.

Advective acceleration

The second term in the simplified along-channel momentum balance (*see* Equation (4.16)) is the advective acceleration term. The magnitude of the advective acceleration term is determined by the along-channel velocity multiplied by the derivative of the along-channel velocity in the along-channel direction. The advective acceleration term is calculated for all depths at which the ADCP has recorded velocity data, for each point x_n at which a CTD vertical was recorded.

In the center points, the derivative of the along-channel velocity gradient in the along-channel direction is calculated by means of centered differences between the previous and following location, x_{n-1} and x_{n+1} respectively. This is combined with first order forward differences at x_1 and first order backward differences at x_N:

$$u\frac{\partial u}{\partial x}\bigg|_n \approx u\begin{cases}\dfrac{u_{n+1}-u_n}{x_{n+1}-x_n} & \text{n = 1}\\ \dfrac{u_{n+1}-u_{n-1}}{x_{n+1}-x_{n-1}} & \text{1 < n < N}\\ \dfrac{u_n-u_{n-1}}{x_n-x_{n-1}} & \text{n = N}\end{cases} \tag{4.18}$$

Barotropic pressure gradient

The barotropic pressure gradient is indicated as term 3 in Equation (4.16). This gradient amounts to the derivative of the local water level elevation multiplied by the gravitational acceleration. Because the water level elevation is not measured directly at each station, it is estimated from the fixed water level measuring stations at Hoek van Holland, Maassluis and Vlaardingen.

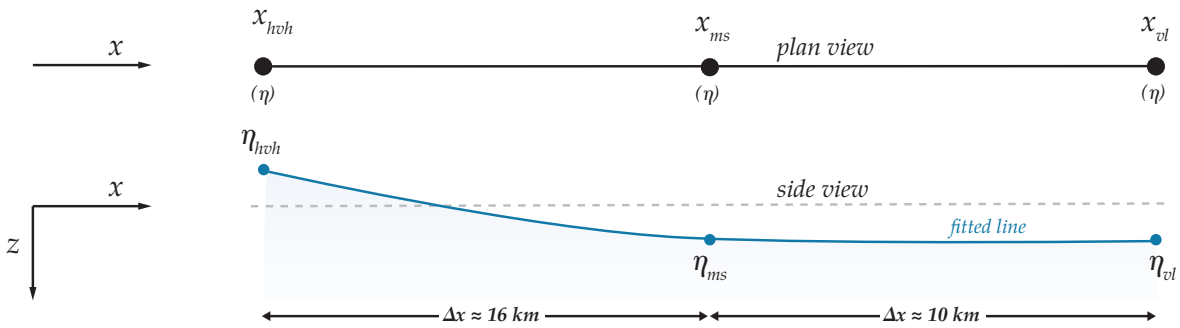

Figure 4.9: A schematic view of the method and grid used to calculate the derivative of the water level elevation in the along-channel direction at point x_n. The water level elevation is available at three fixed measuring stations lining the New Waterway: at *Hoek van Holland*, at *Maassluis* and at *Vlaardingen*. A third order polynomial $f(x)$ is used to estimate the local water level elevation at each of the grid points. The derivative is calculated using centered differences in the center points, taking the difference between the interpolated values of the water level elevations $f(x_{n+1})$ and $f(x_{n-1})$ and the distances x_{n+1} and x_{n-1}. At the endpoints of the grid, a first order scheme is used.

To estimate the derivative of the water level elevation at station x_n at time $t = t_n$, the instantaneous water level at the available stations of Hoek van Holland, Maassluis and Vlaardingen at time $t = t_n$ is used. Through these three points of known water level elevation, a third order polynomial $f(x)$ is fitted, giving values for the water level elevation at distances x_{n+1} and x_{n-1} from Hoek van Holland as $f(x_{n+1})$ and $f(x_{n-1})$, respectively. The derivative of the water level elevation at point n, located at a distance x_n from Hoek van Holland, is then calculated using centered differences. At the endpoints, first order forward and backward differences are used. This leads to the following calculation scheme:

$$\frac{\partial \eta}{\partial z}\bigg|_{n,\ t=t_n} \approx \begin{cases}\dfrac{f(x_{n+1})-f(x_n)}{x_{n+1}-x_n} = \dfrac{\eta_{n+1}-\eta_n}{x_{n+1}-x_n} & \text{n = 1}\\ \dfrac{f(x_{n+1})-f(x_{n-1})}{x_{n+1}-x_{n-1}} = \dfrac{\eta_{n+1}-\eta_{n-1}}{x_{n+1}-x_{n-1}} & \text{1 < n < N}\\ \dfrac{f(x_n)-f(x_{n-1})}{x_n-x_{n-1}} = \dfrac{\eta_n-\eta_{n-1}}{x_n-x_{n-1}} & \text{n = N}\end{cases} \tag{4.19}$$

Baroclinic pressure gradient

The baroclinic pressure gradient accounts for the pressure induced by the density difference between subsequent measuring locations. In Equation (4.16) it is indicated by term 4. Its magnitude at each measuring location is determined by the derivative of the density in the along-channel direction multiplied by a constant term that is equal to the gravitational acceleration divided by the reference density of water.

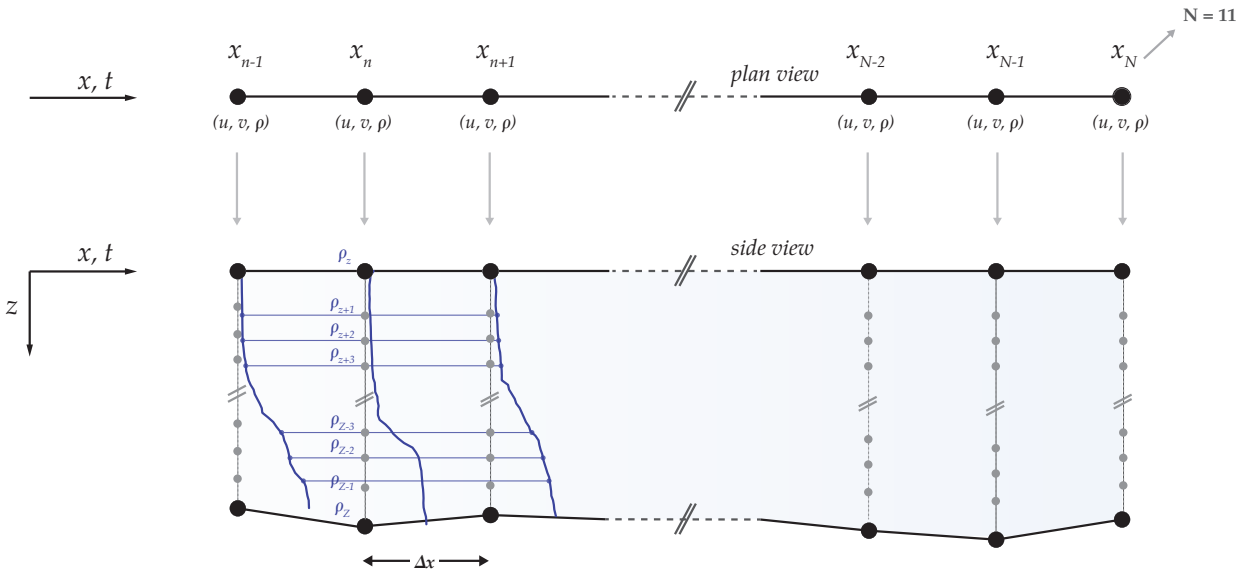

Figure 4.10: Schematic showing the grid and method used to calculate the derivative of the density in the along-channel direction. The derivative is calculated using centered differences in the center points and first order forward and backward differences at the starting point and end point, respectively. Schematic shows calculation method for the derivative at point x_n. Method is the same at each depth z.

The baroclinic pressure gradient is calculated at every measuring location and for every height at which the CTD has recorded data. Since the bathymetry of the channel changes in x-direction, the total depth at subsequent measuring locations is not equal, and the recorded CTD data are also not equally spaced over the depth at subsequent measuring locations. To calculate the density gradient at vertical x_n using the densities at x_{n+1} and x_{n-1}, the density profiles at x_{n+1} and x_{n-1} are linearly interpolated over the vertical to match the corresponding depths at x_n. The horizontal density difference at x_n is then calculated for all depths $z = 1, 2, ..., Z$ using centered differences in the middle depths and first order difference schemes at the endpoints:

$$\left.\frac{\partial \rho_z}{\partial x}\right|_n \approx \begin{cases} \dfrac{\rho_{z,(n+1)} - \rho_{z,n}}{x_{n+1} - x_n} & \text{n = 1} \\ \dfrac{\rho_{z,(n+1)} - \rho_{z,(n-1)}}{x_{n+1} - x_{n-1}} & 1 < \text{n} < \text{N} \\ \dfrac{\rho_{z,(n)} - \rho_{z,(n-1)}}{x_n - x_{n-1}} & \text{n = N} \end{cases} \tag{4.20}$$

Since CTD measurements are done in a Lagrangian reference frame, the method described above introduces an error, which is discussed in Sec. 4.4.3.

Reynolds shear stress term

Turbulent characteristics, such as the turbulent Reynolds shear stresses, can be either measured directly by use of microstructure profilers, or can be estimated. After estimation of each of the separate momentum

balance terms, the Reynolds shear stress term $\langle uw \rangle$ can be estimated by taking the integral of the estimated local acceleration, advective acceleration, barotropic pressure gradient and baroclinic pressure gradient terms, and adding the surface stress. This leads to the following expression for the Reynolds shear stress term:

$$\int_{z=z^*}^{\eta} \frac{\partial}{\partial z} \langle uw \rangle \, dz = -\int_{z=z^*}^{\eta} \Bigg(\underbrace{\frac{\partial u}{\partial t}}_{1} + \underbrace{u \frac{\partial u}{\partial x}}_{2} + \underbrace{g \frac{\partial \eta}{\partial x}}_{3} + \underbrace{\int_{z=z*}^{\eta} \frac{g}{\rho_0} \frac{\partial \rho}{\partial x} dz}_{4} + \underbrace{\frac{\partial \langle uu \rangle}{\partial x}}_{5} \Bigg) dz + \frac{1}{\rho_0} \tau_s \tag{4.21}$$

Because of complexity, the estimation of the Reynolds normal stresses $\langle uu \rangle$ is also omitted. Lastly, the surface stress is neglected, as is also done in reference works by de Nijs *et al.* (2009, 2010a,b). This leads to the final expression for the calculation of the Reynolds shear stress:

$$\int_{z=z^*}^{\eta} \frac{\partial}{\partial z} \langle uw \rangle \, dz = -\int_{z=z^*}^{\eta} \left(\frac{\partial u}{\partial t} + u \frac{\partial u}{\partial x} + g \frac{\partial \eta}{\partial x} + \int_{z=z*}^{\eta} \frac{g}{\rho_0} \frac{\partial \rho}{\partial x} dz \right) dz \tag{4.22}$$

Because the determination of the total Reynolds shear stress requires that all terms are known over the entire depth of the water column, the velocity profiles are extrapolated following the method previously described in Section 4.2.4.

Method-introduced errors

The methodology used to determine the different terms in the simplified along-channel momentum balance, along with its simplified nature, introduces errors and bias. It is important to highlight these errors and bias so the forthcoming results can be put into perspective.

Bias

An insurmountable consequence of the used estimation methodology is the fact that bias is introduced. This is mainly a result of the simplification of the momentum balance, reducing a three-dimensional momentum equation to a one-dimensional momentum balance. Although the lateral simplification is largely justified with a uniformity check (*see* App. A)), there is no guarantee that there is no (higher order) lateral effect on the momentum balance locally during certain parts of the tidal cycle. This will likely be a problem during slack tide. The neglect of the Reynolds normal stress term and the surface stress also introduces bias. All of these factors together contribute to the bias term ϵ_b.

Measuring method errors

Because the measurements obtained from the monitoring survey on August 13th were collected by a boat moving in time and space, the determination of the local acceleration term, the advective acceleration term and the baroclinic pressure gradient introduces errors. It is not possible to correct for these errors. The error introduced as a result of the Lagrangian measuring method will be indicated by ϵ_L.

Furthermore, in the determination of the barotropic pressure gradient term, a measuring method related error is introduced due to the fact that the data from fixed measuring stations at Hoek van Holland, Maassluis and Vlaardingen is given as a 10 minute average. This data is matched to the CTD verticals using a nearest-neighbour algorithm on its time stamp, introducing an error. This error is indicated by the term ϵ_{av}.

Processing method errors

Another error is introduced due to the method used for the determination of the barotropic pressure gradient term. Because there are only few fixed water level measuring stations lining the New Waterway, interpolation between the known water level elevations is necessary to obtain an estimate for the water level elevation at point x_n. This interpolation is done over very long distances (10 - 16 km), obviously introducing an error. This error will be indicated by the term $\epsilon_{int,\, wl}$.

A similar error is introduced by the vertical interpolation of values at the previous and following CTD locations for the determination of the local acceleration term, the advective acceleration term, and the baroclinic pressure gradient term. The term $\epsilon_{int,\,v}$ indicates the error introduced by this interpolation procedure.

Furthermore, in the calculation of the local acceleration and advective acceleration term, it is assumed that the measured velocity profiles are completely stationary, e.g. not moving in space. Yet, the GPS loggers of the boat inevitably log a slight change in position of the boat during these measurements, presumably related to drift of the boat. The error introduced by the assumption of complete stationarity is denoted with ϵ_{dr}.

Lastly, an error is introduced by the extrapolation of the velocity profiles for the determination of the total Reynolds shear stress over the vertical. Although the extrapolation of velocity profiles for the purpose of the calculation of the total Reynolds shear stress is not uncommon (de Nijs *et al.*, 2010a,b; Geyer *et al.*, 2000; Nidzieko *et al.*, 2009; Trowbridge *et al.*, 1999), extrapolation always introduces an error that should be mentioned here. This error is expressed as $\epsilon_{extr,\,R}$.

Total introduced error

The total error introduced by the method described in Section 4.4.3 is the sum of all errors mentioned in Section 4.4.3. This results in a estimation of the total error (including bias), expressed as ϵ:

$$\epsilon \approx \epsilon_b + \epsilon_L + \epsilon_{av} + \epsilon_{int,\,wl} + \epsilon_{int,\,v} + \epsilon_{dr} + \epsilon_{extr,\,R} \tag{4.23}$$

The largest contributor to this error is likely the error due to the Lagrangian measuring method, ϵ_L.

4.4.4 Influence of Coriolis

The (internal) Rossby radius of deformation is a measure for the importance of Coriolis in stratified flows. It defines the length scale of baroclinic variability at which internal vortex stretching becomes more important than relative vorticity (Chelton *et al.*, 1998). The Rossby radii of deformation are derived from the quasi-geostrophic potential vorticity equation for a linearly stratified fluid, which reads:

$$\frac{\mathrm{D}u}{\mathrm{D}t}\left(\nabla_H^2\psi + \frac{\partial}{\partial z}\left[\frac{f^2}{N^2}\frac{\partial\psi}{\partial z}\right] + \beta v\right) \tag{4.24}$$

To get to this quasi-geostrophic equation, it is assumed that the flow is geostrophic to first order. Under this assumption, the geostrophic streamfunction is introduced:

$$u_g = -\frac{\partial\psi}{\partial y} \tag{4.25}$$

$$v_g = \frac{\partial\psi}{\partial x} \tag{4.26}$$

We furthermore assume that buoyancy forcing, wind stress and frictional forces are absent, so the quasi-geostropghic potential vorticity equation reduces to a wave equation for freely propagating linear waves. This equation is separable if it is assumed that the bottom is flat: in such a case, the vertical dependence is separable from the horizontal and temporal dependencies. The solution can then be expressed as a sum of normal modes, each of which have a fixed vertical structure and behave in time and in the horizontal dimension in the same way as a homogeneous fluid with a free surface (Gill, 1982). The vertical velocity can then be expressed as:

$$w(x,y,z,t) = \phi(z)W(x,y,t) \tag{4.27}$$

If this solution is substituted into Equation (4.24), while separating the z-dependent and $x-$, $y-$ and $t-$dependent terms, the following coupled equations are obtained:

$$\frac{\partial}{\partial t}\left(\nabla_H^2 - \frac{f^2}{c^2}\right)W + \beta\frac{\partial W}{\partial x} = 0 \tag{4.28}$$

$$\frac{\mathrm{d}^2\phi}{\mathrm{d}z^2} + \frac{N^2(z)}{c^2}\phi = 0 \tag{4.29}$$

in which c^{-2} is the so-called *separation constant*, $f = 2\Omega \sin\theta$ is the Coriolis parameter with latitude θ and Earth rotation rate $\Omega = 7.29 \times 10^{-5}$ s^{-1}, $\beta = \mathrm{d}f/\mathrm{d}y$ is the latitudinal variation of the Coriolis parameter and ∇_H^2 is the horizontal Laplacian operator, which is defined as:

$$\nabla_H^2 = \frac{\partial^2}{\partial x^2} + \frac{\partial^2}{\partial y^2} \tag{4.30}$$

To obtain the baroclinic solutions of interest, the rigid-lid and flat-bottom boundary conditions are applicable, which read:

$$\phi = 0 \quad \text{at} \quad z = 0 \tag{4.31}$$

$$\phi = 0 \quad \text{at} \quad \text{z=-H} \tag{4.32}$$

Where H is the instantaneous water depth. Together with equation (4.29), these boundary conditions form a Sturm-Liouville eigenvalue problem, which would yield an infinite set of non-negative eigenvalues c_m^{-2} with their corresponding eigenfunctions $\phi_m(z)$. This eigenvalue problem is equivalent to the boundary value problem for the vertical structure of the vertical velocity for long, baroclinic gravity waves, in which c_m represents the phase speed of the mode-m gravity wave (Chelton *et al.*, 1998). The solution to this problem is of the form:

$$\lambda_m = \frac{c_m}{|f|} \quad \text{if} \quad \theta \gtrsim 5° \tag{4.33}$$

$$\lambda_m = \left(\frac{c_m}{2\beta}\right)^{\frac{1}{2}} \quad \text{if} \quad \theta \lesssim 5° \tag{4.34}$$

where λ_m can be recognised as the Rossby radius of deformation, R. Therefore, to calculate the different modi of the Rossby radius of deformation, it is necessary to calculate the phase speed of the mode-m gravity wave. This phase speed can be calculated using several different methods.

WKB-approximation

To obtain the Rossby radius of deformation from the data, the buoyancy frequency profile $N^2(z)$ is estimated from the salinity profiles. After determination of these $N^2(z)$ profiles, the Rossby radii of deformation in the form of Equation (4.34) can be determined by solving the Sturm-Liouville problem posed by Equations (4.28) and (4.29) and the boundary conditions posed by Equation (4.31) and Equation (4.32).

To obtain an analytical solution to the Sturm-Liouville eigenvalue problem, the *Wentzel-Kramers-Brillouin method* or the WKB-approximation is used (Chelton *et al.*, 1998; Morse and Feshbach, 1953). This method makes use of the formal substitution of ϕ by the expected oscillating solution as a function of z:

$$\phi(z) = e^{i\chi(z)} \tag{4.35}$$

where $\chi(z)$ is the phase of the complex oscillation as a function of depth z. For this approximation to be valid, a scale separation between the medium of propagation and the waves has to exist (Tailleux, 2004). In the case of the Rotterdam Waterway, the squared buoyancy frequency $N^2(z)$ varied very little over the depth during the monitoring campaign executed on August 13th, 2019. The largest differences between the maximum and minimum squared buoyancy frequency $N^2(z)$ within the vertical were of $O(0.1)$. Under these conditions, the WKB-approximation is valid. The expression for the m-th baroclinic mode of the wave speed under the WKB-approximation then becomes (Chelton *et al.*, 1998; Nurser and Bacon, 2014):

$$c_m^{WKB} = \frac{1}{\pi m} \int_{-H}^{0} N(z)\mathrm{d}z \qquad m \geq 1 \tag{4.36}$$

Using this approximation, the expression for the internal Rossby radius of deformation for the first baroclinic mode becomes:

$$\lambda_1 = R_I = \frac{\frac{1}{\pi} \int_{-H}^{0} N(z)\mathrm{d}z}{|f|} \tag{4.37}$$

This expression can be used to calculate the baroclinic Rossby radii of deformation using both the TEOS-10 calculation method for $N^2(z)$ and using centered differences to calculate $N^2(z)$.

In the case of barotropic flows, the expression for the Rossby radius of deformation in Equation (4.34) reduces to:

$$R_E = \frac{c_E}{|f|} = \frac{\sqrt{gH}}{|f|} \tag{4.38}$$

where c_E is the external wave phase speed, and H is the total water depth (Chelton *et al.*, 1998; Pietrzak, 2015).

Two-layer system simplification

The water column is continuously stratified in most survey locations, which likely means that the previously elaborated WKB-approximation is the most reliable method to calculate the internal Rossby radius of deformation. However, if only estimates of the order of magnitude of the internal Rossby radius of deformation are sought after, a simplification of the continuously stratified fluid to a two-layer system could also be sufficient. In such a case, the mode-m baroclinic wave phase speed reduces to the internal wave phase speed c_I. This phase speed is the external wave speed c_E multiplied with a factor accounting for the buoyancy effects (Pietrzak, 2015):

$$R_I = \frac{c_I}{|f|} = \frac{\sqrt{g'H}}{|f|} = \sqrt{\frac{\rho_1 - \rho_2}{\rho_0}}\frac{c_E}{|f|} \tag{4.39}$$

where the factor $g' = \frac{\rho_1 - \rho_2}{\rho_0} g$ is the reduced gravity and H is the depth of the stratified flow.

Direct numerical solution to the Taylor-Goldstein equation and coupled Korteweg-de Vies model

The Korteweg-de Vries model, containing the Korteweg-de Vries equation, is a model that is often used to study internal waves in deeper water. Recently, citetPlatell2019InternalModel has extended the Korteweg-de Vries model for a variable bed and verified its workings for application in the Rhine ROFI. The Korteweg-de Vries model is a 2D model that uses the Taylor-Goldstein equation to solve the linear propagation speed and the Korteweg-de Vries equation, describing the propagation in time and space. The total Korteweg-de Vries model requires three inputs: the water depth, the density structure and the background flow. The background flow in this sense is defined as the hydrostatic, non-wave disturbed flow.

The vertical structure $\Phi(z)$ of an internal wave and its linear propagation speed C_0 are determined by the Taylor-Goldstein equation. In full-dimensional form, this equation reads:

$$\frac{\partial}{\partial z}\left((U - C_0)\frac{\partial \Phi}{\partial z}\right) - \frac{\partial \rho_0}{\partial z}\Phi = 0 \tag{4.40}$$

Here, C_0 [m s^{-1}] is the linear wave propagation speed and U is the horizontal along-channel background flow velocity. Physically, this equation describes the dynamics of internal waves in the presence of a (continuous) density stratification under the influence of a shear flow. Since this equation is an eigenvalue-eigenfunction problem with C_0 as eigenvalue and Φ the eigenvalue solution, it can be solved analytically.

The complete Korteweg-de Vries equation, derived by Grimshaw *et al.* (2002), is defined as:

$$\frac{\partial A}{\partial t} + C_0\frac{\partial A}{\partial x} + A_1 A\frac{\partial A}{\partial x} + B_1\frac{\partial^3 A}{\partial x^3} = 0 \tag{4.41}$$

where $A(x,t)$ is the evolution of the internal wave's particle displacement in space and time, and A_1 and B_1 are coefficients. The parameters A_1 and B_1 are calculated from the solution of the linear propagation speed following from the Taylor-Goldstein equation after which the wave form and (small) travelling wave speed can be determined from Eq. (4.41).

To be able to account for bathymetric variations, Platell (2019) adapted the Korteweg-de Vries equation. This adapted variable bed Korteweg-de Vries equation that can be used for application in the Rhine ROFI reads:

$$\frac{\partial A}{\partial t} + (C_0 + C_h)\frac{\partial A}{\partial x} + A_1 A\frac{\partial A}{\partial x} + B_1\frac{\partial^3 A}{\partial x^3} = 0 \tag{4.42}$$

In this equation, C_h is the propagation speed that is related to the variability of the bed. It should be noted that when the bottom is assumed flat, $C_h = 0$.

When the outcome of the Taylor-Goldstein equation is used as an input into the variable bed Korteweg-de Vries equation, a solution C_0 can be obtained, which is the internal wave speed of an internal wave. The total internal wave speed c is then calculated by adding up the linear propagation wave speed C_0, the propagation speed related to the variability of the bed C_h, and the wave propagation speed following from the original Korteweg-de Vries equation (*see* Eq. (4.41)):

$$c = C_0 + C_h + C \tag{4.43}$$

For his thesis, Platell developed a MATLAB® script that solves the abovementioned variable bed Korteweg-de Vries model, giving the total propagation speed c directly, which is used in this thesis as well.

4.4.5 Occurrence of internal waves

Internal waves may be generated perturbation of a stratified fluid. One of the mechanisms that is able to generate internal waves through perturbation of the flow is called the lee wave mechanism (Jackson *et al.*, 2012). This mechanism is based on the theory of supercritical flows, and occurs when an internal wave encounters a sudden change in depth, resulting in a sudden transition from subcritical to supercritical flow. Another mechanism for the generation of internal waves is wave fission from a river plume head (Nash and Moum, 2005). This mechanism was first described by Nash and Moum, who reported three different stages in the generation of the internal wave: frontal growth, wave fission, and free propagation. In the first phase, frontal kinetic energy is converted into potential energy as a result of downward motions at the plume front. These downward motions are induced by the differences in horizontal velocity in the plume and the ambient fluid. When the tidal plume front slackens, the flow becomes subcritical and wave fission is able to occur, after which the internal wave can propagate freely. The result of this potential energy loss in the plume is that the plume increases in area.

In Section 4.4.4, several methods have been discussed to calculate the internal wave speed. For the calculation of the internal Froude number, the internal wave speed is used that follows from numerically solving the Taylor-Goldstein equation and the Korteweg-de Vries equation. The Froude number is calculated according to the definition used in Pietrzak and Labeur (2004):

$$Fr = \frac{|U_0|}{|c_r|} \tag{4.44}$$

where U_0 is the background velocity, and c_r is the phase velocity relative to the speed of the moving fluid. The relationship between the phase velocity relative to the speed of the moving fluid and the linear phase velocity is as follows:

$$c_r = U_0 - c \tag{4.45}$$

Here, we use the total internal wave speed calculated from the variable bed *Korteweg-de Vries* (KdV) model for c [m s^{-1}] and U_0 [m s^{-1}] is the background flow velocity, taken equal to the depth-averaged mean velocity.

Chapter 5

Hydrodynamic model

This chapter focuses on explaining the general set-up and workings of the hydrodynamic models used in this study. To be able to understand the workings of the model from a theoretical point of view, Section 5.1 elaborates on the used computational package and the theory behind the solution methods incorporated into the package. It also covers the used horizontal and vertical coordinate systems. Then, in Section 5.2, an overview of the used models is given, along with the differences and similarities between these models. Hereafter, Section 5.3 covers the models' set-up. This includes the horizontal and vertical grids, the bathymetry, initial conditions, model parameters, and boundary conditions. Lastly, Section 5.4 is comprised of an elaboration on the outputs of the models.

5.1 Theoretical framework

In this study, two different model set-ups are evaluated on their predictive capabilities. The model basis of these set-ups is SIMONA.

SIMONA or *WAQUA in SIMONA* is a computational package developed by The Dutch National Institute of Coastal and Marine Management (RIKZ, former specialty institute of Rijkswaterstaat) in combination with Deltares (formerly Delft Hydraulics) that contains the shallow water flow modules WAQUA and TRIWAQ, which are intended to solve the shallow water equations in two (WAQUA) and three dimensions (TRIWAQ). The following subsections elaborate on the theoretical framework behind SIMONA, covering the solution methods, discretisations, and coordinate system. More elaborate mathematical support on the subject is presented in the documentation by Rijkswaterstaat (2016).

5.1.1 Coordinate systems

Horizontal coordinate system

In the horizontal direction, the SIMONA model uses curvilinear coordinates. Curvilinear grids are convenient, because they enable the grid to follow the horizontal geometry of the estuary smoothly. As a result of the use of curvilinear grids, the grid is refined locally; summer beds have a finer grid than winter beds. Curvilinear grids also allow for local grid refinement in areas with large horizontal gradients (Rijkswaterstaat, 2016). The coordinate transformation used in TRIWAQ uses a coordinate-invariant formulation in orthogonal coordinates.

Vertical coordinate system

The TRIWAQ software uses a general prescription of layer interfaces in vertical direction. The layer interfaces are calculated by means of the sigma-coordinates. Using this approach, the layers are 'fitted' to the bathymetry, and the number of layers is constant over the entire computational domain. Consequently, the grid is finer in shallower parts of the domain.

This approach is significantly different from the z-grid approach, which yields less layers in shallower areas due to the restricted layer height. For clarity on this, the difference between σ-layers and z is illustrated in Fig. 5.1.

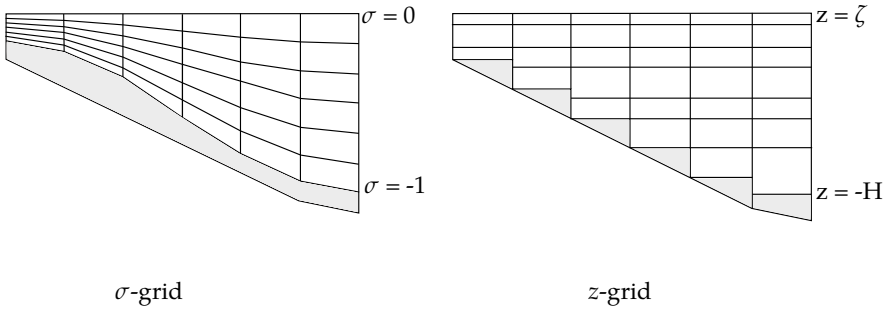

Figure 5.1: Figure illustrating the differences between using a σ-grid and a z-grid in the vertical direction. The z-grid uses a grid with a fixed vertical grid. The vertical grid resolution of the σ-grid, on the other hand, is not fixed. The amount of layers does not change under the influence of bathymetric changes, but the separate layer thicknesses do change. Adapted from Deltares (2020).

5.1.2 Spatial discretisation

In computational space, the mathematical formulations of the 3D shallow water equations cannot be solved analytically. Therefore, these equations are required to be transformed into discrete space before they can be solved.

To do so, the water level and velocity variables are arranged in a Arakawa C-grid arrangement, which is an example of a staggered grid. In such a grid, all scalar variables such as density, water level, salinity, and other substances, are located in the cell center. The velocity components, on the other hand, are located in the center of a cell face orthogonal to the direction of flow. Each of the resulting grids are shifted by one half mesh width with respect to each other. The turbulence quantities are defined in the center of a layer interface, at the relative velocity point (ω point). An illustration of this is shown in Fig. 5.2.

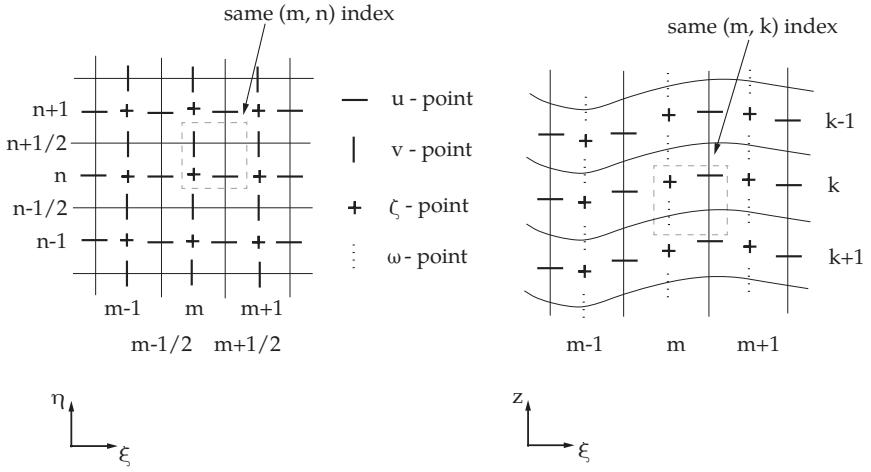

Figure 5.2: Illustration of the Arakawa C-grid implemented in SIMONA. Cell center points, housing the scalar variables are referred to as *water level points*. Center cell face points, storing the velocities, are called the $u-$, v- and ω velocity points, referring to the specific velocities. Adapted from Rijkswaterstaat (2016).

The horizontal advection terms of the transport equation are discretised with the fourth order upwind scheme of Stelling and Leendertse (1992) in one direction and central differences in the other direction. The vertical terms are discretised in time using the θ-method, wherein use is made of a linear combination of the forward and backward Euler schemes (Rijkswaterstaat, 2016).

5.1.3 Time integration

The SIMONA model solves the shallow water equations by an *Alternating Direction Implicit* (ADI) finite difference scheme on a staggered grid (Stelling, 1983). Using this scheme, the time step is split up into two stages, each exactly the length of half a time step. This allows for a locally one-dimensional space splitting

combined with an implicit treatment in the horizontal direction.

The method solves the equation consistently with at least second order accuracy in each stage. The time levels are alternating for each term; the term will be solved implicitly if the term has been solved explicitly in the previous stage. Only two time levels are needed in each stage, requiring less computer storage. A clear advantage of this method is that the implicitly integrated water levels and velocities are coupled along grid lines, which enables the equations to be reduced to a tridiagonal system of equations that can be solved efficiently through Gaussian elimination.

The ADI method used in SIMONA uses a special approach for the discretisation of the cross advection term $v\partial u/\partial \eta$, using the reduced phase error scheme. This scheme splits the third order upwind scheme for the first derivative into two second order central discretisations, which are used separately and successively in both stages of the ADI scheme.

One well-known disadvantage of the ADI method is the ADI-effect. This effect causes inaccurately predicted flow patterns when the ADI method is used for Courant numbers exceeding $4\sqrt{2}$ and the flow direction is not aligned with the grid lines. This upper bound occurs in the case of a narrow channel at an angle of 45 degrees with the computational grid, but in practical situations, the Courant number should not exceed a value of approximately 10. An example of the circumstances under which the ADI-effect will occur is shown in Fig. 5.3.

5.1.4 Turbulence closure models

Different turbulence models are available in WAQUA. In the vertical direction, the user can choose between the implementation of a constant viscosity coefficient, an algebraic model, or the vertical $k-\epsilon$ model.
In the horizontal direction, the user may choose between a constant viscosity coefficient, the horizontal $k-\epsilon$ model, or *horizontal large eddy simulation* (HLES). For the application of the NSC-models in the study presented here, the use of this $k-\epsilon$ model in the vertical direction is most appropriate, which is why the mixing of momentum and mass is modelled using the standard $k-\epsilon$ model implemented in SIMONA. This is in line with many previous modelling studies executed in the Rhine ROFI and New Waterway (de Boer, 2009; de Nijs and Pietrzak, 2012; Rijnsburger *et al.*, 2016, and references therein).

In TRIWAQ, the $k-\epsilon$ model is slightly adapted to be more robust. For this more robust formulation, two assumptions are made:

1. The production and dissipation rates of turbulent energy and the buoyancy govern the level of turbulent energy. This makes the conservation of turbulent kinetic energy and turbulent diffusion less important;
2. In vertical direction, the turbulent diffusion is more important than advection.

The first of these assumptions allows us to write the $k-\epsilon$ equations in non-conservative form, and the second of these assumptions leads to the neglect of the horizontal velocity gradients in the production term and the curvature term.

5.2 Overview used models

Using SIMONA, two different models are integrated to sufficiently cover the hydrodynamic processes in the Rhine-Meuse estuarine system. These models use different bathymetric and geometric grids. In total, three different SIMONA models are available, which are:

- **The Harbour model**: The Harbour model is a 2DH SIMONA model WAQUA) that covers the entire estuary and the larger part of the Rhine ROFI extending along the North Sea coast. Its computational domain covers some 25 kilometers offshore, running from the coast of Schouwen-Duivenland to Zandvoort. The spatial density of the grid on the New Meuse is $\Delta x \approx 100$ m. This model is used to generate the hydrodynamic boundary conditions for the next model (either NSC-Fine or NSC-Coarse).

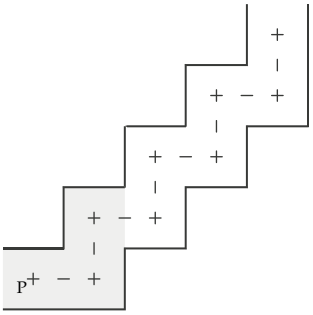

Figure 5.3: Illustration of a zig-zag channel, showing the numerical region of influence. This indicates the circumstances under which the ADI-effect is likely to occur. In this case, the grid lines are not aligned with the flow direction. A wave cannot travel through more than two bends of 90 degrees in one complete ADI step, giving rise to flow inaccuracies. From Deltares (2020).

- **The NSC-Fine model:** The NSC-Fine model is a 3D SIMONA model (TRIWAQ) covering the Rotterdam Waterway and some of its side branches. It includes most of the smaller harbour basins lining the Rotterdam Waterway as well. It is currently used as the main operational model to predict water levels, salinity and velocities by the Port of Rotterdam. The NSC-fine model has previously been validated (Rotsaert, 2010).
- **The NSC-Coarse model:** The NSC-Coarse model is also a 3D SIMONA model (TRIWAQ) covering the Rotterdam Waterway and some of its side branches. It has the same horizontal grid resolution as the Harbour model.

The Harbour model can be combined with either of the NSC-models. For the model comparisons done in this thesis, both combinations are evaluated. The Harbour model and the NSC-models are run independently, and the Harbour model serves as a starting point for the NSC-models by providing the (2DH) boundary conditions for the NSC-models.

The TRIWAQ NSC-Coarse model can be coupled to an SPM model, such as the Delft3D–WAQ NSC-Coarse model first set up by De Groot (2018), providing the hydrodynamic conditions. Although the NSC-Fine model could also be coupled to a Delft3D-WAQ model in theory, computational limits restrict this integration, and coupling is only possible when the NSC-Fine model runs are done for a short time period (i.e. one or multiple days).

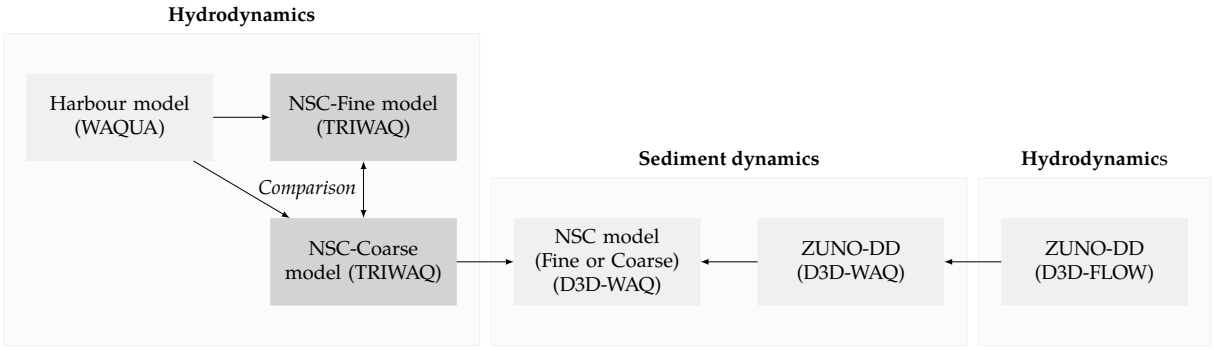

Figure 5.4: Overview of the interaction between different models. Indicated in blue are the models that will be considered in this thesis. The TRIWAQ NSC-Coarse model can be coupled to a Delft3D-WAQ model also using the NSC-Coarse grid, set up by De Groot (2018), to model SPM.

5.3 Model set-up

This section discusses the overall set-up of the hydrodynamic models used in this study. This includes the set-up of the different horizontal and vertical grids, the used bathymetry, imposed boundary and initial

conditions, and model parameters such as the background diffusion and viscosity values.

5.3.1 Computational grids

Horizontal grids

The three different aforementioned models all have different horizontal and vertical grid resolutions. As the name gives away, the NSC-Fine grid has the smallest horizontal grid size of the three with grid sizes of Δx, $\Delta y \approx 25 - 45$ m on the New Meuse and Δx, $\Delta y \approx 20$ m in the Hartel Canal. The Harbour model and the NSC-Coarse model have the same horizontal grid cell size, Δx, $\Delta y \approx 100$ m on the New Meuse. The grid cells in these models are a factor three larger than the grid cells in the NSC-Fine model in each horizontal dimension, which comes down to a factor nine in area.

Compared to the NSC-Fine model, the land boundaries of the NSC-Coarse model and the Harbour model are slightly shifted due to the differences in grid sizes. A comparison figure showing the three different grids compared with each other is depicted in Fig. 5.5.

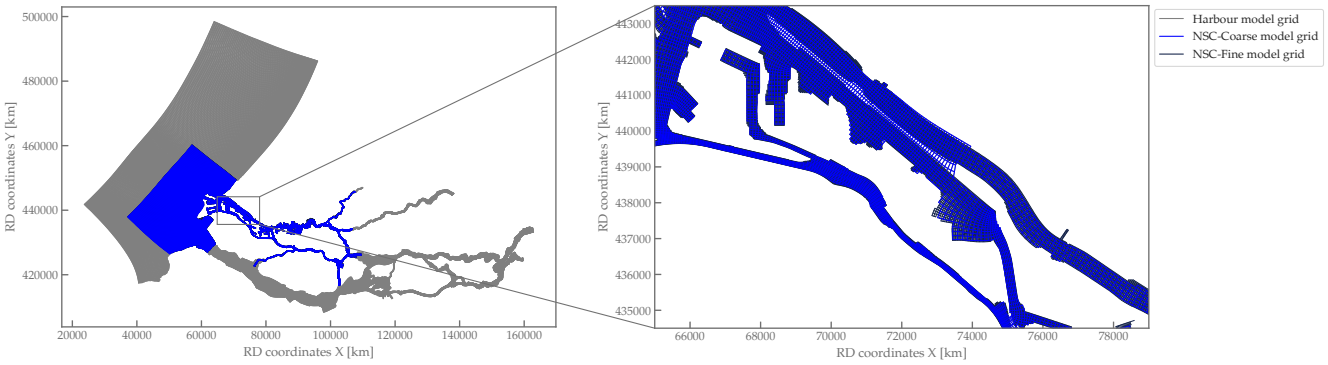

Figure 5.5: Overview of the different SIMONA model grids used in this study. (**Left**) Overview of grid sizes compared to each other. Indicated in grey is the Harbour model, the NSC-Fine grid is shown in dark blue, and the NSC-Coarse grid is depicted in bright blue (**Right**) Zoomed portion of the Rotterdam Waterway that is interest in the framework of the SURICATES pilot project. The NSC-Fine grid is indicated in dark blue and the NSC-Coarse grid is again depicted in bright blue.

Vertical grids

Although the horizontal grids of the operational NSC-Fine and NSC-Coarse model differ, their vertical resolution is the same. Both models have ten sigma layers and the same layer thickness distribution, which is given in Table 5.1. If the TRIWAQ NSC-Coarse model were to be coupled to the Delft3D-WAQ NSC-Coarse model set up by De Groot (2018), however, the number of sigma layers has to be increased to twelve in order to match the number of vertical layers in the Delft3D-WAQ ZUNO-DD model. Since the Harbour model is 2DH, it does not have any vertical layers.

σ-layer [#]	Layer thickness [%]
1	12%
2	12%
3	11%
4	11%
5	11%
6	11%
7	11%
8	9%
9	6%
10	6%

Table 5.1: Layer thickness distributions of the NSC-Coarse and NSC-Fine models.

5.3.2 Bathymetry

The bathymetry used for the model computations are based on the most recent depth information, obtained by sounding vessels, at the end of August, 2019. Sounding vessels navigate the Rotterdam Waterway regularly after which the depth information is transmitted to a larger navigation system directly. By using this depth information, the bathymetry present on August 13th is reproduced as well as possible.

5.3.3 Model parameters

Time step

The time steps used for the NSC-Coarse model and NSC-Fine model differ, and are based on consistency considerations. The NSC-Coarse model uses a time step of 30 seconds and the NSC-Fine model uses a time step of 15 seconds.

Horizontal and vertical background diffusion coefficients

The dispersion/diffusion coefficient is user-defined and can be imposed as spatially varying or spatially uniform. In the current Harbour model, the horizontal diffusion coefficient is spatially varying from values of 50-1500 $m^2\ s^{-1}$ throughout the entire domain. The grid cells at and surrounding the Haringvliet sluices have been imposed a diffusion coefficient of zero $m^2\ s^{-1}$. The horizontal diffusion coefficient in the NSC-models is also spatially varying, but with significantly lower values, in the range of 0.01 to 1.00 $m^2\ s^{-1}$.

Reference density and temperature

The reference density in the entire domain is set to 1000 kg m^{-3}. The reference temperature in the entire domain, for both NSC-models, is set to 10°C. Because the salinities are directly calculated by solving the salt transport equation

5.3.4 Boundary conditions

In order to solve the momentum equation, a set of boundary conditions needs to be imposed on the models. A combination of Riemann conditions at the North Sea boundaries, discharge conditions on the river boundaries and a wind stress at the surface make up the set of these boundary conditions for each model. Furthermore, to resolve the salt balance, salinity boundary conditions are imposed on both the river boundaries and the North Sea boundaries.

Wave conditions are not supplied to the hydrodynamic model. When integration with sediment models is desired, the impact of waves becomes much more important due their influence on the bottom shear stress. In such cases, integration of the SIMONA models with the wave model *Simulating WAves Nearshore* (SWAN) is possible and desired.

Tides, salinity and discharge

As was previously stated, in order to run the NSC-models, it is necessary to first run the Harbour model. This is due to the fact that the larger Harbour model generates the sea boundary conditions. These boundary conditions are generated by the Harbour model following a two-step approach.

In the first step, the Riemann boundary conditions for the Harbour model are made up of harmonic components, which are obtained from a model simulation of 1998 with only the astronomic tide as input. Kalman filtering is used to assimilate boundary conditions from five predetermined reference water level points (Deltares, 2015). These newly assimilated boundary conditions are then imposed on the Harbour model's sea boundaries as Riemann time series in the second step. The discharge boundary conditions, salinity boundary conditions and the wind stress of the Harbour model remain the same throughout these two steps, and are supplied to the model by the user.

For the salinity boundary condition at the boundaries of the Harbour model, a Thatcher-Harleman boundary condition (Thatcher and Harleman, 1972) is applied, which ensures a sinusoidal transition between outflow salinity concentration to the inflow salinity concentration (Rijkswaterstaat, 2016).

The NSC-models can subsequently be run using the results of the Harbour model computation by *nesting*. Since the Harbour model is a 2DH model, and therefore does not have a vertical dimension, the boundary conditions supplied to the NSC-models are also two dimensional. The boundary conditions that are supplied to the NSC-models are Riemann boundary conditions on the sea boundaries, discharge boundary conditions at the Lek, Beneden Merwede, Dordtsche Kil and Spui, and salinity boundary conditions on all of the river boundaries and the sea boundary. The time series used for this are assimilated based on discharge data at Lobith. By using actual data for these boundary conditions, the modelling study is called a *hindcast*.

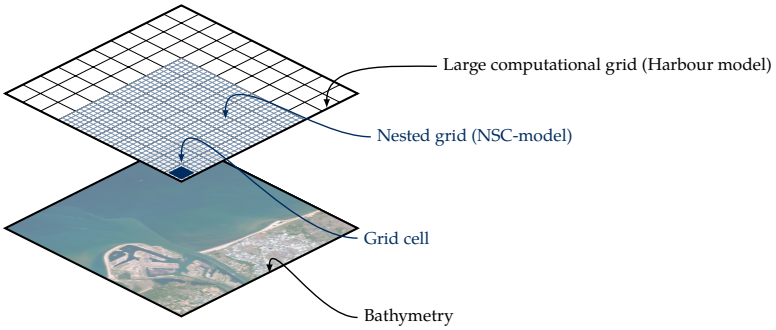

Figure 5.6: Schematic of the principle of nesting of the NSC-models in the Harbour model. In the case of this thesis, the large computational grid is the Harbour model, in which the NSC-models are nested for the numerical computations. Satellite image courtesy of NASA Earth Observatory.

Wind

The wind conditions supplied to the Harbour model and NSC-models are based on wind measurements at the Noorderpier, a pier located near Hoek van Holland. The wind direction and magnitude are measured here at a height of 15 m above ground level. SIMONA directly calculates the wind stress from these wind measurements, and imposes this wind stress as a spatially uniform value on the water surface in the entire domain. On certain parts of the domain, a wind reduction factor is imposed (*see* Fig. 5.7). The calculation of the wind stress is done using a constant drag coefficient C_D of 0.0026 and an air density $\rho_{air} = 1.205$ kg/m^3.

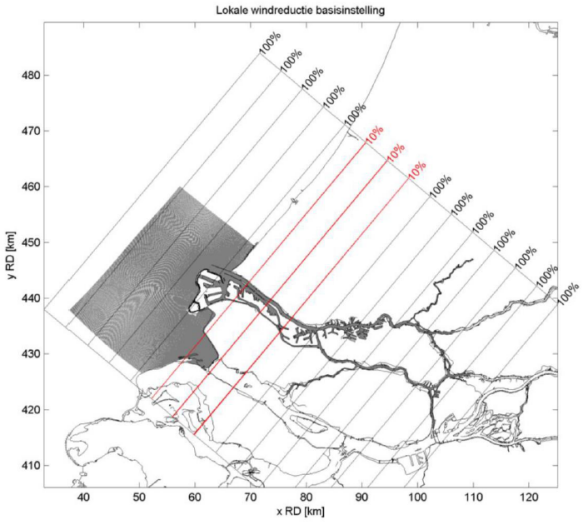

Figure 5.7: Overview of local wind reduction in the NSC-Fine model. From Kranenburg (2015).

5.3.5 Initial conditions

A set of initial conditions is necessary for simulation of both NSC-models and the Harbour model. Restart files are available for the Harbour model, which provide the initial conditions for the water levels, water velocities, temperatures, and the salt concentrations. The availability of restart files enables the Harbour model to be run without spin-up.

The initial conditions for the NSC-models are made from earlier runs of the operational NSC-models instead of a full restart, because the grid of the operational model differs slightly from the NSC-models used for the model runs in this thesis (some small harbours are added). Although this is not technically a restart, these initial conditions have roughly the same effect as doing a full restart. The spin-up effect is therefore minimal and only visible at the boundaries of the added grid.

5.4 Outputs

The standard defined output points at which history files are written are all fixed measuring points within the Rotterdam Waterway and the Port of Rotterdam's harbours that are owned by either The Port of Rotterdam or Rijkswaterstaat. At these points, either the salinity or the water level is given, in agreement with the function of the fixed measuring station. The velocity in three dimensions (u, v and w), is calculated and given for all these fixed measuring points as well. Three different salinity stations and three different water level stations are taken into account to test the predictive capability of the two NSC-models. These stations have been chosen because they enclose the August 13th measurement survey area, and their names, along with the parameters that they measure, are summarised in Table 5.2.

Table 5.2: Overview of the different fixed measuring stations that are used for the predictive capability tests. The numbers indicate the amount of sensors at the location.

Name station	Salinity	Water level	Longitude	Latitude
Hoek van Holland	3	1	4.119842	51.977412
Lekhaven	3		4.429597	51.904099
Brienenoordbrug	3		4.542472	51.905252
Spijkenisserbrug	2		4.339867	51.859611
Maassluis		1	4.249788	51.917507
Vlaardingen		1	4.349048	51.899639

Besides these fixed measuring points, model output points to compare with the August 13th monitoring survey are obtained by inputting the exact measuring locations and times of measurements, based on the GPS coordinate and time logged by the surveying boat, and writing history files from these locations.

Table 5.3: Overview of output coordinates and times for the August 13th monitoring survey comparison. Each transect consists of eleven measuring stations located along the thalweg of the New Waterway (*see* Fig. 4.2).

Name station	Longitude [°]	Latitude [°]	Time [UTC + 1]
1014	4.305958 / 4.307964 / 4.306508	51.894089 / 51.893638 / 51.894319	07:56:54 / 12:11:45 / 12:24:03
1015	4.294441 / 4.295739 / 4.295135	51.896365 / 51.896033 / 51.896200	08:06:26 / 12:02:46 / 12:32:37
1016	4.280099 / 4.281779 / 4.281307	51.899170 / 51.898894 / 51.899050	08:16:29 / 11:53:03 / 12:43:01
1017	4.268018 / 4.269530 / 4.269338	51.904183 / 51.903773 / 51.903795	08:26:51 / 11:43:46 / 12:52:40
1018	4.256165 / 4.257336 / 4.257682	51.909580 / 51.909204 / 51.909168	08:35:58 / 11:32:24 / 13:02:43
1019	4.243964 / 4.245350 / 4.245900	51.915109 / 51.914458 / 51.914300	08:45:30 / 11:22:47 / 13:13:04
1020	4.232180 / 4.233786 / 4.234266	51.920697 / 51.919730 / 51.919351	08:54:30 / 11:12:45 / 13:22:56
1021	4.223922 / 4.225279 / 4.225498	51.928217 / 51.927666 / 51.927404	09:03:31 / 11:02:33 / 13:33:07
1022	4.212606 / 4.213933 / 4.215103	51.934443 / 51.934346 / 51.933744	09:12:44 / 10:49:37 / 13:43:16
1023	4.201396 / 4.202136 / 4.202948	51.939380 / 51.939384 / 51.939056	09:21:29 / 10:36:53 / 13:53:23
1024	4.188311 / 4.189670 / 4.190381	51.943914 / 51.943353 / 51.943427	09:30:27 / 10:26:55 / 14:03:15
1030	4.117836 / - / 4.119356	51.976367 / - / 51.976149	09:54:48 / - / 14:29:32

Part III

RESULTS

This part examines the *results* obtained from a thorough data analysis and numerical modelling study. An assessment of the predictive capability of the used numerical models is used to place the attained results into perspective.

Chapter 6

Internal flow structure in the Rotterdam Waterway

This chapter elaborates on the results of the August 13th monitoring survey analysis following the methodology presented in Chapter 4. The aim of the analysis presented here is to gain insight into the dominant hydrodynamic processes governing SPM transport.

Section 6.1 presents the results of the analysis, and compares these to the results of a similar survey presented in earlier work by de Nijs *et al.* (2010a,b). Each subsection will then elaborate on one or several of the calculated parameters mentioned in Chapter 4, Section 4.3.

The chapter is concluded with a discussion of the results in Section 6.2, and the overall conclusions following from the analysis (Section 6.3).

6.1 Results

6.1.1 Salinity parameters

The two salinity parameters discussed in the following sections are the salinity structure and the pycnocline height distribution over the tidal cycle. The salinity structure is presented alongside the along-channel velocity structure, so the interaction between the velocity and salinity distribution can be examined. Fig. 6.3 covers these results of the ADCP and CTD measurements, depicting the salinity and velocity structure for each of the measured transects in two dimensions (space and depth).

Salinity and velocity structure

The Lagrangian-style measurements conducted on August 13th were set up in such a way that the tidal variation and displacement of the salt wedge could be investigated. A more comprehensive description of this dataset is given in Chapter 4. The dataset covers ADCP and CTD measurements that are collected while navigating up and down along the channel axis of the Rotterdam Waterway three times, resulting in three different transects. The resulting transects can be visualised in three dimensions; time, space and depth. This is done for the salinity measurements as well as the cross-channel and along-channel velocities in Figs. 6.2 and 6.1.

Velocity structure

Whilst navigating the first transect, the downestuary flow direction was prevalent, indicating ebb flow. A positive flow velocity is measured just above the bed in the region of the channel bend at Maassluis, indicative of flow in the upstream direction. Because the channel is locally deeper here, it is possible that these measured positive velocity values are a result of local turbulence phenomena.

During navigation along the second transect, the tide is turning. This is visualised nicely in Fig. 6.1A, showing ebb-directed flow in the upper water column and flood-directed flow in the lower part of the water column. This indicates that slack tide occurs at different times in the upper and lower parts of the water column, the interface between which is the pycnocline (*see* Figs. 6.2 and 6.3). This is in line with observations by de Nijs *et al.* (2010a, Figs. 2 and 11), who mention these distinct phase lags within the water column as well. This return flow profile is visible over the entire measured transect.

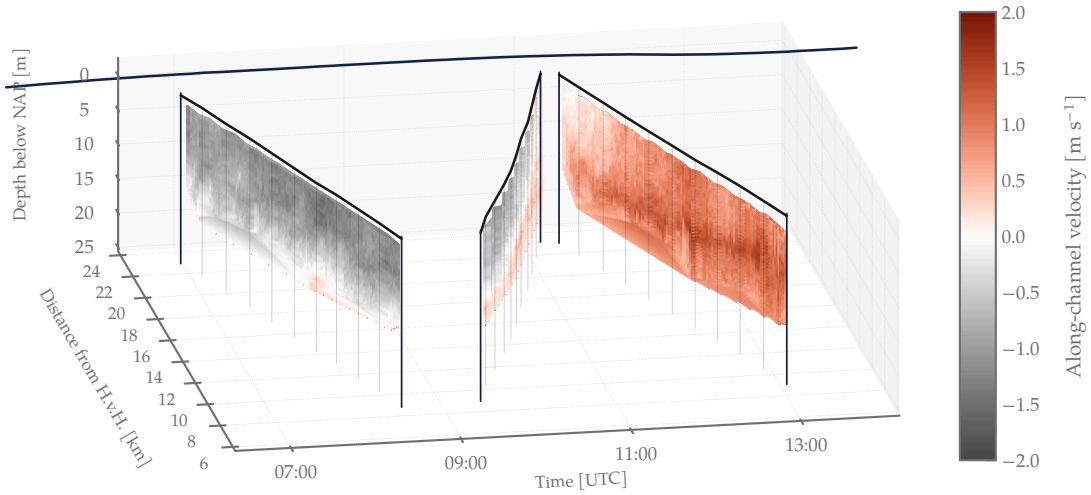

(A) Along-channel velocities

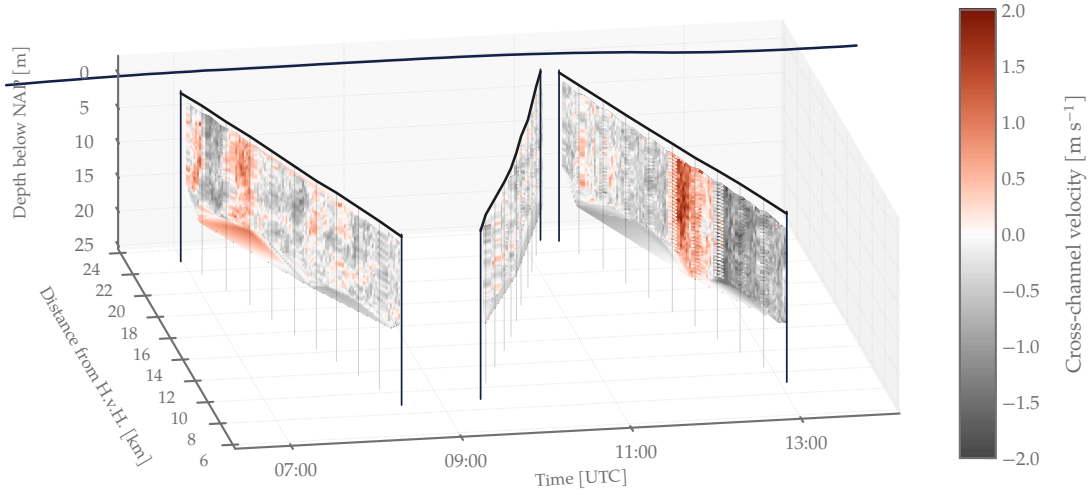

(B) Cross-channel velocities

Figure 6.1: Figure showing the (A) along-channel velocity profile and (B) cross-channel velocity profile during the measurements in three dimensions. The x-axis represents the time , the y-axis represents the distance from Hoek van Holland [km] and the z-axis is representative of the depth below NAP [m]. The locations of individual measured verticals are indicated with the opaque blue vertical lines. The water level at Hoek van Holland is indicated in the back of the plot, in dark blue.

As the tide progresses into flood, the near-bed velocities are larger than the velocities near the surface, after which velocity maxima form at mid-depth suggesting strong internal shear (*see* Figs. 6.1A and 6.3). The evolution of these jet-like features at the height of the pycnocline (*see* Section 6.1.1) has been observed in several different (types of) estuaries (Chant *et al.*, 2007; Cudaback and Jay, 2001; Geyer and Farmer, 1989), including the Rotterdam Waterway (de Nijs *et al.*, 2009). These jet-like features are visible throughout the entire transect during flood, and although our measurements do not extend beyond the head of the salt wedge, de Nijs *et al.* (2010a) has reported these jet-like features even extending beyond the head of the salt wedge in the past. The occurrence of these jet-like features is explained by the fact that the baroclinic driving force (*see* Section 6.1.3) increases with depth, which means that the total pressure gradient in the pycnocline is larger than in the part of the water column that lies above the pycnocline. At the pycnocline,

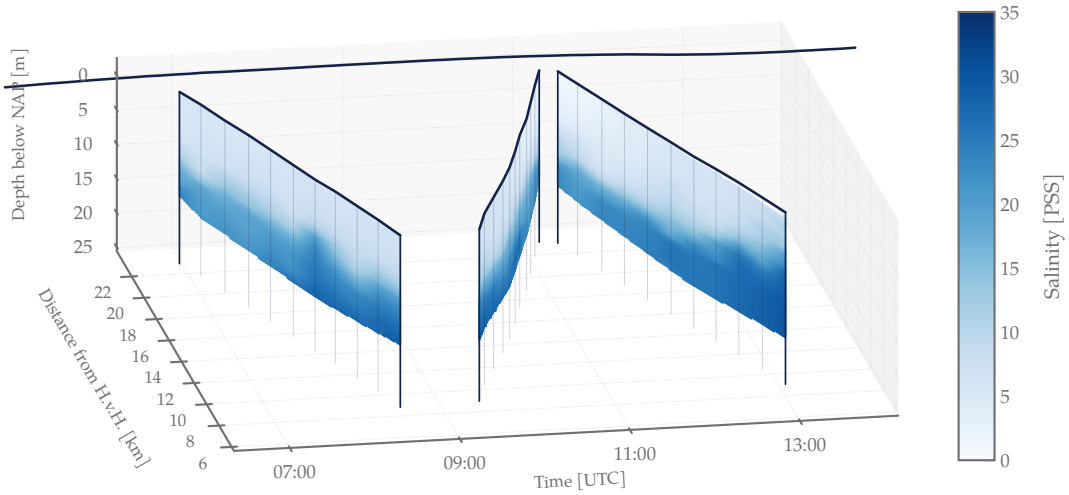

Figure 6.2: Figure showing the salinity profile during the measurements in three dimensions. The x-axis represents the time , the y-axis represents the distance from Hoek van Holland [km] and the z-axis is representative of the depth below NAP [m]. The locations of individual measured verticals are indicated with the opaque blue vertical lines. The water level at Hoek van Holland is indicated in the back of the plot, in dark blue.

stratification dampens the turbulent fluctuations, giving rise to higher velocities locally.

Looking at the cross-channel velocities (*see* Fig. 6.1B), we see that the prevailing cross-channel velocity is negative, indicating that the cross-channel direction is predominantly directed to the right of the upestuary direction. A few exceptions to this are visible. Whilst navigating the first transect, the ADCP recorded positive cross-channel velocities throughout the water column between locations 1014 and 1015, and near location 1017. At locations 1020 and 1021, positive cross-channel velocities are recorded in the upper part of the water column, whereas negative cross-channel velocities are observed in the lower part of the water column. Both of these observations are expected to be related to the channel geometry. The Botlek harbour basin is located approximately between locations 1014 and 1015, which makes it probable that the positive cross-channel velocities here during ebb are related to the outflow of water from the harbour basins. The positive velocities around location 1017 are less easily explained. The positive cross-channel velocities in the upper part of the water column at locations 1020 and 1020 are most likely a result of the geometry of the channel, as locations 1020 and 1021 are located in a channel bend. The notable positive cross-channel velocities observed between locations 1019 and 1020 of transect 3 are also likely related to the geometry of the channel.

Salinity structure

Overall, the salinity structure remained fairly stable over the course of the monitoring survey. A salt wedge was visible throughout the entire duration of the monitoring survey at all locations, although the steepness of the pycnocline varies over the tidal cycle. The evolution of the salinity distribution over the course of the monitoring survey is indicated in Figs. 6.2 and 6.3. As previously mentioned, the first transect is indicative of ebb flow, the second transect is indicative for LWS and the third transect is indicative for flood.

During ebb tide, one measured CTD vertical stands out against the rest of the measured verticals. From Fig. 6.3A it is visible that at a distance of 14 km from Hoek van Holland, a sharp increase in pycnocline height is observed. The pycnocline is not only located higher up in the water column here, but it also seems sharper compared to the previous and following CTD verticals. There may be multiple explanations for this. Firstly, the Rotterdam Waterway channel has a bend that roughly coincides with the location of increased salinity. Secondly, the bathymetry of the channel is locally deeper at this location, an effect of the flow phenomena occurring in the channel bend. These locally higher salinity values are also observed in de Nijs *et al.* (2010a, Fig. 5). In agreement with the observations done here, de Nijs *et al.* measured salinities of 2 PSS close

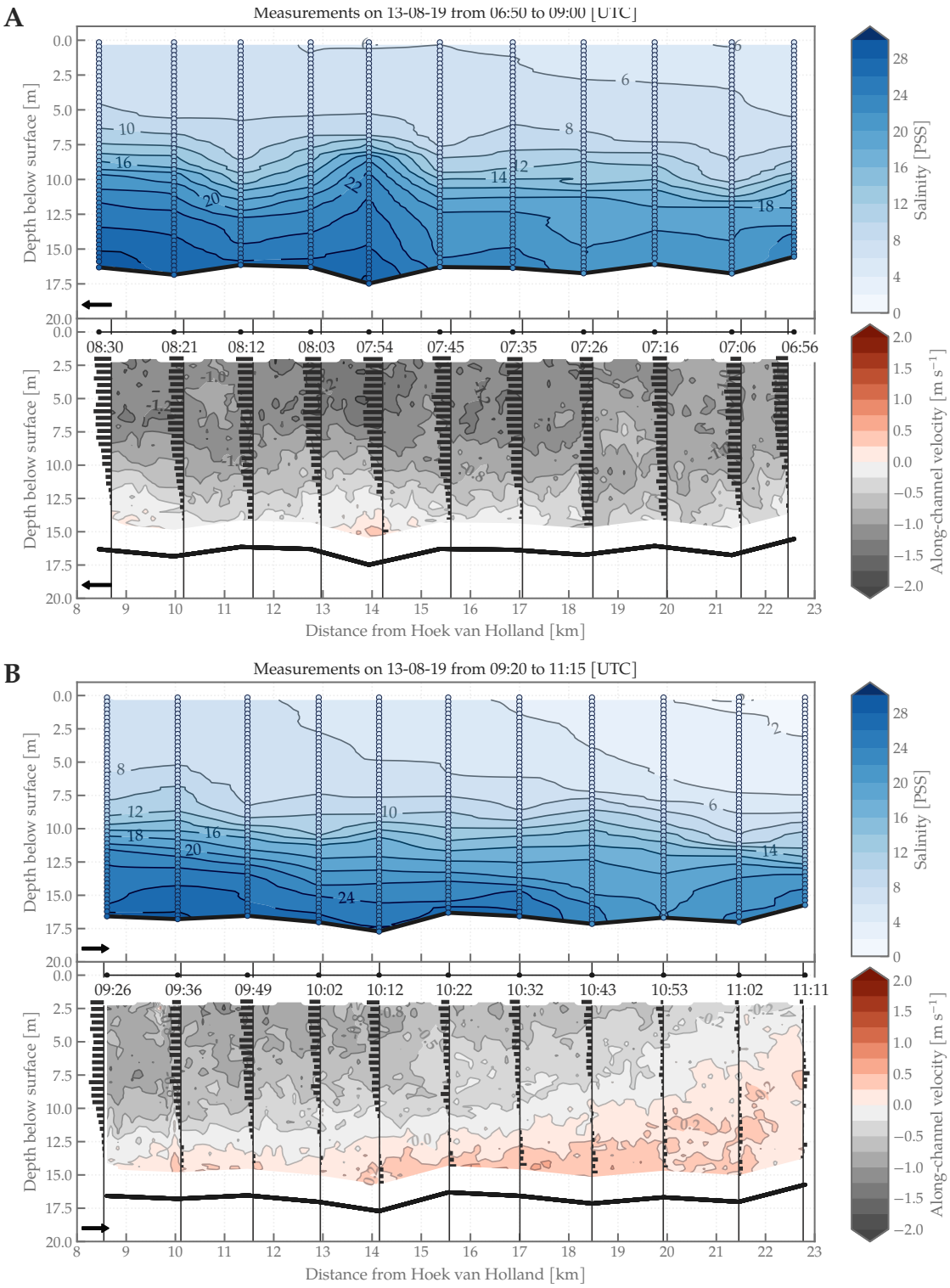

Figure 6.3: Overview of the along-channel vertical distribution of salinity (top panel in figure) and primary velocity component (bottom panel in figure) constructed from data obtained during the monitoring survey conducted on August 13th, 2019. The primary velocity components were calculated by PCA. In the bottom panels, negative velocities (dotted lines) indicate ebb flow. Each figure (**A-C**) refers to a different track: (**A**) 06:50-9:00 UTC, (**B**) 9:20-11:15 UTC, (**C**) 11:20-13:40 UTC.

to the bed at this location, whilst some stations closer to the river mouth were already completely fresh. However, as the tide progresses and the salt wedge advects farther upestuary, de Nijs *et al.* report that the

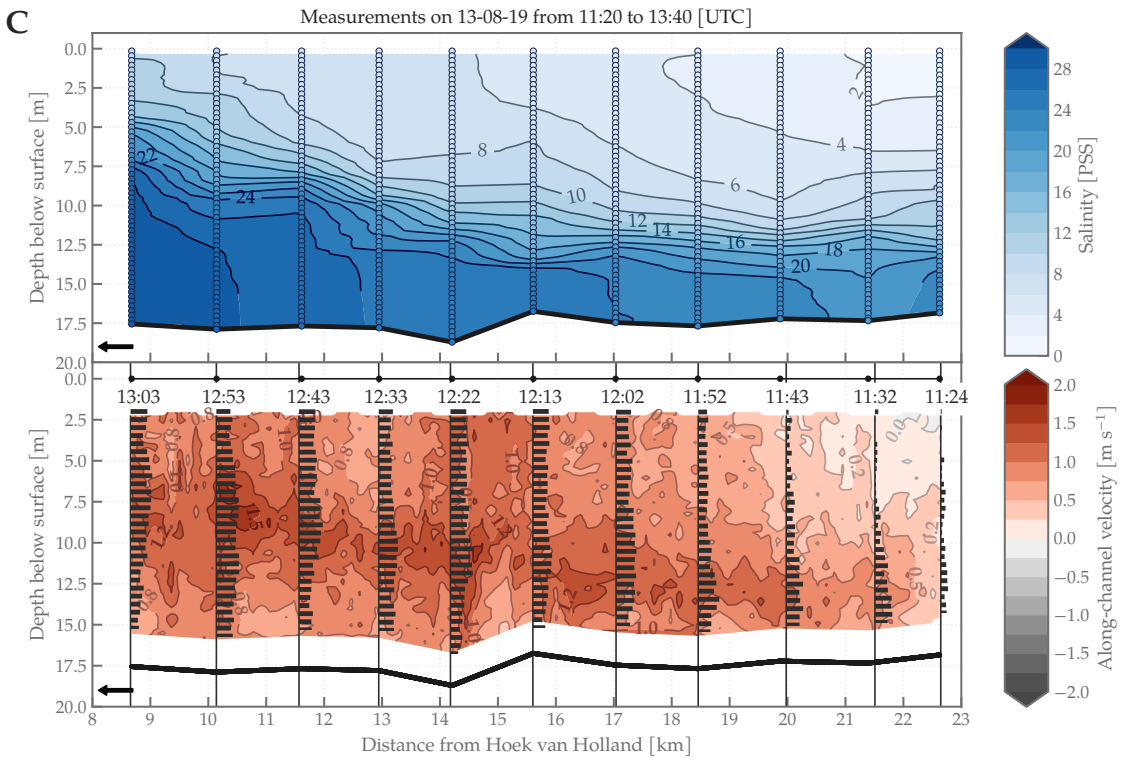

Figure 6.3: *(Continued)*

high 'outlying' salinity values at this location remain, whereas the results presented here do not show such high values after ebb tide. It is hypothesised that the bathymetry here induces locally higher turbulence rates. Under low discharge conditions, the salt wedge protrudes much farther into the estuary, and the presence of this more layered salinity structure may dampen these turbulent fluctuations at the pycnocline. During the high discharge conditions of the survey on April 11th, 2006 (de Nijs *et al.*, 2010a), the turbulent fluctuations are not dampened as much, as a result of the absence of the salt wedge at this location during most of the tidal cycle.

Whilst navigating the second transect, exchange-type processes flatten the isohalines, giving rise to a more layered salinity structure as the salt wedge progresses farther upestuary through the near-bed flow convergence regions.

As the tide progresses into flood (*see* Fig. 6.3C), the protruding mid-depth jet-like features act to steepen the isohalines by advecting waters with lower salinity over the more saline waters confined below the pycnocline. The effect of these advective processes is not to be confused with the effect that turbulent mixing might have on the water column, as Geyer and Farmer (1989) and de Nijs *et al.* (2010a) have previously pointed out.

Indeed, in general, advection-driven processes seem to control the development of the salinity structure in time, as was also suggested by de Nijs *et al.* (2010a,b). This suggests that the stratification acts on turbulent mixing by dampening the turbulent motions at the pycnocline. Whether this is in accord with the observations of the Richardson gradient number, is discussed in Section 6.1.2.

Pycnocline height

The development of the pycnocline height in time and space can be deduced from Figs. 6.2 and 6.3, as well as calculated according to the methodology described in Chapter 4, Section 4.4.1. The results of the calculation of the pycnocline height are summarised in Table 6.1

The pycnocline height is fluctuates throughout the tidal cycle, as is expected. During ebb tide, the pycnocline height is fairly uniform over the entire measured transect. As the tide starts turning, baroclinic

Table 6.1: Calculated values of the pycnocline height per measured CTD vertical and transect on August 13th, 2019. The height of the pycnocline is defined as the height within the water column at which the vertical density gradient is maximal.

	Depth of pycnocline below surface [m]		
Location nr.	**First transect**	**Second transect**	**Third transect**
1014	9.60	12.96	12.96
1015	11.43	11.45	11.15
1016	10.81	10.23	11.75
1017	10.81	8.70	12.35
1018	9.90	14.45	12.64
1019	9.60	15.65	13.53
1020	8.07	9.60	11.72
1021	10.80	10.81	9.59
1022	10.50	9.90	8.37
1023	9.28	10.19	9.25
1024	9.28	10.20	4.71

return flows flatten the isohalines, leading to an even more uniform density profile over the measured transect. The effect of this flattening of isohalines is that the pycnocline as defined in Chapter 4, Section 4.4.1, is shifted slightly over the vertical to a deeper point in the water column. During the early evolution of the flood tide, the pycnocline is shifted to an even slightly larger depth, after which the pycnocline shifts significantly upwards in the water column as the saltier protrude farther into the estuary.

6.1.2 Stability parameters

Buoyancy frequency profiles were calculated for all CTD verticals using a centered differences scheme (*see* Chapter 4, Section 4.4.2). The gradient Richardson number is calculated from the squared Brunt-Vaïsalä and interpolated shear profiles. The results of this computation are shown alongside the results of the computation of the Richardson gradient numbers in Fig. 6.4.

Whilst navigating the first transect, the water column was statically unstable close to the bed and close to the surface, where the squared Brunt-Vaïsalä frequency plummeted below zero. The dark grey patches in the bottom panel of Fig. 6.4A indicate regions of high static stability. These regions are located at the height of the pycnocline (*see* Fig. 6.3A). Overall, static stability is guaranteed during the largest part of transect 1, although the upper part of the water column is statically unstable at the beginning of the transect.

The values of the Richardson gradient number give an indication of the dynamic stability of the water column. Distinct red patches in the upper panels in Fig. 6.4 indicate regions of high dynamic stability. White patches indicate static instability. It follows from 6.4 that dynamic stability is guaranteed for the largest part of the water column during transect 1, although some patches near the bottom and the surface do show values of the Richardson gradient number that fall below 0.25. A distinct red patch is visible in the deeper pit between measuring locations 1017 and 1019, indicating high dynamic stability. At this location, higher salinity values were observed near the bottom (*see* Section 6.1.1). Above this very dynamically stable patch, dynamic instability is observed. This supports the hypothesis posed in Section 6.1.1, as dynamic instability implies that turbulent motions may be present locally.

The second transect again shows static stability around the pycnocline, indicated by the high squared Brunt-Vaïsalä frequency values. The water column is dynamically stable around the pycnocline as well, indicating that turbulent mixing is damped by stratification here. As the tide turns, lower values of the Richardson gradient number are visible at the locations with high amounts of shear, at the interface of the return flows. Close to the bed, the water column even becomes dynamically unstable.

The same trend of static and dynamic stability around the pycnocline is clearly visible at the beginning of flood (*see* Fig. 6.4C). The region below the pycnocline, however, is now more unstable than during previous transects. Instability is observed in the entire region below the pycnocline. Interestingly, the values of the squared Brunt-Vaïsalä frequency and the Richardson gradient number around the pycnocline are higher at flood than during ebb and LWS, indicating that the region around the pycnocline is more stable during the beginning of flood than during LWS and ebb. It is expected from earlier observations by de Nijs *et al.* (2010a) that this effect is reduced again in a later stage of flood.

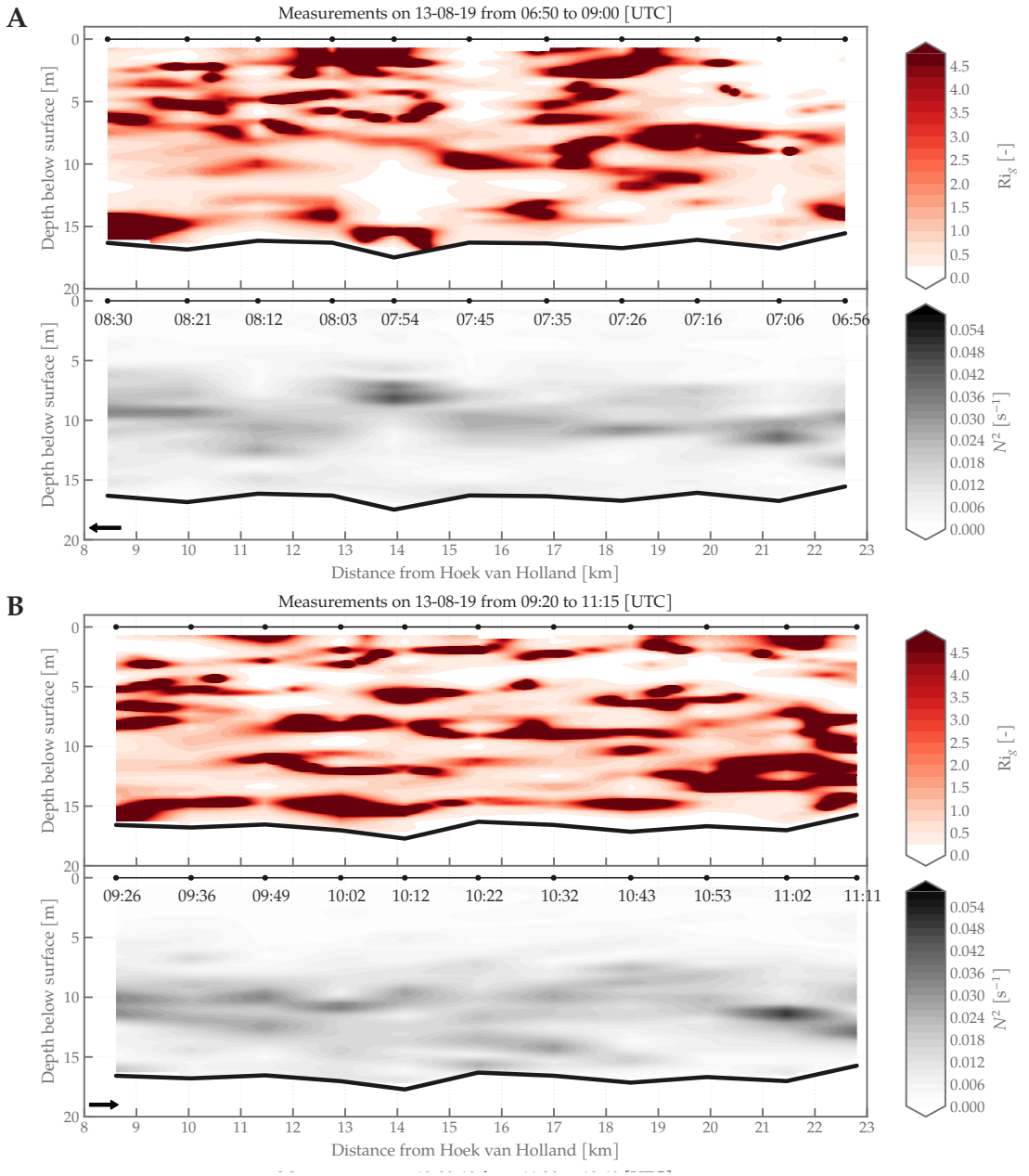

Figure 6.4: Overview of the calculated Richardson gradient numbers and the squared buoyancy frequency measured during a monitoring survey on August 13th, 2019. The primary velocity components were calculated by PCA. Each figure (**A-C**) refers to a different track: (**A**) 06:50-9:00 UTC, (**B**) 9:20-11:15 UTC, (**C**) 11:20-13:40 UTC.

The fact that the Brunt-Vaïsalä frequency and Richardson gradient number profiles indicate static and dynamic stability around the pycnocline, indicates that the salt wedge remains stable throughout the tidal cycle. This finding is in agreement with the observations in de Nijs *et al.* (2010a,b).

6.1.3 Momentum balance terms

Following the methodology presented in Chapter 4, Section 4.4.3, the individual momentum balance terms in a simplified-along channel momentum balance can be quantified. In doing so, we will elucidate the dominant hydrodynamic processes influencing the distribution and transport of SPM. To reduce the amount of introduced error, the estimation of the dominant terms makes use of velocity profiles that are not extrapolated or interpolated, which means that side lobe effects and blanking distance are not accounted for.

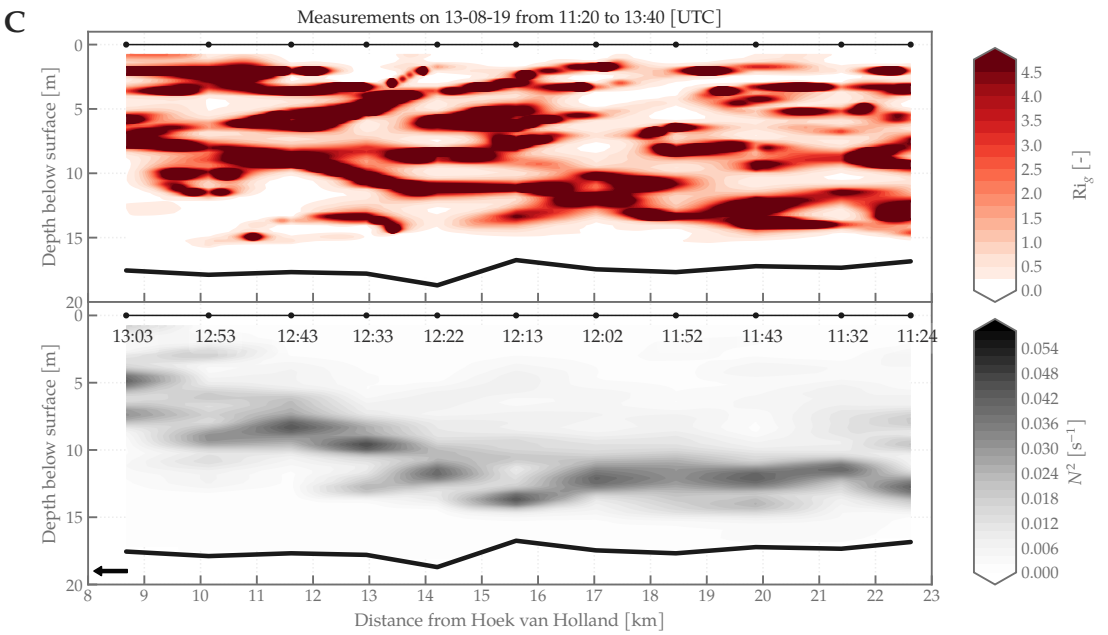

Figure 6.4: *(Continued)*

For the determination of the total Reynolds shear stress distribution over the vertical, however, it is necessary to extrapolate the velocity profiles to cover the entire water column (*see* Chapter 4, Section 4.2.4). The following sections elaborate on the outcome of the analysis, and the parallels between this research and previously executed research in the Rotterdam Waterway.

Individual balance terms

Previous work by de Nijs *et al.* executed in the Rotterdam Waterway reports that the barotropic and baroclinic pressure gradient terms in the momentum balance are dominant. It is thus very interesting to see that the results presented in Figs. 6.5 and 6.6 are not in line with the de Nijs *et al.*'s observations. From the results presented here we could conclude that, given the meteorological and discharge conditions, the dominant term in the momentum balance on August 13th was the local acceleration term. Considering this, it must also be noted that the work by de Nijs *et al.* neglects the calculation of the local acceleration term, as it could not be determined properly (de Nijs *et al.*, 2010a,b). The method used in this thesis to determine the local acceleration is also associated with an error, as was mentioned in Chapter 4, Section 4.4.3. If we would have neglected the local acceleration term here too, the baroclinic pressure gradient term would be dominant, closely followed by the barotropic pressure gradient.

The baroclinic pressure gradient increases with depth as a result of the larger salinities in the lower part of the water column. This baroclinic pressure gradient acts to advance the onset of ebb in the upper part of the water column and retard it in the lower part of the water column, thus lengthening the flood period relative to the ebb period in the lower part of the water column. Vice versa, baroclinity leads to lengthening of the ebb period relative to the flood period in the upper part of the water column. This is illustrated nicely by the along-channel velocity profiles in Figs. 6.1A and 6.3, too.

During ebb tide, the baroclinic pressure gradient dominates the barotropic pressure gradient, whereas the barotropic pressure gradient dominates the barotropic forcing during LWS. During flood tide, the competition between both pressure gradients seems more balanced. Furthermore, during ebb tide and LWS, both gradients (generally) oppose each other, whereas during flood tide, the gradients enforce each other. The few exceptions to this are a result of local salinity peaks (*see* Section 6.1.1).

Compared to the results of the monitoring survey presented in de Nijs *et al.* (2010a), Figs. 6.5 and 6.6 present a much larger variation of the barotropic pressure gradient along the channel axis. This could well be a result of the difference in calculation methods, as de Nijs *et al.* does not explicitly mention the method used

Table 6.2: Minimum, maximum and mean values of the calculated Btransectt-Vaïsäla frequency profiles at locations 1023, 1022 and 1021 using the raw data from CTD measurements conducted on August 13th, 2019.

First transect							
Name	**Time [UTC]**	$\mathbf{N^2_{mean}}$ **[s^{-1}]**	$\mathbf{N^2_{min}}$ **[s^{-1}]**	$\mathbf{N^2_{max}}$ **[s^{-1}]**	$\mathbf{c_1}$ **[m/s]**	$\mathbf{R_I}$ **[m]**	$\mathbf{R_E}$ **[m]**
1020	07:54:30	0.0098	-0.0210	0.0578	0.4709	4113.3	114360
1021	08:03:31	0.0093	-0.0051	0.0239	0.4562	3984.2	110422
1022	08:12:44	0.0091	0.0005	0.0334	0.4247	3708.7	109882
1023	08:21:29	0.0092	-0.0002	0.0416	0.4499	3928.5	112240
Second transect							
Name	**Time [UTC]**	$\mathbf{N^2_{mean}}$ **[s^{-1}]**	$\mathbf{N^2_{min}}$ **[s^{-1}]**	$\mathbf{N^2_{max}}$ **[s^{-1}]**	$\mathbf{c_1}$ **[m/s]**	$\mathbf{R_I}$ **[m]**	$\mathbf{R_E}$ **[m]**
1023	09:36:53	0.0096	-0.0001	0.0298	0.4577	3996.5	112056
1022	09:49:37	0.0094	0.0003	0.0375	0.4203	3670.0	111215
1021	10:02:33	0.0094	-0.0005	0.0455	0.4531	3957.3	112853
1020	10:12:45	0.0084	-0.0167	0.0313	0.4642	4054.3	115136
Third transect							
Name	**Time [UTC]**	$\mathbf{N^2_{mean}}$ **[s^{-1}]**	$\mathbf{N^2_{min}}$ **[s^{-1}]**	$\mathbf{N^2_{max}}$ **[s^{-1}]**	$\mathbf{c_1}$ **[m/s]**	$\mathbf{R_I}$ **[m]**	$\mathbf{R_E}$ **[m]**
1020	12:22:56	0.0076	-0.0002	0.0424	0.3987	3482.2	118305
1021	12:33:07	0.0083	-0.0012	0.0568	0.3706	3236.7	115381
1022	12:43:16	0.0084	-0.0014	0.0504	0.3827	3341.9	114989
1023	12:53:23	0.0084	-0.0203	0.0355	0.4270	3728.6	115655

Table 6.3: Mean, maximum and minimum values of the Brunt-Vaïsäla frequency profiles, first baroclinic wave speed, and internal and external Rossby radius of deformation at the Hoek van Holland measuring location of the monitoring survey on August 13th.

First transect							
Name	**Time [UTC]**	$\mathbf{N^2_{mean}}$ **[s^{-1}]**	$\mathbf{N^2_{min}}$ **[s^{-1}]**	$\mathbf{N^2_{max}}$ **[s^{-1}]**	$\mathbf{c_1}$ **[m/s]**	$\mathbf{R_I}$ **[m]**	$\mathbf{R_E}$ **[m]**
1030	08:54:48	0.0095	0.0011	0.0273	0.4794	4183.9	111760
1030	13:29:32	0.0088	-0.0124	0.0455	0.3750	3273.2	115931

Table 6.4: Mean, maximum and minimum values of the Btransectt-Vaïsäla frequency profiles at the Hoek van Holand measuring location of the monitoring survey on August 13th.

First transect							
Name	**Time [UTC]**	$\mathbf{N^2_{mean}}$ **[s^{-1}]**	$\mathbf{N^2_{min}}$ **[s^{-1}]**	$\mathbf{N^2_{max}}$ **[s^{-1}]**	$\mathbf{c_1}$ **[m/s]**	$\mathbf{R_I}$ **[m]**	$\mathbf{R_E}$ **[m]**
1030	08:54:48	0.0095	0.0011	0.0273	0.4794	4183.9	111760
1030	13:29:32	0.0088	-0.0124	0.0455	0.3750	3273.2	115931

to calculate the barotropic pressure gradient. It could also be a result of the difference in Rhine discharge conditions, or a side-effect of recent human-induced changes into the system, such as the deepening of the Rotterdam Waterway.

As in de Nijs *et al.* (2010a,b), it is clear from Figs. 6.5 and 6.6 that advection of momentum influences the resulting shape of the velocity profiles by determining the strength of the differential advection and mixing. Advection minima are observed in the pycnocline region during flood and advection maxima are observed in the same region during ebb, although the effect is not as apparent nor as uniform for each measuring location as it is in de Nijs *et al.* (2010a, Fig. 13).

From Fig. 6.5, it is visible that the baroclinic terms in the momentum incidentally become positive over the vertical, rather than taking on—what is expected—negative values over the vertical. This is due to the locally higher measured salinity values at these locations. Later, Section 6.1.5 will dive deeper into whether this may be caused by occurrence of internal waves.

An important side note to all the abovementioned information, is that the Rhine discharge mentioned in de Nijs *et al.* (2010a), was much higher than usual. Conversely, the Rhine discharge on the August 13th survey was much lower than usual, almost a factor three lower than the discharge mentioned in de Nijs *et al.* (2010a), putting significantly less buoyancy into the system. Furthermore, the survey in de Nijs *et al.*

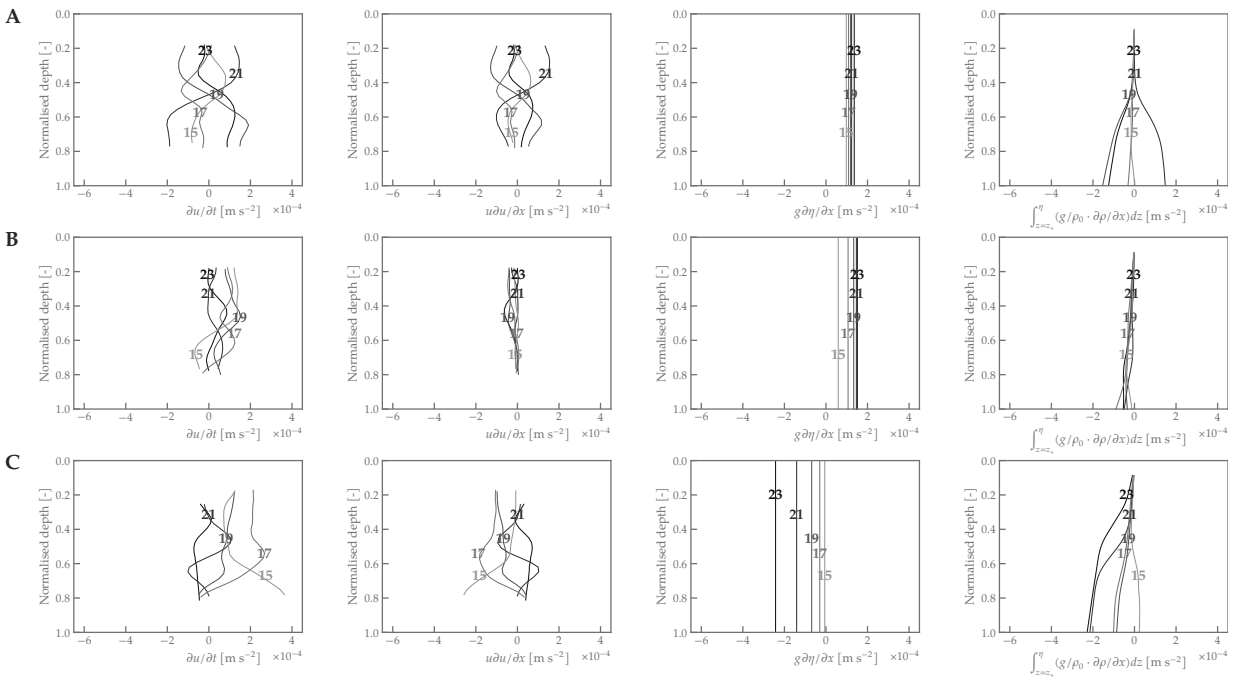

Figure 6.5: Overview of the estimated terms in an along-channel momentum balance for the uneven numbered measuring locations of the August 13th survey. Locations are numbered according to the last numbers in their Rhine kilometer numbering, i.e. 14 corresponds to location 1014. From left to right, the local acceleration term, the advective acceleration term, the barotropic pressure gradient term, and the baroclinic pressure gradient term are shown for (**A**) the first (*approx. ebb*) (**B**) second (*approx. LWS)*, and (**C**) third (*beginning of flood)* measured transect.

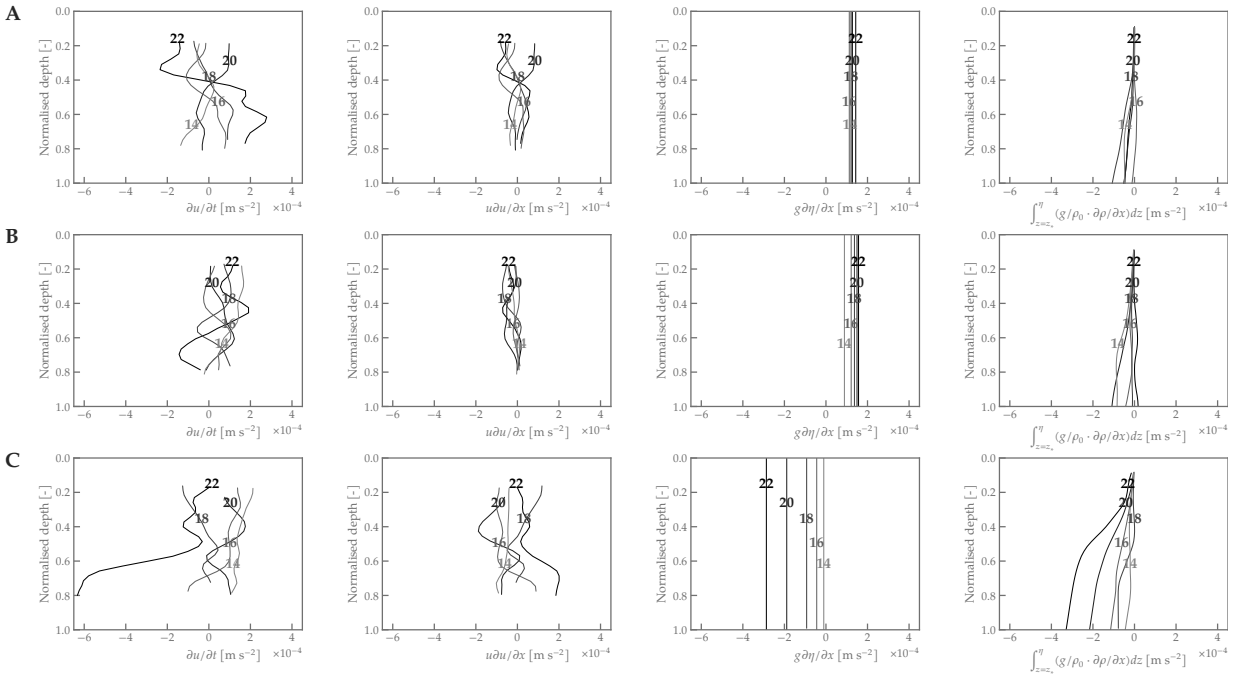

Figure 6.6: Overview of the estimated terms in an along-channel momentum balance for the even numbered measuring locations of the August 13th survey. Locations are numbered according to the last numbers in their Rhine kilometer numbering, i.e. 14 corresponds to location 1014. From left to right, the local acceleration term, the advective acceleration term, the barotropic pressure gradient term, and the baroclinic pressure gradient term are shown for (**A**) the first (*approx. ebb*) (**B**) second (*approx. LWS)*, and (**C**) third (*beginning of flood)* measured transect.

(2010a) was set-up in such a way that the head of the salt wedge was followed. Although the survey

presented here grossly covers the same area, the head of the salt wedge protrudes much farther inland due to the smaller amount of buoyancy in the system. This, in turn, leads to a pycnocline that is much less sharp than the one observed in de Nijs *et al.* (2010a). Concerning the advective acceleration term, the advection peaks and minima will therefore not be as obviously located around one specific depth as in de Nijs *et al.* (2010a, Fig. 13, transect 3), but will occur at different depths as the boat travels in time and space, since the pycnocline height varies more. The occurring processes, however, are the same.

Reynolds shear stress

As explained in Chapter 2, the Reynolds shear stress is effectively the covariance of the turbulent velocity fluctuations. It can also be considered analogously to the viscous shear stress, providing the eddy viscosity as a parameterisation of the eddy momentum flux. It is approximated here as the sum of the previously calculated momentum balance terms, with the extrapolated velocity values used for the calculation of the local acceleration and advective acceleration terms, integrated over the depth of the water column (*see* Chapter 4, Section 4.4.3). To be able to compare the outcome with previously presented results by de Nijs *et al.* (2010b), the local acceleration term is neglected. The results of this computation are presented in Figs. 6.7 and 6.8.

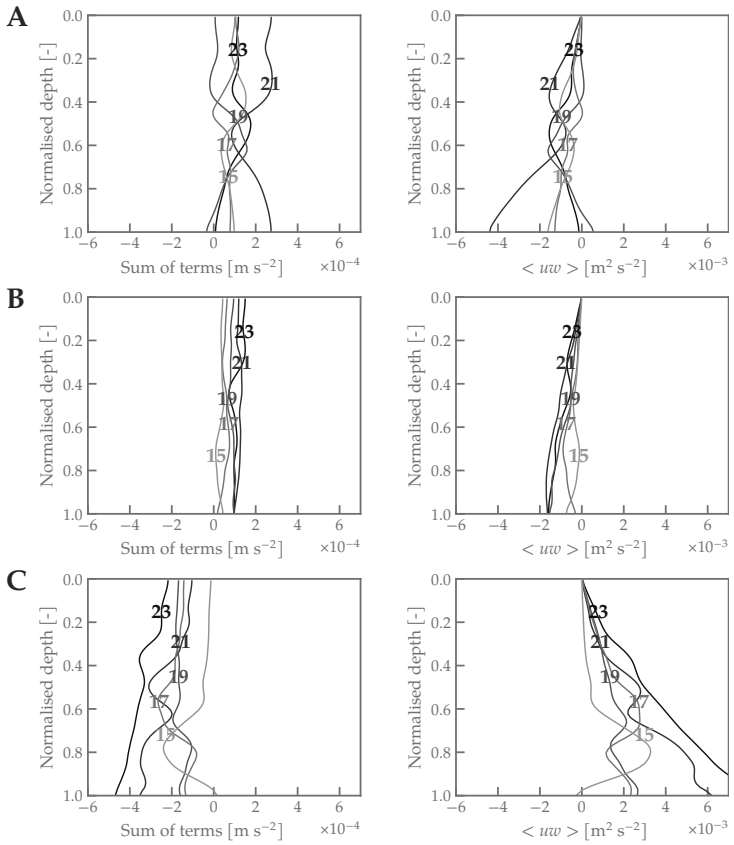

Figure 6.7: Overview of the sum of all terms in the momentum balance alongside the total Reynolds shear stress calculated for the uneven numbered CTD verticals. The total sum of terms is the sum of the advective acceleration term, baroclinic pressure gradient and the barotropic pressure gradient. The Reynolds shear stress is the calculated by integrating this sum over the depth. Results are shown for the (**A**) first (*approx. ebb*), (**B**) second (*approx. LWS)*, and (**C**) third (*beginning of flood*) transect.

Generally speaking, the maximal Reynolds shear stress values are higher during flood tide than during ebb tide. The maximal Reynolds shear stress values are lowest during LWS.
The profiles of the Reynolds shear stress (*see* Figs. 6.7 and 6.8) show that the maximum values during ebb are generally located higher up in the water column than where the maximum is located as the tide progresses into flood. In the beginning of transect three, as the tide progresses into flood, the Reynolds

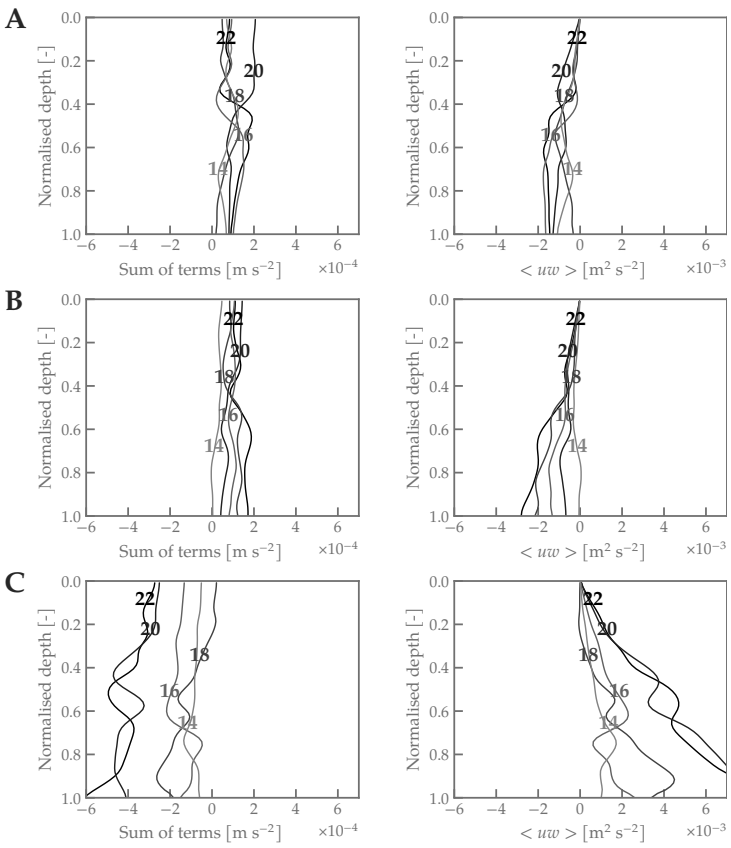

Figure 6.8: Overview of the sum of all terms in the momentum balance alongside the total Reynolds shear stress calculated for the even numbered CTD verticals. The total sum of terms is the sum of the advective acceleration term, baroclinic pressure gradient and the barotropic pressure gradient, and the Reynolds shear stress is the calculated by integrating this sum over the depth. Results are shown for the (**A**) first (*approx. ebb*), (**B**) second (*approx. LWS)*, and (**C**) third (*beginning of flood*) transect.

shear stress profiles are strongly modulated by advective processes, giving profiles that are more curved. As the tide goes into full flood (*see* Figs. 6.7C and 6.8C, locations 20-24), the Reynolds shear stresses follow a straighter profile.

Comparing these results with the Reynolds shear stress terms presented in de Nijs *et al.* (2010b, Fig. 6), we observe that the profiles for the full ebb and full flood case look similar. We don't know whether the Reynolds stress terms obtained during LWS and in the beginning of flood correspond, as de Nijs *et al.* (2010b) does not mention what the profiles look like during these parts of the tidal cycle. There is one remarkable difference between the Reynolds stress terms presented de Nijs *et al.* (2010b) and the ones presented here, as the maximal values of the Reynolds stress terms depicted in Figs. 6.7 and 6.8 are generally a factor 2-3 larger during (the beginning of) flood tide. It is hypothesised that the Reynolds stress terms computed from the measurement on August 13th, 2019, are larger due to to the low amounts of buoyancy in the system. Because of these low amounts of buoyant forcing, the tide has a larger influence on the movement of the salt wedge, thus increasing the effect of barotropic tidal advection and advection of momentum on the stress profiles.

6.1.4 Influence of Coriolis

To assess whether Coriolis is of influence on the flow, we calculate the Rossby radius of deformation. As there are many ways to calculate the first baroclinic wave mode, we assess and compare three different methods. Firstly, we compute the first baroclinic wave mode using the WKB-approximation solving method. This method uses the buoyancy frequency calculated from the potential density method and centered differences. Then, we use a simpler two-layer approximation for the calculation of the first baroclinic wave speed, to lastly compare this with the calculation of the first baroclinic wave speed directly from the

Taylor-Goldstein equation using the MATLAB® scripts developed by Platell (2019).

The outcomes of these computations are all summarised in Fig. 6.9.In these graphs, the survey measurements have been subdivided into three different categories, referring to the part of the tidal cycle that the measurements were done. Only LWS was measured during the survey. To differentiate whether a measurement was done during slack tide, the corresponding along-channel velocity ensembles (*see* App. A, Figs. A.4, A.5, and A.6) were visually analysed.

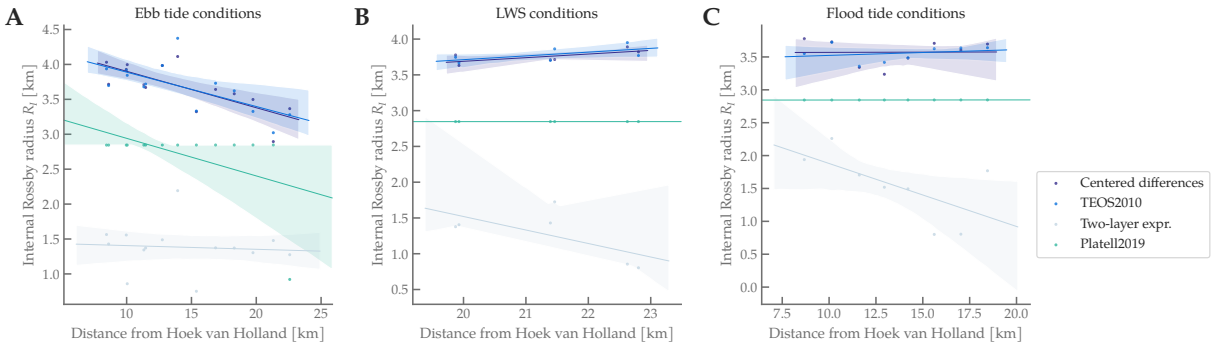

Figure 6.9: Calculated Rossby radii for each measuring location using several different methods. Measurements are subdivided into three categories; (**A**) ebb tide conditions, (**B**) LWS conditions, and (**C**) flood tide conditions. Four different methods to calculate the first baroclinic wave mode speed are evaluated. Lines indicate linear regression fit through the data.

Fig. 6.9 shows a considerable variation in the values of the calculated Rossby radii of deformation between the four used methods. The Rossby radii following from the wave speeds calculated using the WKB-approximation follow a similar trend. The Rossby radii following from the WKB-approximations vary along the axis of the estuary and throughout the tidal cycle. According to the output of these computations, the Rossby radius increases in the downestuary direction during ebb tidal conditions, and stays constant at a value of approximately 3.75 kilometers during LWS and flood tidal conditions.

The values of the Rossby radius of deformation following from the two-layer simplification show values for the Rossby radius that are a factor 2-3 higher than the values following from the WKB-approximations, and also seem to follow different trends throughout the tidal cycle; approximately constant during ebb tide, marginally increasing in the downestuary direction during LWS, and strongly increasing in the downestuary direction during flood tide.

The values for the baroclinic wave speed following from the direct numerical solution to the Taylor-Goldstein equation in combination with Platell's variable bed KdV model also show a different trend. All Rossby radii calculated utilising this method seem to be approximately constant at a value of 2.83 kilometers. The one exception to this is the value measured during ebb tide at CTD vertical 1014, where the Rossby radius is 1.09. It is not clear what causes this outlier.

Assuming that the two-layer simplification is not accurate enough to represent the internal wave speed well, we mainly look at the Rossby radii following from the WKB-approximation and the direct numerical calculation of the baroclinic wave speed. From these calculations, it can be inferred that Coriolis becomes important for flows with length scales in the order of 2500-4000 m. The Rotterdam Waterway has widths in the order of 400-700 m, and therefore the transverse flows in the Rotterdam Waterway itself are not expected to be a result of the Earth's rotation. Since the width increases in downestuary direction, however, the effect of Coriolis could become a higher-order effect farther downstream and at the mouth of the estuary.

6.1.5 Internal wave occurrence

We investigate whether internal waves occur by analysis of the internal Froude number according to the definition presented in Platell (2019). We also look at the modal structure of the internal wave and its development in space and time.

Internal Froude number

The Froude number is a dimensionless parameter expressing the ratio of the fluid velocity to the velocity of a (small-amplitude) internal wave on the surface. If the Froude number is less than 1, the internal wave velocity is larger than the fluid velocity, and the flow is *subcritical*. This means that information can move upstream, because the wave velocity exceeds the fluid velocity. Conversely, when the Froude number is less than 1, the flow is *supercritical* and the information can only propagate downstream. The critical Froude number is reached when the Froude number is exactly equal to 1. In this case, a disturbance on the interface will resonate and internal waves may form.For the analysis presented here, the definition of the internal Froude number used in Pietrzak and Labeur (2004), repeated here in Equation (4.44). The internal Froude number is calculated for each CTD vertical. The results of this calculation are presented in Table 6.5.

Table 6.5: Overview of the calculated internal Froude numbers per CTD vertical. Froude numbers were calculated using the definition presented in Pietrzak and Labeur (2004), using the solution from the variable bed KdV model for the propagation speed of the internal wave. Values of the Froude number lower than one indicate subcritical flow, in which information is able to propagate upstream. When the Froude number equals one, the flow is critical, giving a resonance condition for potential energy, resulting in the creation of internal waves. If the Froude number is larger than one, the flow is supercritical, indicating a state in which information cannot propagate further upstream.

	Internal Froude number [-]		
Location nr.	**First transect**	**Second transect**	**Third transect**
1014	0.87	0.09	0.08
1015	0.89	0.04	0.31
1016	0.94	0.10	0.40
1017	0.93	0.27	0.90
1018	0.75	0.30	1.04
1019	1.03	0.34	1.58
1020	0.99	0.46	1.72
1021	0.94	0.51	1.18
1022	0.95	0.59	2.73
1023	0.90	0.60	6.98
1024	0.83	0.70	6.46

During ebb, the flow is subcritical at the majority of the CTD verticals. In agreement with the observed salinity and velocity values (*see* Figs. 6.2 and 6.3A), the flow becomes supercritical between location 1019 and 1020. This transition from subcritical to supercritical may generate an internal wave. Looking at the overall structure of the salinity (*see* Section 6.1.1, Fig. 6.3), buoyancy frequency (*see* Section 6.1.2, Fig. 6.4), and backscatter (*see* Section 6.1.6, Fig. 6.10) during this part of the tide, a wave-like perturbation of the salinity structure seems visible, although values of vertical velocity cannot confirm this because vertical velocities have not been measured.As the tide progresses into LWS, the values of the internal Froude number decrease. The lowest internal Froude number occurs at location 1015 during LWS.

After LWS, the internal tidal asymmetry leads to a very fast increase of the Froude number between locations 1014 and 1015 as flood tide comes in. After this, the Froude number increases fast, and the flow becomes supercritical as the boat passes location 1018. As flood tide progresses, much higher values of the internal Froude number are found. These values also exceed the values of the internal Froude number in the Rhine ROFI, as reported in Platell (2019), although it must be noted that a different definition of the internal Froude number is used here.

6.1.6 SPM distribution

This section presents the Siltprofiler measurements along with the measurements of the acoustic backscatter by the boat-mounted ADCP. The workings and settings of the Siltprofiler and ADCP have been discussed in Section 4.1.1. The measurements, presented as a contour plot along each separate transect, are visualised in Figure 6.10[1]. Because the results using both methods vary, we first separately discuss the results of the Siltprofiler and the ADCP backscatter, respectively, after which we discuss why discrepancies occur and what they could mean.

[1]The Siltprofiler vertical at location 1014 is missing for the first transect, as it was not measured.

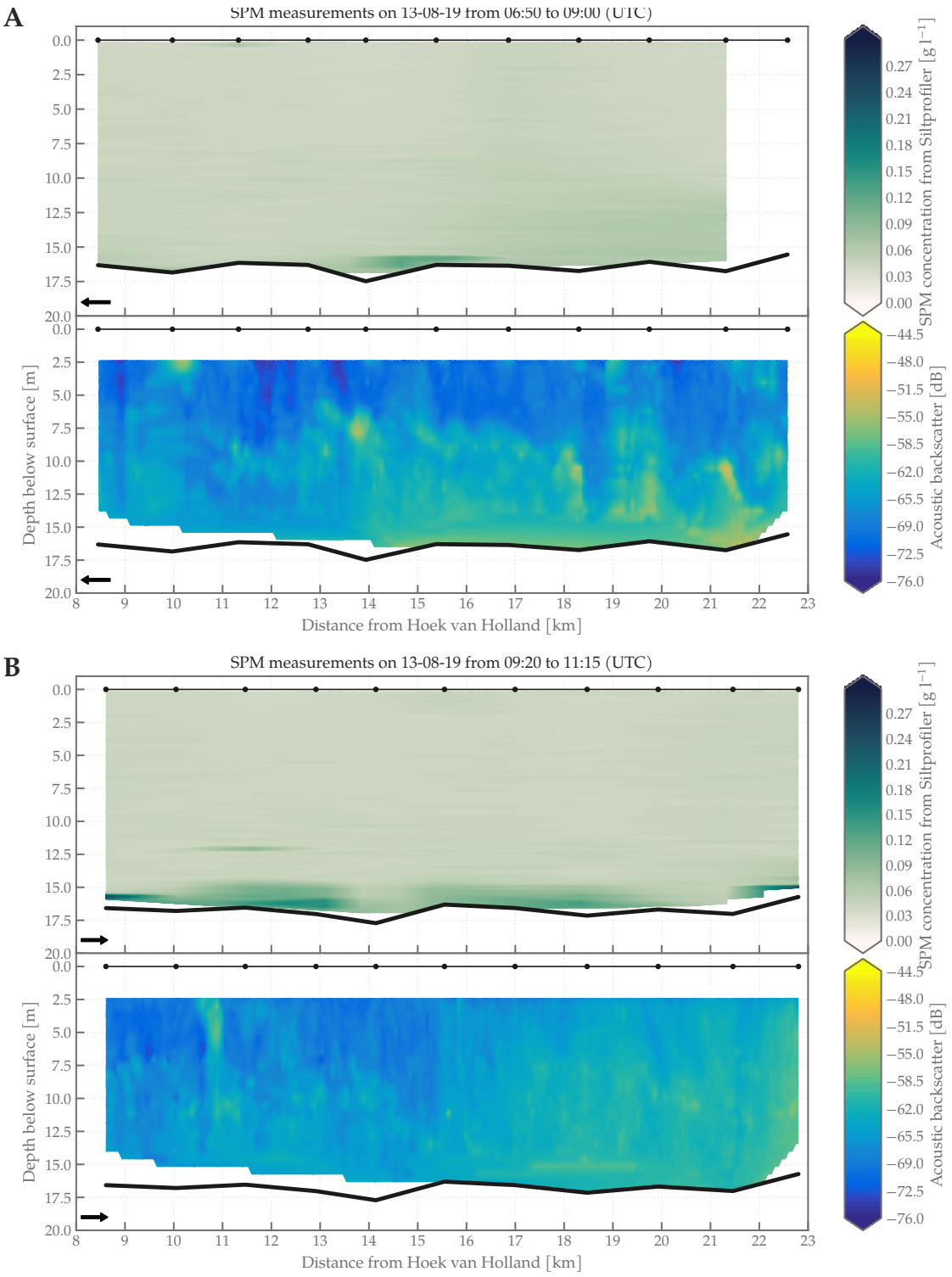

Figure 6.10: Overview of the distribution of SPM, measured using the OBS sensors mounted on the Siltprofiler, depicted alongside the values of the acoustic backscatter measured by the ADCP. Arrows indicate navigation direction of the boat. Each figure (**A-C**) refers to a different track: (**A**) 06:50-9:00 UTC, (**B**) 9:20-11:15 UTC, (**C**) 11:20-13:40 UTC.

Siltprofiler measurements

From the Siltprofiler measurements (see Fig. 6.10), it is found that in the largest part of the water column, the SPM concentration is very low, with an average value of approximately 0.05 g L^{-1}. Higher values of the

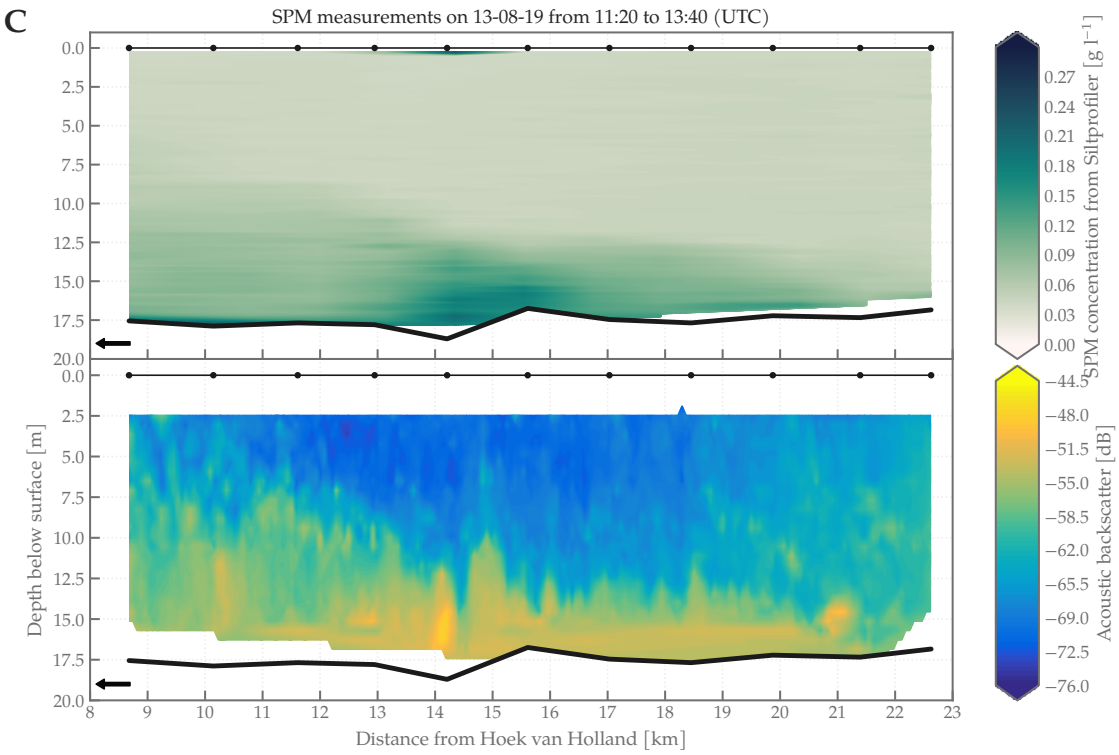

Figure 6.10: *(Continued)*

SPM concentration are found near the bed during ebb tide and at LWS, where peaks of SPM concentration up to 0.25 g L^{-1} are found. Only when the tide moves into flood, higher values of SPM concentration start appearing. From Fig. 6.10, it is found that high SPM concentrations are transported upstream along the bed. As the SPM reaches the channel bend, local turbulence phenomena seem to resuspend the SPM, dispersing the SPM vertically over the water column. Since turbulence quantities were not directly measured, this hypothesis could not be verified using measurements directly.

ADCP backscatter measurements

The results of the ADCP backscatter analysis are presented using the raw values of the acoustic backscatter, since the development of a suitable mass concentration calibration formula to derive the SPM concentrations from these backscatter values is outside of the scope of this thesis. The used ADCP measured with 600 kHz, which means that it is sensitive to particles in the medium to fine range. An ADCP of e.g. 1200 kHz would be more suitable to map density fronts.

As a consequence of the higher spatial density of the ADCP measurements, the backscatter results may provide more detailed information on the behaviour of the SPM. High values of measured backscatter are indicative for higher amounts of SPM or density (Deines, 1999; Park and Lee, 2016; Rijnsburger *et al.*, 2018) and conversely, lower values are indicative for lower amounts of SPM.

Looking at the distribution of SPM in the water column during ebb tide (*see* Fig. 6.10), it is observed that SPM is mainly in suspension underneath the pycnocline and near the bottom. Only a few patches of high backscatter intensity are visible in the upper part of the water column. Although these patches could indicate locally higher SPM concentrations, they could also be an artefact of propeller wash from nearby vessels. The observation of low amounts of SPM above the pycnocline is in agreement with the principle of turbulence damping at the pycnocline Geyer (1993), which has been confirmed by data to occur (*see* Section 6.1.2). During ebb, fluvial SPM supplied from upstream is advected over the salt wedge, where turbulence is damped locally. Through this mechanism of turbulence damping, SPM is rained out from above the pycnocline and trapped underneath. Furthermore, SPM also seems to be advected in a small region above the pycnocline, visible in Fig. 6.10. This observation may be explained by a mechanism proposed in de Nijs

et al. (2010b), which states that this is a result of the relative motions between saline and turbid waters, leading to favourable transport conditions above the pycnocline during ebb and below it during flood.

During LWS, it is clearly visible that SPM particles are distributed more uniformly over the water column as the tide turns. This is attributed to turbulent diffusion induced by the turning of the tide. This observation of widespread turbulent mixing over the water column is in contrast with what was found in de Nijs *et al.* (2010b), where it was shown that the pycnocline still damps turbulent diffusion when resuspension lags occur. It was hypothesised in de Nijs *et al.* (2010b) that this would be able to occur when the remaining stratification would become too weak to damp turbulent mixing. The relatively low buoyancy frequency numbers following from the stability analysis presented in Section 6.1.2 are in line with this hypothesis, but a more detailed analysis would be needed to confirm this hypothesis.

As the tide progresses into flood, saline water carries sediments into the estuary. During this phase of the tide, SPM is transported mainly along the bed and remains confined underneath the pycnocline. High acoustic backscatter values indicate higher SPM amounts during this phase of the tide than during ebb, which may be due to the import of sediments of marine origin, but could also be a result of resuspension of SPM at the bed. High Reynolds stresses during flood (*see* Section 6.1.3) support the latter hypothesis. Of course, the elevated amounts of SPM could also be a result of a combination of both mechanisms. Furthermore, the ADCP backscatter figure of the third transect clearly indicates that peak SPM values lag peak velocity values, as was also observed by de Nijs *et al.* (2010b). According to de Nijs *et al.*, this indicates that the tidal potential entrainment-erosion rate is larger than the availability of sediments at the bed, and consequently that SPM transport is more dependent on processes driven by buoyancy forces.

6.2 Discussion

Using a boat-mounted ADCP in combination with a CTD and several OBSs, an elaborate dataset was obtained during a special monitoring study conducted on August 13th, 2019. This dataset has been analysed to elucidate the spatial and temporal development of the flow structure in the Rotterdam Waterway. The results of this analysis, presented in this chapter, give insight into the dominant physical processes controlling the flow structure and their interactions, albeit with some limitations.

From the results presented in this chapter, it can be deduced that the transport of SPM is primarily affected by the position and tidal excursion of the salt wedge. In prior work by de Nijs *et al.* (2009, 2010a,b), a similar analysis was done on a similar survey. The main findings presented here are in line with this previously executed survey and analysis. Barotropic asymmetry imposed at the mouth of the estuary, in turn, determines the displacements of the salt wedge throughout the tidal cycle and the internal tidal asymmetries following from this (*see* Chapter 2).

Additionally, a calculation of the first baroclinic wave speed and an analysis of the internal Froude number indicate that under ebb tidal conditions, a transition from subcritical to supercritical flow conditions is predicted. This transition occurs in the river bend, where the bathymetry is deeper locally. This could indicate the presence of internal waves during ebb tide. Observations of the squared buoyancy frequency, salinity structure and SPM concentrations could also indicate an occurrence of such internal wave phenomena, although measured data on the vertical velocities are lacking to substantiate this. As the tide goes into flood tide, another flow transition takes place from subcritical to supercritical.

6.2.1 Difference between results and previous work

Although the main findings presented here are in line with the work by de Nijs *et al.* (2009), there are some notable differences as well. In agreement with the findings of de Nijs *et al.* (2010a), advective processes strongly modulate the sum of momentum balance terms. However, the contribution of these advective processes quantitatively exceeds the contribution of the advective processes presented in de Nijs *et al.* (2010a) with multiplication factors that, in some cases, exceed two. Furthermore, the contribution of barotropic processes to the development of the flow structure is larger than the contribution mentioned in de Nijs *et al.* (2010a). This may (partly) be explained by the reduced amounts of buoyancy in the system, as the difference between Rhine discharges during de Nijs *et al.*'s measurements and the measurements

presented here was almost a factor three. Due to these low amounts of buoyant forcing, the movement of the tide has a larger effect on the advection of the salt wedge. Most differences between the results of the survey presented here and the survey presented in de Nijs *et al.* (2010a) seem to be a result of this difference in discharge conditions, although the deepening of the Rotterdam Waterway may also have had an effect on e.g. the increased flow velocities. Unfortunately, the effects of these two conditions cannot be separated satisfactorily. It is recommended to do an additional survey under similar —or slightly lower—discharge conditions as the one executed on April 11th, 2006.

6.2.2 Limitations and challenges

Limitations on the interpretability and comparability of the results presented in this chapter should be noted as well. Although the methods used here are mostly harmonious with the methodology adopted in de Nijs *et al.* (2009), they have their own set of limitations. These can be divided into different categories, each of which are briefly be discussed below.

Instrumentation limitations: As discussed above, there are multiple discrepancies between the measurements obtained using the Siltprofiler and the measurements obtained using the ADCP backscatter. The origin of these discrepancies may be due to either (1) the difference between the sampling frequency or (2) the difference in measurement methods. The former possible explanation cannot be assessed. The latter possible explanation, however, can be assessed qualitatively.

The plotted values of the Siltprofiler are the measured quantities in the *'Long'* range, which is measured using a transmission probe (Borst and Vellinga, 2013). This range measures the highest SPM concentrations in the water column. A transmission probe measures optically, as it measures light transmission. ADCP backscatter, however, measures the scattering acoustically. When measuring SPM using ADCP backscatter, the scattering strength of the suspended material is measured by relating the strength of the transmitted sound pulse to the received sound pulse.

Inherently, there are differences between measurements done using these two different measuring methods. It is commonly known that acoustic methods are more sensitive to larger particles than optic sensors (Hawley, 2004; Hill *et al.*, 2011; Hoitink and Hoekstra, 2005, and references therein), to which Hoitink and Hoekstra (2005) added another two drawbacks that complicate the interpretation of ADCP backscatter measurements. First off, the formation and destruction of flocs may results in an increase or decrease of the acoustic backscatter, respectively. This is the result of the increase in the—acoustically normative—grain size. Secondly, the presence of other anomalous scatterers, e.g. organic scatterers, may cause strong acoustic gain. These effect of these possible anomalies cannot be distinguished with only the data presented here, and possible methods to quantify this with additional data are outside of the scope of this thesis.

Furthermore, although OBS measurements with the Siltprofiler were calibrated prior to its use, the values of SPM over the vertical could not be validated with bottle samples after they had been obtained. This is due to the fact that bottle samples could not be taken during the monitoring survey on August 13th, 2019. This, along with the fact that extreme values of SPM outside of the measuring range of the sensor with the largest measuring range (4.5 mg l^{-1}), means that these Siltprofiler measurements could not be used to validate the ADCP backscatter measurements (F. Buschman, personal communication, December 9, 2019); the ADCP backscatter profiles may therefore only be assessed qualitatively.

The limitations of the available measuring equipment only justify qualitative assessment of the data here, which means that any results on the SPM distribution during the August 13th monitoring survey remain inconclusive. Statements on this end require new measurements with, possibly, different or additional measuring equipment.

Measurement method limitations: The used velocity data were obtained from an ADCP mounted on a moving boat. This fact alone already introduces an error. Although the ADCP corrects for this movement, errors still remain, especially when the boat exceeds a velocity of approximately 3 m s^{-1}.

According to the ADCP records, the absolute velocity error may be in the order of 10-25% of the measured along-channel velocity estimates. Especially in the estimation of momentum balance terms, velocity errors of this order of magnitude may impact the outcome of computations significantly.

Instrument setting limitations: In the measurement survey presented in de Nijs *et al.* (2009, 2010a,b), the settings were optimised for research purposes. During the August 13th monitoring survey, the ADCP settings have not been optimised with this purpose, but rather had settings for a routine profiling. For future research, it is recommended to increase the amount of pings to the allowed maximum; this would yield more accurate ensemble averages and makes it easier to compare the results from the survey presented here with the survey presented in de Nijs *et al.* (2010a). Additional measurements of ADCP backscatter using a 1200 kHz ADCP would be able to validate whether ADCP backscatter results presented are fully indicative of SPM (and not of density).

Pre-processing limitations: In the case of ADCP velocity and backscatter measurements, outliers can e.g. be induced by propeller wash from a nearby vessel. The same goes for the Siltprofiler measurements. In the pre-processing stage, outliers associated with these processes were manually corrected for. This introduces human-induced errors, because this step is subject to the interpretation of the human filtering the data. This is also relevant to take into account when interpreting the results of the PCA (*see* Appendix A).

Post-processing limitations: The assumptions made in post-processing are also a source of possible inaccuracies. Mainly the approach taken as described in Section 4.4.3 is expected to be a cause of erroneousness, while this methodology is, in turn, a result of the chosen measurement strategy. Section 4.4.3 in Chapter 4 dives deeper into the origin of these inaccuracies.
Furthermore, for the calculation of the Reynolds shear stresses, the velocity profiles were extrapolated. The calculation of the shear stresses is extremely sensitive to the extrapolation method. The results presented here should therefore be consulted with caution.

Comparability limitations: As mentioned, during the survey conducted on August 13th, 2019, the Rhine discharge was much lower than the Rhine discharges described in de Nijs *et al.* (2010a). Furthermore, the wind conditions and the timing within the spring-neaps cycle was different. This poses a limitation on the comparability of the results of both monitoring surveys with each other.

6.3 Conclusions

It is substantiated by the data presented here that the primary hydrodynamic processes in the Rotterdam Waterway are mainly related to the tidal excursion of the salt wedge. Barotropic forcing at the entrance of the estuary imposes a time scale on the tidal excursion of the salt wedge. The influence of the barotropic tidal forcing at the reallocation location is evident from a momentum balance analysis; an analysis of the terms in a simplified along-channel momentum balance showed that the barotropic and baroclinic terms are dominant, but that—under the specific discharge conditions that were present on August 13th, 2019—advection strongly modulates the sum of terms. Earlier work by de Nijs *et al.* (2010b) has also shown that advection modulates the sum of terms, but to a lesser extent than is measured here. Partly, this may be caused by the differences in instrumentation settings. Further research could lead to more conclusive statements about the cause(s) of this difference.

The tidal excursion of the salt wedge imposes a (vertical) length scale on the SPM distribution in combination with the effect of turbulence damping at the pycnocline, by confining SPM underneath the pycnocline during the largest part of the measured tidal cycle. A qualitative analysis of ADCP backscatter gives reason to believe that—under certain hydrodynamic conditions—the stratification at the pycnocline becomes too weak, and turbulence damping at the pycnocline is suppressed, leading to a more uniform distribution of SPM over the water column. Furthermore, baroclinically driven exchange flow processes—occurring at slack tide—may influence the SPM distribution at the reallocation location through the formation of mid-depth jets.

In addition to these processes, a calculation and analysis of the internal Froude number has shown that internal waves may have formed in the river bend near Maassluis during the August 13th monitoring

survey. Visually, from observations of the ADCP backscatter and Siltprofiler measurements, substantiated by findings from the momentum balance analysis, this seems plausible, although measurements of the vertical velocity are necessary to confirm this.

Chapter 7

Modelled internal flow structure

This chapter covers the analysis of the model output generated by both NSC-models. The set-up of this chapter is similar to Chapter 4, with the aim to make comparisons between the model output and measurements as orderly as possible. The outputs of the NSC-Coarse and NSC-Fine models are discussed separately.

Firstly, the output of the NSC-Fine model is discussed in Section 7.1. We analyse the reproduced salinity structure, velocity structure, and temporal development of the pycnocline height, whereafter the stability parameters calculated from the NSC-Fine model output are discussed. Then, these same parameters are considered for the NSC-Coarse model output in Section 7.2, before concluding the chapter with a discussion of the results in Section 7.3.

Later, Chapter 8 will aim to quantify and elaborate on the differences in outcome between the NSC-Coarse and NSC-Fine models. The differences between both NSC-models' output and actual measurements will be covered therein as well, and is therefore an extension to the results presented here.

7.1 NSC-Fine model results

In the following sections, the modelled salinity structure, velocity structure, (evolution of) the pycnocline height, and stability of the modelled water columns are discussed. The findings presented here are restricted to the outcome of the NSC-Fine model.

7.1.1 Salinity and velocity structure

Salinity structure

The NSC-Fine model output, visualised in Fig. 7.1, shows the occurrence of a clear salt-wedge structure. The salinity values recorded in this predicted salt wedge are high: model output of the first transect shows that the NSC-Fine model predicts high salinity values of up to 30 PSU at the most downestuary output location. Near locations 1020 and 1017, slightly increased salinity values are predicted higher up in the water column, indicating that the NSC-Fine model resolves turbulent motions occurring as a result of changes in bathymetry well.

Interestingly, as the tide progresses into LWS, the salt wedge structure seems to retreat; lower values of salinity are predicted at the most upestuary locations than the NSC-Fine model predicted during ebb tide. The pycnocline is also predicted to be sharper during this phase of the tide; the vertical distance between the isohalines has decreased. Sharpening of the pycnocline during this phase of the tide is has been attributed to the occurrence of baroclinic exchange flows (de Nijs *et al.*, 2010a,b).

As the tide progresses into flood tide, the salt wedge is advected upestuary, and advective processes steepen the isohalines. This effect is reproduced well by the NSC-Fine model, as can be seen from the model output presented in Fig. 7.1C. Still, slightly higher salinity values are found near the channel bend (CTD vertical 1020) than in the surrounding output points.

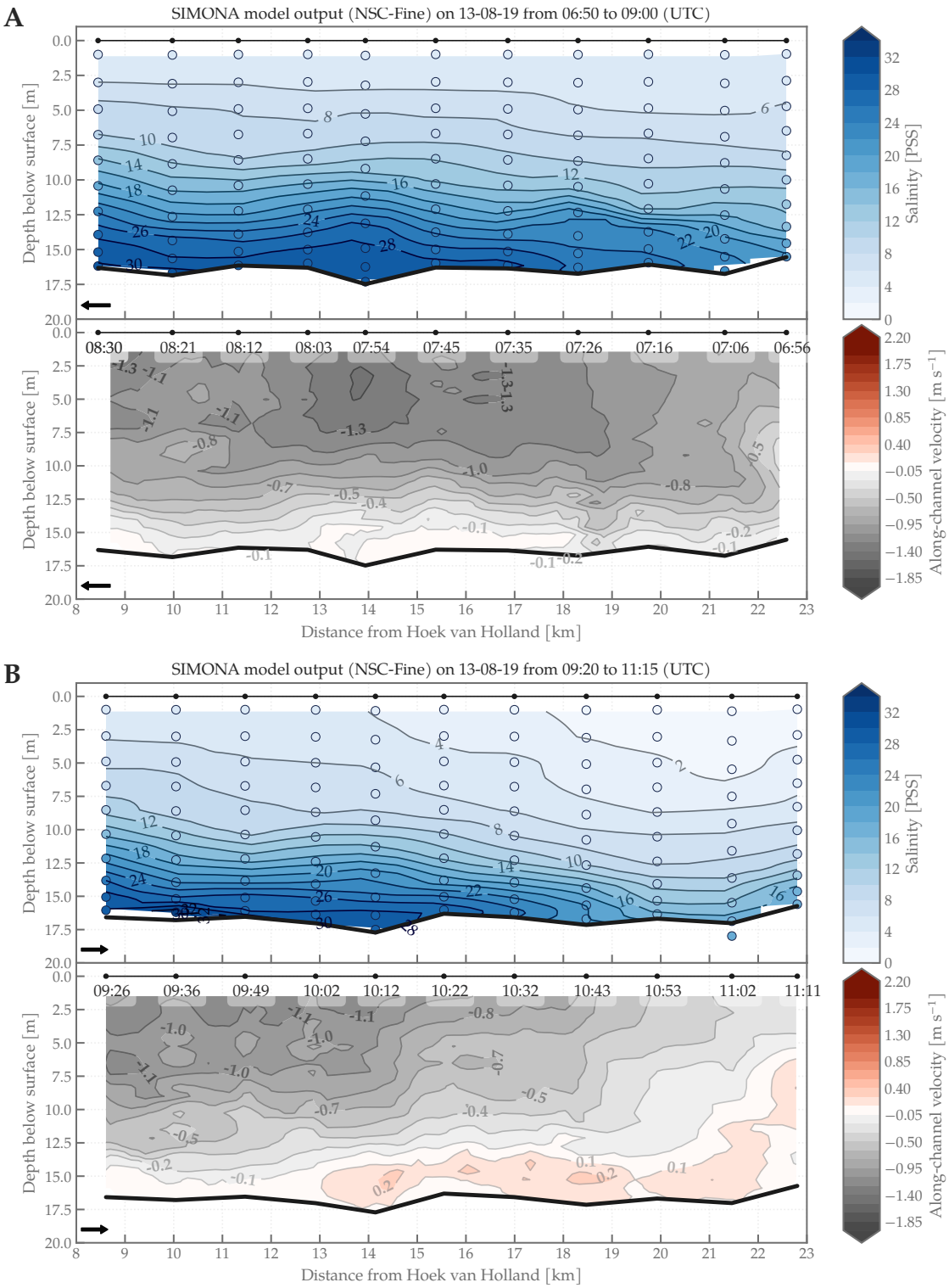

Figure 7.1: Overview of the along-channel vertical distribution of salinity (top panel in figure) and primary velocity component (bottom panel in figure), computed using the NSC-Fine model. The primary velocity components were determined from the PCA results of the measured data. In the bottom panels, negative velocities (dotted lines) indicate ebb flow. Each figure (**A-C**) refers to a different track: (**A**) 06:50-9:00 UTC, (**B**) 9:20-11:15 UTC, (**C**) 11:20-13:40 UTC, with arrows in the lower left corner indicating the navigation direction of the boat.

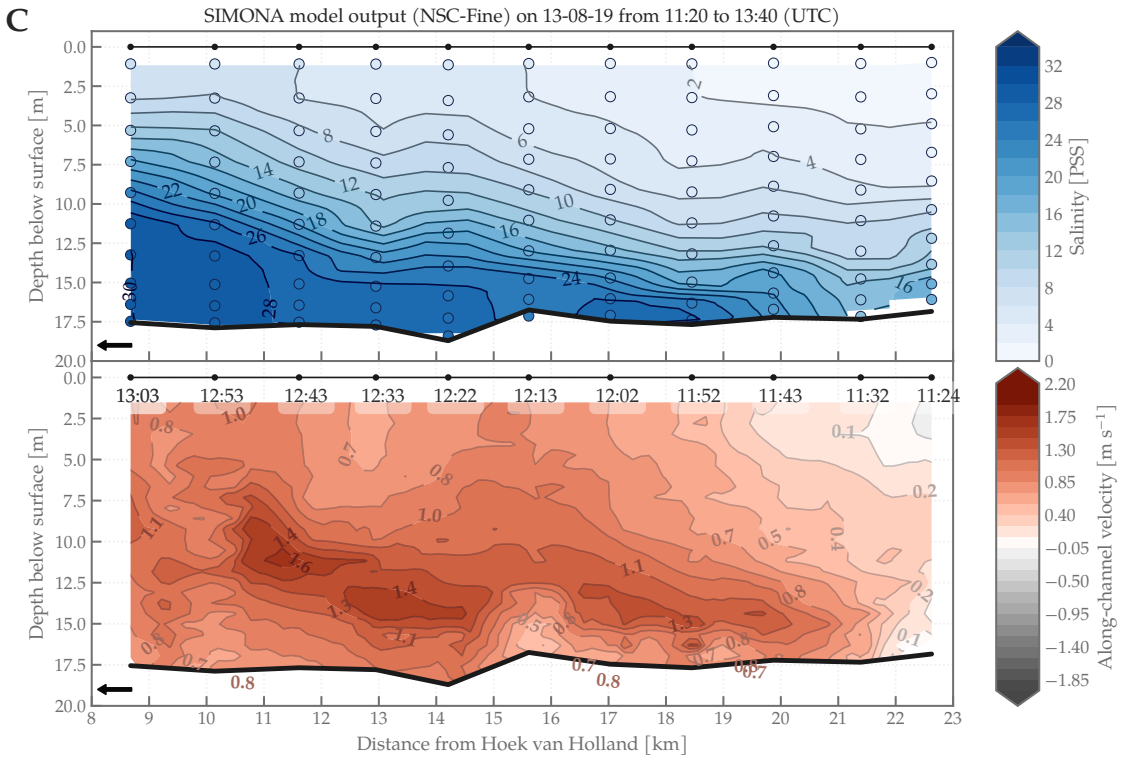

Figure 7.1: *(Continued)*

Velocity structure

Looking at the predicted ebb velocity values presented in Fig. 7.1, the NSC-Fine model predicts a typical ebb velocity profile, with higher (downestuary directed) velocity values near the surface and lower (downestuary directed) velocities near the bed. The effect of the bathymetry change in the river bend leading to flow in the upestuary direction locally (*see* Ch. 6, Sec. 6.1.1), is not resolved by the model.

During LWS, the return flow profile is also clearly visible. Positive velocity values, indicating upestuary flow, are predicted to occur up to measuring location 1021 at 10:00. The highest predicted positive velocity values at this tidal phase are 0.2 m s^{-1}. Comparing the observed velocity profile from this model output with the measurements presented in Chapter 6, it is visible that positive velocities are predicted to occur at a later time than they are observed in measurements. This may indicate a phase shift between modelled velocities and measured velocities—the model lags the measurements.

The visualisation of the NSC-Fine model output, for the third transect, shows that the highest velocity values occur at the approximate height of the pycnocline. One patch of lower velocities is visible around location 1019. Although such a region of low velocities is also recorded by the ADCP measurements (*see* Ch. 6, Sec. 6.1.1), the NSC-model's predicted values of the velocity are lower than the measured velocities.

7.1.2 Pycnocline height

In contrast with the NSC-Coarse model output (*see* Section 7.2.1), the NSC-Fine model output shows a clear salt wedge structure throughout the entire modelled duration. The height of the pycnocline changes throughout the tidal cycle.

In Fig. 7.1A, showing ebb tide conditions, the pycnocline is located in the middle of the water column. The isohalines are relatively flat.

As the tide progresses into LWS, the pycnocline shifts slightly downwards over the vertical. The isohalines do not seem to flatten nor steepen. The flooding tide model output, however, does show isohalines steepening, shifting the pycnocline upwards in the water column as the salt wedge propagates into the estuary.

This effect is mainly visible at the four most downestuary locations.

7.1.3 Stability parameters

The outcome of the computation of the Richardson gradient number and the Brunt-Vaïsalä frequency based on NSC-Fine model output is depicted in Fig. 7.2. This figure shows these parameters, visualised as contours, per navigated transect.

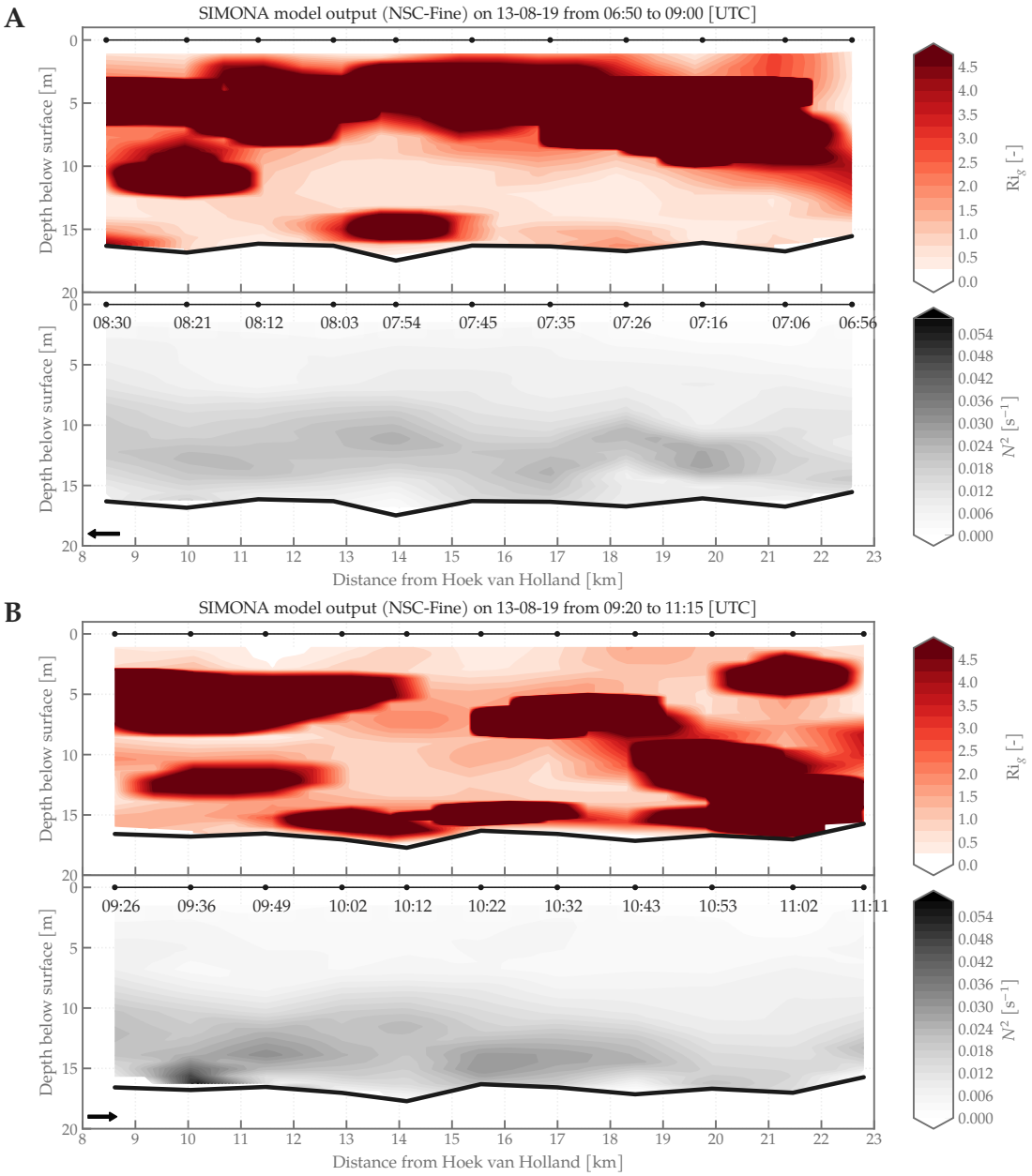

Figure 7.2: Calculated Richardson gradient numbers (top panel in figure) and squared buoyancy frequency (bottom panel) from NSC-Fine model output. The primary velocity components were determined from the PCA results of the measured data. Each figure (**A-C**) refers to a different track: (**A**) 06:50-9:00 UTC, (**B**) 9:20-11:15 UTC, (**C**) 11:20-13:40 UTC, with arrows in the lower left corner indicating the navigation direction of the boat.

The contours of the modelled squared Brunt-Vaïsalä frequency show that the NSC-Fine model predicts the water column to remain statically stable throughout the largest part of the tidal cycle. The highest values

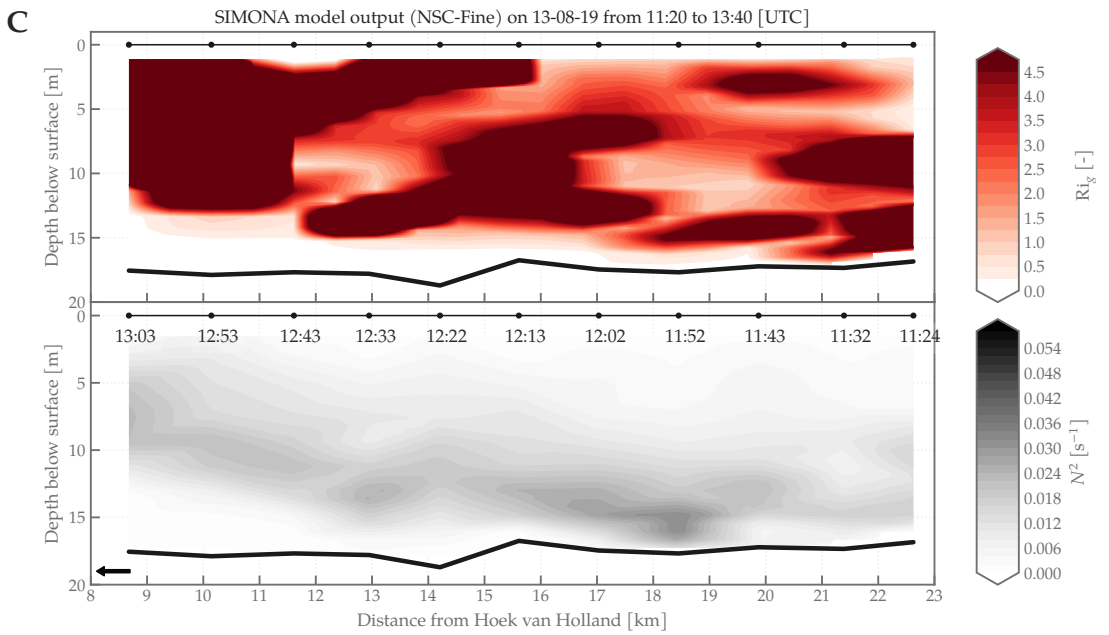

Figure 7.2: *(Continued)*

of the squared Brunt-Vaïsalä are consistently located at the predicted pycnocline height. The Richardson gradient numbers also consistently comply with the stability criterion around the modelled location of the pycnocline. This indicates that the model is able to reproduce the phenomenon of turbulence damping at the pycnocline (Geyer, 1993).

Large patches of red indicate that the top of the water column is most dynamically stable during the first transect. A small patch of dynamic stability is observed near the river bend (approx. 14 km from Hoek van Holland). The model output of the second transect shows similarly large patches of high dynamic stability, although no clear pattern is visible (*see* Fig. 7.2B). The same is true for the model output of the third transect (*see* Fig. 7.2C).

The model output only indicates static instability during the third transect in the bottom part of the water column. This instability is confined underneath the pycnocline. Close to the bed, the water column even becomes statically unstable.

7.2 NSC-Coarse model results

The following sections elaborate on the hydrodynamic NSC-Coarse model output, following from the modelling study. The set-up of this section similar to the previous section, covering the NSC-Fine model output.

7.2.1 Salinity and velocity structure

The Lagrangian-style measurements conducted on August 13th, 2019, were modelled using the NSC-Coarse model. The outcome of this modelling effort is depicted in Fig. 7.3, showing the modelled salinity values alongside the modelled values of the velocity.

Salinity structure

The salinity structure presented in Fig. 7.3 shows a continuously stratified profile over the water column. The pycnocline is not very sharp, likely as a result of the small amount of vertical layers. From the model results of the first transect (*see* Fig. 7.3), a peak salinity value is found in the bathymetry pit located around measuring location 1020. Interestingly, the salinity value found here is larger than the salinity values found on the most downestuary measuring location, indicating that the salinity value here is a remnant of an earlier stage in the tidal cycle. The NSC-Coarse model does not predict this increased amount of salinity

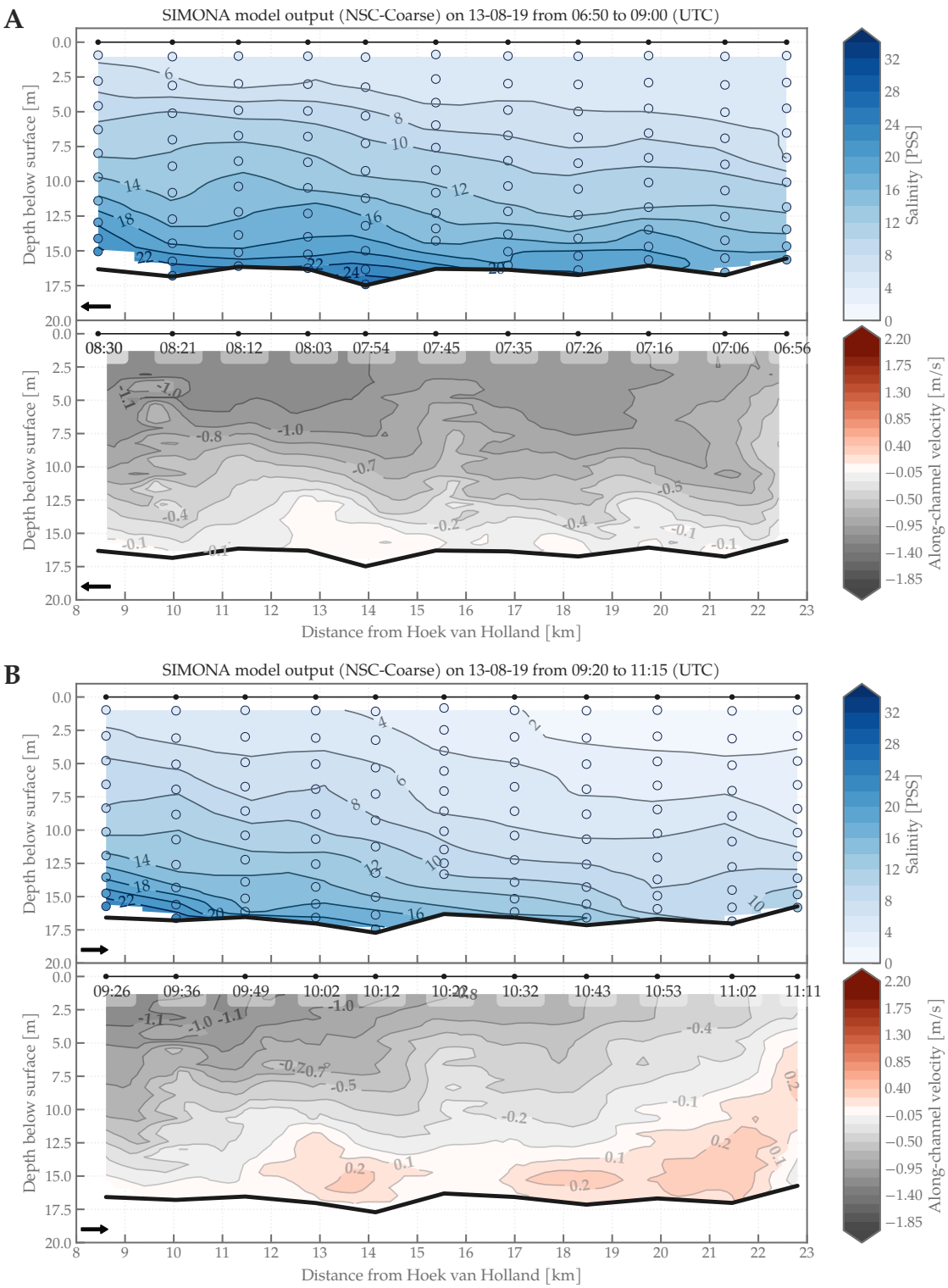

Figure 7.3: Overview of the along-channel vertical distribution of salinity (top panel in figure) and primary velocity component (bottom panel in figure), computed using the NSC-Coarse model. The primary velocity components were determined from the PCA results of the measured data. In the bottom panels, negative velocities (dotted lines) indicate ebb flow. Each figure (**A-C**) refers to a different track: (**A**) 06:50-9:00 UTC, (**B**) 9:20-11:15 UTC, (**C**) 11:20-13:40 UTC.

to be diffused to locations higher up in the water column.

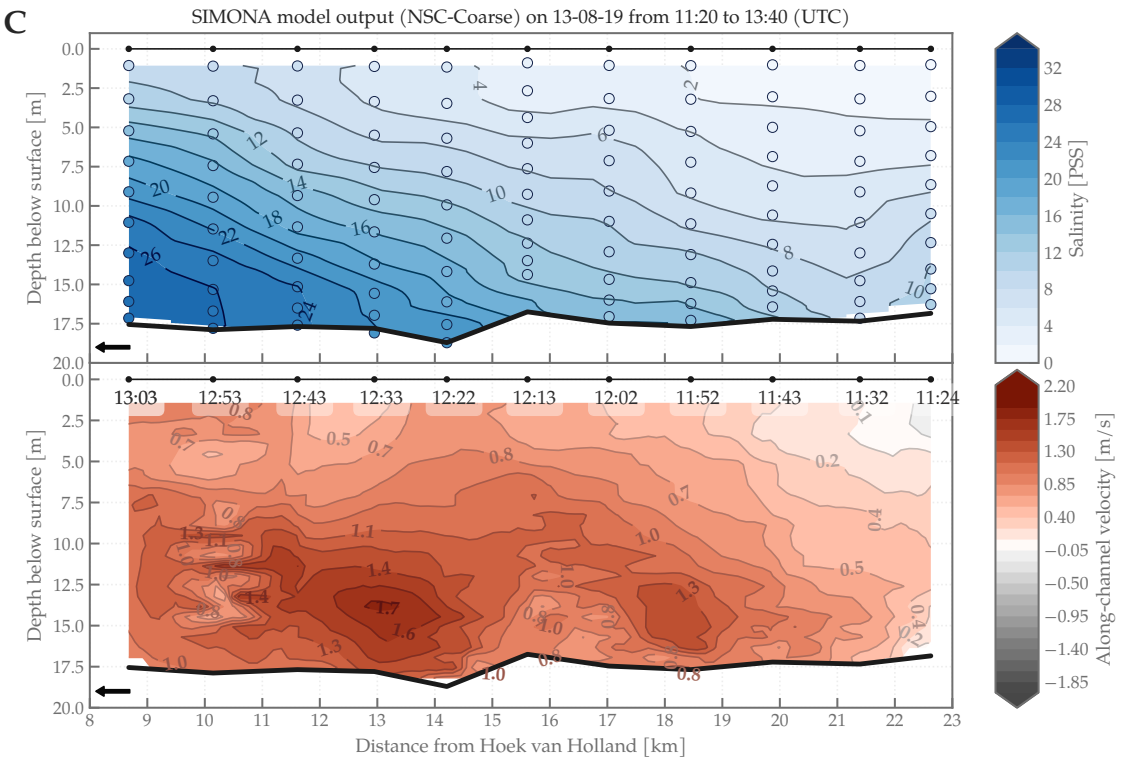

Figure 7.3: *(Continued)*

As the tide progresses into LWS, the NSC-Coarse model predicts that the salt wedge keeps moving downestuary. In the process of this, the isohalines steepen slightly. This is not in agreement with the observations, which show that the isohalines actually flatten during this phase of the tidal cycle (*see* Fig. 6.3). This indicates that the baroclinic return flow processes are not accurately reproduced by the model. In fact, from Fig. 7.3, the effect of superimposed baroclinic return flows does not seem to be reproduced by the model at all.

At the beginning of flood, the model results show a steepening of the isohalines. This is in line with the observations reported in Chapter 4. At this point, the salt wedge has stopped propagating downestuary. The salinity values near the river bend are flattened out.

Velocity structure

At all phases of the tidal cycle, three measuring locations show patches of lower velocity than the surrounding locations: this effect is visible at CTD vertical 1023, 1019, and 1015 (*see* Fig. 7.3). There may be multiple explanations for this, but the seemingly most likely explanation is that the principal directions are not reproduced well by the model locally. This may be due to the coarseness of the horizontal grid.

During the first transect, the velocity profile looks as expected—with higher values of (negative) velocity at the surface and velocities close to zero at the bottom. As the tide turns to LWS, the velocities predicted in the bottom part of the water column start to increase gradually. The first positive velocity values at the bottom are found between CTD vertical 1021 and 1020, which indicates that the model predicts a longer LWS in the bottom layers than is found from measurements (*see* Fig. 6.3). This could also be an indication that baroclinic exchange flows are not reproduced well by the NSC-Coarse model.

7.2.2 Pycnocline height

From the output of the NSC-Coarse model presented in Fig. 7.3, a pycnocline cannot be visually deduced well at every measured location. From the NSC-Coarse model output of the first transect, the pycnocline seems to be located near the bed or a few meters up in the water column. During LWS, the pycnocline

seems to shift upwards in the water column, but this is merely due to the fact that salinities decrease as a whole in the upestuary direction. As the tide progresses into flood, a sharper pycnocline seems to appear, although the exact location of the pycnocline in the water column remains hard to observe visually.

7.2.3 Stability parameters

The results of the calculation of the Richardson gradient number and the buoyancy frequency from the output of the NSC-Coarse model are depicted in Figure 7.4.

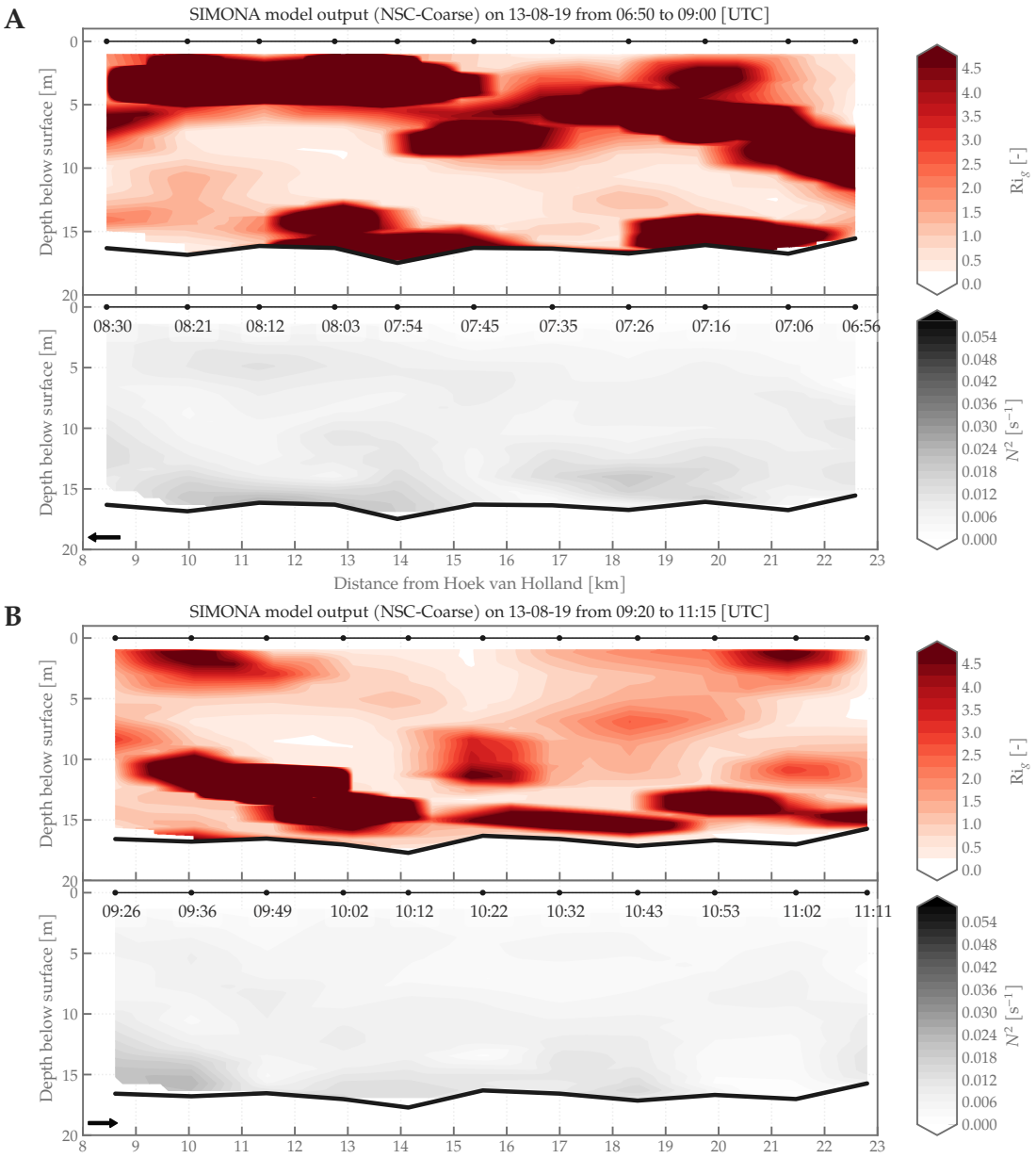

Figure 7.4: Calculated Richardson gradient numbers (top panel in figure) and squared buoyancy frequency (bottom panel) from NSC-Coarse model output. The primary velocity components were determined from the PCA results of the measured data. Each figure (**A-C**) refers to a different track: (**A**) 06:50-9:00 UTC, (**B**) 9:20-11:15 UTC, (**C**) 11:20-13:40 UTC, with arrows in the lower left corner indicating the navigation direction of the boat.

During ebb tide, the NSC-Coarse model predicts the water column to be most dynamically stable near the water surface and near the bottom. In the center of the flow, the model predicts the flow to be (dynamically)

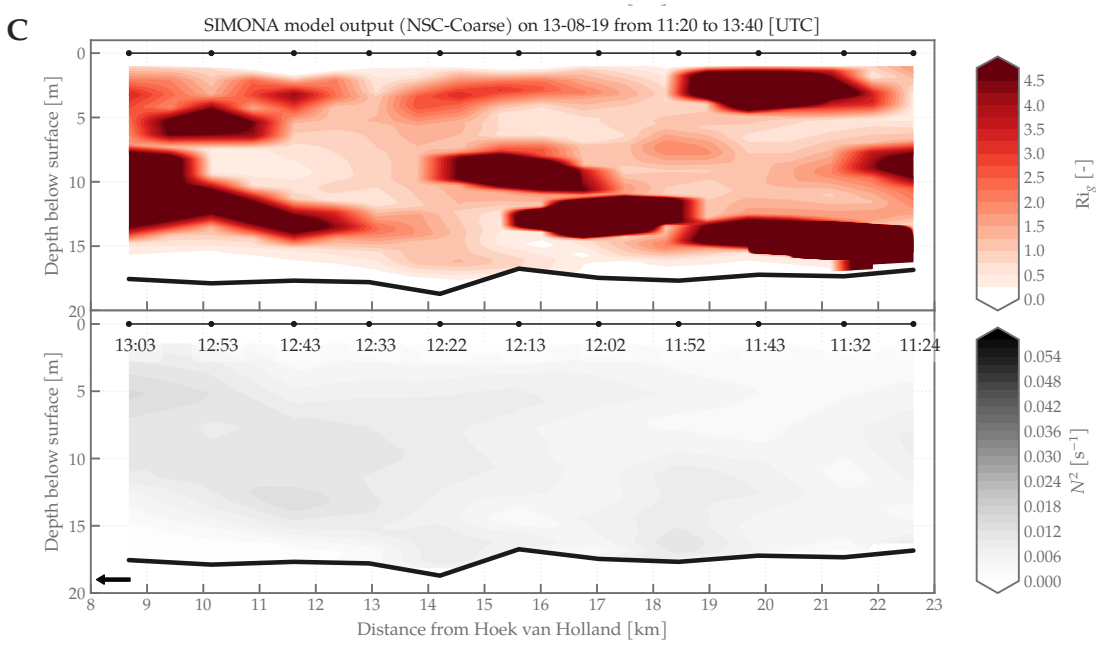

Figure 7.4: *(Continued)*

stable, but with low values of the Richardson gradient number. Static stability is estimated to be guaranteed throughout the entire water column, for the entire transect. It is notable that the values of the squared Brunt-Vaïsalä frequency and Richardson gradient number are larger near the bottom and the surface than in the center of the water column. This indicates that the NSC-model is not able to resolve the pycnocline height well, which was also already implied in Section 7.2.1.

As the tides moves into LWS, the NSC-Coarse model predicts the largest part of the water column to remain dynamically stable; only at the bottom and at the surface, Richardson gradient numbers fall below the dynamic stability limit. Static stability remains guaranteed throughout the entire water column.

7.3 Discussion

The internal flow structure in the Rotterdam Waterway is modelled using two different SIMONA models: the NSC-Coarse model and the NSC-Fine model. The NSC-Fine model has a higher horizontal resolution than the NSC-Coarse model, but the vertical resolution of both models is the same.

Contrary to the NSC-Coarse model, the NSC-Fine model is able to reproduce some kind of pycnocline, although this pycnocline seems to be located lower in the water column than what is shown from measurements. Flattening of the isohalines during LWS indicates that certain baroclinic return flow processes are captured by the model, although they might be underpredicted—the internal tidal asymmetry, mainly visible from the velocity profiles during LWS, seems to be lagging the measurements.

In the NSC-Coarse model output, a distinct pycnocline could not be observed. This, therefore, leads to arbitrary values of the pycnocline height. During LWS the isohalines hardly flatten, and the predicted tidal asymmetry seems to lag the measurements. These two observations indicate that baroclinic exchange processes and the barotropic tidal asymmetry at the mouth are not reproduced accurately by the model. A previous modelling study by de Nijs and Pietrzak (2012)—also executed in the Rotterdam Waterway—using a similar modelling suite, has also noted this.

Although this chapter gives a first insight into the predictive capability of both NSC-models and the differences in model performance between them, these results have yet to be quantified. This is done in Chapter 7, where the outcome of a predictive capability study is also compared to previous validation studies.

Chapter 8

Comparative model validity study

This chapter considers a quantitative and qualitative comparison between modelled hydrodynamics and measured hydrodynamics. This is done for both NSC-models. To this end, several correlation parameters are defined, and the phase shift between model and measurements is estimated. The used methodology to calculate the phase shift and these correlation parameters is described in Section 8.1. Thereafter, the results of the comparison are presented in Section 8.3. The comparison results of the NSC-Coarse and NSC-Fine models are presented side by side, so the predictive capability of the models can also be compared to each other. The results are discussed in Section 8.4, and conclusions regarding the performance of the models are drawn in Section 8.5.

8.1 Methodology

In this chapter, the predictive capability of the used SIMONA models is assessed. To do so, we define several parameters that are used to determine the correlation between the model output and measurements. Furthermore, we compare the predictive capability of both models with each other. For verticals that cannot be compared one-to-one, a visual analysis is done.

The model predictive skill is tested based on time series of fixed measurement stations and based on the incidental monitoring survey measurements of August 13th. To be able to correctly interpret any calculated correlation parameters, it is critical to first assess whether a phase difference is present between the model output and the measurements. This phase difference is estimated by comparing measured time series with time series obtained from the model. An overview of the total model-measurement comparison is indicated in Fig. 8.1. This particular chapter mainly focuses on the quantitative comparisons, whereas the qualitative comparison has been handled in Chapter 7. The link between the qualitative and quantitative comparisons is discussed in Section 8.4.

Three different water level stations as well as four different salinity stations are considered for the time series evaluation. The locations of these measuring stations are indicated in Fig. 4.2B. The station at Hoek van Holland has sensors for water level as well as salinity. These stations have specifically been chosen because they enclose the area of the monitoring survey conducted on August 13th. Additionally, to assess the predictive capability of the model further upstream, the measuring station *Brienenoordbrug* is added.

The following sections discuss the considered correlation parameters and the methodology used to estimate the phase difference between models and measurements.

8.1.1 Correlation parameters

The predictive capability of a numerical model can be evaluated using many different parameters. In research by de Nijs and Pietrzak (2012), a similar model of the Rotterdam Waterway was run, for the evaluation of which two measures were used: the magnitude of the MAE and the index of agreement (d) (de Nijs and Pietrzak, 2012; Warner *et al.*, 2005; Willmott, 1981). To harmonise this work with previously conducted research, the predictive capability was investigated by evaluation of these same parameters. Furthermore, the R^2-score is added as an extra correlation parameter. This chapter therefore focuses on the quantitative evaluation of the predictive capability of the models, based on these three correlation parameters:

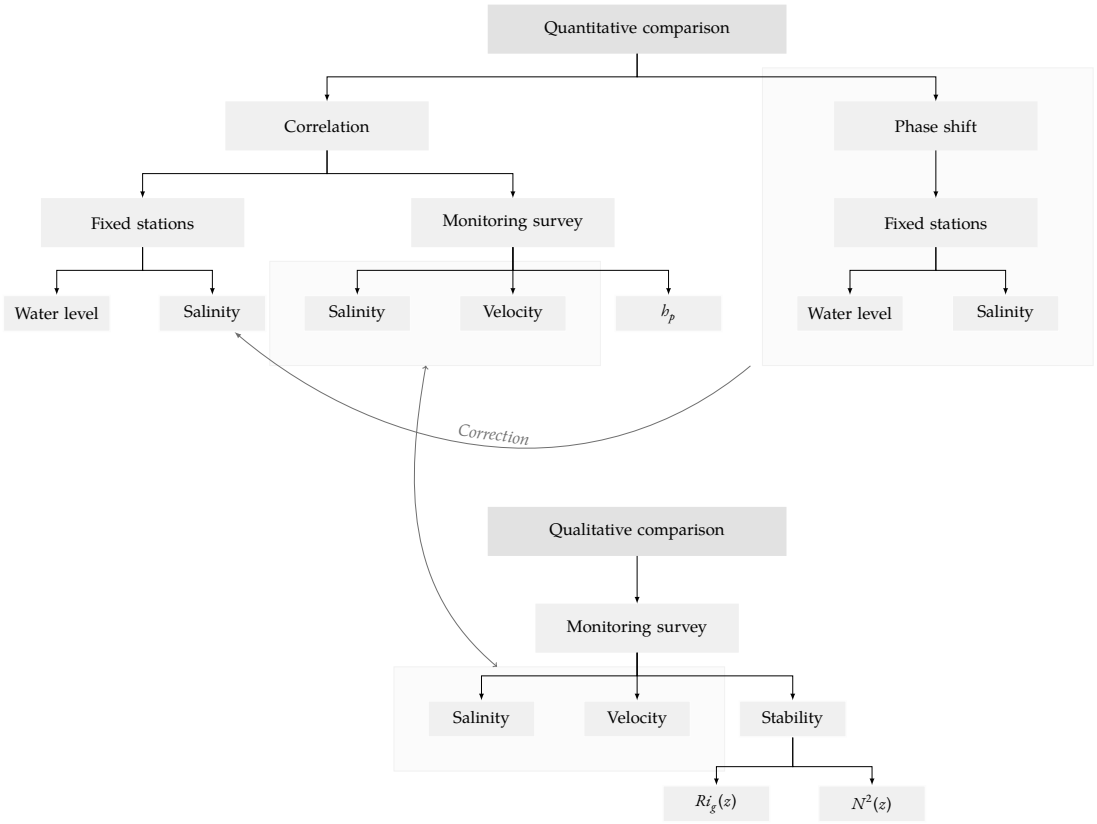

Figure 8.1: Overview of quantitative and qualitative analyses of the model predictive capability. Arrows indicate comparisons, correlations or feedback loops between separate parameters. The correlation parameters considered under "correlation" are the magnitude of the *mean absolute error* (MAE), the index of agreement and the R^2-score.

1. The magnitude of the MAE;
2. The R^2-score;
3. The index of agreement.

The following sections elaborate on the definitions of the correlation parameters.

Magnitude of the mean absolute error

Although the mean absolute error is one of the simplest regression error metrics, it is in very useful in many applications. The MAE is the mean of the absolute values of the individual residuals over all instances in the set. The MAE is formally defined as:

$$MAE = \frac{1}{N}\sum_{i=1}^{N}|y_i - x_i| \tag{8.1}$$

where N is the number of measurements, y_i represents the model results, and x_i are the measurements. Because the MAE uses the absolute values of the residuals, the MAE does not indicate whether the model over- or underperforms: each residual contributes proportionally to the total error amount. It also does not take into account outliers. The use of the MAE is often compared to the use of the *root mean square error* (RMSE). The advantage of the MAE over the RMSE is that it is much easier to interpret: a higher MAE is simply the average (absolute) error, whereas the RMSE penalises large errors more, and thus has other implications. A lower value of the MAE is therefore desirable.

Linear regression and R^2-score

When applying *linear regression*, an equation is calculated that minimises the difference between all of the data points and a fitted line. Oftentimes, ordinary least squares regression is used, which minimises the sum of the squared residuals.

To evaluate the goodness of fit of a model result compared to a measurement, the *coefficient of determination* R^2 can be used. This is essentially the proportion of variance in the dependent variable that is predictable from the independent variable, the dependent variable being the model results and the independent variable being the measurements. The R^2 score effectively compares the fit of the regression line with a 'null hypothesis', the null hypothesis being simply a straight line through the mean of the dataset. All of this can be written in the form of an equation as follows:

$$R^2 = 1 - \frac{\text{explained variance}}{\text{total variance}} = 1 - \frac{\sum_{i=1}^{n} (x_i - y_i)^2}{\sum_{i=1}^{n} (x_i - \langle x \rangle)^2} \tag{8.2}$$

where, y_i are the model results, x_i are the measurements and $\langle x \rangle$ is the mean of the measurements. The main limitation of using this method to determine the correlation between model performance and measurements is that the R^2-score cannot determine whether the coefficient estimates are biased. It is therefore of importance to check the residuals individually as well, e.g. visually using a plotting function.

Since the R^2-score effectively compares the fit of the model results with a null hypothesis, a negative R^2-score indicates that a regression line through the model results fits worse than a simple horizontal line through the mean, so the model results do not follow the trend of the measurements.

Index of agreement

The index of agreement d, also known as the model skill (Warner *et al.*, 2005), was first proposed by Willmott (1981) to overcome the insensitivity of e.g. the coefficient of determination to differences in the observed and model simulated means and variances. It is defined as follows (de Nijs and Pietrzak, 2012; Willmott, 1981):

$$d = 1 - \frac{\sum_{i=1}^{N} (y_i - x_i)^2}{\sum_{i=1}^{N} (|y_i - \langle x \rangle| + |x_i - \langle x \rangle|)^2} \tag{8.3}$$

In this equation, N is again the total number of measurements, y_i depicts the model results, x_i are the measurements, and $\langle x \rangle$ is the mean of the measurements. It therefore effectively calculates the ratio of the mean square error and the potential error, multiplied by the amount of observations and subtracted from one. The index of agreement can therefore obtain values between zero and one, where an index of agreement of one indicates perfect agreement and an index of agreement of zero indicates complete disagreement.

8.1.2 Phase difference

To deduce whether a phase difference between model and measurements is present, the cross-correlation between the model time series and the measurement time series is calculated. In signal processing, the cross-correlation is a measure of the similarity between two series as a function of the lag of one relative to the other. Therefore, the maximum time lag of the model relative to the measurements is at the point of maximum cross-correlation. The formal definition of the cross-correlation for two complex functions $f(t)$ and $g(t)$ is as follows (Rabiner and Gold, 1975):

$$(f \star g)(t) \equiv \int_{-\infty}^{\infty} \bar{f}(\tau) g(t + \tau) d\tau \tag{8.4}$$

where $*$ denotes convolution and $\bar{f}(t)$ is the complex conjugate of $f(-t)$. Since we are working with discrete

(measured) signals, we use the cross-correlation definition for discrete functions (Rabiner and Gold, 1975):

$$(f \star g)[n] \equiv \sum_{m=-\infty}^{\infty} \bar{f}[m] g[m+n] \tag{8.5}$$

It should be noted that in this thesis, the signals have been normalised by subtracting the mean of the signal from the signal. The lag Δt [s] at which the cross-correlation is maximum, is thereafter used to calculate the phase lag using:

$$\phi = 2\pi f \Delta t \tag{8.6}$$

where f [s^{-1}] is the frequency of the signal and ϕ [rad] is the phase difference. Since a tidal analysis, along with the research presented in de Nijs *et al.* (2010a,b), has shown that the governing tidal component is the M2 component, the frequency of the M2 component is used for this computation, $f_{M2} = 0.080511$ s^{-1}. This computation is done for all time series. It should be noted that a positive phase difference means that the model leads the measurements, and conversely, that a negative phase difference means that the model lags the measurements.

Because there might be an increase or decrease in phase difference over time, both long and short time series are considered. The short time series are time series from August 13th. The long time series start on July, 15th, 2019, and end on August 15th, 2019.

8.2 Hypotheses

Using the calculated correlation parameters and the phase difference estimates, the key parameters that impact the predictive capability of the currently operational 3D numerical models are sought. To this end, three hypotheses are tested, based on the preliminary results presented in Chapter 7:

1. The NSC-Fine model is able to reproduce the water level, velocities, and salinity better than the NSC-Coarse model;
2. The NSC-Fine model is able to reproduce the pycnocline height better than the NSC-Coarse model, even though the vertical resolution of both NSC-models is the same;
3. The predictive capability of the NSC-models for salinity decreases in the upestuary direction.

The results presented in Section 8.3 shed light on the validity of these hypotheses.

8.3 Results

The following sections cover the results of the predictive capability tests. First, the reproducibility of the water level is tested, by calculating the phase shift and correlation parameters between measured and modelled water level signals. The same is done for salinity time series. When the phase shift introduced by the models is known, the correlation between model output and measurements is calculated and discussed for the August 13th monitoring survey.

8.3.1 Water level stations

Three different fixed water level stations have been assessed to evaluate the performance of the model on predicting water levels. The measuring station *Hoek van Holland* is located closest to the river mouth, *Maassluis* is located near the river bend on the river bank, and *Vlaardingen* is located somewhat higher upstream (*see* Fig. 4.2B).

Phase differences

The phase lag is computed following the methodology presented in Section 8.1.2. The result of this computation, giving the cross-correlation, is shown for Hoek van Holland in Fig. 8.3 (short time series), and at

Vlaardingen in Figs. 8.2 and 8.4 (both durations). Other figures substantiating statements made throughout this chapter are given in Appendixes B and C.

When the phase shift is calculated from the short time series, no phase shift is apparent at either of the three stations. However, when calculating the phase difference from the long time series, it seems that a small phase difference is introduced by the NSC-Coarse model at the Vlaardingen station. This phase shift equals -0.008π rad, which equates to a time lag of one minute. It should be noted that a negative phase difference means that the model lags the measurements.

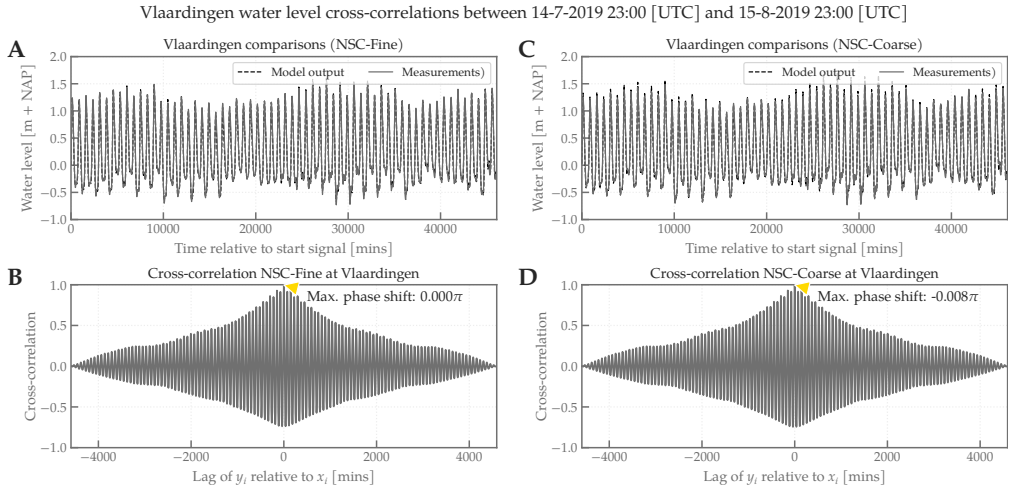

Figure 8.2: Water level time series and cross-correlations for model output and measurement at Vlaardingen between 14-07-2019 23:00 and 15-08-2019 23:00. (**A**) and (**C**) depict the measured time series and model output of the NSC-Fine and NSC-Coarse model, respectively, and (**B**) and (**D**) depict the calculated cross-correlations between the measured and modelled signals.

Overall, it can be concluded from these calculations that no phase difference is introduced between water level model output and measurements, in either of the NSC-models. When looking at longer time series, a small phase difference of approximately one minute seems to be introduced farther upstream at the Vlaardingen station. It should be kept in mind, however, that this could also be an artefact of an incorrect subtraction of the trend of the signal before the phase shift calculation. An overview of all calculated water level phase shifts is given in Table 8.1.

Table 8.1: Overview of the phase differences between the model and the measured water level time series for all fixed water level stations. A green dot (●) indicates that the NSC-Fine model has a smaller phase shift, whereas a red dot (●) indicates that the NSC-Coarse model has a smaller phase shift. An empty dot (○) indicates that the phase shift in both NSC-models is identical.

	Short duration		
	Fine	**Coarse**	**F > C**
	Phase difference [-]	**Phase difference [-]**	
Hoek van Holland	0.000 π	0.000 π	○
Maassluis	0.000 π	0.000 π	○
Vlaardingen	0.000 π	0.000 π	○
	Long duration		
	Fine	**Coarse**	**F > C**
	Phase difference [-]	**Phase difference [-]**	
Hoek van Holland	0.000 π	0.000 π	○
Maassluis	0.000 π	0.000 π	○
Vlaardingen	0.000 π	-0.008 π	●

Correlation

Upon first inspection of Fig. 8.3, showing the results of the analysis for Hoek van Holland, the model output seems to follow the time series measurements perfectly. Two high waters and two low waters are discernible. Upon closer inspection, however, the model seems to slightly underpredict the extremities (slightly lower maxima, slightly higher minima). There is no clear difference in performance between both NSC-models. The same trend is visible when looking at a different time scale.

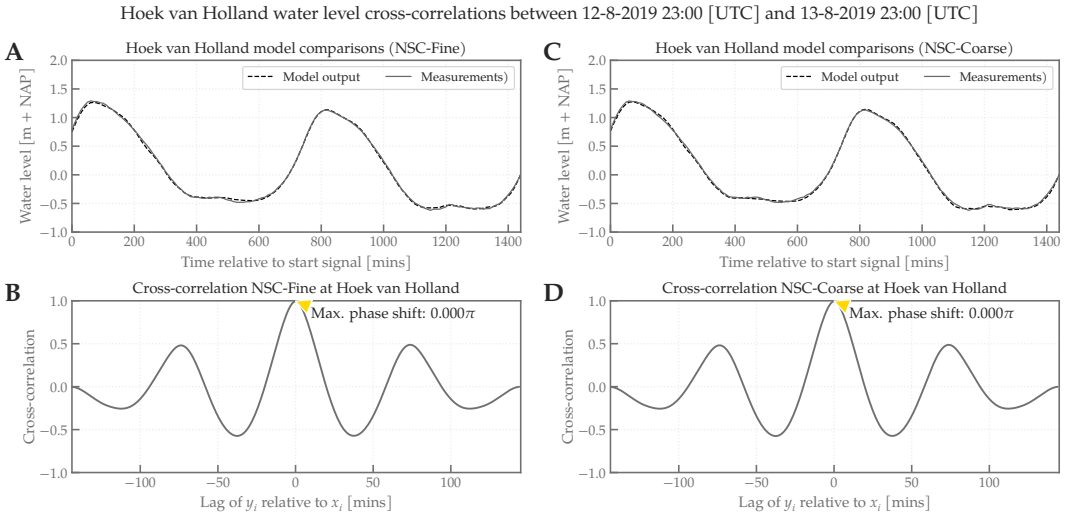

Figure 8.3: Water level time series and cross-correlations for model output and measurement at Hoek van Holland on August 13th, 2019. (**A**) and (**C**) depict the measured time series and model output of the NSC-Fine and NSC-Coarse model, respectively, and (**B**) and (**D**) depict the calculated cross-correlations between the measured and modelled signals.

At the most upstream station, Vlaardingen (Figure 8.4), the model still slightly underpredicts the extremities, and it seems as though the difference at the minima and maxima are slightly larger than the differences at Hoek van Holland. Again, the same trend is visible when looking at the longer time scale.

The correlation parameters support the observation of high correspondence between model output and measurements. The values of these correlation parameters are summarised in Table 8.2. For all stations and all time series durations, the index of agreement is equal to one, indicating a perfect score. The R^2-value is also near-perfect for all stations. This indicates a great correspondence between model output and measurement. Although the mean absolute error is also very small at all stations, a trend of increasing mean absolute error in upstream direction is discernible.

8.3.2 Fixed salinity stations

To assess the performance of the model on predicting the salinity at the fixed measuring stations, four different fixed measuring stations are considered. The station located closest to the river mouth is *Hoek van Holland*, which has three CTD sensors at 2.5 m, 5.0 m, and 9.0 m depth. Unfortunately, only the CTD sensor at a depth of 2.5 m was operational for the duration of the SURICATES project.
The *Lekhaven* and *Brienenoordbrug* stations are both located farther upstream, in the New Meuse. The Lekhaven station has three operational CTD sensors at 2.5 m, 5.0 m and 7.0 m depth, and the Brienenoordbrug station has two CTD sensors at depths of 2.5 m and 6.5 m. These stations are used to deduce whether the predictive capability of the model decreases in the upstream direction. The Brienenoordbrug is furthermore specifically interesting because it is located close to a tap water intake point, and salinities should never be higher than a certain threshold there.

The last station, the *Spijkenisserbrug* station, has two operational CTD sensors at depths of 2.5 m and 4.5 m. Normally, another sensor is located at a depth of 9.0 m, but this sensor was not operational during the considered time duration. Furthermore, it is not located in the same Rhine tributary, but in the Old Meuse. Evaluation of the model results at this station is necessary to assess whether the model can accurately

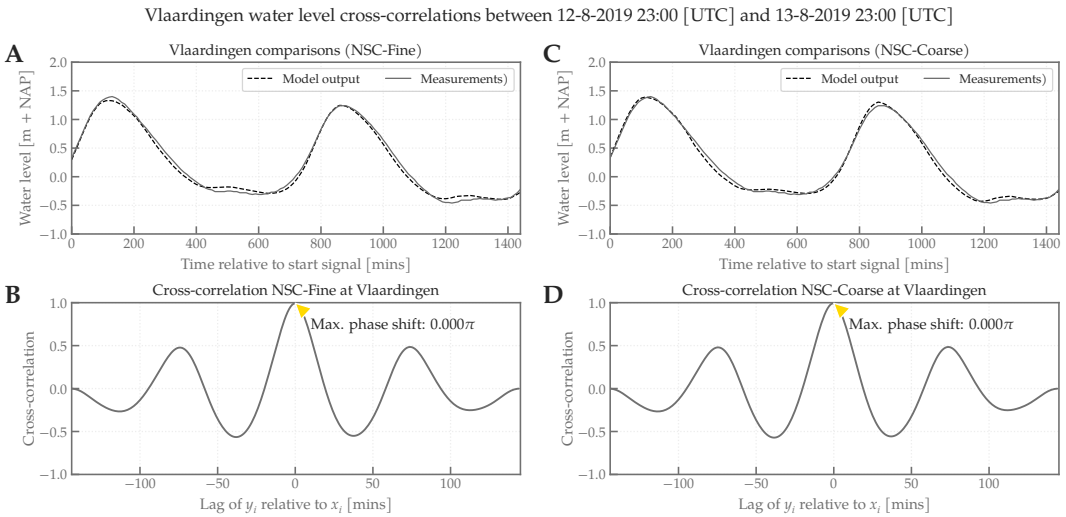

Figure 8.4: Water level time series and cross-correlations for model output and measurement at Vlaardingen on August 13th, 2019. (**A**) and (**C**) depict the measured time series and model output of the NSC-Fine and NSC-Coarse model, respectively, and (**B**) and (**D**) depict the calculated cross-correlations between the measured and modelled signals.

Table 8.2: Correlation parameters for the water level time series at fixed measuring points. This is done for water level time series with a long duration (≈ a month) and for water level series with a short duration (August 13th only). A green dot (●) indicates that the NSC-Fine model generally performs better based on the correlation parameters, whereas a red dot (●) indicates that the NSC-Coarse model performs better. An empty dot (○) indicates that the models perform identically, based on the correlation parameters.

	Short duration						
	Fine			**Coarse**			**F > C**
	d [-]	**MAE** [m]	**R^2** [-]	**d** [-]	**MAE** [m]	**R^2** [-]	
Hoek van Holland	1.00	0.02	1.00	1.00	0.02	1.00	○
Maassluis	1.00	0.03	1.00	1.00	0.03	1.00	○
Vlaardingen	1.00	0.05	0.99	1.00	0.04	0.99	●
	Long duration						
	Fine			**Coarse**			**F > C**
	d [-]	**MAE** [m]	**R^2** [-]	**d** [-]	**MAE** [m]	**R^2** [-]	
Hoek van Holland	1.00	0.03	1.00	1.00	0.03	1.00	○
Maassluis	1.00	0.04	0.99	1.00	0.04	0.99	○
Vlaardingen	1.00	0.05	0.99	1.00	0.04	0.99	●

predict the distribution of salinity over the different Rhine tributaries. All of the abovementioned stations are also depicted in Fig. 4.2.

Phase shift

The phase shift in the salinity time series is calculated for each of the aforementioned stations at all operational depths. The results of the cross-correlation computation at Hoek van Holland station for the August 13th time series are depicted in Fig. 8.5A. It is interesting to see that, in contrast to the near-perfect prediction of water levels at Hoek van Holland, it is visible that a salinity phase shift is introduced in the model. The phase shift introduced by the NSC-Fine model is slightly smaller than the phase shift introduced by the NSC-Coarse model. This amounts to a time shift of one minute compared to a time shift of two minutes, respectively. When looking at the correlation parameters obtained from the longer time series, the NSC-models both introduce the same phase shift.

Of all the evaluated salinity stations, the calculated phase differences are largest at the Brienenoordbrug station, which supports the hypothesis that the phase difference increases in the upstream direction. Upon

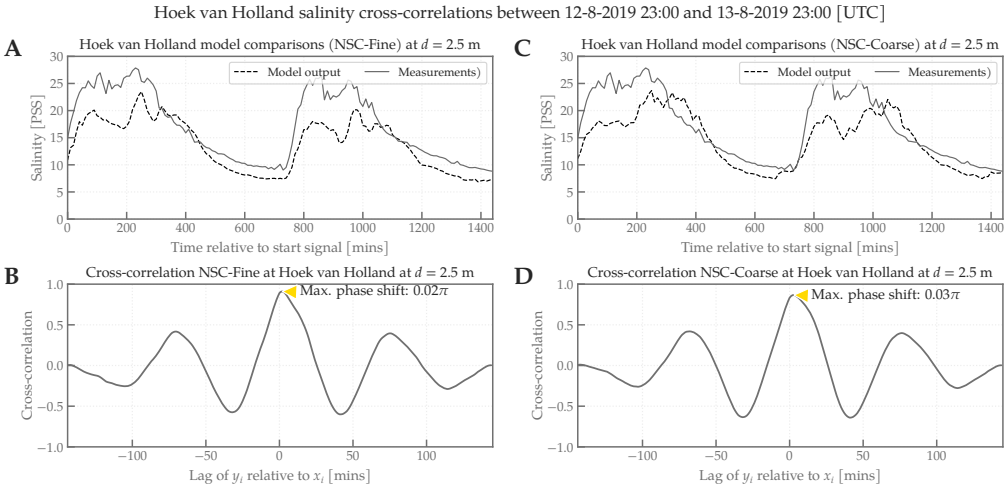

(A) Salinity time series and cross-correlations for model output and measurement at Hoek van Holland on August 13th, 2019.

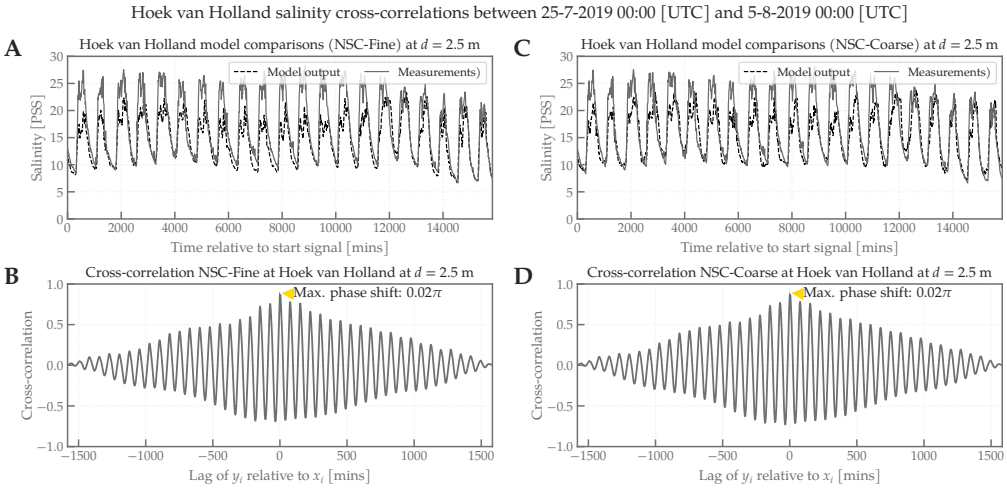

(B) Salinity time series and cross-correlations for model output and measurement at Hoek van Holland between 25-07-2019 23:00 and 05-08-2019 23:00 (approximately 1 1/2 weeks).

Figure 8.5: Salinity time series and cross-correlations for model output and measurement at Hoek van Holland. (**A**) and (**C**) of each subfigure depict the measured time series and model output of the NSC-Fine and NSC-Coarse model, respectively, and (**B**) and (**D**) depict the calculated cross-correlations between the measured and modelled signals. *Please note that the y-axis scaling is different from the y-axis scaling of all other salinity stations, due to the relatively high salinities occurring at Hoek van Holland station.*

closer inspection of the Brienenoordbrug salinity time series, however, it seems as though the larger time difference could also be induced by the fact that the model does not reproduce the amount of salinity well. This is visible from Fig. 8.6.

Of all the evaluated salinity stations, the calculated phase difference is smallest at the Lekhaven station. Here, the phase shift is zero at all depths for the NSC-Fine model when looking at August 13th only, and maximally two minutes (0.017π) for the NSC-Coarse model when considering the longer time series. This result is in contrast with the hypothesis of an increasing phase difference in the upstream direction, because the phase difference seems to reduce between Hoek van Holland and Lekhaven, only to increase again at Brienenoordbrug. It should be noted, however, that the trend of the Lekhaven salinity signal for the longer time series could not be resolved well, which likely has an influence on the phase shift estimate.

A complete overview of the calculated phase differences is given in Table 8.3. In general, the NSC-Fine model performs the same or slightly better than the NSC-Coarse model. Only when calculating the phase difference from a short time series at the Brienenoordbrug station, the NSC-Coarse model has a smaller phase difference than the NSC-Fine model. This could well be explained by the aforementioned fact that

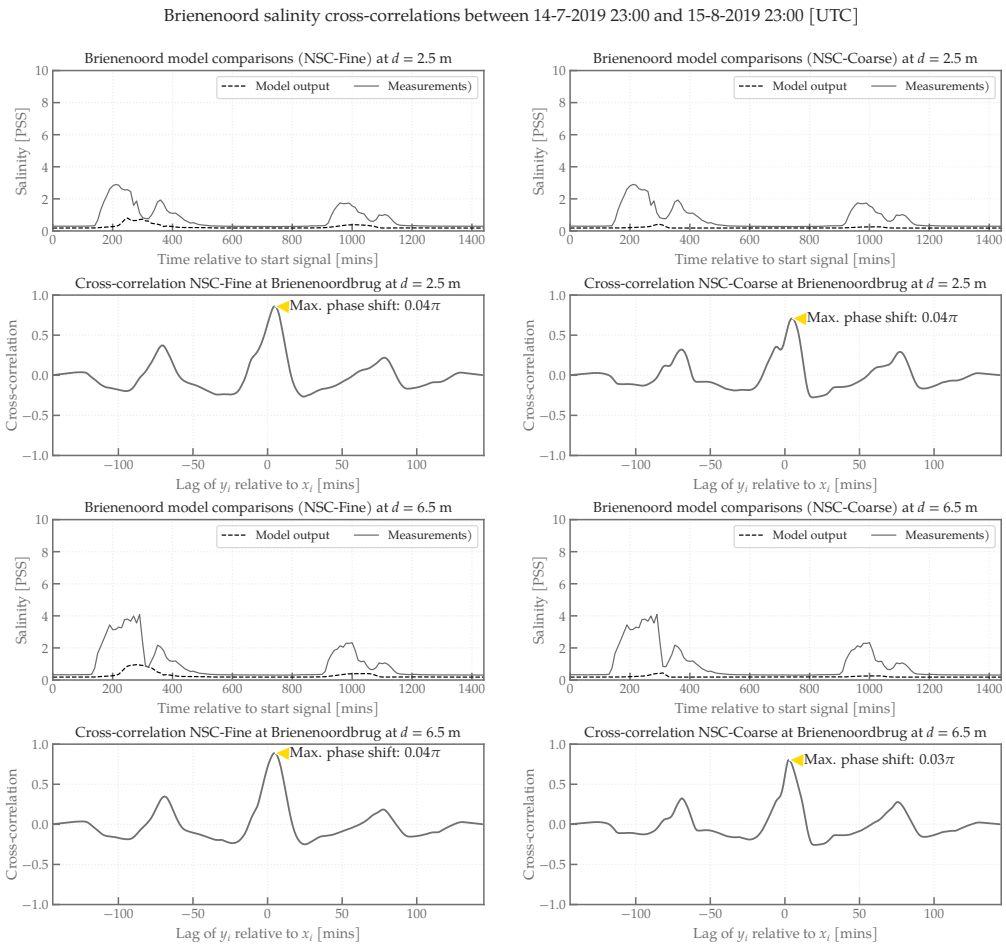

Figure 8.6: Salinity time series and cross-correlations for model output and measurement at Brienenoordbrug on August 13th, 2019. Model output is compared to measurement data at two different depths. Left column shows the computations for the NSC-Fine model, and right column shows the computations for the NSC-Coarse model.

the salinity hardly rises above 0 PSS, and that the calculated phase difference is therefore erroneous.

Correlation

Upon visual inspection of the model output time series and the measured time series at each of the fixed measuring stations, it is visible that the model consistently underpredicts the amount of salinity. At the Hoek van Holland station, the salinity difference on August 13th between the NSC-models and the measurements can reach up to 10 PSS. Furthermore, the pycnocline height is not represented well by either of the NSC-models, and also seems to be less sharp than is measured. This is visible from measuring stations Lekhaven and Spijkenisserbrug specifically. The NSC-model output salinity series at both of these stations show only a weak increase in salinity with depth, whereas the measurements show a more obvious increase of salinity with depth. The model appears to predict a more well-mixed state than is present in reality.

Original time series

To be able to place the qualitative visual inspection in a more quantitative frame of reference, all three previously defined correlation parameters have been calculated for all salinity stations, at all CTD sensor depths. The results of this computation are summarised in Table 8.4.

The MAE is largest for the Hoek van Holland station, for both the NSC-Coarse and NSC-Fine model. The R^2-scores and the index of agreement values, however, are not extraordinarily low or high. This indicates that the NSC-model output follows the trend of the measurements relatively well, although the salinity

Table 8.3: Overview of the phase differences between the model and the measurement salinity time series for all fixed salinity stations. A green dot (●) indicates that the NSC-Fine model has a smaller phase shift, whereas a red dot (●) indicates that the NSC-Coarse model has a smaller phase shift. An empty dot (○) indicates that the phase shift in both NSC-models is identical.

Short duration				
		Fine	**Coarse**	**F > C**
	Depth [m]	**Phase difference [-]**	**Phase difference [-]**	
Hoek van Holland	2.5	0.017 π	0.025 π	●
Lekhaven	2.5	0.000 π	0.008 π	●
	5.0	0.000 π	0.008 π	●
	7.0	0.000 π	0.008 π	●
Spijkenisserbrug	2.5	0.017 π	0.025 π	●
	4.5	0.017 π	0.017 π	○
Brienenoordbrug	2.5	0.042 π	0.042 π	○
	6.5	0.042 π	0.025 π	●
Long duration				
		Fine	**Coarse**	**F > C**
	Depth [m]	**Phase difference [-]**	**Phase difference [-]**	
Hoek van Holland	2.5	0.017 π	0.017 π	○
Lekhaven	2.5	0.008 π	0.017 π	●
	5.0	0.000 π	0.017 π	●
	7.0	0.000 π	0.008 π	●
Spijkenisserbrug	2.5	0.017 π	0.017 π	○
	4.5	0.017 π	0.017 π	○
Brienenoordbrug	2.5	0.034 π	0.034 π	○
	6.5	0.025 π	0.025 π	○

Table 8.4: Correlation parameters for the salinity time series at fixed measuring points, without correcting for the phase shift between the measured signal and the model output. These correlation parameters have been calculated for a time series with a duration of approximately one month (the 'long' series, with the exception of the Hoek van Holland station), and for August 13th only (the 'short' series). A green dot (●) indicates that the NSC-Fine model generally performs better based on the correlation parameters, whereas a red dot (●) indicates that the NSC-Coarse model performs better. An empty dot (○) indicates that the models perform identically, based on the correlation parameters.

Short duration								
			Fine			**Coarse**		**F > C**
	Depth [m]	**d [-]**	**MAE** [PSS]	**R^2 [-]**	**d [-]**	**MAE** [PSS]	**R^2 [-]**	
Hoek van Holland	2.5	0.85	3.56	0.49	0.86	3.40	0.54	●
Lekhaven	2.5	0.47	2.20	-4.88	0.43	2.37	-5.86	●
	5.0	0.51	2.28	-3.47	0.46	2.45	-4.21	●
	7.0	0.51	2.89	-3.12	0.48	3.05	-3.56	●
Spijkenisserbrug	2.5	0.95	0.65	0.82	0.93	0.62	0.78	●
	4.5	0.96	0.73	0.85	0.95	0.65	0.84	●
Brienenoordbrug	2.5	0.49	0.46	-0.27	0.44	0.52	-0.55	●
	6.5	0.49	0.64	-0.20	0.44	0.71	-0.49	●
Long duration								
			Fine			**Coarse**		**F > C**
	Depth [m]	**d [-]**	**MAE** [PSS]	**R^2 [-]**	**d [-]**	**MAE** [PSS]	**R^2 [-]**	
Hoek van Holland	2.5	0.85	2.82	0.56	0.88	3.15	0.61	●
Lekhaven	2.5	0.64	1.45	-0.89	0.60	1.57	-1.16	●
	5.0	0.67	1.53	-0.73	0.65	1.59	-0.82	●
	7.0	0.70	1.69	-0.43	0.67	1.76	-0.52	●
Spijkenisserbrug	2.5	0.94	0.73	0.75	0.96	0.57	0.84	●
	4.5	0.91	1.12	0.51	0.94	0.74	0.76	●
Brienenoordbrug	2.5	0.69	0.38	0.22	0.61	0.43	0.05	●
	6.5	0.69	0.51	0.25	0.61	0.57	0.07	●

differences at certain points can become quite high.

The Spijkenisserbrug salinity model output time series have the best correlation with the measurement series according to the three correlation parameters. The index of agreement and the R^2-values are highest here, and the MAE is relatively small. Looking at the actual Spijkenisserbrug time series, the sharp increase of the salinity when the salt wedge passes the station is estimated well by the model, and the salinity differences are maximally 2 PSS.

At the Brienenoordbrug station, very low values of the R^2-score and the index of agreement are obtained. Conversely, the MAE is very small. This can be explained by the fact that the salinity at the Brienenoordbrug station is generally very low, and hardly surpasses the 2 PSS. Both models, however, do not predict salinity to be present at all during the largest part of the tidal cycle, although measurements do indicate that saline water is present. This leads to the low R^2-scores and d-values.

According to the correlation parameters, both NSC-models seem to be least accurate in reproducing the salinity at Lekhaven compared to the other stations. This is an interesting result given the fact that the NSC-models perform best in reproducing the water levels at this location. Futhermore, the NSC-Fine model generally performs better in reproducing the hydrodynamics than the NSC-Coarse model according to these correlation parameters. The hypothesis that the NSC-Fine model performs better than the NSC-Coarse model is only rejected at the Hoek van Holland station and at the Spijkenisserbrug station—that is, when considering the long time series.

Phase shift corrected time series

To be able to assess what the influence of the phase shift is on the correlation parameters, another calculation of the correlation parameters was done after the salinity time series were corrected for their respective resolved phase shifts. The results of this computation are summed up in Table 8.5.

Table 8.5: Correlation parameters for the salinity time series at fixed measuring points, after a correction for the phase shift between the measured signal and the model output has been applied. These correlation parameters have been calculated for a time series with a duration of approximately one month (the 'long' series, with the exception of the Hoek van Holland station), and for August 13th only (the 'short' series). A green dot (●) indicates that the NSC-Fine model generally performs better based on the correlation parameters, whereas a red dot (●) indicates that the NSC-Coarse model performs better. An empty dot (○) indicates that the models perform identically, based on the correlation parameters.

Short duration								
			Fine			**Coarse**		**F > C**
	Depth [m]	**d** [-]	**MAE** [PSS]	**R²** [-]	**d** [-]	**MAE** [PSS]	**R²** [-]	
Hoek van Holland	2.5	0.85	3.56	0.49	0.86	3.40	0.54	●
Lekhaven	2.5	0.47	2.20	-4.88	0.44	2.37	-5.81	●
	5.0	0.51	2.28	-3.47	0.47	2.45	-4.17	●
	7.0	0.51	2.89	-3.12	0.48	3.05	-3.53	●
Spijkenisserbrug	2.5	0.97	0.51	0.89	0.96	0.52	0.87	●
	4.5	0.98	0.51	0.92	0.97	0.53	0.90	●
Brienenoordbrug	2.5	0.49	0.46	-0.27	0.44	0.52	-0.55	●
	6.5	0.49	0.64	-0.20	0.44	0.71	-0.49	●
Long duration								
			Fine			**Coarse**		**F > C**
	Depth [m]	**d** [-]	**MAE** [PSS]	**R²** [-]	**d** [-]	**MAE** [PSS]	**R²** [-]	
Hoek van Holland	2.5	0.86	2.84	0.58	0.89	2.48	0.68	●
Lekhaven	2.5	0.64	1.45	-0.89	0.61	1.57	-1.13	●
	5.0	0.67	1.53	-0.73	0.65	1.59	-0.80	●
	7.0	0.70	1.69	-0.43	0.67	1.76	-0.52	●
Spijkenisserbrug	2.5	0.95	0.67	0.79	0.97	0.52	0.87	●
	4.5	0.92	1.04	0.57	0.95	0.68	0.80	●
Brienenoordbrug	2.5	0.73	0.37	0.31	0.64	0.42	0.12	●
	6.5	0.72	0.50	0.31	0.63	0.57	0.12	●

Because the phase difference resolved from the salinity time series at Lekhaven is almost zero for most depths, the correlation parameters for this station hardly change. Remarkably, the NSC-Coarse phase shift correction at the Lekhaven station actually lowers the index of agreement and R^2-values, although the MAE stays the same. Moreover, at the station where the phase shift correction is expected to have the most positive impact, at the Brienenoordbrug, the correction only seems to have a positive effect on the correlation parameters calculated from the long time series. The correlation parameters calculated from the short time series do not change at all. This demonstrates that the salinities calculated from the NSC-models on August 13th are too small for the phase correction to make any difference at this location.

Furthermore, it is interesting to note that the phase shift correction has the largest (positive) influence on the correlation parameters that were already largest. The amount of times that the NSC-Fine model predicts the salinity better than the NSC-Coarse model does not increase or decrease.

8.3.3 Internal flow structure survey

Now that the phase differences are calculated for all of the fixed salinity stations, and a better view of the predictive capability of the NSC-models over a tidal cycle is obtained, the results of the monitoring survey of August 13th can be placed in perspective. Since the monitoring survey executed on August 13th gives data moving in a Lagrangian reference frame, a phase difference between model and measurement can give skewed results. Although a phase shift may have been found in Sections 8.3.1 and 8.3.2, the results presented here have *not* been corrected for this estimated phase shift. The results presented here could not be corrected for such a phase shift, since an estimate of the phase shift at the specific locations could not be determined. he correlation parameters and results presented in this section are thus to be evaluated carefully with the previously calculated phase differences at other points in the model domain kept in mind.

To assess the correlation, the vertical model output profiles and measurement profiles are matched to each other. Because the vertical resolution of the model output is much smaller than the vertical resolution of the CTD measurements, a nearest neighbour algorithm is used. This algorithm picks the CTD measurement that is closest to the model output. Because the CTD measurements are taken approximately every 0.30 m, the maximum depth-related error is approximately 0.15 m. This is negligible in comparison with the vertical resolution of the model output. For these depths, the difference between the model output and measurements are calculated.

The differences between the NSC-Fine model output and the measurements from the August 13th survey are visualised by gridding both data on the same grid and subtracting the model output y_i from the measurements x_i. The contour plots that are a result of this computation are shown in the separate designated (sub)sections. The results of the analysis are discussed separately for the NSC-Fine and NSC-Coarse model.

For brevity, only the results of the salinity computation are given here. The results of the correlation calculations of the velocity structure are elaborated on in Appendix B, Section B.2, which may be consulted when statements about the velocity structure are made.

NSC-Fine model correlation

The NSC-Fine model generally underpredicts salinity. This is found from the salinity difference calculations, which are summarised in Table 8.7, and visualised in Fig. 8.7. The model reproduces the salinity distribution best during ebb tide (*see* Fig. 8.7A), where the maximum absolute salinity difference is approximately 4 PSS. It has most difficulties predicting the salinities during LWS.

Furthermore, salinity is generally overpredicted underneath the pycnocline. This overprediction is larger during ebb tide and LWS than during flood tide (*see* Fig. 8.7C); above the pycnocline, the NSC-model does fairly well in predicting salinities. Absolute differences outside of this range are rarely higher than 2 PSS.

The general overprediction of salinity under the pycnocline and small underprediction of salinity above the pycnocline could entail that superimposed baroclinic effects such as described in research by de Nijs *et al.* (2009, 2010a) are not well reproduced by the model. This was also indicated in Chapter 7. Furthermore,

from additional analyses on the model's ability to reproduce the velocities (*see* Appendix B, Section B.2), it seems as if a phase lag is introduced in the velocity structure. This phase lag delays the onset of LWS, and therefore also delays the onset of the baroclinic effects. This may explain the model's underpredicted salinity values near LWS.

NSC-Coarse model correlation

The same computation as was applied to the NSC-Fine model comparisons was also applied to the NSC-Coarse model output. The results of this computation are shown as contour plots in Fig. 8.8. This figure reveals that the NSC-Coarse model more strongly underpredicts the salinity at the pycnocline than the NSC-Fine model does. The largest salinity differences occur during slack tide and flood tide, for which Figs. 8.8B and 8.8C are representative, respectively. These salinity differences can get as large as 14 PSS during slack tide.

Remarkably, instead of overpredicting the salinity beneath the pycnocline as we have seen in the comparison between the NSC-Fine model and measurements, the NSC-Coarse model consistently underpredicts the salinity beneath the pycnocline. This is in line with the observation of relatively steep isohalines and uniform isohalines as discussed in Chapter 7.

Another remarkable observation is that the bathymetry at monitoring location 1020 does not seem to be represented well in the NSC-Coarse model. During selection of the optimal locations for the August 13th survey, the coordinates of the measurement locations were chosen such that the boat would ideally navigate along the thalweg. It is possible, however, that the thalweg is locally very narrow and deep, something that cannot be resolved by the NSC-Coarse model's horizontal resolution.

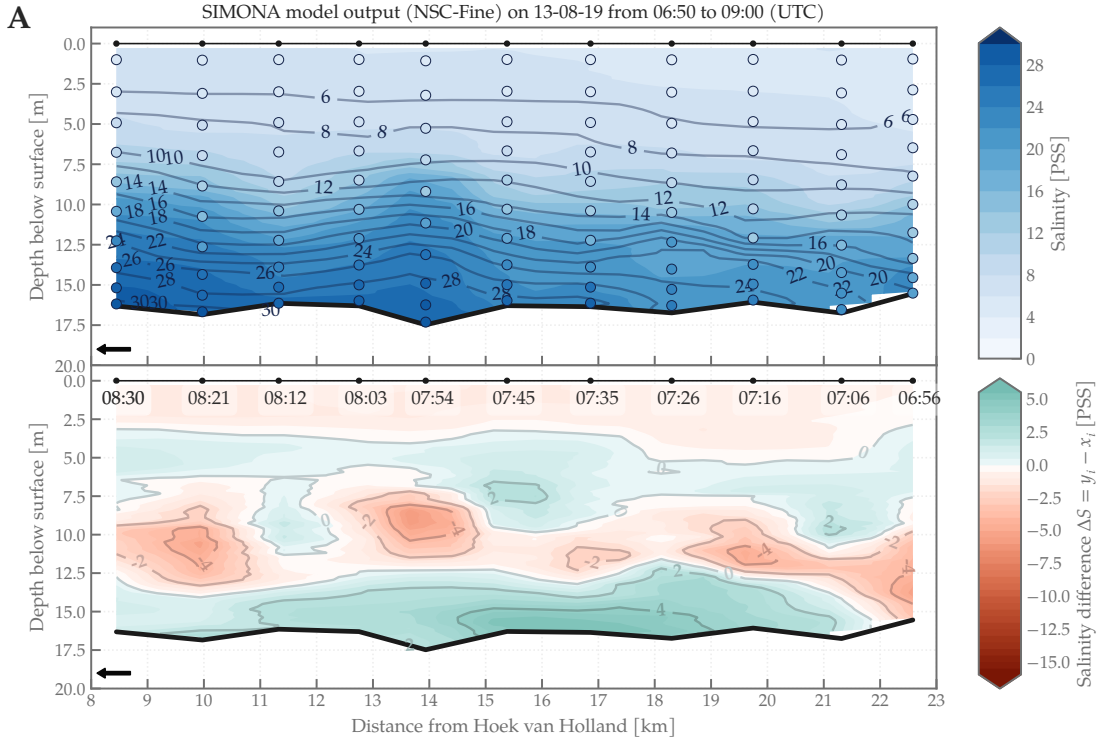

Figure 8.7: Overview of the calculated salinity difference between model output y_i and measurements x_i for the NSC-Fine model. The model output is visualised by the individual dots and contour lines in the upper panels, a dot indicating an output point. The actual salinity distribution is plotted in colour in the background. The difference between model and measurement is indicated in the bottom part of the figure, green indicating an overprediction of the model and red indicating an underprediction of the model. Arrows in the bottom left corner indicate the navigation direction of the vessel.

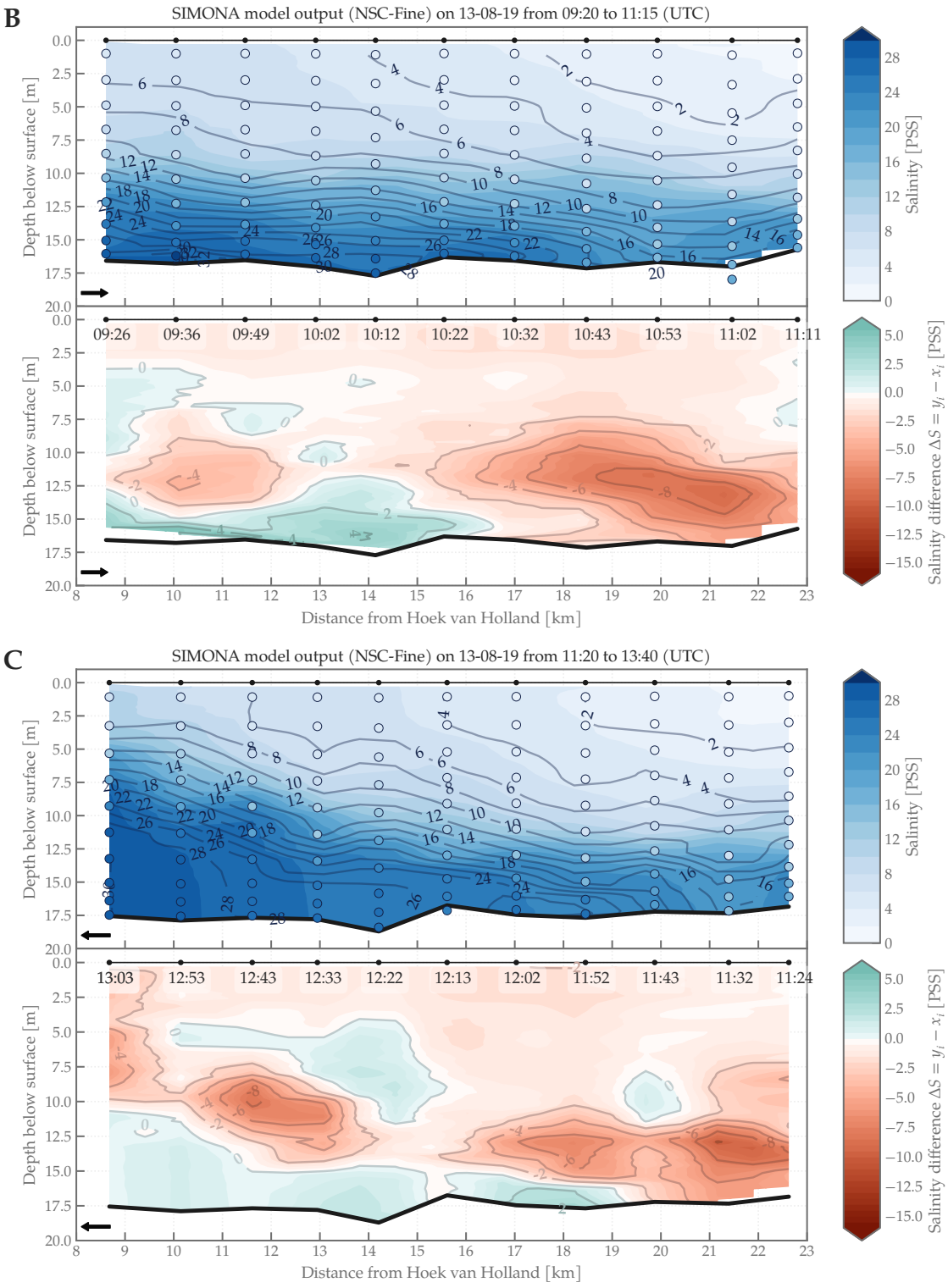

Figure 8.7: (*Continued*)

8.3.4 Pycnocline height

The results presented in previous sections have all indicated that the NSC-models likely have difficulty reproducing the pycnocline height. Therefore, this section specifically focuses on comparing the pycnocline height estimate from the NSC-models to the pycnocline estimate following from the August 13th

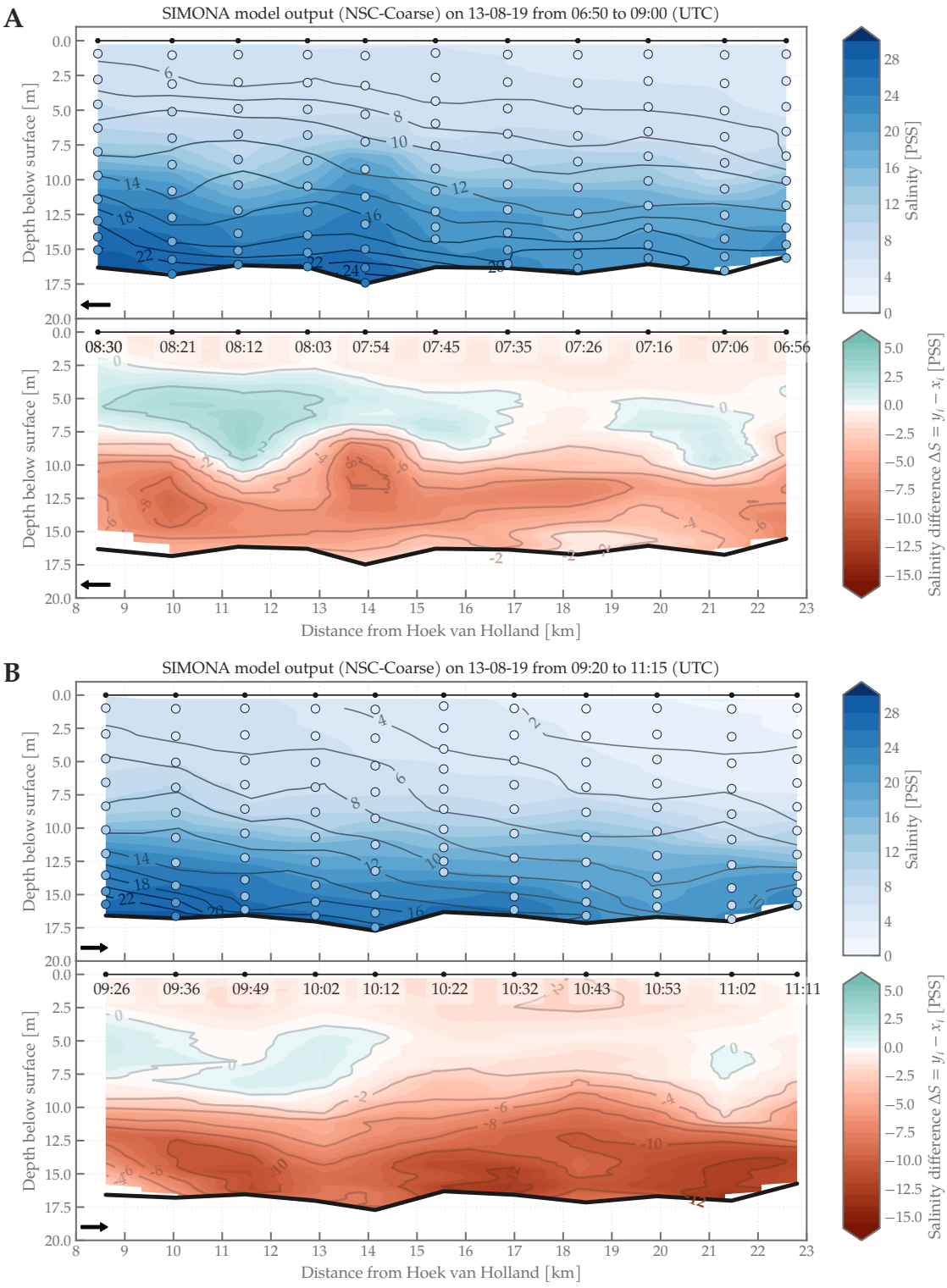

Figure 8.8: Overview of the calculated salinity difference between model output y_i and measurements x_i for the NSC-Coarse model. The model output is visualised by the individual dots and contour lines in the upper panels, a dot indicating an output point. The actual salinity distribution is plotted as a contour behind these dots. The difference between model and measurement is indicated in the bottom part of the figure, green indicating an overprediction of the model and red indicating an underprediction of the model. Arrows in the bottom left corner indicate the navigation direction of the vessel.

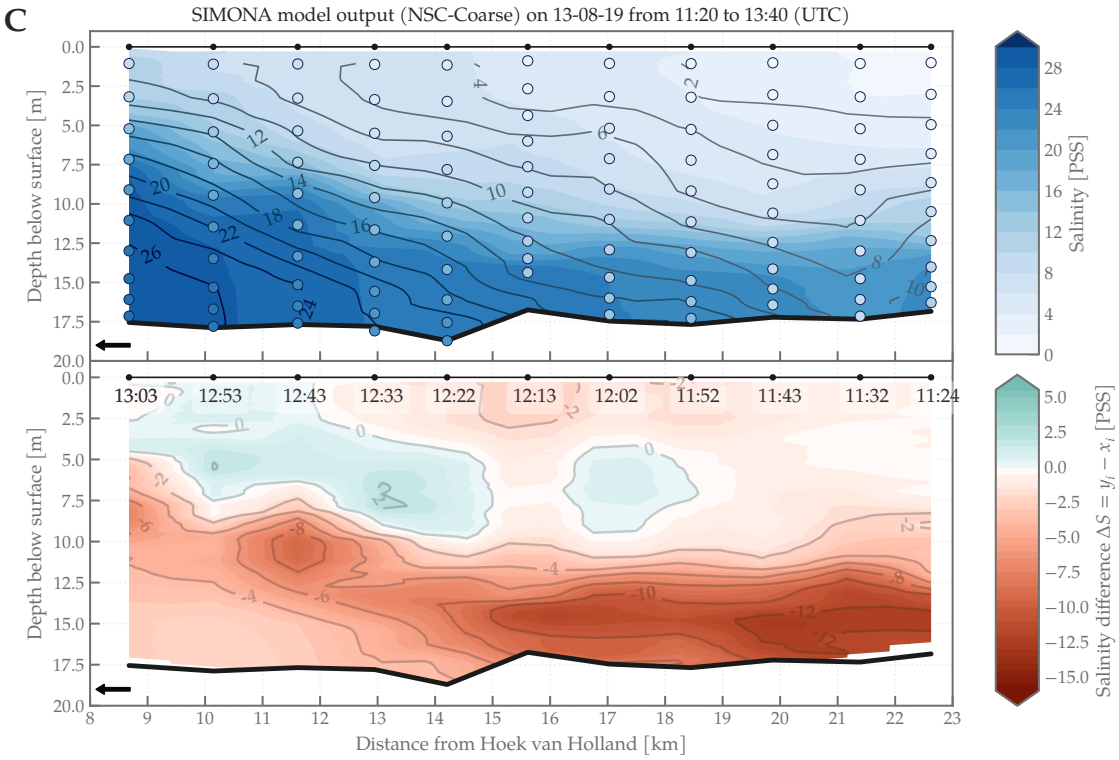

Figure 8.8: (*Continued*)

monitoring survey. The measured and modelled pycnocline heights are depicted in Fig. 8.9.

The general impression from Fig. 8.9 is that the NSC-Fine model indeed outperforms the NSC-Coarse model in estimating the pycnocline height. It is also visible that both models more often estimate the pycnocline height to be lower than the observed pycnocline height. For both models, the MAE is largest during slack tide.

During ebb tide and slack tide, the NSC-models both perform poorly, which is indicated by the low values for the index of agreement and the negative R^2-scores. The LWS pycnocline heights are reproduced slightly better than the ebb tide pycnocline heights. The pycnocline heights are also represented better during flood tide (third transect), although the NSC-Coarse model does not seem to follow the trend of the actual pycnocline height well given the negative R^2-score. This negative R^2-score is likely a result of the pycnocline height outlier (*see* Fig. 8.9), which, in turn, is a result of an erroneous bathymetry representation at this location.

Table 8.6: Overview of the correlation parameters relating the calculated pycnocline height from measurements to the calculated pycnocline height from NSC-model output. The correlation parameters are calcuted for all of the three transects and both NSC-models.

	Fine			Coarse		
	d	**MAE**	**R^2**	**d**	**MAE**	**R^2**
First transect	0.40	1.90	-4.44	0.24	3.57	-17.48
Second transect	0.46	2.72	-1.46	0.31	3.67	-3.02
Third transect	0.85	1.50	0.48	0.66	3.47	-1.88

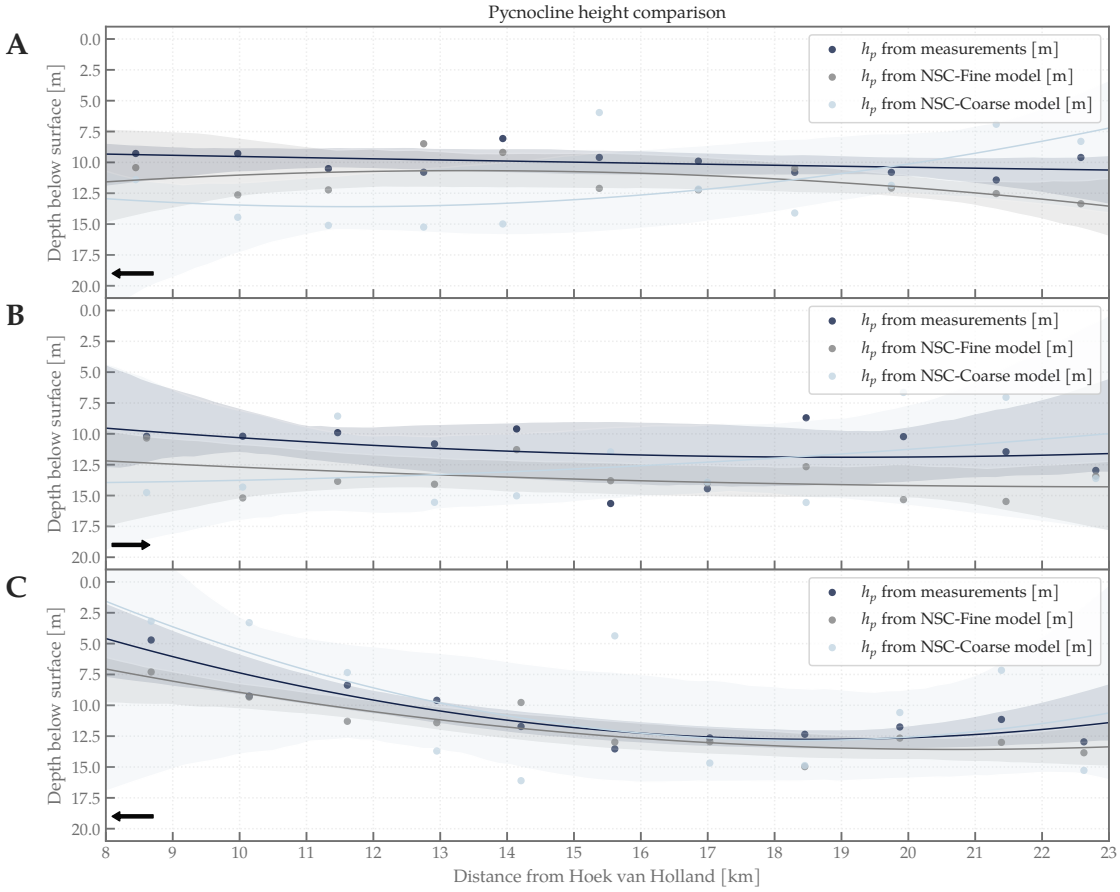

Figure 8.9: Overview of calculated pycnocline heights over the duration of the August 13th measurement survey. Right side of the figure indicates the correlation parameters of the NSC-coarse model (denoted with subscript *c*) and the NSC-Fine model (denoted with subscript *f*) for (**A**) the first, (**B**) the second, and (**C**) the third transect. Lines indicate fitted second order regression lines through the data points.

8.4 Discussion

The predictive capability of both SIMONA models is quantified based on three correlation parameters: the magnitude of the mean absolute error, the index of agreement, and the R^2-score. This is done for time series—both long and short—and a special monitoring survey executed on August 13th, 2019. The time series analysis focuses on two types of time series: salinity time series and water level time series. Additionally, to assess whether a correction for this phase shift leads to better correlation results, all salinity time series have been corrected with the resolved phase shift. The resolved phase shift in the water level time series was so small that a correction was unnecessary. An overview of the phase shift corrected correlation parameters for the time series comparison is given in Table 8.5.

Furthermore, the predictive capabilities of the models were tested based on the velocity and salinity measurements of August 13th, 2019. An overview of all correlation parameters calculated for the August 13th monitoring survey is given in Table 8.7.

8.4.1 Introduced phase shift

From the phase shift analysis, it was found that a small phase shift between salinity time series is introduced in both NSC-models. Generally, this phase shift is larger in the NSC-Coarse model than the NSC-Fine model, and seems to be mainly related to an incorrect prediction of the salt intrusion length. A trend of increasing phase shift in the upestuary direction could thus not be distinguished. A time series correlation analysis also did not provide evidence for the hypothesis that the predictive capability of the NSC-models increases in upestuary direction. However, the misrepresentation of the salt intrusion length led to low

salinities at the fixed stations located higher upstream, which obfuscated the results.

8.4.2 Vertical structure representation

Considering the vertical salinity structure, the NSC-Fine model predicts the salinity distribution over the vertical relatively well. The lowest index of agreement over the course of all three runs is equal to $d_f = 0.84$ at Rhine kilometer 1015, and the largest index of agreement, $d_f = 0.99$, is observed at multiple locations. Interestingly, the calculated R^2-scores are generally much lower, although negative values of the R^2-score do not occur.

The NSC-Coarse model comparison shows a slightly different trend. The indices of agreement are generally lower than the indices of agreement calculated for the NSC-Fine model, with values ranging between $d_c = 0.68$ and $d_c = 0.97$. The R^2-scores are also generally smaller, and around slack after ebb, even a negative R^2-score is reported.

Table 8.7: Overview of correlation parameters between model output and measurements of August 13th, 2019. A green dot (●) indicates that the NSC-Fine model generally performs better according to the previously defined correlation parameters, whereas a red dot (●) indicates that the NSC-Coarse model performs better.

			Fine			Coarse		F > C
Name	**Time** [UTC]	**d** [-]	**MAE** [PSS]	**R²** [-]	**d** [-]	**MAE** [PSS]	**R²** [-]	
First run								
1014	06:56:54	0.95	2.20	0.84	0.87	3.63	0.59	●
1015	07:06:26	0.99	1.32	0.94	0.92	2.47	0.76	●
1016	07:16:29	0.96	2.21	0.81	0.95	2.04	0.83	●
1017	07:26:51	0.97	1.85	0.84	0.92	2.42	0.70	●
1018	07:35:58	0.97	1.95	0.84	0.90	2.96	0.68	●
1019	07:45:30	0.97	2.02	0.85	0.86	2.91	0.64	●
1020	07:54:30	0.97	2.63	0.86	0.88	4.66	0.55	●
1021	08:03:31	0.99	1.47	0.95	0.93	2.92	0.80	●
1022	08:12:44	0.99	1.17	0.96	0.90	3.47	0.73	●
1023	08:21:29	0.98	2.02	0.92	0.87	4.40	0.59	●
1024	08:30:27	0.99	1.13	0.98	0.91	3.39	0.74	●
Second run								
1024	09:26:55	0.99	1.53	0.94	0.92	2.93	0.75	●
1023	09:36:53	0.97	2.28	0.87	0.87	3.96	0.60	●
1022	09:49:37	0.98	2.00	0.91	0.76	4.77	0.39	●
1021	10:02:33	0.99	1.20	0.96	0.87	3.30	0.64	●
1020	10:12:45	0.98	1.75	0.93	0.84	4.34	0.53	●
1019	10:22:47	0.99	1.71	0.94	0.69	4.10	0.09	●
1018	10:32:24	0.96	2.52	0.86	0.72	6.03	0.16	●
1017	10:43:46	0.91	3.59	0.64	0.75	5.87	0.12	●
1016	10:53:03	0.86	4.00	0.52	0.68	5.69	-0.06	●
1015	11:02:46	0.91	3.86	0.69	0.69	5.21	0.17	●
1014	11:11:45	0.95	2.44	0.83	0.76	4.83	0.36	●
Third run								
1014	11:24:03	0.93	3.28	0.76	0.75	4.78	0.35	●
1015	11:32:37	0.84	4.40	0.49	0.68	5.79	0.02	●
1016	11:43:01	0.99	1.51	0.96	0.71	4.93	0.26	●
1017	11:52:40	0.96	3.03	0.82	0.82	4.60	0.49	●
1018	12:02:43	0.98	2.23	0.90	0.75	4.66	0.37	●
1019	12:13:04	0.99	1.48	0.95	0.79	3.93	0.36	●
1020	12:22:56	0.99	1.14	0.98	0.92	3.26	0.75	●
1021	12:33:07	0.97	2.32	0.86	0.94	3.23	0.80	●
1022	12:43:16	0.95	2.35	0.80	0.91	3.53	0.71	●
1023	12:53:23	0.99	1.33	0.96	0.97	2.14	0.90	●
1024	13:03:15	0.94	3.01	0.66	0.93	3.29	0.74	●

Both models have most difficulty reproducing the vertical salinity distribution around slack after ebb. This is visible from Table 8.7; the predictive capability of both models decreases around 10:43:46, only to increase

again around 11:43:01. This could imply that the model is not able to resolve the superimposed baroclinic exchange flows occurring at slack tide (de Nijs *et al.*, 2010a,b). A similar model limitation has been previously noted by de Nijs and Pietrzak (2012). Both models seem to reproduce the salinity structure best during flood tide. The pycnocline height prediction is least accurate during ebb tide, followed by LWS. This is not advantageous for modelling the SURICATES pilot project. This misrepresentation of the pycnocline height, may have a large influence on modelling of the distribution of SPM over the water column (de Nijs and Pietrzak, 2012). Conversely, the vertical salinity distribution outside of the pycnocline region is represented best during ebb tide, which leads to seemingly contradictory conclusions.

Overall, both models have difficulties reproducing the pycnocline height well. In contrast to what earlier model studies by de Nijs and Pietrzak (2012) and Warner *et al.* (2005)—admittedly, under different discharge conditions—have found, the models underpredict the pycnocline height above the bed. This misrepresentation, in turn, has an influence on the representation of the velocity structure (*see* Appendix B).

The NSC-models' ability to reproduce velocities was also assessed. For brevity, the extensive analyses are kept out of the main text, and can be found in Appendix B. From these analyses, it seems as if a phase shift is introduced inthe mode, which is visible from the consistently negative differences during LWS. This would be in line with the qualitative comparisons presented in Chapter 7. This phase lag could not be quantified, however, because there are no fixed velocity stations near the considered domain. For more quantitative conclusions on this, more fixed monitoring stations should be deployed along the Rotterdam Waterway.

8.4.3 Limitations and challenges

Limitations arise from the methodology used to determine the applicability of the NSC-models and the comparison between these two models. These limitations are briefly discussed below.

Quantification methods: Three different correlation parameters are used to quantify the correlation between model output and measurements. These correlation parameters were chosen based on similar research (de Nijs and Pietrzak, 2012). However, many different correlation parameters can be used to quantify the predictive capability of the models. The use of other correlation parameters may lead to different conclusions, hence, it might be useful to also consider other correlation parameters in future predictive capability assessments.

Compared parameters: In this study, only the correlation parameters for salinity, water level, and horizontal velocity have been assessed. To gain more insight into the workings of the models, it would be beneficial to also assess the models' capability to reproduce vertical velocities; this is mainly important when assessing the predictability of internal wave phenomena (*see* Chapter 6, Section 6.1.5).

Limited data at deeper profiling points: Although a comparison over the entire vertical is done for the August 13th, 2019, monitoring survey, most salinity stations only measure salinity in the top nine meters of the water column. More insight into the reproducibility of the salt intrusion length over time could be obtained if time series of measuring points located deeper in the water column were also compared.

Generalisation of outcome: Since the modelling study presented here only presents the outcome of a predictive capability assessment of one 6-hour monitoring survey, results may not be generalised for other conditions. In order to make more substantiated statements about the overall predictive capability of the models, longer time series and more incidental monitoring surveys—over a wider range of boundary conditions—should be assessed as well.

Furthermore, there are some limitations to the predictive capabilities of the models that are related to the set-up of the models. These are elaborated on below.

Vertical resolution: Both NSC-models have a low vertical resolution, which may explain the models' difficulty to reproduce (part of) the vertical salinity structure. Ralston *et al.* (2010) has shown that in the

Merrimack River—a similarly strongly forced salt wedge estuary—an increase of the vertical resolution to twenty vertical levels provided much better results. Preliminary analysis of model runs with a higher vertical resolution, presented in Appendix B, show that a higher vertical resolution indeed increases the models' capability to reproduce the salinity distribution over the vertical, although further research into the optimisation of the amount of vertical limits—taking into account operational and computational limits—is recommended anyhow.

Background diffusivity values: Another interesting area of further research is the model response to different values of the background diffusivity values. Sensitivity of models to the background values of turbulent diffusivity has been reported in similarly shallow and stratified estuarine systems (Ralston *et al.*, 2010), indicating that this value has to be very small ($O(10^{-7})$) in order to reproduce the strong pycnocline satisfactorily. The fact that the background diffusivity value is currently set to values varying from 0.01 m^2 s^{-1} to 1.00 m^2 s^{-1} throughout the model domain (Kranenburg, 2015), indicates that there is considerable potential in this.

Wave coupling: Currently, there is no coupling between a wave model and the used SIMONA models. Especially in the case of SPM modelling, it is beneficial to accurately model processes like wave resuspension of SPM. Although a first effort has been made by De Groot (2018), this first effort only included a parameterisation of the influence of waves through addition of bottom shear stresses. The influence that the coupling between a wave model and the presented SIMONA model has on the predictive capability of the models is an interesting area of further research.

Conservative scheme: Enhancement of the model results may be achieved by modelling the estuary using a numerical model that implements a conservative momentum scheme. Since the model results presented here indicate that baroclinic flow processes are likely not reproduced well, a conservative scheme may aid in reproducing a more realistic return current celerity (Bijvelds, 2001). This was also one of the recommendations in de Nijs and Pietrzak (2012).

Turbulence closure: Furthermore, modelling studies by Ralston *et al.* (2010), Li *et al.* (2005) and Warner *et al.* (2005) have indicated that the results of Reynolds-averaged quantities such as salinity are relatively insensitive to the used turbulence closure, although it may be useful to test whether this is also true for the Rotterdam Waterway specifically.

Wind description: Wind is incorporated in both NSC-models. It is distributed non-uniformly over the model domain, and the magnitude is based on measurements at Noorderpier. The wind magnitude is not uniform over the entire domain, but is artificially reduced at certain points in the model domain. An overview of this wind reduction is indicated in Fig. 5.7. As is visible from Fig. 5.7, the wind is locally reduced to only 10% of the value at Noorderpier, whereas in reality, the wind magnitude would decrease landinwards, and such harsh transitions would not occur. It should be assessed what the effect of a more physical representation of the wind distribution would be on the stratification representation.

8.5 Conclusions

Two currently operational hydrodynamic models were tested on their ability to predict the velocities, water level, and salinities—in a hindcast sense—based on a monitoring survey conducted on August 13th, 2019. This was done based on both time series and individually measured verticals.

From the correlation calculations based on water level time series, it was found that the water level predictions—by both NSC-models—are highly correlated to the actual measurements. At all stations, for all compared durations, the index of agreement was equal to one, indicating perfect agreement between both signals. These same signals were considered to calculate a—possible—phase shift between model and measurements, from it was found that no phase shift could be resolved for the majority of the considered stations.

In line with qualitative comparisons, quantitative comparisons between individual velocity measurements and the velocity model output indicate that a phase lag may be introduced in the velocity predictions,

although this phase lag cannot be quantified due to a lack of velocity time series. Besides this, both NSC-models are able to adequately reproduce velocities—with indices of agreement ranging between 0.28 and 0.98 for the NSC-Coarse model, and 0.55-0.97 for the NSC-Fine model. The correlations are largest during LWS, and—on average—lowest during the beginning of flood.

Furthermore, it is shown in this chapter that both models represent the pycnocline height best during (the beginning of) flood tide, and worst during ebb tide. Following from the results presented in Chapter 6, this may have a significant influence on the distribution of SPM if either of the evaluated NSC-models are used to represent the hydrodynamics. Conversely, the vertical salinity structure outside of the pycnocline region is represented best during ebb tide. Because the misrepresentation of the pycnocline height could be related to the vertical resolution of the model, it may be advantageous to research whether an increase in the vertical resolution of the model leads to a performance increase on this front.

The NSC-Fine model performs well in representing the overall salinity structure over the vertical, with values of the index of agreement ranging between 0.84 and 0.99. The NSC-Coarse model performs adequately, with values of the index of agreement ranging between 0.68 and 0.95. Overall, both NSC-models predict the salinity structure over the vertical best during ebb tide. Conversely, both evaluated NSC-models do not perform well in reproducing the pycnocline height. Both models represent the pycnocline height best during (the beginning of) flood tide, and worst during ebb tide.

Furthermore, the NSC-Fine and NSC-Coarse model were compared to each other. To this end, three hypotheses were tested, which are each elaborated below.

1. *The NSC-Fine model is able to reproduce the water level, velocities, and salinity better than the NSC-Coarse model;*

   When looking at the models' capability to predict velocities over the vertical, it is found that neither of the models clearly outperform each other. Overall, the NSC-Coarse model is better at predicting the velocities during LWS, but the NSC-Fine model—generally—is better at predicting the velocities outside of the LWS period. This is found from the correlation parameters given in Table B.1.

   The hypothesis that the NSC-Fine model reproduces the salinity structure of the August 13th, 2019, monitoring survey—over the vertical—better than the NSC-Coarse model is substantiated for all measurement locations, for the entire tidal cycle. This is validated from the correlation parameters presented in Table 8.7. Looking at the reproducibility of salinity time series, however, the NSC-Coarse model outperforms the NSC-Fine model in several cases; at Hoek van Holland, and at the Spijkenisserbrug location, although the latter is only true when assessing the correlation from a month long time series. Furthermore, both models perform almost equally well in predicting the water level; in fact, the NSC-Coarse model even outperforms the NSC-Fine model in predicting the water level higher upstream.

2. *The NSC-Fine model is able to reproduce the pycnocline height better than the NSC-Coarse model, even though the vertical resolution of both NSC-models is the same;*

   The pycnocline height development is calculated from the NSC-Coarse and NSC-Fine model output of the August 13th survey. From the results, presented in Fig. 8.9, it can be concluded that the NSC-Fine model indeed outperforms the NSC-Coarse model in predicting the pycnocline height—this true throughout the entire modelled monitoring survey.

3. *The predictive capability of the NSC-models for salinity decreases in the upestuary direction.*

   The validity of this hypothesis is tested based on the outcome of a time series analysis. Based on the correlation parameters calculated between model time series and measured time series at several salinity stations lining the Rotterdam Waterway, it can be deduced that no trend is found relating the predictive capability of the salinity of the NSC-models to the position of the station along the Rotterdam Waterway. Although the phase shift analysis shows that the phase shift does increase in

the upestuary direction, it is recognised that this result is obfuscated due to the misrepresentation of the salt intrusion length by both models.

Part IV

CONCLUDING REMARKS

This part covers the *concluding remarks*, where it is aimed to answer the posed research questions and reflect upon the presented work.

Chapter 9

Discussion

This chapter discusses and reflects on the study as a whole. Limitations on the applicability of the study are elaborated. To compartmentalise, this chapter first separately discusses the set-up and data analysis of the special monitoring survey in Section 9.1, after which the set-up and outcome of the modelling study is discussed in Section 9.2.

9.1 Monitoring survey

On August 13th, 2019, an elaborate dataset was obtained from a special 6-hour monitoring survey executed in the Rotterdam Waterway. During this survey, a combination of instruments measured the salinity structure, velocity structure, and the SPM distribution along a transect crossing the SURICATES reallocation location. During the measurements, a measured discharge of 1960 m^3 s^{-1} provided buoyancy forcing, although measured discharges ranging from 1200 m^3 s^{-1} to 1550 m^3 s^{-1} were measured in the preceding weeks. The average wind conditions were mild (7.44 m s^{-1}), and tidal conditions were halfway between spring and neaps. A boat crossed the same transect three times, capturing the dynamics at—approximately—ebb tide, LWS and the beginning of flood.

The results of an analysis of this dataset were compared to earlier work by de Nijs *et al.* to be able to make statements about possible changes in the workings of the natural system. It was found that many of the previously identified processes in earlier work by de Nijs *et al.* (2009, 2010a,b) are still governing—in spite of the many human interferences in the natural system since the survey conducted in the work by de Nijs *et al.*. There are some differences too, however. From a momentum balance analysis it was found that the influence of the advective acceleration was much higher than during the survey presented in de Nijs *et al.* (2010a). In Chapter 6, it is hypothesised that this may be due to the difference in discharge conditions, but the deepening of the Rotterdam Waterway may also play a role.

Other notable differences were the higher Reynolds shear stresses over the water column. However, the Reynolds stress values were very sensitive to the extrapolation method. Additionally, the Reynolds shear stresses—due to a lack of suitable data—have been calculated using a different methodology than presented in de Nijs *et al.* (2010a), which makes a one-to-one comparison difficult.

The distribution of SPM over the water column was researched by analysis of two different measured quantities; (1) the optical backscatter—measured with OBSs mounted on the Siltprofiler—and (2) ADCP backscatter. Because fundamentally different quantities are measured, and because ADCP backscatter is measured continuously in stead of discretely—like the Siltprofiler measurements—analysis of these quantities gives mixed results. This is one of the main limitations of the set-up of the monitoring survey. Furthermore, although the Siltprofiler was calibrated beforehand, no bottle samples were taken to validate the data over the vertical. This lack of validation, along with the fact that SPM concentrations in the Rotterdam Waterway have been noted to exceed the range in which the OBSs are able to measure, implies that only qualitative statements on the SPM distribution are justified. Combining the results of both methods and assessing them qualitatively, it is found that SPM is mainly present near the bed, although the ADCP backscatter also indicate higher SPM concentrations in the water column underneath the pycnocline. During flood, SPM is resuspended, but remains confined underneath the pycnocline. Interestingly, the ADCP backscatter measurements indicate that SPM is mixed over the entire water column during LWS, as opposed to it being confined underneath the pycnocline, which has not been observed before. It

should—again—be stressed, however, that any conclusive statements about the SPM distribution could not be made based solely on the available data. Further research, preferably including bottle samples and OBSs that have a larger maximum range, is necessary to make such conclusive statements.

In addition, an internal Froude number analysis was conducted which showed that the internal Froude number locally exceeds one during ebb tide. Another transition from subcritical to supercritical takes place during flood tide. This may indicate that internal waves are generated, but an analysis of vertical velocities—not measured during this survey—is needed to verify this.

There are a number of other limitations to the interpretability of the results presented in Chapter 6 and the comparability of the results with the research presented in de Nijs *et al.* (2010a). The most important limitations are related to the instrument settings and the post-processing methods. Firstly, the settings of the ADCP during the August 13th monitoring survey had the routine profiling settings, in which the amount of pings was not optimised for research purposes. This limits the accuracy of the calculation of the momentum terms. Furthermore, the accuracy of the results following from the calculation of the along-channel momentum balance terms is limited as a result of assumptions made in the post-processing methodology—the main source of erroneousness in this sense is the assumption that subsequent measurements are done at the same time, which is not possible as a result of the used measurement strategy (Lagrangian measurements). Lastly, the comparability of the outcome of the monitoring survey is impeded by the difference in water level, wind, and discharge conditions, as well as changes to the natural system, compared to the monitoring survey presented in de Nijs *et al.* (2010a). It is not possible to decouple the contributions from either of these processes and interventions, and therefore we can only generalise the outcome of the data analysis for similar surveys under the influence of this very specific set of circumstances.

Taking into account the limitations to the used methods and the comparability of this study to previously executed studies in the Rotterdam Waterway, the outcome of the data analysis presented here still contributes to understanding the workings of the complex Rhine-Meuse estuarine system, which is an advance.

9.2 Model set-up and comparative study

The aim of the study presented here is to map the predictive capability of hydrodynamic models that are currently used by the Port of Rotterdam in modelling studies: a fine model (NSC-Fine), mostly used for studying the effect of interventions in the natural system on the salinity distribution, and a coarse model (NSC-Coarse), mostly used as the basis of SPM modelling studies. The predictive capability of these models is tested for the August 13th, 2019, monitoring survey and month-long salinity and water level time series. The time series analysis is restricted to the analysis of water level an salinity time series, and the monitoring survey analysis is restricted to the analysis of measured velocity and salinity verticals. Additionally, the outcome of both models is compared to each other. This is done using three chosen correlation parameters; (1) the magnitude of the MAE, (2) the index of agreement, and (3), the R^2-score. It is also assessed whether a phase shift is introduced.

The outcome of this analysis shows that mainly the pycnocline height cannot be reproduced by either of the models (*see* Chapter 8), which is known to pose an upper limit to the distribution of SPM over the water column by turbulence damping at the pycnocline (de Nijs *et al.*, 2010a,b; Geyer, 1993). It is noted that these results are only specifically valid under the boundary conditions—water level, discharge, and wind conditions—that were observed during the monitoring survey on August 13th, 2019. The models' difficulties with reproducing the pycnocline height may be related to the limited vertical resolution of both models. In a modelling study of a similarly dynamic and shallow estuary, Ralston *et al.* (2010) found that an increase of the amount of layers to twenty sufficiently increased the predictive capability on this front. Further research on whether this indeed increases the pycnocline height predictability of the models is recommended.

Limitations associated with the model comparison arise from the quantification methods, compared parameters, limited data at deeper profiling points and a limited substantiation for the generalisation of the presented comparative model validity study.

The most pressing of these limitations is the fact that too reductive generalisation of the comparative model study may result in faulty and incoherent conclusions. Although this study contributes to the general understanding of the Rhine-Meuse estuarine system and potential modelling difficulties of the system, further research is necessary into the response of the system and the models under different conditions. Furthermore, a more thorough assessment of the predictive capability of both models may be obtained when taking into account additional hydrodynamic parameters—the most obvious one being the vertical velocities. These are mainly of interest when assessing the occurrence of internal wave phenomena.

General limitations relating to the model set-up have also been identified, which can be translated into recommendations. The main limitation of the currently used models is the limited amount of vertical layers, although the high background diffusion values may also be a source of errors. Another possible limitation of the model is the absence of wave coupling. It is recommended that the influence of varying these parameters is tested more thoroughly in future research. It is noted that an optimisation of these parameters may be different for either of the two NSC-models.

Chapter 10

Conclusions and recommendations

Effective implementation of the SURICATES pilot project and other eco-innovative projects alike requires a thorough understanding of the physical processes impacting the (re-)distribution of sediments. With the objective to '*elucidate the hydrodynamic processes in the Rotterdam Waterway within the framework of the SURICATES pilot project, and assess the reproducibility of these processes by currently operational 3D hydrodynamic models at the Port of Rotterdam, based on the results of a special monitoring survey.*', this research set out to map the current state and possible improvements of two presently operational hydrodynamic models of the Rotterdam Waterway. By doing so, this study contributes to the development of a model that is more accurate in modelling the salinity and velocity structure in the Rotterdam Waterway, and that may be used to optimise several aspects of similar projects in the future. The study is not only valuable through its contributions on this part, but also because it contributes to the understanding of the hydrodynamic processes in the Rotterdam Waterway in general by analysing and presenting the findings of a special monitoring survey carried out during the SURICATES pilot project.

This chapter elaborates on the key findings of this study and the recommendations stemming from these findings. In support of the objective, answers to each of the research questions are presented and briefly discussed.

10.1 Key findings

The key findings of this study are summarised by firstly answering the research subquestions, after which an overall conclusion is drawn based on the main research question and research objective. Each of the research subquestions have already been elaborately answered in the dedicated chapters, and will be briefly discussed here.

1. *What are the primary hydrodynamic processes occurring in the Rotterdam Waterway and in the larger Rhine-Meuse estuarine system?*

   The primary hydrodynamic processes occurring in the Rotterdam Waterway are barotropic tidal asymmetry imposed at the river mouth, advection of the salt wedge, baroclinically driven exchange flows, and turbulence damping at the pycnocline. The interaction between all of these processes produces differences in ebb tide and flood tide duration; the ebb tide duration is longer. Furthermore, this interaction leads to flood dominance in the upper part of the water column, ebb dominance in the lower part of the water column, differences in the onset of slack water at the bed and surface, and the formation of mid-depth jets. Farther upestuary in the Rhine-Meuse estuarine system, however, the effect of buoyancy—supplied by the freshwater discharge—outweighs the effect of the barotropic tidal asymmetry, which means that the effect of internal differences in flood or ebb dominance is reduced.

   At the limit of salt intrusion, the baroclinically driven exchange-type processes lead to flow convergence at the bed, and flow divergence at the surface. Baroclinically driven exchange-type processes at the limit of saltwater intrusion are also the driving force for the exchange of SPM with surrounding harbour basins.

2. *What are the governing hydrodynamic processes near the SURICATES reallocation location, and how may*

these influence the SPM distribution?

It is found that the aforementioned governing hydrodynamic processes are still governing near the SURICATES reallocation location, which are (1) the barotropic tidal asymmetry imposed at the river mouth, (2) advection of the salt wedge, (3) baroclinically driven exchange flows, and (4) turbulence damping at the pycnocline. From a momentum balance analysis it is found that the baroclinic and barotropic pressure gradients are the dominant terms, and that advective processes modulate the sum of terms strongly—under the specific boundary conditions of August 13th, 2019. Qualitative analyses of ADCP backscatter and calculated internal Froude numbers, additionally, give reason to believe that internal waves may form in the river bend near Maassluis, although statements on this remain inconclusive based on the available data.

In combination with the effect of turbulence damping at the pycnocline, the advection of the salt wedge poses an upper limit to the SPM distribution over the vertical. The mid-depth jets formed as a result of the interaction between baroclinic forcing and the barotropic tidal asymmetry, may advect water—with SPM—from regions of higher momentum to regions of lower momentum. Furthermore, qualitative analyses of ADCP backscatter data seem to indicate that diffusion processes may dilute the SPM concentration over the entire water column during LWS, even though higher squared buoyancy frequencies and Richardson gradient numbers at the pycnocline—indicative of turbulence damping—imply that this turbulent diffusion should be damped around mid-depth. This has not been observed before in the Rotterdam Waterway.

3. *How accurately can two currently operation 3D numerical models reproduce the hydrodynamics of a monitoring survey conducted in the Rotterdam Waterway during the SURICATES pilot project?*

   The barotropic tidal asymmetry imposed at the mouth, represented by the velocity distribution, onset of LWS, and the water level elevation, was adequately reproduced. A small velocity phase shift seems to be introduced in both NSC-models, visible from the delayed onset of LWS, but generally, both NSC-models reproduce the velocity structure adequately. Furthermore, a phase shift is also observed when comparing salinity time series and measurements. The salinity structure influences the velocity structure, and vice versa—thus, the observation of phase shifts in these signals are closely related. Additionally, the water levels were reproduced very well by both models—indices of agreement were all equal to 1.00, indicating "perfect" agreement between the model output and the measurements.

   The advection of the salt wedge, however, is not reproduced well; both NSC-models predict a shorter salt intrusion length than is observed from measurements. Additionally, neither of the tested models could predict the pycnocline height satisfactorily. This conclusion is based on the values of the correlation parameters: over the entire duration of the monitoring survey, the mean value of the index of agreement equated 0.57 for the NSC-Fine model and 0.4 for the NSC-Coarse model, MAEs were all above 1.5 meter, and the R^2-scores were only positive during flood tide. Because the pycnocline height determines the height at which turbulence damping will take place, this misrepresentation influences the ability of the model to reproduce pycnocline damping, and may thus also influence the reproducibility of the SPM distribution in future research. Besides the reproducibility of the pycnocline height, the rest of the salinity structure over the vertical is reproduced adequately to well by both considered NSC-models.

4. *What are the key parameters that impact the predictive capability of the currently operational 3D numerical models used by the Port of Rotterdam?*

   From this study it is found that one of the key parameters that impact the predictive capability of the two considered and currently operational 3D numerical models is the horizontal grid resolution. From a series of comparisons between a model with a coarse horizontal grid (NSC-Coarse) and a model with a fine horizontal grid (NSC-Fine) model, it is found that the NSC-Fine model consistently outperforms the NSC-Coarse model in predicting the salinities. The velocities are not consistently reproduced better by the NSC-Fine model, although the NSC-Fine model outperforms the NSC-Coarse model at most measured verticals.

> Additionally, preliminary analyses using a model grid with a higher vertical resolution have shown that the vertical resolution also impacts the predictive capability—a higher vertical resolution leading to better salinity estimates over the vertical.

Now that the individual research subquestions are answered, the answer to the main research question can be formulated. For convenience, it is repeated here:

> *What are the governing hydrodynamic processes relevant within the scope of the SURICATES pilot project, and how well can these processes be reproduced by the currently operational numerical models used in the Port of Rotterdam?*

The governing hydrodynamic processes relevant within the scope of the SURICATES pilot project are the barotropic tidal asymmetry imposed at the river mouth, the advection of the salt wedge, baroclinically driven exchange flows, and turbulence damping at the pycnocline. Additionally, the river bend at Maassluis may induce internal wave phenomena which may influence the hydrodynamics at the reallocation location, but this could not be directly concluded from the data presented in this thesis, and requires additional research.

It is found from literature that accurate representation of the pycnocline height and salt intrusion length is of crucial importance in the accurate modelling of SPM in the Rotterdam Waterway. In this research, it is found that currently used models are flawed in this aspect, and have difficulties predicting either of these parameters. The barotropic tidal asymmetry, however, could be accurately reproduced by both NSC-models, although a small phase shift seems to be introduced when calculating salinities and velocities.

Finally, we can assess whether the research objective was obtained, which was to:

> ***Elucidate the hydrodynamic processes in the Rotterdam Waterway within the framework of the SURICATES pilot project, and assess the reproducibility of these processes by currently operational 3D hydrodynamic models at the Port of Rotterdam, based on the results of a special monitoring survey.***

An elaboration of all governing hydrodynamic and sediment dynamic processes, substantiated with the results of a data analysis based on a special monitoring survey set up during the SURICATES pilot project, provides more insight into the processes that are governing in the Rotterdam Waterway—in general, and around the SURICATES reallocation location. Understanding these processes allows for comprehension of the output two operational hydrodynamic models. Subsequently, the conclusions following from an evaluation of this output provide the basis for recommendations on model improvements and aid in placing the outcome of future modelling studies that use these models into perspective. This study therefore contributes to the improvement of future modelling studies—both related to hydrodynamics and SPM—in the framework of the SURICATES pilot project.

10.2 Recommendations

Considering the presented conclusions and the discussed limitations, a set of recommendations can be made. These recommendations can be categorised into recommendations concerning the data analysis—specifically, the data acquisition—and recommendations concerning model improvements. Both of these categories are briefly discussed below.

Data acquisition

In order to make more accurate statements about the models' capability of reproducing the hydrodynamic processes occurring in the Rotterdam Waterway, several recommendations can be made related to the data acquisition, concerning the monitoring survey of August 13th, 2019.

Dataset duration: The monitoring survey executed on August 13th, 2019, took up approximately six hours. For future studies, it is useful to at least capture an entire cycle.

Dataset variability: This thesis only covers the results of one dataset, which has been obtained in between neap and spring tide, and with low discharges at Lobith. It is recommended to look at multiple datasets covering a variety of boundary conditions, e.g. the spring-neap tidal variability, high-low discharge variability and storm conditions, in order to cover the entire range of forcing conditions under which the system may react differently.

Vertical velocities: The boat-mounted ADCP used for the acquisition of velocity and backscatter data in this thesis only has two active beams, which means that vertical velocities are not recorded. It is recommended to conduct a similar survey—possibly, under similar discharge conditions—using three beams to verify whether internal waves are actually generated near the river bend.

Amount of fixed measuring stations: Several time series were used in the predictive capability test presented in Chapter 8. These were all located relatively far away from the domain that was monitored on August 13th, 2019. Currently, there are no fixed salinity or velocity measuring stations located near the reallocation location—the closest salinity stations are at Hoek van Holland and at in the Lekhaven, and the closest (operational) velocity measuring station is located at Dordrecht. Additionally, these few salinity stations only have one or two operational CTDs. It is therefore recommended for future work on similar projects to place more stations that measure salinity and velocity in time, so phase shifts can be calculated more accurately and possible factors contributing to the introduction of phase shifts can be discerned. These stations may also be temporary, as in previous work by de Nijs *et al.*. Furthermore, it is recommended to place these stations deeper into the water column, so that the (evolution) of the salt intrusion length can be monitored.

Instrument setting optimisation: There are a few instruments that were not optimally utilised during the monitoring survey on August 13th, 2019. Firstly, no water samples were taken to validate the SPM data obtained using the Siltprofiler. Moreover, the maximum measuring range of the Siltprofiler's OBSs is lower than the maximum SPM concentrations that have previously been recorded in the Rotterdam Waterway. This implies that, even if the Siltprofiler's data would have been validated, the Siltprofiler data could not be used to calibrate the ADCP backscatter results. This implies that the ADCP backscatter data can only be assessed qualitatively. It is recommended to at least take bottle samples in a possible future monitoring survey, to validate the Siltprofiler results. Additionally, it is recommended to look into other instrumentatino to measure the maximum SPM concentrations.

Besides this, the boat-mounted ADCP used during the monitoring survey of August 13th, 2019, did not have the optimal settings for research purposes. In order to yield more accurate results—both in general, and specifically, in the momentum term estimation—as well as increase the comparability of the results with previous work by de Nijs *et al.* (2010a), it is recommended to increase the amount of pings to the instrument's maximum. It is furthermore encouraged to additionally measure ADCP backscatter using a 1200 kHz ADCP; a comparison between measurements using different frequencies may uncover the contribution of different sediment fractions or even density.

Model improvements

Several recommendations on further improvements for the considered NSC-models can be made on the basis of the results presented in this thesis. These have already been mentioned throughout the text (*see* Section 8.4), but are briefly discussed again and summarised in the following paragraphs.

Increased vertical resolution: Both NSC-models only have ten vertical sigma layers. This may—partly—explain the models' difficulty in predicting the pycnocline height. Research by Ralston *et al.* (2010) suggests that adding an additional ten vertical sigma layers may yield better representation of the pycnocline height. Preliminary analyses presented in Appendix B substantiate this, as an increase of the amount of vertical sigma layers to 30 generally increases the capability of the models to reproduce salinities. Further research into the optimal layer settings—within operational and computational limits—is still recommended.

Lowered background diffusion: The background diffusivities used in the NSC-models have been increased in recent years (Deltares, 2015). This was justified by the fact that this adjustment seemingly increased the predictive capability of the NSC-models, however, the value of these background diffusivities is non-physical. In fact, Ralston *et al.* (2010) and Warner *et al.* (2005) have indicated that numerical models may be sensitive to high values of the background diffusivity, and that it is recommended to keep these values low—in the order of $O(10^{-6} - 10^{-7})$. It is recommended to further investigate the influence of lowering this background diffusivity value.

Coupling with wave processes: Processes like wave resuspension are important in modelling the distribution of SPM. Wave-current interactions may also influence stratification. Although De Groot (2018) has made a first effort in including the effect of waves in the NSC-Coarse model by a parameterisation of the waves as bottom shear stresses, the effect that direct coupling of a wave model will have on the predictive capability has not yet been assessed. This may be a good area of further research.

Physically justified wind description: In the currently operational models, the wind description is non-physical; the magnitude of the wind is based on measurements at Noorderpier—a pier that is placed relatively far offshore—after which this magnitude is imposed as a uniform value on the largest part of the domain. This in itself is already non-physical, as the wind magnitude generally decreases landinwards. Additionally, a wind reduction is imposed on a certain part of the domain, which reduces the wind magnitude to 10% of the value at Noorderpier, but the transition is very harsh (*see* Fig. 5.7). It is recommended to look further into imposing a more realistic wind reduction factor on the domain, and assess the effect that this may have on the models' ability to reproduce salinities.

Bibliography

M. Bijvelds. *Numerical modelling of estuarine flow over steep topography*. PhD thesis, Delft University of Technology, 2001.

Wil Borst and Tiedo Vellinga. The Monitoring Programme for the Maasvlakte 2 - Construction at the Port of Rotterdam. *Terra et Aqua*, (130):16–29, 2013.

Hans Burchard and Robert D. Hetland. Quantifying the contributions of tidal straining and gravitational circulation to residual circulation in periodically stratified tidal estuaries. *Journal of Physical Oceanography*, 40(6):1243–1262, 2010. ISSN 00223670. doi: 10.1175/2010JPO4270.1.

Hans Burchard, Robert D. Hetland, Elisabeth Schulz, and Henk M. Schuttelaars. Drivers of residual estuarine circulation in tidally energetic estuaries: Straight and irrotational channels with parabolic cross section. *Journal of Physical Oceanography*, 41(3):548–570, 2011. ISSN 00223670. doi: 10.1175/2010JPO4453.1.

Robert J. Chant, Wayne R. Geyer, Robert Houghton, Elias Hunter, and James Lerczak. Estuarine boundary layer mixing processes: Insights from dye experiments. *Journal of Physical Oceanography*, 37(7):1859–1877, 2007. ISSN 00223670. doi: 10.1175/JPO3088.1.

Dudley B. Chelton, Roland A. Deszoeke, Michael G. Schlax, Karim El Naggar, and Nicolas Siwertz. Geographical variability of the first baroclinic Rossby radius of deformation. *Journal of Physical Oceanography*, 28(3):433–460, 1998. ISSN 00223670. doi: 10.1175/1520-0485(1998)028<0433:GVOTFB>2.0.CO;2.

Daniel L. Codiga. Unified Tidal Analysis and Prediction Using the UTide Matlab Functions. Technical Report September, Graduate School of Oceanography, University of Rhode Island, 2011.

Cynthia N. Cudaback and David A. Jay. Tidal asymmetry in an estuarine pycnocline: 2. Transport. *Journal of Geophysical Research: Oceans*, 106(C2):2639–2652, 2001. ISSN 2169-9291. doi: 10.1029/2000jc900151.

Gerben J. de Boer. *On the interaction between tides and stratification in the Rhine Region of Freshwater Influence*. PhD thesis, Delft University of Technology, 2009. URL http://www.narcis.nl/publication/RecordID/oai:tudelft.nl:uuid:c5c07865-be69-4db2-91e6-f675411a4136%5Cnhttp://repository.tudelft.nl/view/ir/uuid:c5c07865-be69-4db2-91e6-f675411a4136/.

Gerben J. De Boer, Julie D. Pietrzak, and Johan C. Winterwerp. On the vertical structure of the Rhine region of freshwater influence. *Ocean Dynamics*, 56(3-4):198–216, 2006. ISSN 16167341. doi: 10.1007/s10236-005-0042-1.

Gerben J. de Boer, Julie D. Pietrzak, and Johan C. Winterwerp. Using the potential energy anomaly equation to investigate tidal straining and advection of stratification in a region of freshwater influence. *Ocean Modelling*, 22(1-2):1–11, 2008. ISSN 14635003. doi: 10.1016/j.ocemod.2007.12.003.

Gerben J. de Boer, Julie D. Pietrzak, and Johan C. Winterwerp. SST observations of upwelling induced by tidal straining in the Rhine ROFI. *Continental Shelf Research*, 29(1):263–277, 2009. ISSN 02784343. doi: 10.1016/j.csr.2007.06.011.

Sjoerd De Groot. *Suspended Sediment Modelling in the Port of Rotterdam*. PhD thesis, Delft University of Technology, 2018.

Michel A.J. de Nijs. *On sedimentation processes in a stratified estuarine system*. PhD thesis, Delft University of Technology, 2012.

Michel A.J. De Nijs and Julie D. Pietrzak. An explanation for salinity- and SPM-induced vertical countergradient buoyancy fluxes. *Ocean Dynamics*, 61(4):497–524, 2011. ISSN 16167341. doi: 10.1007/s10236-011-0375-x.

Michel A.J. De Nijs and Julie D. Pietrzak. On total turbulent energy and the passive and active role of buoyancy in turbulent momentum and mass transfer. *Ocean Dynamics*, 62(6):849–865, 2012. ISSN 16167341. doi: 10.1007/s10236-012-0536-6.

Michel A.J. de Nijs and Julie D. Pietrzak. Saltwater intrusion and ETM dynamics in a tidally-energetic stratified estuary. *Ocean Modelling*, 49-50:60–85, 6 2012. ISSN 14635003. doi: 10.1016/j.ocemod.2012.03.004.

Michel A.J. de Nijs, Johan C. Winterwerp, and Julie D. Pietrzak. SPM variations in a harbour basin. *Sediment and Ecohydraulics*, pages 357–378, 2005. doi: 10.1093/benz/9780199773787.article.b00173687.

Michel A.J. de Nijs, Johan C. Winterwerp, and Julie D. Pietrzak. On harbour siltation in the fresh-salt water mixing region. *Continental Shelf Research*, 29(1):175–193, 2009. ISSN 02784343. doi: 10.1016/j.csr.2008.01.019.

Michel A.J. de Nijs, Julie D. Pietrzak, and Johan C. Winterwerp. Advection of the Salt Wedge and Evolution of the Internal Flow Structure in the Rotterdam Waterway. *Journal of Physical Oceanography*, 41(1):3–27, 2010a. ISSN 0022-3670. doi: 10.1175/2010jpo4228.1.

Michel A.J. de Nijs, Johan C. Winterwerp, and Julie D. Pietrzak. The Effects of the Internal Flow Structure on SPM Entrapment in the Rotterdam Waterway. *Journal of Physical Oceanography*, 40 (11):2357–2380, 2010b. ISSN 0022-3670. doi: 10.1175/2010jpo4233.1.

Kent L. Deines. Backscatter estimation using broadband acoustic Doppler current profilers. In *Proceedings of the IEEE Working Conference on Current Measurement*, pages 249–253, 1999. doi: 10.1109/ccm.1999.755249.

Deltares. Evaluatie van het OSR-model voor zoutindringing in de Rijn-Maasmonding (II). Technical report, Deltares, 2015. Internal document of the Port of Rotterdam.

Deltares. *Delft3D-FLOW, Simulation of multi-dimensional hydrodynamic flows and transport phenomena, including sediments*. Deltares, 2020.

D. Eisma, J. Kalf, and M. Veenhuis. The formation of small particles and aggregates in the Rhine Estuary. *Netherlands Journal of Sea Research*, 14(2):172–191, 1980.

D. Eisma, P. Bernard, G. C. Cadée, V. Ittekkot, J. Kalf, R. Laane, J. M. Martin, W. G. Mook, A. van Put, and T. Schuhmacher. Suspended-matter particle size in some West-European estuaries; part II: A review on floc formation and break-up. *Netherlands Journal of Sea Research*, 28(3):215–220, 1991. ISSN 00777579. doi: 10.1016/0077-7579(91)90018-V.

D. M. Farmer. Maximal two-layer exchange through a contraction with barotropic net flow. *Journal of Fluid Mechanics*, 164:27–51, 1986. ISSN 14697645. doi: 10.1017/S0022112086002458.

M. G.G. Foreman and R. F. Henry. The harmonic analysis of tidal model time series. *Advances in Water Resources*, 12(3):109–120, 1989. ISSN 03091708. doi: 10.1016/0309-1708(89)90017-1.

Mike G.G. Foreman, J. Y. Cherniawsky, and V. A. Ballantyne. Versatile harmonic tidal analysis: Improvements and applications. *Journal of Atmospheric and Oceanic Technology*, 26(4):806–817, 2009. ISSN 07390572. doi: 10.1175/2008JTECHO615.1.

W. R. Geyer and D. K. Ralston. *The Dynamics of Strongly Stratified Estuaries*, volume 2. Elsevier Inc., 2012. ISBN 9780080878850. doi: 10.1016/B978-0-12-374711-2.00206-0. URL http://dx.doi.org/10.1016/B978-0-12-374711-2.00206-0.

W. R. Geyer, J. H. Trowbridge, and M. M. Bowen. The dynamics of a partially mixed estuary. *Journal of Physical Oceanography*, 30(8):2035–2048, 2000. ISSN 00223670. doi: 10.1175/1520-0485(2000)030<2035:TDOAPM>2.0.CO;2.

W. Rockwell Geyer. The Importance of Suppression of Turbulence by Stratification on the Estuarine Turbidity Maximum. *Estuaries*, 16(1):113–125, 1993.

W. Rockwell Geyer and David M. Farmer. Tide-Induced Variation of the Dynamics of a Salt Wedge Estuary, 1989. ISSN 0022-3670.

W. Rockwell Geyer and Parker MacCready. The Estuarine Circulation. *Annual Review of Fluid Mechanics*, 46(1):175–197, 2014. ISSN 0066-4189. doi: 10.1146/annurev-fluid-010313-141302.

A. Gill. *Atmosphere-Ocean Dynamics*. Academic Press, San Diego, California 92101-4495, USA, volume 30 edition, 1982. ISBN 0122835204.

Gabriel Godin. *The analysis of tides*. University of Toronto Press, 1972.

R. Grimshaw, E. Pelinovsky, and O. Poloukhina. Higher-order Korteweg-de Vries models for internal solitary waves in a stratified shear flow with

a free surface. *Nonlinear Processes in Geophysics*, 9(3/4):221–235, 2002. ISSN 1023-5809. doi: 10.5194/npg-9-221-2002.

Nathan Hawley. A comparison of suspended sediment concentrations measured by acoustic and optical sensors. *Journal of Great Lakes Research*, 30(2):301–309, 2004. ISSN 03801330. doi: 10.1016/S0380-1330(04)70348-2. URL http://dx.doi.org/10.1016/S0380-1330(04)70348-2.

Kenneth D Hill, Thomas M Dauphinee, and J Woods. The Extension of the Practical Salinity Scale 1978 to Low Salinities. *IEEE Journal of Oceanic Engineering*, 11(8407100):1–4, 1986.

P. S. Hill, E. Boss, J. P. Newgard, B. A. Law, and T. G. Milligan. Observations of the sensitivity of beam attenuation to particle size in a coastal bottom boundary layer. *Journal of Geophysical Research: Oceans*, 116(2):1–14, 2011. ISSN 21699291. doi: 10.1029/2010JC006539.

A. J.F. Hoitink and P. Hoekstra. Observations of suspended sediment from ADCP and OBS measurements in a mud-dominated environment. *Coastal Engineering*, 52(2):103–118, 2005. ISSN 03783839. doi: 10.1016/j.coastaleng.2004.09.005.

Leo H. Holthuijsen. *Waves in Oceanic and Coastal Waters*. Cambridge University Press, Cambridge, 2007. ISBN 9780511618536. doi: 10.1017/CBO9780511618536.

Interreg NWE. SURICATES - Sediment Uses as Resources In Circular and Territorial EconomieS. http://www.nweurope.eu/projects/project-search/suricates-sediment-uses-as-resources-in-circular-and-territorial-economies/, 2018. Accessed 25-07-2019.

Interreg NWE. What is Interreg NWE? http://www.nweurope.eu/about-the-programme/what-is-interreg-nwe/, 2019. Accessed 25-07-2019.

IOC SCOR. IAPSO: The international thermodynamic equation of seawater–2010: Calculation and use of thermodynamic properties, Intergovernmental Oceanographic Commission, Manuals and Guides No. 56. *UNESCO, Manuals and Guides*, 56:1–196, 2010.

C.R. Jackson, J.C.B. Da Silva, and G. Jeans. The generation of nonlinear internal waves. *Oceanography*, 25(2):56–67, 2012. ISSN 10428275. doi: http://dx.doi.org/10.5670/oceanog.2012.46. URL http://dx.doi.org/10.5670/oceanog.2011.80.

David A. Jay and Jeffery D. Musiak. Particle trapping in estuarine tidal flows. *Journal of Geophysical Research*, 99(C10):20445, 1994. ISSN 0148-0227. doi: 10.1029/94jc00971.

Benjamin King, Mark Stone, H P Zhang, Theo Gerkema, Robert B, Michael Marder, and Harry L Swinney. Buoyancy frequency profiles and semidiurnal internal tide turning points in the deep ocean. *Nonlinear Dynamics*, 117:1–37, 2012. doi: 10.1029/2011JC007681.

W.M. Kranenburg. Evaluatie van het OSR-model voor zoutindringing in de Rijn- Maasmonding (II). Technical report, Deltares, Delft, The Netherlands, 2015.

E.J. Langendoen. *Flow patterns and transport of dissolved matter in tidal harbours*. PhD thesis, Delft University of Technology, 1992.

James A. Lerczak and W. Rockwell Geyer. Modeling the lateral circulation in straight, stratified estuaries. *Journal of Physical Oceanography*, 34(6):1410–1428, 2004. ISSN 00223670. doi: 10.1175/1520-0485(2004)034<1410:MTLCIS>2.0.CO;2.

Ming Li, Liejun Zhong, and William C. Boicourt. Simulations of Chesapeake Bay estuary: Sensitivity to turbulence mixing parameterizations and comparison with observations. *Journal of Geophysical Research: Oceans*, 110(12):1–22, 2005. ISSN 21699291. doi: 10.1029/2004JC002585.

Parker MacCready and W. Rockwell Geyer. Advances in Estuarine Physics. *Annual Review of Marine Science*, 2(1):35–58, 2010. ISSN 1941-1405. doi: 10.1146/annurev-marine-120308-081015.

Federico Maggi. *Flocculation dynamics of cohesive sediment*. PhD thesis, 2005.

Rooni Mathew and Johan C. Winterwerp. Surficial sediment erodibility from time-series measurements of suspended sediment concentrations: development and validation. *Ocean Dynamics*, 67(6):691–712, 2017. ISSN 16167228. doi: 10.1007/s10236-017-1055-2.

MATLAB. *version 9.7.0.1190202 (R2019b)*. The MathWorks Inc., Natick, Massachusetts, 2019.

Ministerie van Infrastructuur en Waterstaat. Zoutafleiding. Technical Report November, Ministerie van Infrastructuur en Milieu, Rijkswaterstaat (RWS), 2005.

Ministerie van Infrastructuur en Waterstaat. De Rijkswaterstaat standaard voor de inwinning, verwerking en uitgifte van hydrologische en meteorologische gegevens. Technical report, Rijkswaterstaat (RWS), 2010.

Stephen G. Monismith, Wim Kimmerer, Jon R. Burau, and Mark T. Stacey. Structure and flow-induced variability of the subtidal salinity field in northern San Francisco Bay. *Journal of Physical Oceanography*, 32(11):3003–3019, 2002. ISSN 00223670. doi: 10.1175/1520-0485(2002)032<3003:SAFIVO>2.0.CO;2.

P.M. Morse and H. Feshbach. *Methods of theoretical physics*. McGraw-Hill, 1953.

Jonathan D. Nash and James N. Moum. River plumes as a source of large-amplitude internal waves in the coastal ocean. *Nature*, 437(7057):400–403, 2005. ISSN 14764687. doi: 10.1038/nature03936.

Nicholas J. Nidzieko, James L. Hench, and Stephen G. Monismith. Lateral circulation in well-mixed and stratified estuarine flows with curvature. *Journal of Physical Oceanography*, 39(4):831–851, 2009. ISSN 00223670. doi: 10.1175/2008JPO4017.1.

Jacques C.J. Nihoul and Francois C. Ronday. The Influence of the "tidal stress" on the residual circulation: Application to the Southern Bight of the North Sea. *Tellus*, 27(5):484–490, 1975. doi: 10.1111/j.2153-3490.1975.tb01701.x. URL https://onlinelibrary.wiley.com/doi/abs/10.1111/j.2153-3490.1975.tb01701.x.

A. J.G. Nurser and S. Bacon. The rossby radius in the arctic ocean. *Ocean Science*, 10(6):967–975, 2014. ISSN 18120792. doi: 10.5194/os-10-967-2014.

OpenStreetMap contributors. Planet dump retrieved from https://planet.osm.org . https://www.openstreetmap.org, 2017.

Hyo Bong Park and Guan hong Lee. Evaluation of ADCP backscatter inversion to suspended sediment concentration in estuarine environments. *Ocean Science Journal*, 51(1):109–125, 2016. ISSN 17385261. doi: 10.1007/s12601-016-0010-3.

Etienne Pauthenet. *Unraveling the thermohaline structure of the Southern Ocean using functional data analysis*. PhD thesis, Stockholm University, 2018. URL http://urn.kb.se/resolve?urn=urn:nbn:se:su:diva-161034.

Ronald G. Perkin and Edward Lyn Lewis. The Practical Salinity Scale 1978 : Fitting the Data. *IEEE Journal of Oceanic Engineering*, OE-5(1):9–16, 1980.

J.D. Pietrzak. *Class Notes for CIE5302: An Introduction to Stratified Flows for Civil and Offshore Engineering*. PhD thesis, Delft University of Technology, 2015.

Julie Pietrzak and Robert Jan Labeur. Trapped internal waves over undular topography in a partially mixed estuary. *Ocean Dynamics*, 54(3-4):315–323, 2004. ISSN 16167341. doi: 10.1007/s10236-003-0081-4.

Hugo Platell. Internal gravity waves in the Rhine ROFI; applicability of the KdV model. Technical report, Delft University of T, 2019.

Port of Rotterdam. Werkplan: Interreg project Sediment Uses as Resources In Circular and Terretorial EconomieS. Technical report, Port of Rotterdam, 2018. Unpublished internal document, Port of Rotterdam.

Rudolph W. Preisendorfer. *Principal Component Analysis in Meteorology and Oceanography*. Elsevier Science Publishers B.V., 17 edition, 1988. ISBN 0-444-43014-8.

Markus Quante and Franciscus Colijin, editors. *North Sea Region Climate Assessment (NOSCCA)*. Number October. Springer Nature, 2016. ISBN 9783319397436. doi: 10.1007/978-3-319-39745-0.

Lawrence R. Rabiner and Bernard Gold. *Theory and application of digital signal processing*. Englewood Cliffs, N.J. : Prentice-Hall, 1975.

David K Ralston, W Rockwell Geyer, James A Lerczak, and Malcolm Scully. Turbulent mixing in a strongly forced salt wedge estuary. 115 (December 2009):1–19, 2010. doi: 10.1029/2009JC006061.

L. F. Richardson. The Supply of Energy from and to Atmospheric Eddies. *Proceedings of the Royal Society A: Mathematical, Physical and Engineering Sciences*, 97(686):354–373, 1920. ISSN 1364-5021. doi: 10.1098/rspa.1920.0039.

Rijkswaterstaat. WAQUA/TRIWAQ - two- and three-dimensional shallow water flow model. Technical documentation. Technical Report 99, Rijkswaterstaat, 2016. URL http://simona.deltares.nl/release/doc/techdoc/waquapublic/sim1999-01.pdf.

Sabine Rijnsburger, Carola M. van der Hout, Onno van Tongeren, Gerben J. de Boer, Bram C. van Prooijen, Wil G. Borst, and Julie D. Pietrzak. Simultaneous measurements of tidal straining and advection at two parallel transects far downstream in the Rhine ROFI. *Ocean Dynamics*, 66 (5):719–736, 2016. ISSN 16167228. doi: 10.1007/s10236-016-0947-x. URL http://dx.doi.org/10.1007/s10236-016-0947-x.

Sabine Rijnsburger, Raúl P. Flores, Julie D. Pietrzak, Alexander R. Horner-Devine, and Alejandro J. Souza. The Influence of Tide and Wind on the Propagation of Fronts in a Shallow River Plume. *Journal of Geophysical Research: Oceans*, 123(8): 5426–5442, 2018. ISSN 21699291. doi: 10.1029/2017JC013422.

Johann Rodhe. The Baltic and North Seas: A process-oriented review of the physical oceanography. *The Sea*, 11:1029–1072, 2004.

M. Rotsaert. Afregeling OSR systeem. Technical report, Havenbedrijf Rotterdam, 2010.

H. H. G. Savenije. Influence of Rain and Evaporation on Salt Intrusion in Estuaries. *Journal of Hydraulic Engineering*, 114(12):1509–1524, 2008. ISSN 0733-9429. doi: 10.1061/(asce)0733-9429(1988)114:12(1509).

Elisabeth Schulz. *Residual circulation in tidally energetic estuaries: contributions and dependencies*. PhD thesis, Universität Rostock, 2014.

Elisabeth Schulz, Henk M. Schuttelaars, Ulf Gräwe, and Hans Burchard. Impact of the depth-to-width ratio of periodically stratified tidal channels on the estuarine circulation. *Journal of Physical Oceanography*, 45(8):2048–2069, 2015. ISSN 15200485. doi: 10.1175/JPO-D-14-0084.1.

Science Research Council (Great Britain) and United States Naval Observatory Nautical Almanac Office. *Explanatory supplement to the Astronomical ephemeris and the American ephemeris and nautical almanac*. London : Her Majesty's Stationery Office, 1961. "Issued by H.M. Nautical Almanac Office by order of the Science Research Council".

J. H. Simpson, J. Brown, J. Matthews, and G. Allen. Tidal Straining, Density Currents, and Stirring in the Control of Estuarine Stratification. *Estuaries*, 13(2):125, 1990. ISSN 01608347. doi: 10.2307/1351581. URL http://link.springer.com/10.2307/1351581.

J.H Simpson and A.J Souza. Semidiurnal switching of stratification in the region of freshwater influence of the Rhine. *Journal of Geophysical Research*, 100(C4):7037–7044, 1995. ISSN 0148-0227. doi: 10.1029/95JC00067.

John H. Simpson, Wim G. Bos, Florian Schirmer, J. Alejandro Souza, Thomas P. Rippeth, Sarah E. Jones, and David Hydes. Periodic stratification in the Rhine ROFI in the North Sea, 1993. ISSN 0399-1784.

CastAway CTD User's Manual. SonTek, a Xylem brand, 2012.

R. Spanhoff and P. A.J. Verlaan. Massive sedimentation events at the mouth of the Rotterdam Waterway. *Journal of Coastal Research*, 16(2):458–469, 2000. ISSN 0749-0208.

M. T. Stacey, T. P. Rippeth, and J. D. Nash. *Turbulence and Stratification in Estuaries and Coastal Seas*, volume 2. Elsevier Inc., 2012. ISBN 9780080878850. doi: 10.1016/B978-0-12-374711-2.00204-7. URL http://dx.doi.org/10.1016/B978-0-12-374711-2.00204-7.

G.S. Stelling. *On the construction of computational methods for shallow water flow problems*. PhD thesis, Delft University of Technology, 1983.

Guus S Stelling and Jan J Leendertse. Approximation of convective processes by cyclic aoi methods. In *Estuarine and coastal modeling*, pages 771–782. ASCE, 1992.

Rémi Tailleux. A WKB analysis of the surface signature and vertical structure of long extratropical baroclinic Rossby waves over topography. *Ocean Modelling*, 6(3-4):191–219, 2004. ISSN 14635003. doi: 10.1016/S1463-5003(02)00065-3.

M.L. Thatcher and D.R.F. Harleman. A mathematical model for the prediction of unsteady salinity intrusion in estuaries. Technical report, R. M. Parsons Laboratory for Water Resources and Hydrodynamics, Department of Civil Engineering Massachusetts, Institute of Technology, T, Cambridge, 1972.

Richard E. Thomson and William J. Emery. The Spatial Analyses of Data Fields. In *Data Analysis Methods in Physical Oceanography*, pages 313–424. 2014. ISBN 9780123877826. doi: 10.1016/b978-0-12-387782-6.00004-1.

John H. Trowbridge, W. R. Geyer, M. M. Bowen, and A. J. Williams. Near-bottom turbulence measurements in a partially mixed estuary: Turbulent energy balance, velocity structure, and along-channel momentum balance. *Journal of Physical Oceanography*, 29(12):3056–3072, 1999. ISSN 00223670. doi: 10.1175/1520-0485(1999)029<3056:NBTMIA>2.0.CO;2.

UNESCO. Tenth report of the joint panel on oceanographic tables and standards. Technical Report 26, UNESCO, Division of Marine Sciences, Sidney, Canada, 1981.

A. Valle-Levinson. *Classification of Estuarine Circulation*, volume 1. Elsevier Inc., 2012. ISBN 9780080878850. doi: 10.1016/B978-0-12-374711-2.00106-6. URL http://dx.doi.org/10.1016/B978-0-12-374711-2.00106-6.

A. van der Giessen, W. P.M. De Ruijter, and J. C. Borst. Three-dimensional current structure in the Dutch coastal zone. *Netherlands Journal of Sea Research*, 25(1/2):45–55, 1990. ISSN 00777579. doi: 10.1016/0077-7579(90)90007-4.

Paul van Gastel and Josep L. Pelegrí. Estimates of gradient Richardson numbers from vertically smoothed data in the Gulf Stream region. *Scientia Marina*, 68(4):459–482, 2004. ISSN 02148358. doi: 10.3989/scimar.2004.68n4459.

Wim van Leussen. *Estuarine macroflocs and their role in fine-grained sediment transport*. PhD thesis, Utrecht University, 1994.

Andre W. Visser, Alejandro J. Souza, Katrin Hessner, and John H. Simpson. The effect of stratification on tidal current profiles in a region of freshwater influence. *Oceanologica Acta*, 17(4):369–381, 1994.

John C. Warner, W. Rockwell Geyer, and James A. Lerczak. Numerical modeling of an estuary: A comprehensive skill assessment. *Journal of Geophysical Research C: Oceans*, 110(5):1–13, 2005. ISSN 01480227. doi: 10.1029/2004JC002691.

Cort J. Willmott. On the validation of models. *Physical Geography*, 2(2):184–194, 1981. doi: 10.1080/02723646.1981.10642213. URL https://doi.org/10.1080/02723646.1981.10642213.

J. C. Winterwerp. On the flocculation and settling velocity of estuarine mud. *Continental Shelf Research*, 22(9):1339–1360, 2002. ISSN 02784343. doi: 10.1016/S0278-4343(02)00010-9.

J. C. Winterwerp. The Physical Analyses of Muddy Sedimentation Processes. In *Treatise on Estuarine and Coastal Science*, volume 2, chapter 2.15, pages 311–360. Elsevier Inc., 2011. ISBN 9780080878850. doi: 10.1016/B978-0-12-374711-2.00214-X.

Johan C. Winterwerp and Walther G.M. van Kesteren. Erosion and Entrapment. In *Introduction to the physics of cohesive sediment in the marine environment*, chapter 9, pages 343–358. Elsevier B.V., 1 edition, 2004a. ISBN 0070-4571.

Johan C. Winterwerp and Walther G.M. van Kesteren. Flocculation processes. In *Introduction to the Physics of Cohesive Sediment in the Marine Environment*, chapter 4, pages 87–119. Elsevier B.V., 1 edition, 2004b. ISBN 0-444-51553-4. doi: 10.1016/S0070-4571(04)80005-0.

J. Wolf, J. M. Brown, R. Bolaños, and T. S. Hedges. *Waves in Coastal and Estuarine Waters*, volume 2. Elsevier Inc., 2012. ISBN 9780080878850. doi: 10.1016/B978-0-12-374711-2.00203-5. URL http://dx.doi.org/10.1016/B978-0-12-374711-2.00203-5.

Alexander E. Yankovsky and David C. Chapman. A simple theory for the fate of buoyant coastal discharges. *Journal of Physical Oceanography*, 27(7):1386–1401, 1997. ISSN 00223670. doi: 10.1175/1520-0485(1997)027<1386:ASTFTF>2.0.CO;2.

Glossary

ADI-effect The effect that flow patterns are inaccurately predicted using the ADI method when Courant numbers are larger than $4\sqrt{2}$. It is related to the fact that the numerical region of influence does not correspond to the mathemtical region of influence. A free surface wave can thus not travel through more than two bends of 90 degrees in one ADI time step (Stelling, 1983).

Adiabatically Taking place without transferring heat or mass. An adiabatic process does not exchange heat or mass with its surroundings.

Advectively driven circulation The effect of lateral differential advection on the residual circulation, as described by Burchard *et al.* (2011).

Aggregation Growth of floc size as a result of the coalescence of flocs

Amphidromic point Geographical location in an ocean or sea with zero tidal amplitude for one harmonic constituent, around which a tidal wave rotates.

Baroclinic pressure gradient The part of the pressure gradient that is a consequence of density difference along the channel axis. In most cases, the baroclinic pressure varies over the depth.

Barotropic pressure gradient The part of the pressure gradient that is a result of the gradient in the free surface along the channel axis.

Breakup Decrease in floc size as a result of breaking of flocs into smaller entities

Brunt-Vaïsalä frequency The frequency at which a vertically displaced parcel will oscillate in a statically stable environment.

Buoyancy frequency *see* Brunt-Vaïsalä frequency.

Classical estuarine circulation *see* gravitational circulation.

Delft3D A modelling framework for a 3D numerical computations in coastal areas, estuarine areas, rivers and lakes. Several modules cover a specific domain of interest, covering processes such as flow, near-field and far-field water quality, wave generation, sediment transport and many others.

Differential advection The phenomenon of vertical or horizontal velocity gradients. Differential advection may occur when depth averaged velocity differs over the width of the channel due to depth differences associated with natural channels, but can also occur in the vertical direction. Because of this velocity difference, particles are advected at different speeds, which may lead to density differences and subsequent (lateral) flow phenomena.

Energy cascade The process of transfer of energy from the largest to the smallest turbulent length scales.

Estuarine circulation Residual flow pattern in an estuary induced by the density difference between seawater and river water.

Floc The particles that make up fine sediments.

Floc erosion Disruption and break-up of individual flocs or parts of flocs from the bed surface. Occurs when the mean bed shear stress is at or above a nominal critical shear stress for surface erosion.

Flocculation The net effect of aggregation and breakup processes.

Gravitational circulation The combined flow produced by the horizontal density differences and the water level slope associated with the river discharge Valle-Levinson (2012).

Index of agreement The index of agreement, also known as the model skill (Warner *et al.*, 2005), is a correlation parameter that was first proposed by Willmott (1981) to overcome the insensitivity of e.g. the coefficient of determination to differences in the observed and model simulated means and variances. It effectively calculates the ratio of the mean square error and the potential error, multiplied by the amount of observations and subtracted from one. Therefore, a value of one indicates perfect agreement, whereas a value of zero indicates complete disagreement.

Isohaline Contours connecting points of equal salinity

Korteweg-de Vries equation Equation derived by Grimshaw *et al.* (2002), describing the propagation of internal waves in space and time. This equation is used as part of the Korteweg-de Vries model, introduced by Korteweg and de Vries (1895).

Korteweg-de Vries model Model first introduced by Korteweg and de Vries (1895), developed to describethe propagation of internal waves in a stratified fluid under the influence of background flow. Model consists of the Taylor-Goldstein equation and the Korteweg-de Vries equation, using the output of the Taylor-Goldstein equation as input for the Korteweg-de Vries equation.

Liquefaction The structural breakdown of the bed sediment matrix which leads to the formation of a layer of fluid mud. This process is often induced by wave action on the bed.

Mass erosion An undrained process in which local failure within the bed occurs. This process occurs due to a

failure of the sediment matrix along a shear plane in the bed.

MATLAB® A commercial matrix-based programming platform designed mainly for use by engineers and scientists (MATLAB, 2019). [1]

Model skill *see* index of agreement.

Ozmidov length scale The upper limit to the turbulent length scales, posed by stratification in a stratified fluid (Stacey *et al.*, 2012). This limit is defined as $\lambda_O = \left(\frac{\epsilon}{N^2}\right)^{1/2}$.

Principal velocities The principal velocities are the velocity along the principal axes of the estuary. These principal axes are the axes along which the variance of the observed velocity fluctuations is maximised Thomson and Emery (2014). The principal axes, and thus the principal velocities, can be found by PCA.

Pycnocline A layer in a body of water where the density increases rapidly over depth; the pycnocline is the layer with the largest density gradient.

Python An open source general-purpose object-oriented programming language. [2]

Siltprofiler A measuring device developed by Deltares (formerly Delft Hydraulics) in combination with Ravensrodd Consultants, Ltd., that is equipped with several high-frequency turbidity sensors that are able to sample at high frequencies (de Nijs *et al.*, 2010b). The Siltprofiler used here is equipped with to OBS sensors and one transmission probe for turbidity measurements, and is additionally equipped with conductivity, Chlorophyll, pressure, and temperature sensors (Borst and Vellinga, 2013). Three Niskin water samplers, each with a volume of 1.8 litres, are mounted on the Siltprofiler as well.

SIMONA The numerical model architecture for preprocessing, memory management, data storage and postprocessing used in this study. Four models are classified under this heading, namely WAQUA, TRIWAQ, SIMPAR and SLIB3D.

Simpson number The Simpson number is a dimensionless numbers that has been shown to be able to determine the basic dynamics in (non-rotational) tidal estuaries (Burchard *et al.*, 2011). It is interpreted as the relative buoyancy gradient, and defined as $\mathrm{Si} = \frac{\partial_x b H^2}{U_*^2}$, where $\partial_x b$ is the tidally averaged longitudinal buoyancy gradient, H is the reference water depth, U_* is a scale for the bottom friction velocity and ω is the tidal frequency.

Static stability The ability of a fluid at rest to become turbulent or laminar due to the effects of buoyancy.

Strain Induced Periodic Stratification Semi-diurnal (re-)stratification pattern arising from the process of tidal straining (Simpson *et al.*, 1990). Also referred to as 1SIPS (Schulz *et al.*, 2015).

Surface erosion A drained process that occurs when the mean bed shear stress is just above the mean critical threshold shear stress, which causes a rupture in the physiochemical bonds between flocs at the surface. In this process, eroded particles are replaced with water, and flocs are entrained into the water column.

Thalweg The deepest channel.

Tidal straining The effect of differential advection by a vertical velocity shear on a horizontal density gradient de Boer (2009). It is the causal link between observed semi-diurnal cross-shore velocity signal and the semi-diurnal (re-)stratification signal, and was first identified by Simpson and Souza (1995).

Tidal straining circulation The circulation resulting from tidal straining.

TRIWAQ Computational package developed by the Dutch National Institute of Coastal and Marine Management in combination with Deltares that solves the shallow water equations in three dimensions.

Turbulence damping The damping of turbulent motions by buoyancy effects in a stratified fluid.

WAQUA Computational package developed by the Dutch National Institute of Coastal and Marine Management in combination with Deltares that solves the shallow water equations in two dimensions.

WKB-approximation The Wentzel-Kramers-Brillouin method is a mathematical method that can be used to find approximate solutions to linear differential equations with spatially varying coefficients. In the application of this method to the wave equation for a freely propagating linear wave, the wave function is recast as an exponential function and expanded. This yields an expression for the wave speed.

[1] More information available via `https://nl.mathworks.com/`.
[2] More information available via: `www.python.org`.

Part V

APPENDICES

Appendix A

Principal component analysis

As is mentioned in Chapter 4, a PCA is conducted on the velocity data measured by an ADCP to identify the principal axes which, after a coordinate transformation, yield the principal velocities. This chapter focuses on the outcome of the PCA, for the stationary measurements as well as the moving-boat measurements.

A.1 Methodology

Although the principle behind PCA has been explained in Chapter 4, Section 4.2.2, the numerical details haven't been elaborated on. Several packages exist to execute a PCA directly, although the code is also not too difficult to write from scratch. To reduce the chance of errors, a pre-made Python library is used to execute the PCA. The used function is the `PCA` function, which is a part of the `skikit-learn` machine learning library. This library is based on the libaries `numpy`, `matplotlib`, and `scipy`. The function itself is part of the package `sklearn.decomposition` in Python.[1] After the principal axes are found, the rotation of the principal axes with respect to the original North-East coordinate system is calculated. This is done using a simple function coordinate transform.

A.2 Principal axes

Moving boat measurements

The PCA is executed for the moving-boat ADCP measurements, accumulating all measurements between subsequent measurement locations into one larger dataset that the PCA is applied to in its entirety. The forthcoming principal axes are then used to transform all the velocities in the separate datasets from a North-East reference frame to along-channel and cross-channel reference frame. These different datasets, including the calculated principal axes following from the PCA, are shown in Fig. A.1.

Looking at the general shape of the scatter plots, several things can be deduced. It is clearly visible that during the first and second runs, there is a distinct preferred direction. This is visible from the long principal axes and stretched appearance of the scatter cloud. During the third run, however, the principal directions are less obvious in several locations. This is seemingly in contrast with logic, as the third run started at the end of slack tide lasting until full flood. In actuality, this is likely a result of increased mixing, related to the principle of tidal straining as discussed in Chapter 2.

Stationary measurements

The PCA applied to the stationary ADCP measurements is done using the same scripts. The only differences between the PCA for the moving-boat measurements and the stationary measurements are that the stationary measurements are shorter, resulting in less data points, and that the datasets can be directly coupled to a measuring location. The results of the PCA for each stationary ADCP dataset, giving the principal components, are shown in Fig. A.2.

The scatter plots in Fig. A.2 show that at most locations, the principal directions calculated by the PCA

[1] More information: `https://scikit-learn.org/stable/modules/generated/sklearn.decomposition.PCA.html` (accessed on April 22, 2020).

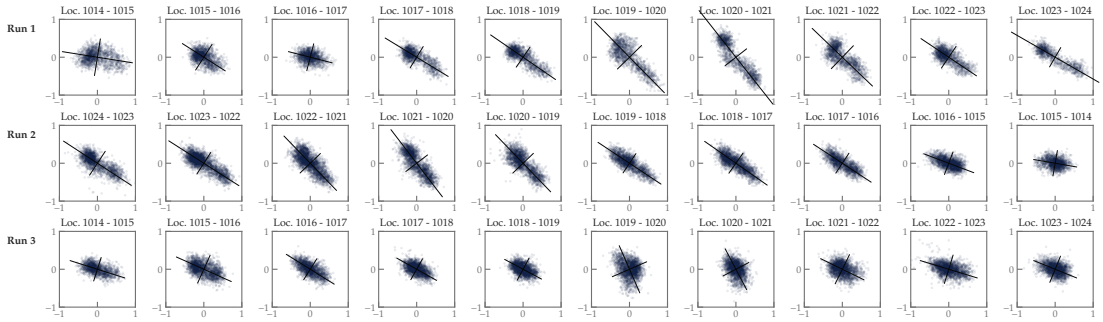

Figure A.1: Normalised scatter plot with indicated principal axes for moving-boat ADCP measurements. The principal axis indicated with the longest line is the axis along which the variance is maximal, indicating the along-channel direction, and it follows that the line perpendicular to this line is the axis of smallest variance. The y-axis in this figure represents the Northwards directed velocity component and the x-axis represents the Eastwards directed velocity component.

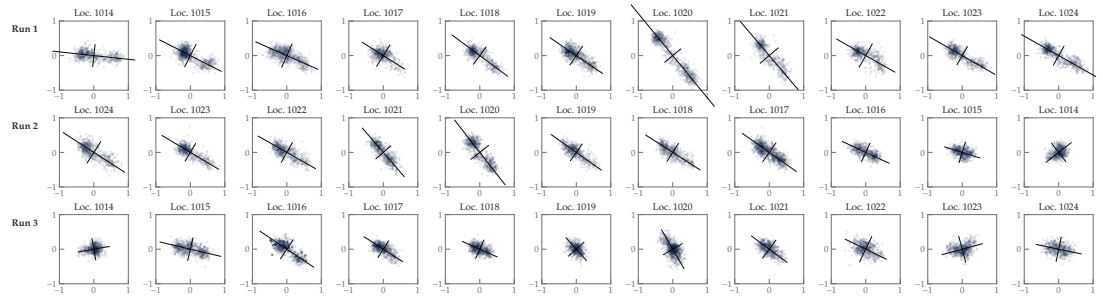

Figure A.2: Normalised scatter plot with indicated principal axes for stationary ADCP measurements. The principal axis indicated with the longest line is the axis along which the variance is maximal, indicating the along-channel direction, and it follows that the line perpendicular to this line is the axis of smallest variance. The y-axis represents the Northwards directed velocity component and the x-axis represents the Eastwards directed velocity component.

applied to the moving-boat measurements are in agreement with the principal directions calculated by the PCA on the stationary measurements. Nonetheless, there are a few exceptions to this that are visible from Fig. A.2. Two of these exceptions are visible in the dataset of the third measured transect (*see* locations 1014 and 1023) and one is evident in the second measured transect dataset (*see* location 1014). Upon inspection of the overall direction change over the tidal cycle, it seems as if the PCA was likely unable to detect the principal components well in these instances. When looking at the `PCA.explained_variance` attribute of the `sklean.decomposition.PCA` script, this also seems to be the case. These parameters shed a light on how much of the variance is explained by each component. Here, we look at the `PCA.explained_variance_ratio` of these locations, the values of which are summarised in Table A.1. This number represents the percentage of variance explained by each of the components.

Transect	Location nr.	explained_variance_ratio	
		1st comp.	2nd comp.
2	1014	0.6498	0.3502
3	1014	0.6817	0.3183
3	1023	0.7092	0.2908

Table A.1: Overview of values of `PCA.explained_variance_ratio` for each of the seemingly inconsistent values resulting from the PCA on the stationary measurements.

The average of the explained variance ratio of the first component amounts to 0.8486, and the average of the explained variance ratio of the second component is equal to 0.1514. These mean values are significantly higher than the explained variance ratios indicated in Table A.1. This means that the amount of spread in

these locations is much larger than in the other locations. This could be due to several factors;

Faulty equipment or inadequate pre-processing: There is a chance that there is an error in the recorded velocities due to faulty equipment or incorrect filtering of outliers in pre-processing;

Too much drift: The stationary measurements were assumed to be stationary in time, although the GPS logger does record some drift. This drift could have pushed the boat to the sides of the channel, where transverse flow patterns could be more dominant than in the thalweg;

Scarcity of data points: The stationary measurements are only taken during a relatively short time duration of approx. five to ten minutes, depending on the time needed to deploy the CTD. This could mean that the amount of data points is not large enough for the PCA to detect the principal directions well.

Furthermore, the inconsistencies at location 1014 are likely superposed on the effect of increased mixing during slack tide.

Assuming that, at these specific locations, the PCA of the stationary measurements has a faulty outcome, the calculated principal components are replaced by the principal components following from the PCA in corresponding moving-boat datasets. The result of this substitution is shown in figure A.3.

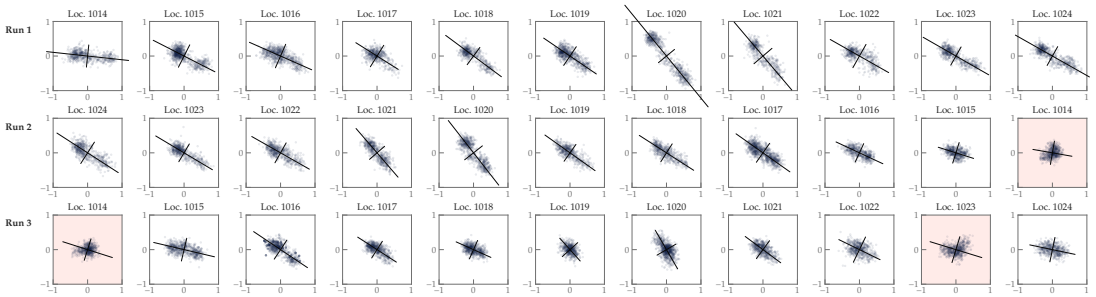

Figure A.3: Normalised scatter plot with indicated principal axes for stationary ADCP measurements, including substituted principal directions for locations with faulty PCA outcome. The scatter plots with the light red coloured background are the scatter plots from the datasets for which the principal components are swapped with the outcome of the PCA of the moving-boat datasets. The y-axis represents the Northwards directed velocity component and the x-axis represents the Eastwards directed velocity component.

A.3 Overview of velocities in along-channel coordinate system

After the coordinate transform is applied to the datasets, the principal velocities are obtained. The resulting along-channel velocities for the moving-boat measurements are presented in Chapter 6. For the stationary measurements, the situation is a little different, because a time series is obtained. This results in multiple ensembles, that may be ensemble averaged to get the ensemble mean along-channel and cross-channel velocities that are used in the computation of the momentum balance terms (*see* Chapter 4, Section 4.4.3). A 95% and 50% confidence interval can also be calculated.

The following sections elaborate on the individual velocity ensembles and mean velocity profiles in the new along-channel coordinate system.

A.3.1 Non-extrapolated velocity profiles

For the determination of the dominant terms in the momentum balance, the velocity profiles are post-processed as described in Section 4.2, but not extrapolated. This is done with the aim to reduce the amount of man-induced errors. This leads to velocity profiles that are cut-off at the blanking distance and a few

meters above the bed (side lobe effects). An overview of the individual ensembles in the along-channel coordinate system for each of the measured transects are depicted in Figs. A.4, A.5, and A.6.

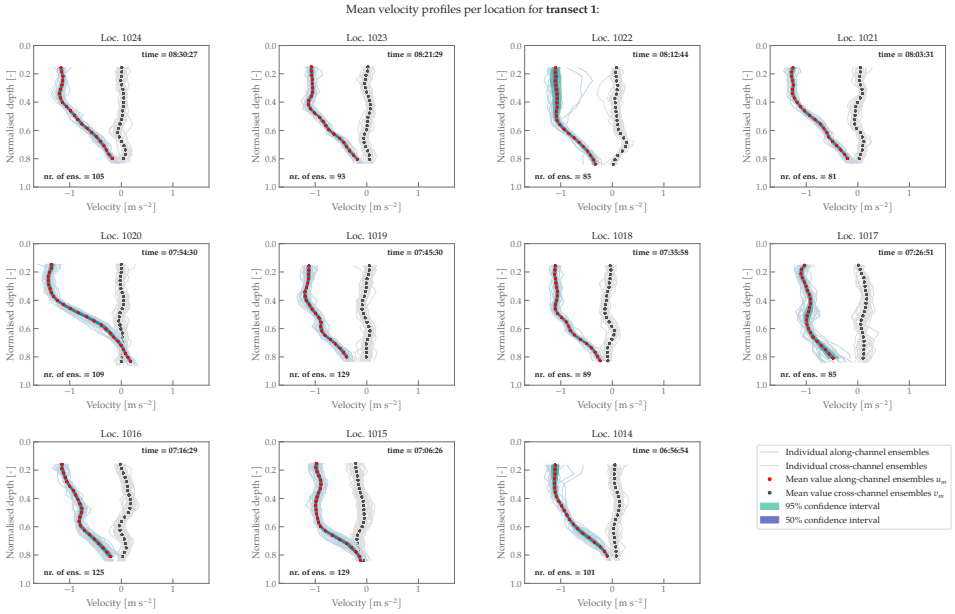

Figure A.4: Non-extrapolated stationary velocity profile ensembles for all measuring locations on the first transect of the August 13th measuring survey. Individual along-channel velocity ensembles are indicated in light blue, and cross-channel velocity ensembles are indicated in light grey. Red dots indicate the mean along-channel velocity in each ADCP bin. Black dots indicate mean cross-channel velocity in each bin.

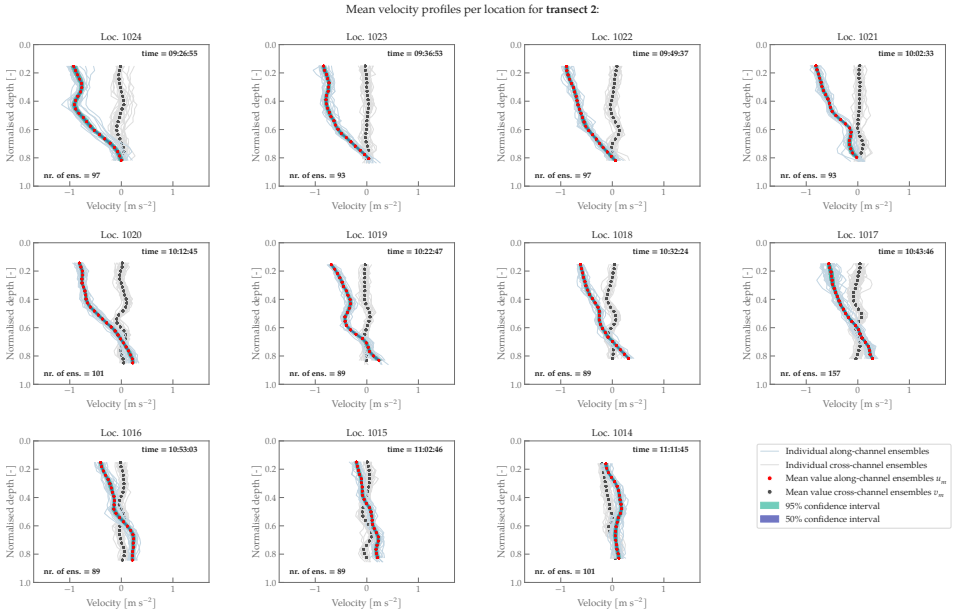

Figure A.5: Non-extrapolated stationary velocity profile ensembles for all measuring locations on the second transect of the August 13th measuring survey. Individual along-channel velocity ensembles are indicated in light blue, and cross-channel velocity ensembles are indicated in light grey. Red dots indicate the mean along-channel velocity in each ADCP bin. Black dots indicate mean cross-channel velocity in each bin.

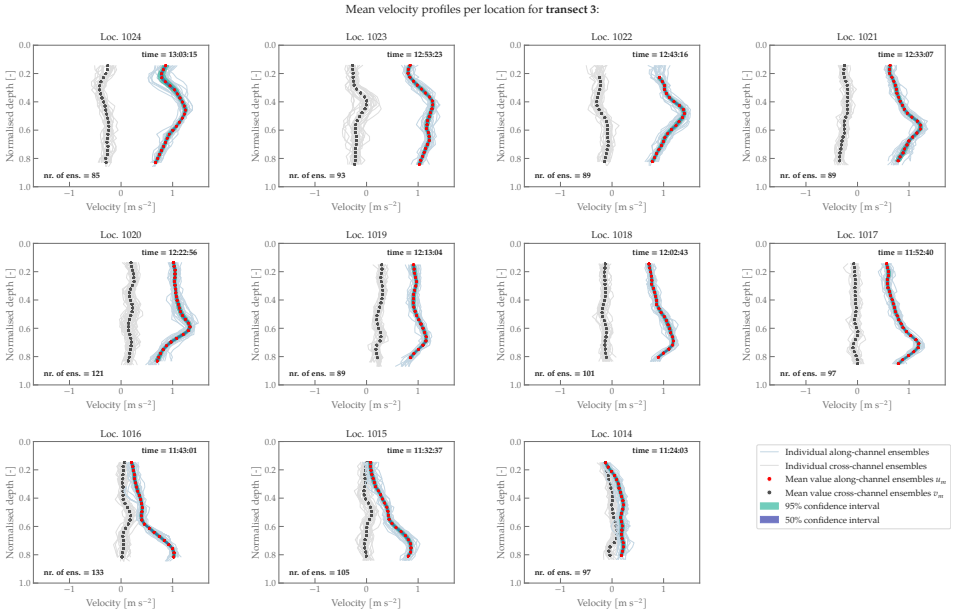

Figure A.6: Non-extrapolated stationary velocity profile ensembles for all measuring locations on the third transect of the August 13th measuring survey. Individual along-channel velocity ensembles are indicated in light blue, and cross-channel velocity ensembles are indicated in light grey. Red dots indicate the mean along-channel velocity in each ADCP bin. Black dots indicate mean cross-channel velocity in each bin.

A.3.2 Extrapolated velocity profiles

The velocity profiles in the along-channel coordinate system are interpolated and extrapolated according to the methods described in Chapter 4, Sections 4.2.3 and 4.2.4. This is done to be able to calculate the total Reynolds shear stress over the water column. The extrapolated and interpolated velocity profiles are depicted in Figs. A.7, A.8, and A.9.

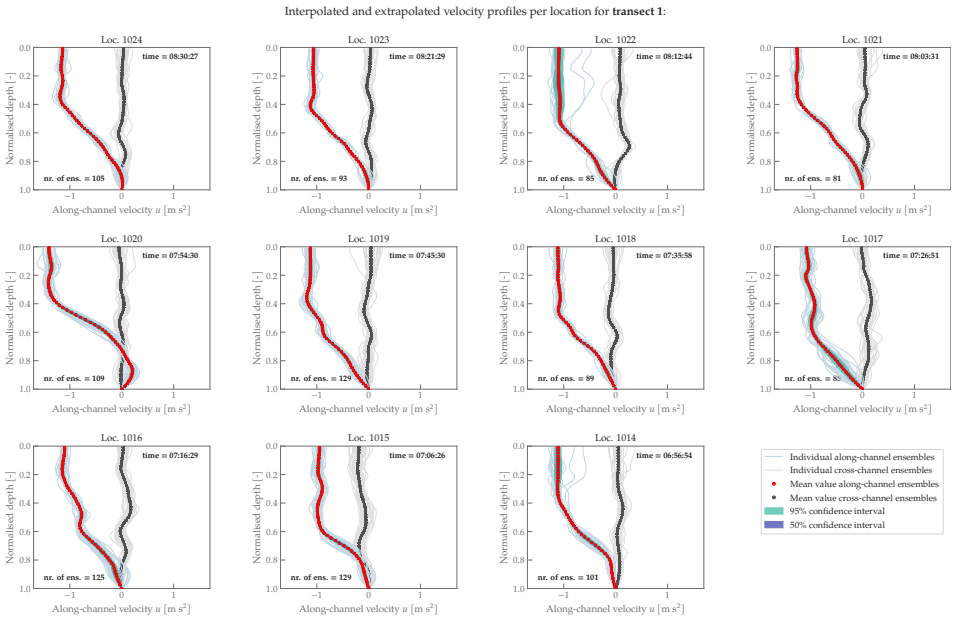

Figure A.7: Interpolated and extrapolated stationary velocity profile ensembles for all measuring locations on the first transect of the August 13th measuring survey. Individual along-channel velocity ensembles are indicated in light blue, and cross-channel velocity ensembles are indicated in light grey. Red dots indicate the mean along-channel velocity in each ADCP bin. Black dots indicate mean cross-channel velocity in each bin.

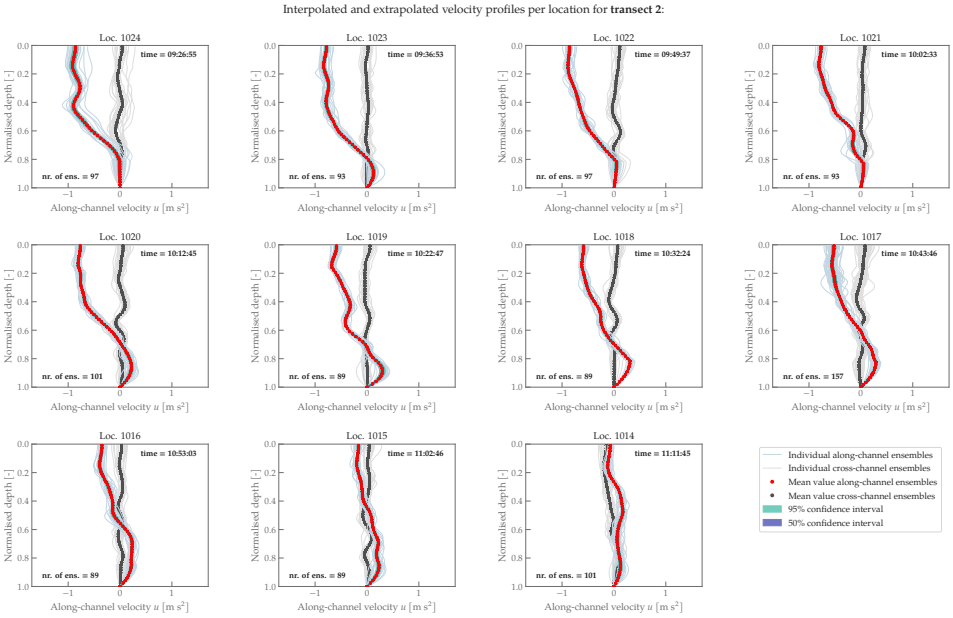

Figure A.8: Interpolated and extrapolated stationary velocity profile ensembles for all measuring locations on the second transect of the August 13th measuring survey. Individual along-channel velocity ensembles are indicated in light blue, and cross-channel velocity ensembles are indicated in light grey. Red dots indicate the mean along-channel velocity in each ADCP bin. Black dots indicate mean cross-channel velocity in each bin.

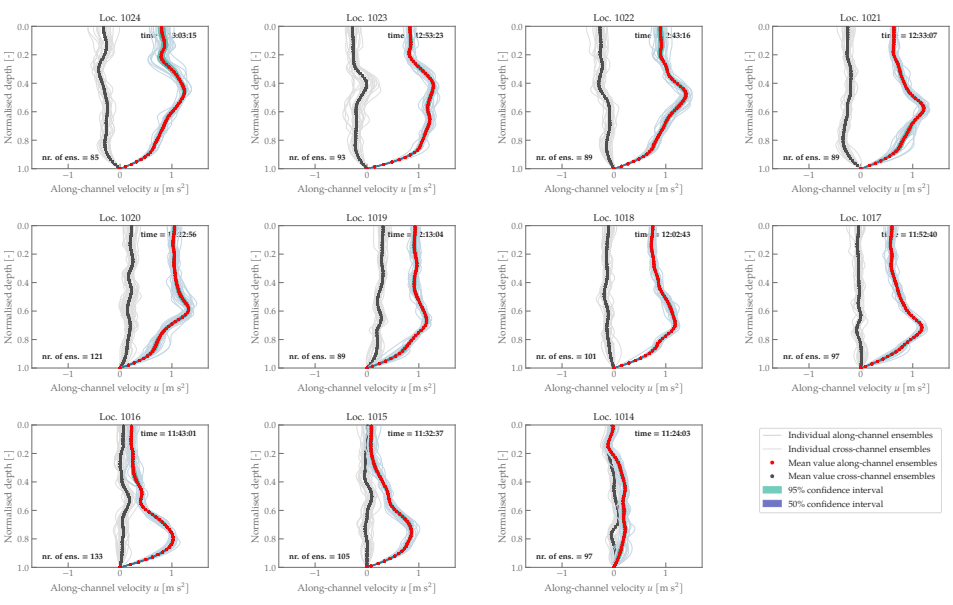

Figure A.9: Interpolated and extrapolated stationary velocity profile ensembles for all measuring locations on the third transect of the August 13th measuring survey. Individual along-channel velocity ensembles are indicated in light blue, and cross-channel velocity ensembles are indicated in light grey. Red dots indicate the mean along-channel velocity in each ADCP bin. Black dots indicate mean cross-channel velocity in each bin.

Appendix B

Supporting analyses

This appendix covers all analyses that support statements made in the core of the report. It covers all of the figures, tables and analyses that have been omitted in the main text for brevity. The first section, Section B.1, discusses the analysis of the internal wave modal structure, which is part of the data analysis presented in Chapter 6. The other two analyse,s presented in Sections B.2 and B.3, respectively, are related to the predictive capability analyses of the two hydrodynamic models—NSC-Fine and NSC-Coarse—in reproducing the observed hydrodynamics of the August 13th monitoring survey. Section B.2 presents and discusses the results of the velocity correlation calculations and visualisations. Then, Section B.3 covers the salinity correlation calculations for model runs with the NSC-Fine and NSC-Coarse model with increased vertical resolution.

B.1 Internal wave modal structure analysis

In Chapter 6, the results of a data analysis were presented, which focused on a dataset of a monitoring survey executed on August 13th, 2019. One of the analyses presented in Chapter 6 was an analysis of the internal Froude number. The analysis presented in the following section is an extension to this internal Froude number analysis, and provides insight into the evolution of the internal wave modal structure throughout the duration of the August 13th monitoring survey. It is omitted from the main text as it mainly provides background information.

The internal modes of a continuously stratified fluid are are associated with the displacement of the interface between fluids of different densities. We can find the modal structure of a continuously stratified fluid by solving the Taylor-Goldstein equation, which, together with boundary conditions imposed at the bottom and surface, form a Sturm-Liouville eigenvalue problem. This eigenvalue problem has an infinite number of solutions, corresponding to the eigenfunctions. These eigenfunctions are computed using the MATLAB® scripts written by Platell (2019). These functions solve the Taylor-Goldstein equation by first writing the problem as a *quadratic eigenvalue problem* (QEP), then linearising the QEP so a *general eigenvalue problem* (GEP) is obtained, and subsequently rewriting this GEP as a *standard eigenvalue problem* (SEP), so the problem can be solved using the built-in MATLAB® function `eigs`[1].

The results of this computation are presented in Figs. B.1, B.2, and B.3, as a function of the normalised depth. These figures also show the density distribution over the depth.

During ebb tide, the peak of the vertical velocity amplitude is located near the bottom of the channel. At most locations, this peak is very sharp, indicating that the vertical velocity amplitude is largest locally near the bottom. This region coincides with the region with lowest static and dynamic stability (*see* Fig. 6.4A). Outside of this region, the vertical velocity fluctuations are small. As the tide progresses into LWS, the peak of the vertical velocity amplitude shifts upwards in the water column. The peak also becomes less sharp, indicating that vertical velocity amplitude fluctuations are more widespread over the water column. During most of LWS, the peak remains located at the same depth in water column.

At the end of LWS, when the tide turns to the beginning of flood tide, the peak again shifts slightly further upwards in the water column. At first the modal structure exhibits a more round shape than before (*see* Fig. B.2, location 1024), but not long after, a sharper peak is again visible. This peak again remains visible

[1]More information regarding this function: `https://nl.mathworks.com/help/matlab/ref/eigs.html`

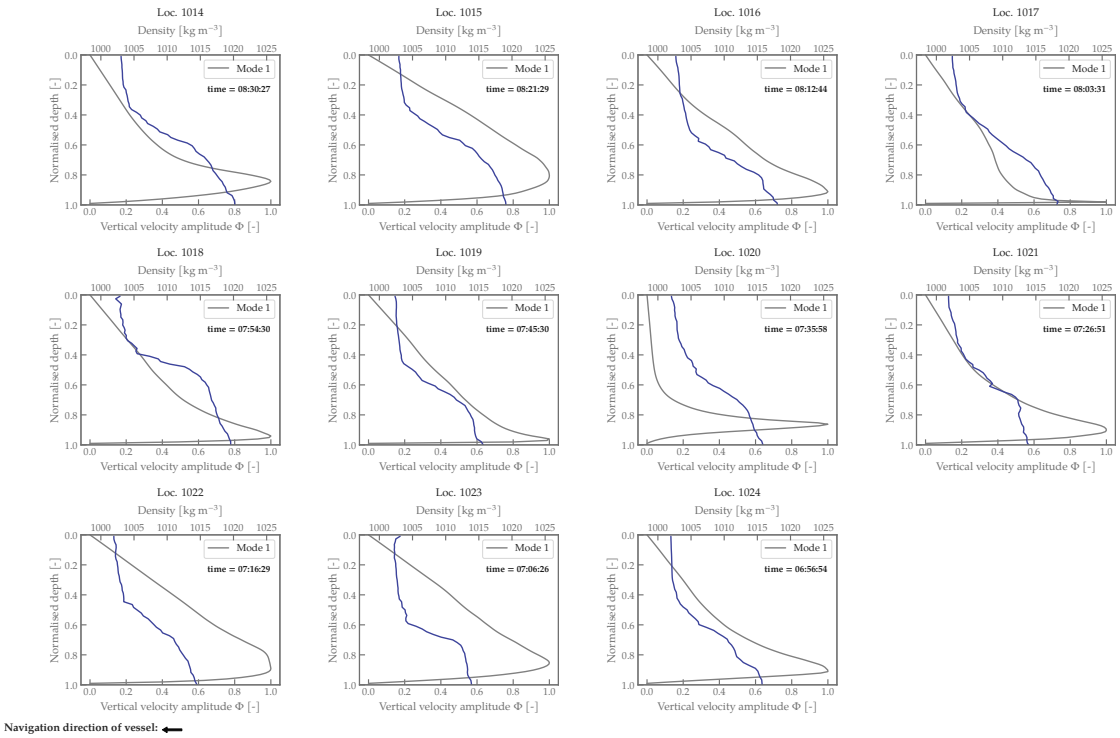

Figure B.1: Baroclinic modal structure as a function of the normalised depth per CTD vertical obtained whilst traversing the first transect. Indicated in gray is the modal structure, or the vertical velocity amplitude Φ, and indicated in green is the density profile at each location.

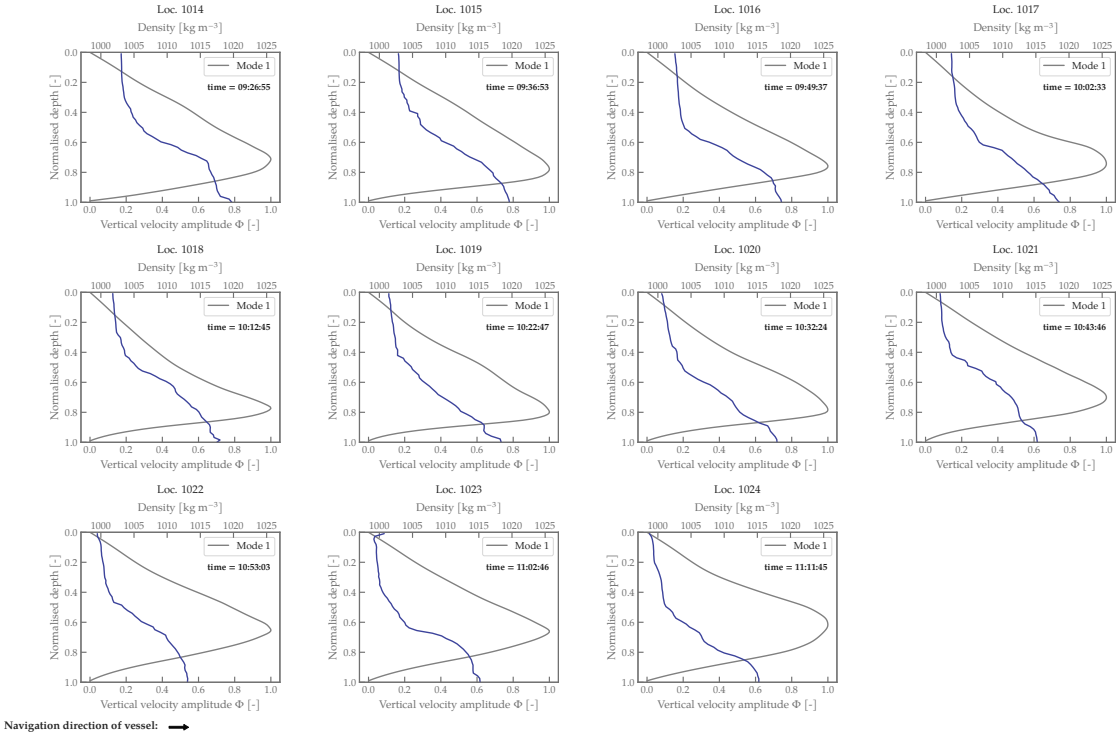

Figure B.2: Baroclinic modal structure as a function of the normalised depth per CTD vertical obtained whilst traversing the second transect. Indicated in gray is the modal structure, or the vertical velocity amplitude Φ, and indicated in green is the density profile at each location.

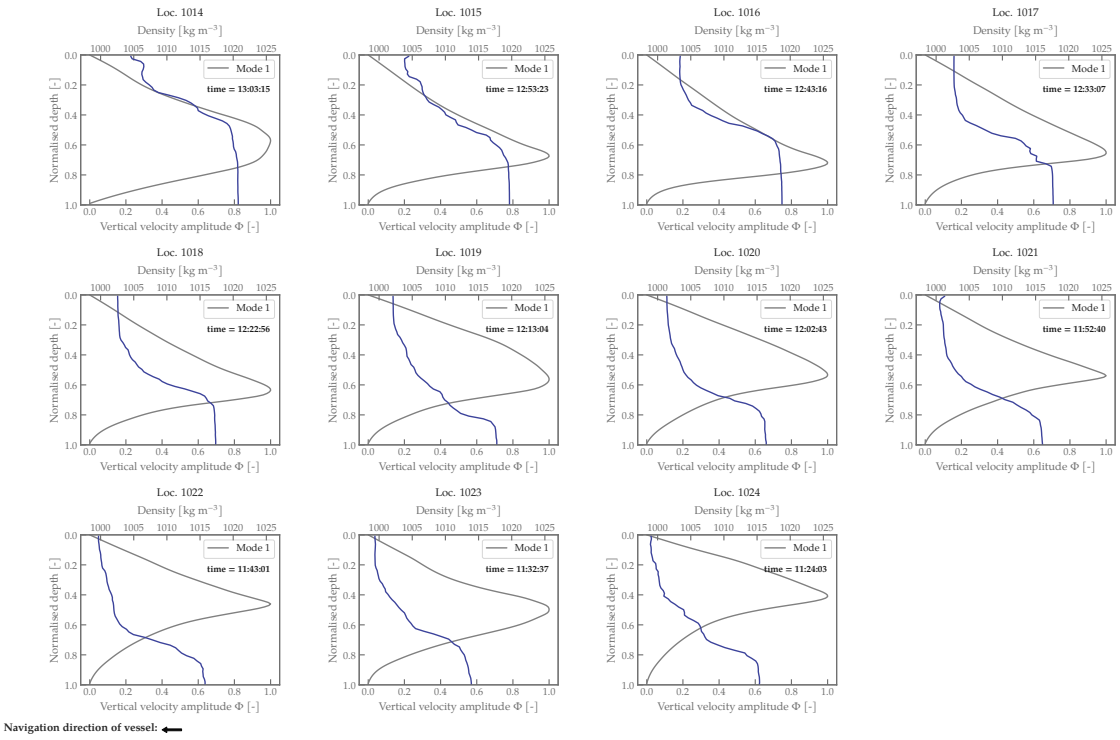

Figure B.3: Baroclinic modal structure as a function of the normalised depth per CTD vertical obtained whilst traversing the third transect. Indicated in gray is the modal structure, or the vertical velocity amplitude Φ, and indicated in green is the density profile at each location.

throughout the third transect, and seems to stay confined underneath the pycnocline. This indicates that turbulent motions are unable to penetrate the pycnocline, which is in line with the observations of the Richardson gradient number and squared Brunt-Vaïsalä frequency profiles discussed in Section 6.1.2.

B.2 Velocity correlation analysis

This section covers the analysis of the velocity correlation parameters calculated as part of the comparative validity study presented in Chapter 8. For this model comparison, the separate model runs are done wherein the output coordinates are based on the ADCP measurement coordinates per transect. There is a limitation of one output coordinate per grid cell, which means that, since the ADCP was continuously measuring, an output point is created at almost each grid cell in the along-channel direction. This means that more output points are created for the NSC-Fine model than for the NSC-Coarse model.

In the following sections, the results of the velocity difference and correlation computations are presented separately for each of the models, starting with the NSC-Fine model and then the NSC-Coarse model. Lastly, the outcome of these analyses, as well as a comparison between the performance of the NSC-Fine model and the NSC-Coarse model, is discussed in Section B.3.3.

NSC-Fine model correlation

The NSC-Fine model was assessed based on its capability to correctly predict the velocity structure on August 13th. For the analysis presented here, the differences between the model output and the measurements are calculated by subtracting the model output y_i from the measured values x_i. To correctly do so, both quantities are gridded onto the same 100 × 100 grid, in a similar manner as discussed in Chapter 4, Section 4.2.3. The results of the difference calculations are depicted in Fig. B.4. The qualitative results of the calculation of the correlation parameters are summarised in Table B.1.

As was already noted in Chapter 7, the modelled velocity seems to lag the velocities recorded by the ADCP

measurements. This can be deduced visually from Fig. B.4, as the velocity differences (*see* Fig. B.4, lower panels) are found to be primarily negative over the largest part of the considered domain and during all measured transects.

Looking at the calculated correlation values (*see* Table B.1), it is found that the index of agreement ranges between 0.54 and $d_f = 0.98$. These extreme values are both found during ebb tidal conditions. Interestingly, the smallest index of agreements do not occur near the location where the wrong bathymetry is observed (*see* Ch. 7, Sec. 7.1). The indexes of agreement are highest under ebb tidal conditions. As the tide progresses into LWS, the indexes of agreement, as well as the R^2-score, decrease slightly.

The correlation parameters summarised in Table B.1 reveal that the NSC-Fine model has most difficulties reproducing the velocity structure during the third transect, which is representative of the beginning of flood. This is indicated by the relatively low values of the index of agreement ($0.55 < d_f < 0.85$) and negative R^2-scores. This is interesting, because it has previously been shown in Chapter 8 that the NSC-Fine model seems to reproduce the salinity structure relatively well throughout this phase of the tide. It is hypothesised here that, since the pycnocline height is not well reproduced by the NSC-Fine model, the height at which mid-depth jets occur is shifted, giving deviating values of the velocity around the pycnocline height.

NSC-Coarse model correlation

Results of the velocity correlation analysis for the NSC-Coarse model are visualised in Figure B.5 and summarised quantitatively in Table B.1.

Again, the model's velocity prediction seems to lag the measurements. From the contour plots of the difference between model output and measurements, depicted in Fig. B.5, this is not as clearly visible as from the direct output plots shown in Chapter 7, Fig. 7.3, since the difference between measured and

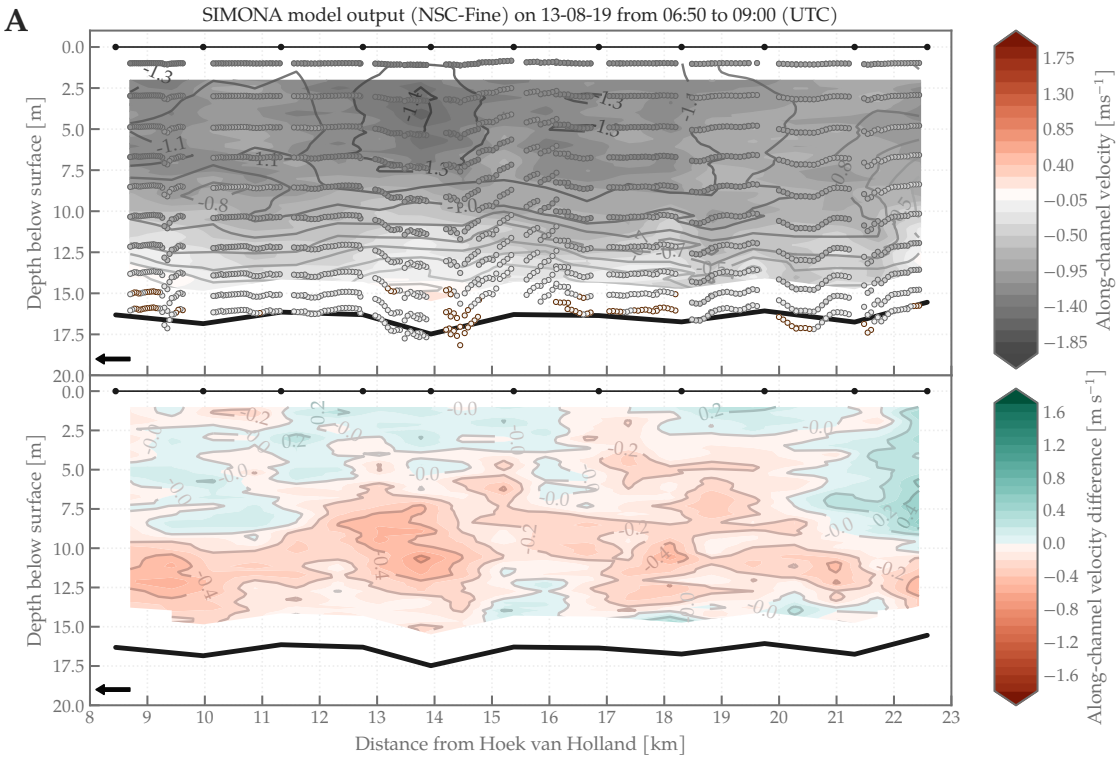

Figure B.4: Overview of the calculated velocity difference between model output y_i and measurements x_i for the NSC-Fine model. The model output is visualised by the individual dots and contour lines in the upper panels, a dot indicating an output point. The actual velocity distribution is plotted as a contour behind these dots. The difference between model and measurement is indicated in the bottom part of the figure, green indicating an overprediction of the model and red indicating an underprediction of the model. Arrows in the bottom left corner indicate the navigation direction of the vessel.

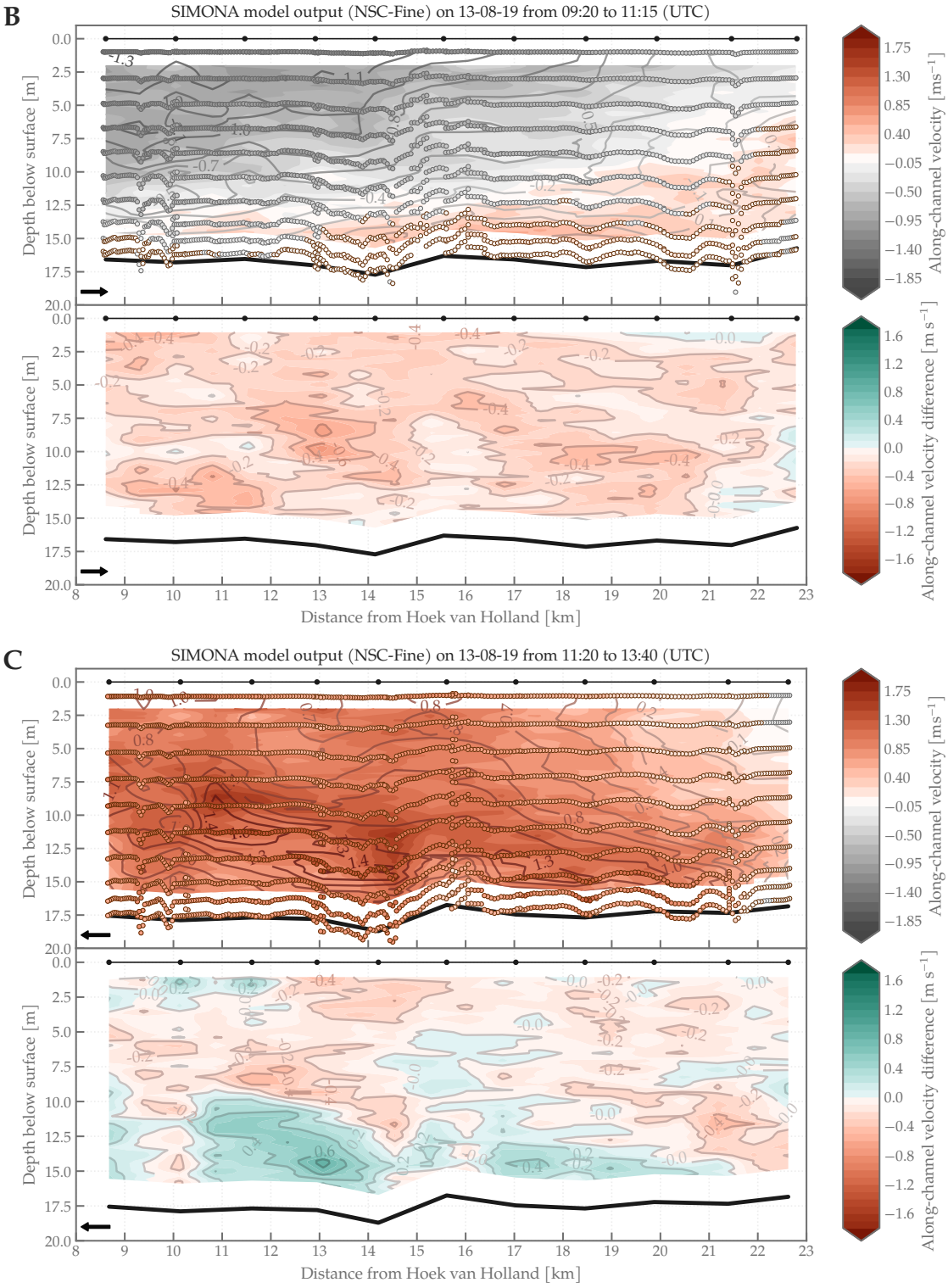

Figure B.4: *(Continued)*

modelled velocity is not consistently negative nor consistently positive during all transects. There also does not seem to be a decoupling between the bottom and top parts of the water column. Nevertheless, the calculated differences during the second transect do reveal that under LWS conditions, the velocity differences are mainly negative, indicating that LWS may not be reproduced well. This may entail that the

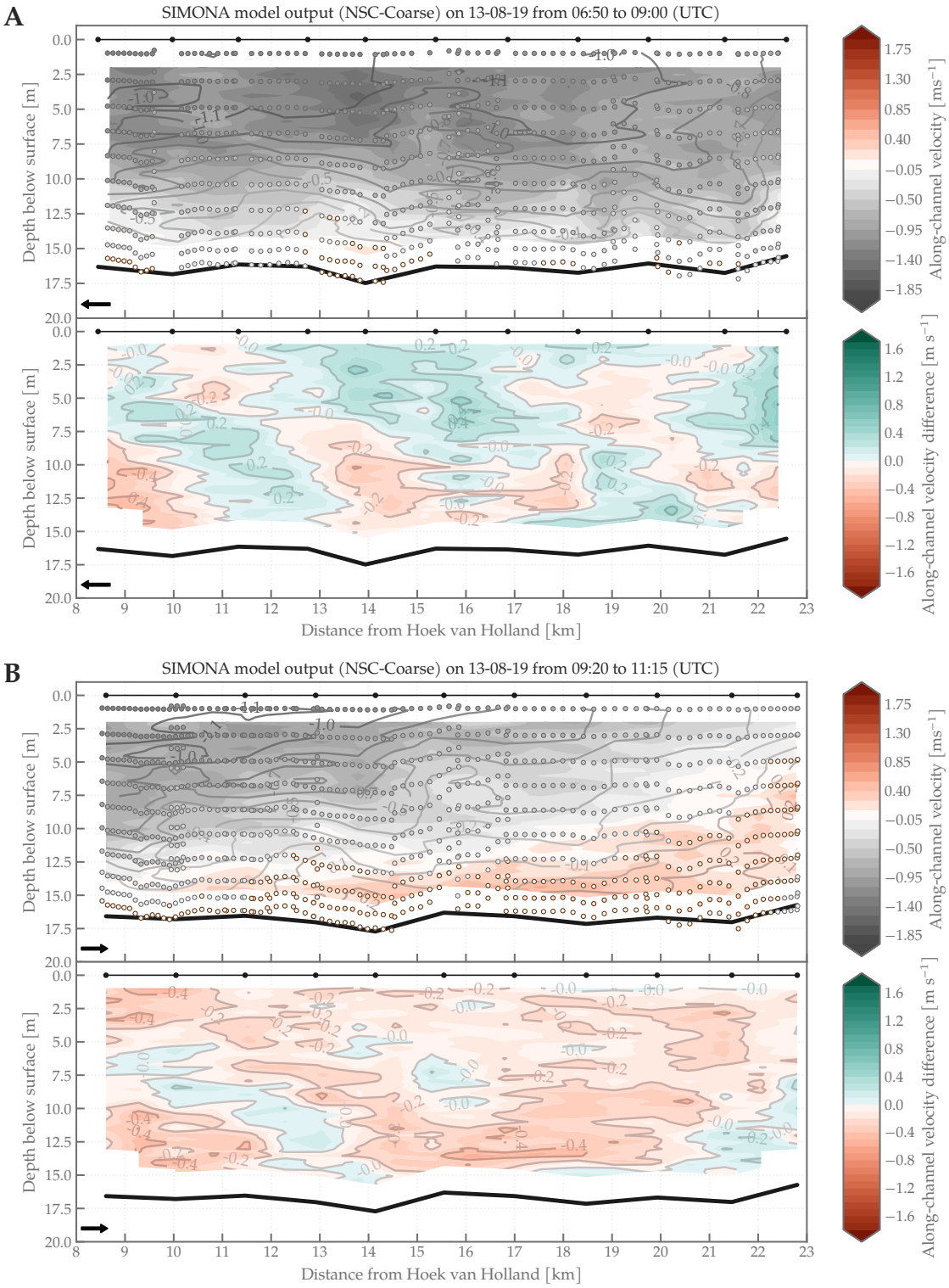

Figure B.5: Overview of the calculated velocity difference between model output y_i and measurements x_i for the NSC-Coarse model. The model output is visualised by the individual dots and contour lines in the upper panels, a dot indicating an output point. The actual velocity distribution is plotted as a contour behind these dots. The difference between model and measurement is indicated in the bottom part of the figure, green indicating an overprediction of the model and red indicating an underprediction of the model. Arrows in the bottom left corner indicate the navigation direction of the vessel.

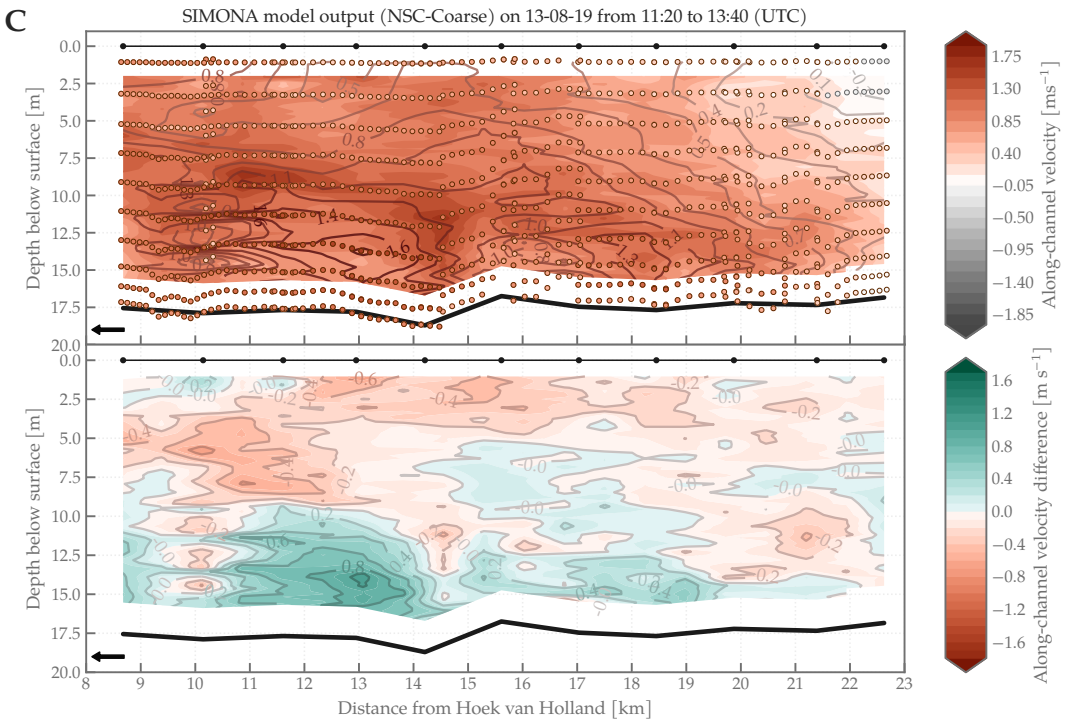

Figure B.5: *(Continued)*

LWS period is modelled to last longer or that LWS sets in later in the model compared to measurements.

Seemingly in contrast with the observation of predominantly negative velocity differences during LWS, the calculated correlation parameters (*see* Table B.1) indicate that the model actually reproduces the velocity structure best during LWS—the correlation parameters calculated from the second transect are, on average, higher than the correlation parameters calculated for every other transect. Similarly to the outcome of this computation based on the NSC-Fine model output, the correlation parameters indicate that the model does not perform well in predicting the velocity structure during the beginning of flood, where the index of agreement ranges between $d_c = 0.28$ and $d_c = 0.92$, and the R^2-scores are negative for most of the third transect.

Discussion

Together with the qualitative comparisons of the velocity output to actual velocity measurements (*see* Chapter 7), the quantitative results and difference visualisation presented here give insight into the ability of the NSC-Fine and NSC-Coarse model to predict the velocity structure.

Both the qualitative comparisons and the quantitative comparisons—of both NSC-models—show that a phase lag seems to be introduced in the model that delays the onset of LWS. Unfortunately, this possible phase lag cannot be quantified. Velocity measuring stations are only sparsely located along the Rhine tributaries, and are located at a considerable distance from the domain of the August 13th monitoring survey. Therefore, any cross-correlation calculations that could have been executed on these time series, would not give an accurate representation of the phase lag estimate locally. These cross-correlation calculations are therefore not within the scope of this thesis.

Both NSC-models have most difficulties reproducing the flood tide velocities and perform best in reproducing the velocities during LWS. It is hypothesised that the model has difficulties reproducing the velocities during flood tide because the pycnocline height is not reproduced well, which in turn leads to the misrepresentation of the mid-depth jets. It is explained in Chapter 8 that the misrepresentation of the pycnocline height may be related to the limited vertical resolution of the NSC-models.

Furthermore, in contrast with the outcome of the comparative model validity study presented in Chapter 8,

Table B.1: Overview of correlation parameters between along-channel velocity model output and measurements of August 13th, 2019. The last column tests the hypothesis that the NSC-Fine model outperforms the NSC-Coarse model. A green dot (●) indicates that the NSC-Fine model generally performs better based on the correlation parameters, whereas a red dot (●) indicates that the NSC-Coarse model performs better. An empty dot (○) indicates that the models perform identically, based on the correlation parameters.

			Fine			Coarse		F > C
Name	**Time [UTC]**	**d** [-]	**MAE** [m s^{-1}]	**R^2** [-]	**d** [-]	**MAE** [m s^{-1}]	**R^2** [-]	
First transect								
1014	06:56:54	0.72	0.35	0.27	0.74	0.30	0.39	●
1015	07:06:26	0.94	0.15	0.82	0.91	0.21	0.69	●
1016	07:16:29	0.92	0.14	0.56	0.83	0.20	-0.03	●
1017	07:26:51	0.54	0.45	-7.73	0.59	0.31	-3.97	●
1018	07:35:58	0.95	0.15	0.79	0.95	0.14	0.85	●
1019	07:45:30	0.95	0.17	0.70	0.84	0.24	0.38	●
1020	07:54:30	0.97	0.19	0.89	0.95	0.22	0.85	●
1021	08:03:31	0.98	0.10	0.93	0.95	0.19	0.80	●
1022	08:12:44	0.93	0.15	0.65	0.91	0.18	0.48	●
1023	08:21:29	0.95	0.14	0.83	0.94	0.17	0.80	●
1024	08:30:27	0.97	0.14	0.88	0.98	0.11	0.93	●
Second transect								
1024	09:26:55	0.92	0.22	0.61	0.95	0.16	0.80	●
1023	09:36:53	0.82	0.32	0.14	0.90	0.24	0.57	●
1022	09:49:37	0.92	0.22	0.65	0.95	0.15	0.79	●
1021	10:02:33	0.91	0.20	0.58	0.97	0.12	0.85	●
1020	10:12:45	0.94	0.21	0.73	0.98	0.08	0.93	●
1019	10:22:47	0.90	0.24	0.61	0.90	0.11	0.61	●
1018	10:32:24	0.89	0.24	0.51	0.89	0.21	0.63	●
1017	10:43:46	0.84	0.28	0.27	0.90	0.19	0.63	●
1016	10:53:03	0.87	0.16	0.53	0.96	0.09	0.84	●
1015	11:02:46	0.81	0.13	-0.32	0.91	0.10	0.32	●
1014	11:11:45	0.66	0.13	-0.04	0.91	0.07	0.63	●
Third transect								
1014	11:24:03	0.68	0.15	-0.39	0.77	0.13	0.00	●
1015	11:32:37	0.82	0.20	0.57	0.83	0.20	0.61	●
1016	11:43:01	0.96	0.11	0.86	0.92	0.13	0.74	●
1017	11:52:40	0.68	0.17	-2.19	0.66	0.22	-2.78	●
1018	12:02:43	0.64	0.19	-0.99	0.70	0.17	-0.92	●
1019	12:13:04	0.67	0.14	-0.34	0.28	0.21	-6.20	●
1020	12:22:56	0.63	0.24	-0.04	0.29	0.44	-3.13	●
1021	12:33:07	0.55	0.17	-4.96	0.34	0.37	-13.05	●
1022	12:43:16	0.64	0.22	-0.18	0.28	0.40	-2.61	●
1023	12:53:23	0.63	0.17	-0.58	0.73	0.18	-1.17	●
1024	13:03:15	0.85	0.14	0.66	0.46	0.27	-0.23	●

the NSC-Fine model does not always outperform the NSC-Coarse model in predicting the velocity distribution over the vertical. During LWS, the NSC-Coarse model actually consistently outperforms the NSC-Fine model. During the first transect—representative of ebb tide—and the third transect—representative of the beginning of flood—the NSC-Fine model still generally outperforms the NSC-Coarse model.

B.3 Increased vertical resolution predictive capability

From Chapters 7 and 8, it is found that the salinity structure over the vertical is reproduced relatively well. Contrastingly, it is also found that the pycnocline height cannot be reproduced adequately. Several recommendations are given that may improve the capability of the models to reproduce the pycnocline height. One of these recommendations is related to increasing the vertical resolution of the models. This recommendation is explored in this additional analysis. To do so, the amount of vertical layers is increased to 30. The new layer distribution, and its relation to vertical distribution of the 10-layer model, is given in Table B.2.

It is accented here that the analysis presented here is only a preliminary analysis. Therefore, it is cho-

sen to omit the phase shift analysis and only cover the correlation analysis between model output and measurements of the August 13th monitoring survey. Furthermore, for brevity, the model output of the 30-layer NSC-models is not discussed separately—only the correlation parameters and the model difference visualisations are shown. First, the outcome of the correlation for the NSC-Fine model with 30 vertical layers is covered in Section B.3.1, after which Section B.3.2 covers the results of the 30-layer NSC-Coarse model. Finally, Section B.3.3 discusses the results and compares the NSC-Fine model output to the NSC-Coarse model output.

10-layer models		30-layer models	
σ-layer [#]	**Layer thickness [%]**	**σ-layer [#]**	**Layer thickness [%]**
1	12%	1 – 3	4.00% / 4.00% / 4.00%
2	12%	4 – 6	4.00% / 4.00% / 4.00%
3	11%	7 – 9	3.67% / 3.66% / 3.67%
4	11%	10 – 12	3.67% / 3.66% / 3.67%
5	11%	13 – 15	3.67% / 3.66% / 3.67%
6	11%	16 – 18	3.67% / 3.66% / 3.67%
7	11%	19 – 21	3.67% / 3.66% / 3.67%
8	9%	22 – 24	3.00% / 3.00% / 3.00%
9	6%	25 – 27	2.00% / 2.00% / 2.00%
10	6%	28 – 30	2.00% / 2.00% / 2.00%

Table B.2: Layer thickness distributions of the NSC-Coarse and NSC-Fine models. Left side of the table indicates the layer distribution of the originally assessed 10-layer models and the right side of the table shows the layer distribution of the associated 30-layer version of the models.

B.3.1 NSC-Fine model correlation

A similar comparison between salinity output and measurements as is presented in Figs. 8.7 and 8.8 is also done for the 30-layer version of the NSC-models. The results of the salinity difference calculation for the 30-layer NSC-Fine model are presented in Fig. B.6.

Comparing the outcome of the salinity difference calculation of the 30-layer NSC-Fine model (*see* Fig. B.6) with the related 10-layer NSC-Fine model comparison figure (*see* Fig. 8.7), it is observed that the 30-layer NSC-Fine model predicts higher salinities around the pycnocline height than the 10-layer NSC-Fine model does. The salt wedge also seems to penetrate further inward in the 30-layer NSC-Fine model output than the 10-layer NSC-Fine model output, at all measured transects. These observations together may indicate that baroclinic effects are enhanced compared to the 10-layer model output.

Looking at the quantitative comparison, however, it is found that the 30-layer NSC-Fine model actually does not perform better than the 10-layer variant during all phases of the tide. Comparing the correlation parameters calculated from the 30-layer model and the 10-layer model, the 30-layer model is actually found to have a decreased performance at certain verticals during ebb tide and LWS.

B.3.2 NSC-Coarse model correlation

An analysis of the correlation between NSC-Coarse model salinity output and salinity measurements is repeated for an increased vertical resolution. The results, visualised as contour plots of the difference between model and measurements, are shown in Fig. B.7.

Generally, the 30-layer NSC-Coarse model underpredicts salinities underneath the pycnocline. This is true during all measured parts of the tidal cycle. Compared to the NSC-Coarse model with 10 vertical σ-layers, the 30-layer version of the model generally predicts slightly higher salinities underneath the actual pycnocline. Nevertheless, the pycnocline height is still not well resolved. The increased vertical resolution leads to a stronger pycnocline, but the predicted pycnocline is located just above the bed during most transects. This may indicate that the salt intrusion length is still not reproduced well. The rest of the water column has a similar structure as the 10-layer variant of the model.

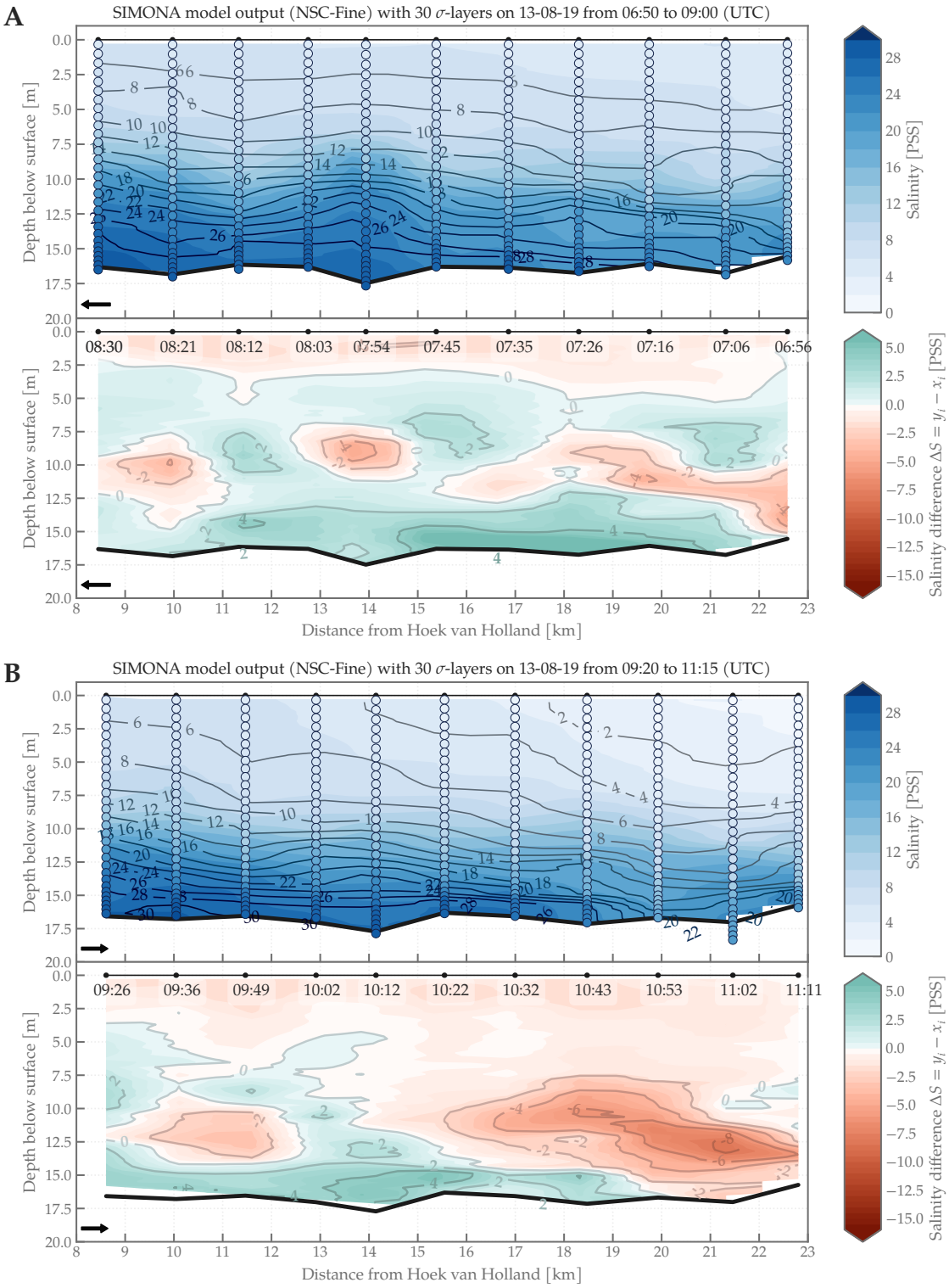

Figure B.6: Overview of the calculated velocity difference between model output y_i and measurements x_i for the NSC-Fine model with 30 vertical layers. The model output is visualised by the individual dots and contour lines in the upper panels, a dot indicating an output point. The actual velocity distribution is plotted as a contour behind these dots. The difference between model and measurement is indicated in the bottom part of the figure, green indicating an overprediction of the model and red indicating an underprediction of the model. Arrows in the bottom left corner indicate the navigation direction of the vessel.

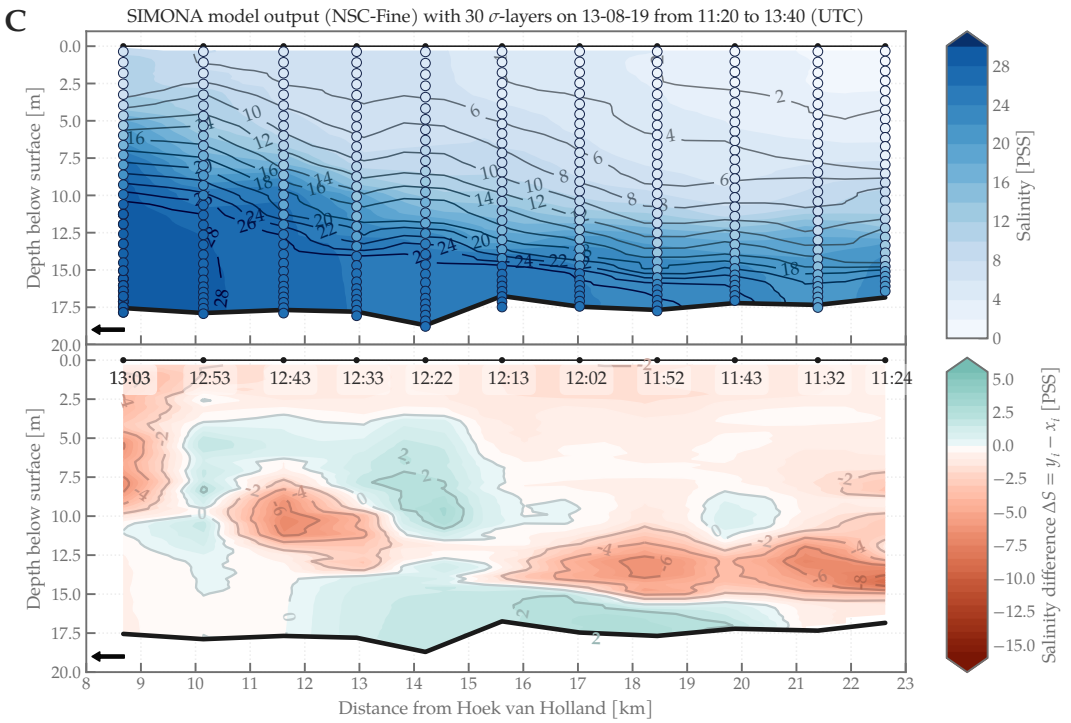

Figure B.6: *(Continued)*

B.3.3 Discussion

The effect of the increased amount of vertical σ-layers is therefore mainly visible from the increased salinities near the bed. This effect is reflected by the results of the quantitative correlation calculation (*see* Table B.3), which shows overall higher values of the index of agreement and R^2-score at all measured locations and throughout all measured transects.

The model still reproduces the vertical distribution of the salinity best during the first transect (ebb tide). At certain measured locations, the NSC-Coarse 30-layer model even outperforms the NSC-Fine 30-layer model, although the NSC-Coarse 30-layer model does not outperform the NSC-Fine 10-layer model in any case.

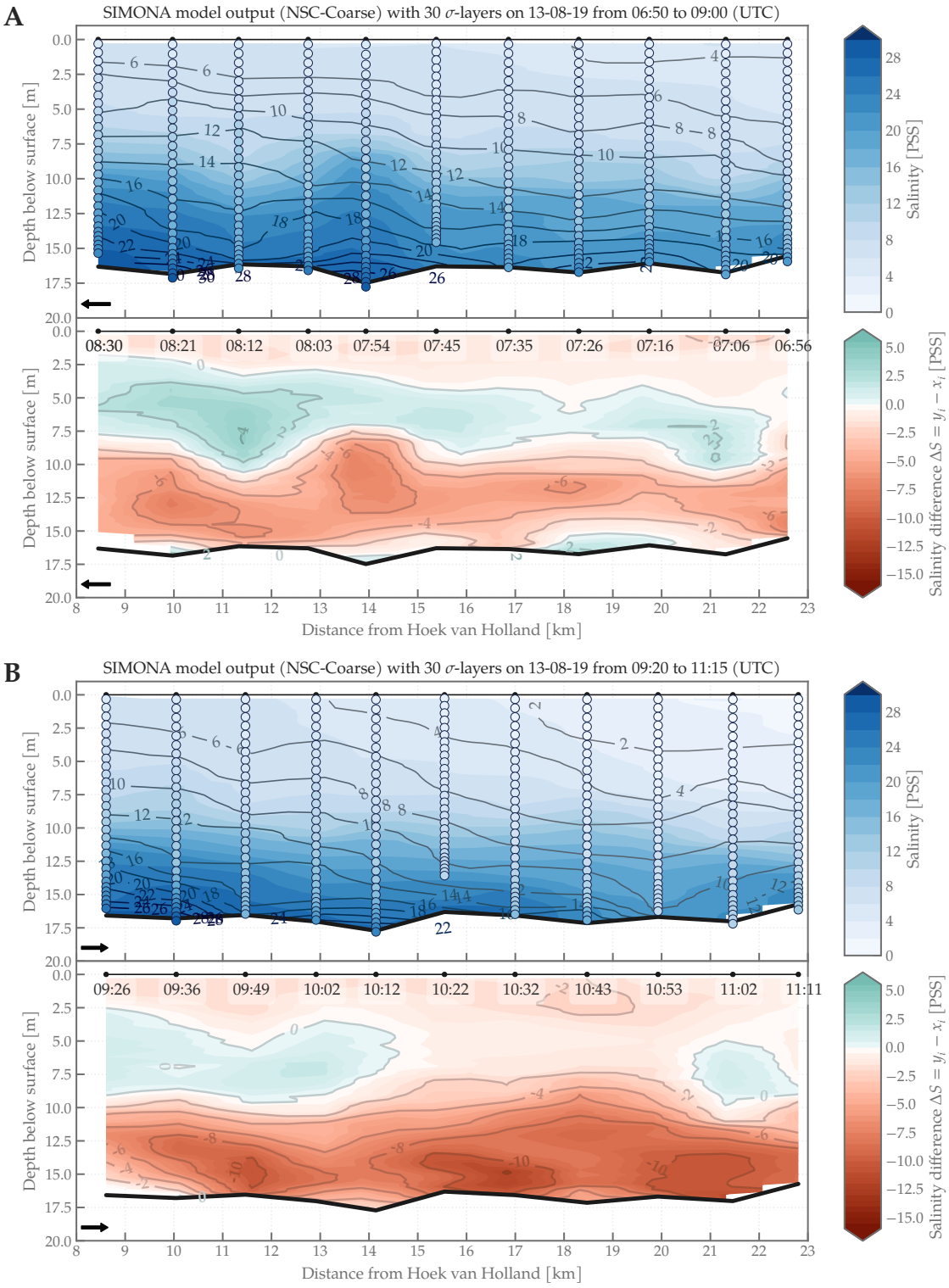

Figure B.7: Overview of the calculated velocity difference between model output y_i and measurements x_i for the NSC-Coarse model with 30 vertical layers. The model output is visualised by the individual dots and contour lines in the upper panels, a dot indicating an output point. The actual velocity distribution is plotted as a contour behind these dots. The difference between model and measurement is indicated in the bottom part of the figure, green indicating an overprediction of the model and red indicating an underprediction of the model. Arrows in the bottom left corner indicate the navigation direction of the vessel.

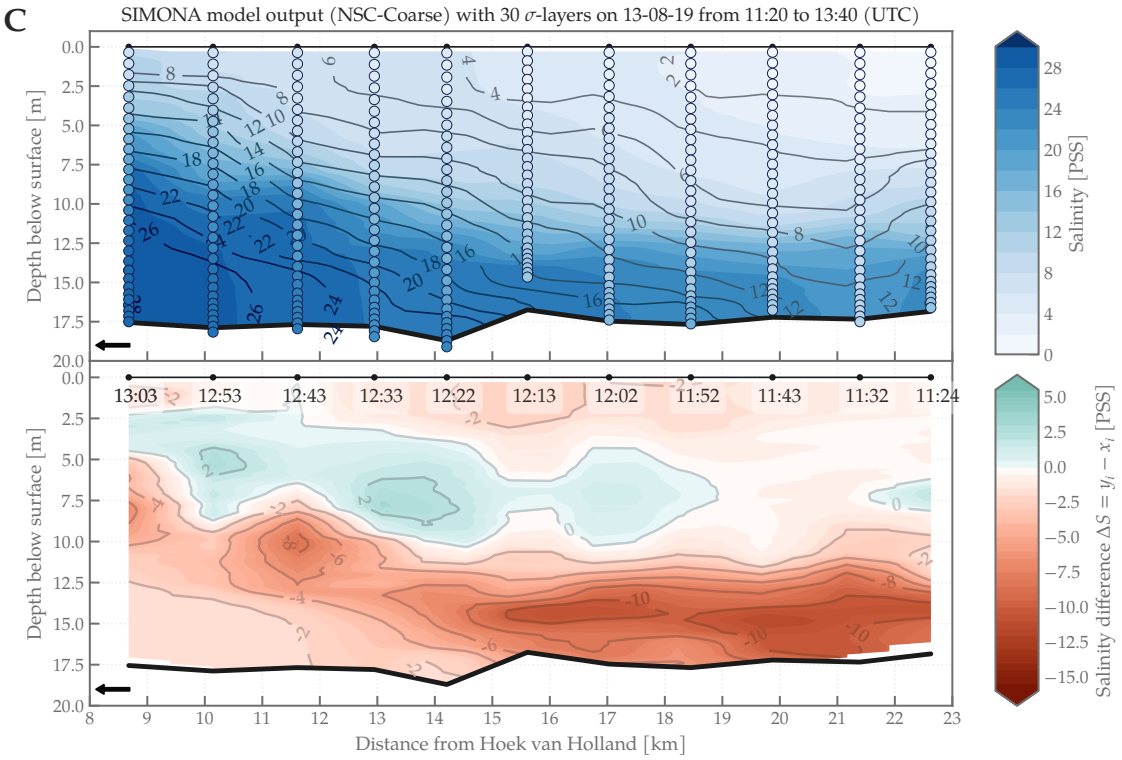

Figure B.7: *(Continued)*

Table B.3: Overview of correlation parameters between model output and measurements of August 13th, 2019. Correlation parameters were calculated from the output of the 30-layer NSC-models. The last column tests the hypothesis that the NSC-Fine model outperforms the NSC-Coarse model. A green dot (●) indicates that the NSC-Fine model generally performs better based on the correlation parameters, whereas a red dot (●) indicates that the NSC-Coarse model performs better. An empty dot (◦) indicates that the models perform identically, based on the correlation parameters. Green triangles (▲) indicate that the 30-layer version of the model performs better based on the correlation parameters than the 10-layer version, and, vice versa, a red triangle (▼) indicates that the 10-layer model outperforms the 30-layer version of the model.

First transect										
		Fine				**Coarse**				**F > C**
Name	**Time [UTC]**	**d** [-]	**MAE** [PSS]	**R^2** [-]		**d** [-]	**MAE** [PSS]	**R^2** [-]		
1014	06:56:54	0.96	1.78	0.88	▲	0.90	3.05	0.69	▲	●
1015	07:06:26	0.97	1.96	0.87	▼	0.95	2.14	0.84	▲	●
1016	07:16:29	0.96	2.04	0.82	▼	0.97	1.60	0.89	▲	●
1017	07:26:51	0.94	2.49	0.66	▼	0.95	1.89	0.80	▲	●
1018	07:35:58	0.97	1.98	0.84	▼	0.94	2.34	0.80	▲	●
1019	07:45:30	0.96	2.36	0.80	▼	0.91	2.59	0.74	▲	●
1020	07:54:30	0.98	1.89	0.92	▲	0.92	3.67	0.69	▲	●
1021	08:03:31	0.99	1.42	0.95	▲	0.94	2.72	0.83	▲	●
1022	08:12:44	0.98	1.78	0.92	▲	0.89	3.56	0.72	▲	●
1023	08:21:29	0.99	1.35	0.96	▲	0.93	3.31	0.76	▲	●
1024	08:30:27	1.00	1.02	0.98	▲	0.94	2.88	0.83	▲	●
Second transect										
1024	09:26:55	0.99	1.54	0.95	▲	0.96	2.25	0.87	▲	●
1023	09:36:53	0.99	1.39	0.96	▲	0.93	3.05	0.75	▲	●
1022	09:49:37	0.98	1.90	0.92	▲	0.78	4.44	0.46	▲	●
1021	10:02:33	0.99	0.94	0.97	▲	0.89	3.09	0.71	▲	●
1020	10:12:45	0.98	1.77	0.91	▼	0.91	3.12	0.71	▲	●
1019	10:22:47	0.99	1.72	0.93	▲	0.71	3.54	0.23	▲	●
1018	10:32:24	0.98	1.81	0.92	▲	0.75	5.32	0.29	▲	●
1017	10:43:46	0.96	2.76	0.80	▲	0.82	5.00	0.35	▲	●
1016	10:53:03	0.91	3.19	0.68	▲	0.72	5.25	0.11	▲	●
1015	11:02:46	0.95	2.78	0.81	▲	0.75	4.77	0.39	▲	●
1014	11:11:45	0.97	1.56	0.91	▲	0.85	3.55	0.61	▲	●
Third transect										
1014	11:24:03	0.96	2.35	0.85	▲	0.84	3.72	0.58	▲	●
1015	11:32:37	0.96	2.19	0.85	▲	0.73	5.03	0.26	▲	●
1016	11:43:01	0.99	1.12	0.97	▲	0.76	4.18	0.42	▲	●
1017	11:52:40	0.97	2.43	0.87	▲	0.86	4.01	0.60	▲	●
1018	12:02:43	0.98	1.66	0.93	▲	0.80	4.23	0.51	▲	●
1019	12:13:04	0.99	1.12	0.97	▲	0.83	3.18	0.52	▲	●
1020	12:22:56	0.99	1.79	0.94	▲	0.94	2.79	0.82	▲	●
1021	12:33:07	0.99	1.59	0.94	▲	0.96	2.78	0.87	▲	●
1022	12:43:16	0.97	1.59	0.90	▲	0.94	2.86	0.78	▲	●
1023	12:53:23	1.00	0.78	0.98	▲	0.98	1.79	0.93	▲	●
1024	13:03:15	0.97	1.66	0.83	▲	0.95	2.64	0.82	▲	●

Appendix C

Supporting figures

C.1 Internal flow structure survey

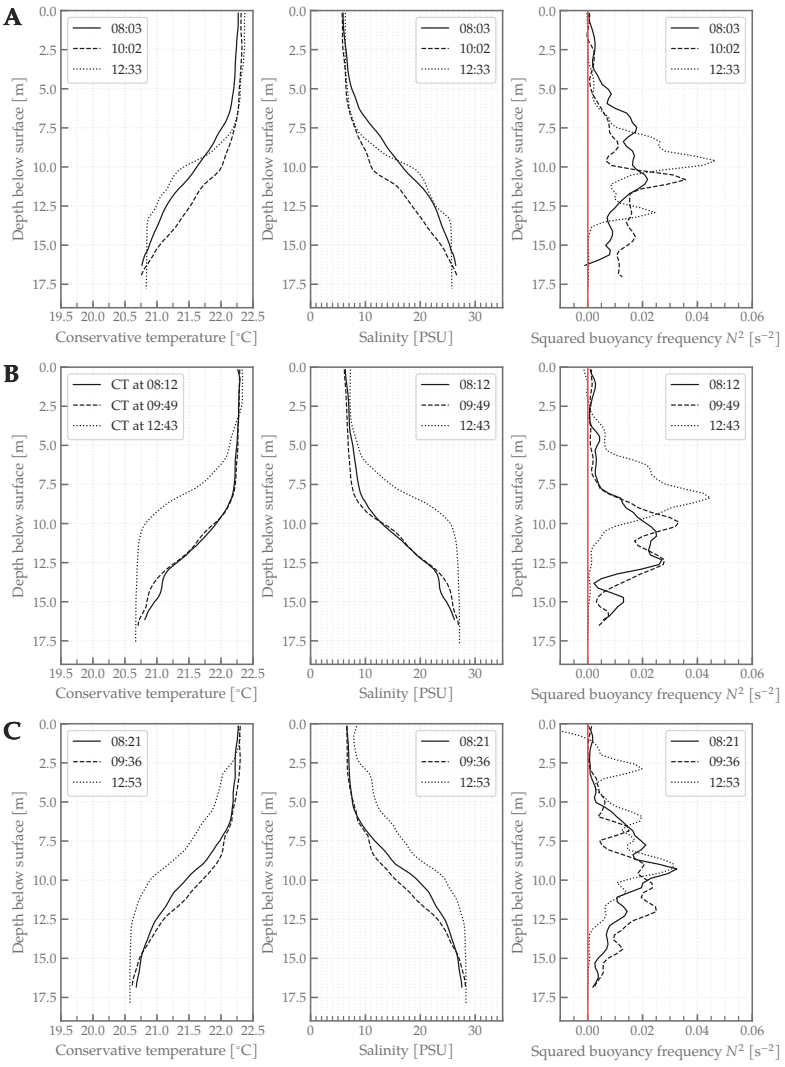

Figure C.1: Profiles of the conservative temperature CT [°C], salinity (PSU) and the squared buoyancy frequency $N^2(z)$ [s^{-2}] for locations 1021 (**A**), 1023 (**B**) and 1030 (**C**). Roughly, the line vertical is representative for ebb tide conditions, the dashed vertical is indicative for slack tide conditions and the dotted vertical is indicative of flood tide conditions. Indicated with the red line in the right-hand figures is the stability criterion $N^2 < 0$. For the calculations of the conservative temperature CT use was made of TEOS-10.

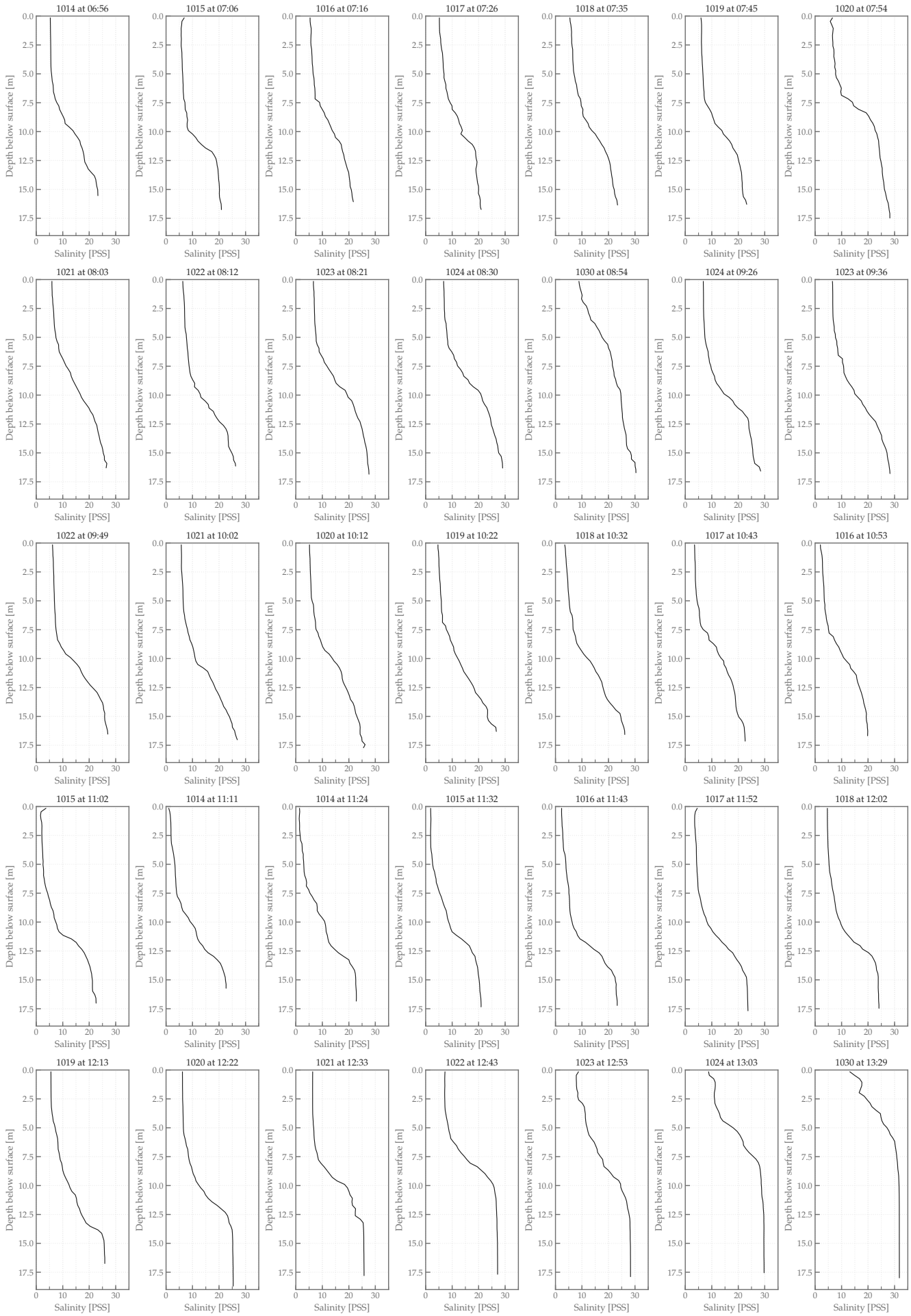

Figure C.2: Overview of the raw salinity profiles at all CTD measuring locations during the internal flow structure survey on August 13th, 2019. From left to right and top to bottom, subplots are in chronological order.

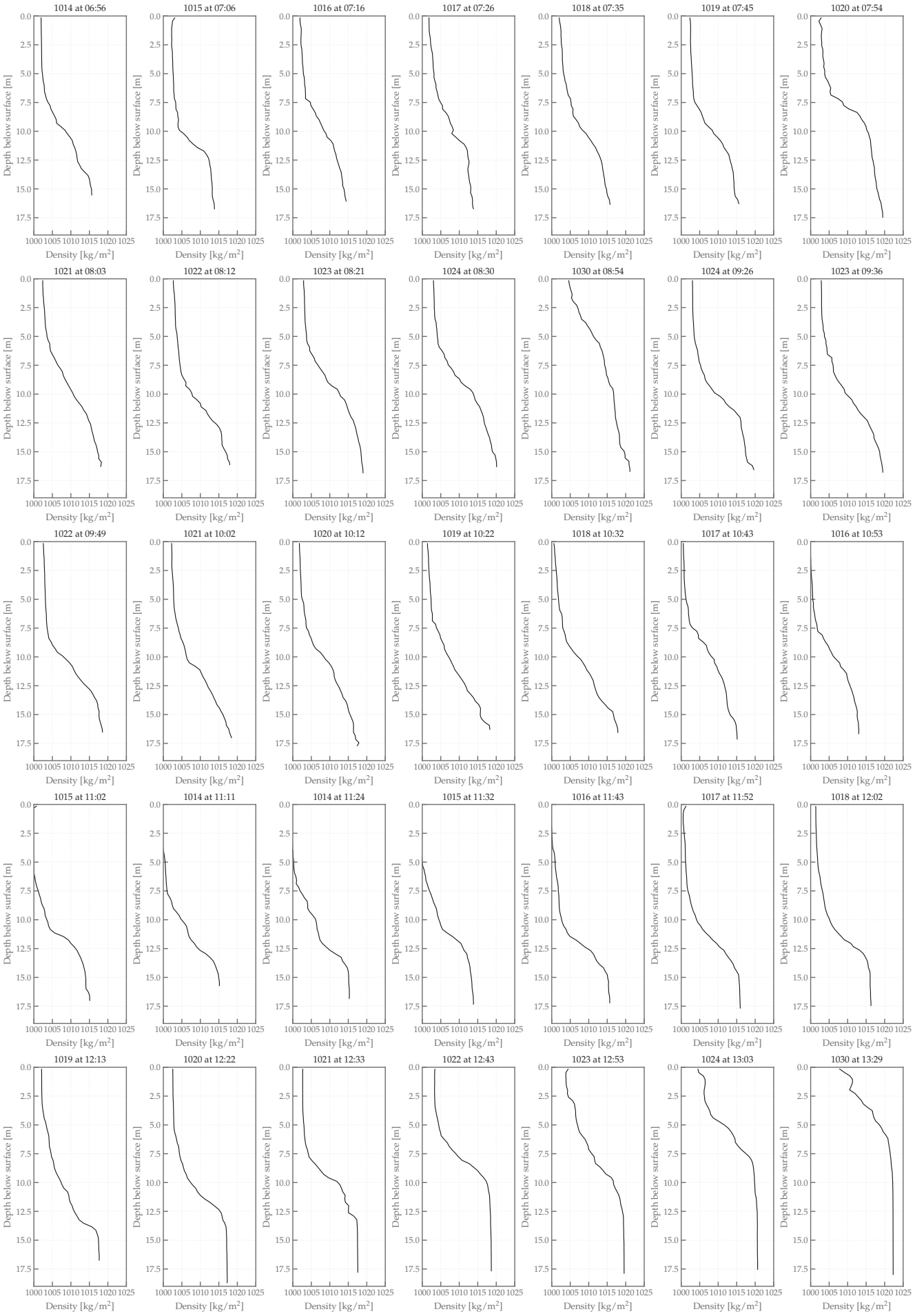

Figure C.3: Overview of the raw density profiles at all CTD measuring locations during the internal flow structure survey on August 13th, 2019. From left to right and top to bottom, subplots are in chronological order.

Figure C.4: Overview of the calculated buoyancy frequency profiles from the raw data at all CTD measuring locations during the internal flow structure survey on August 13th, 2019. From left to right and top to bottom, subplots are in chronological order.

C.1.1 Siltprofiler measured profiles

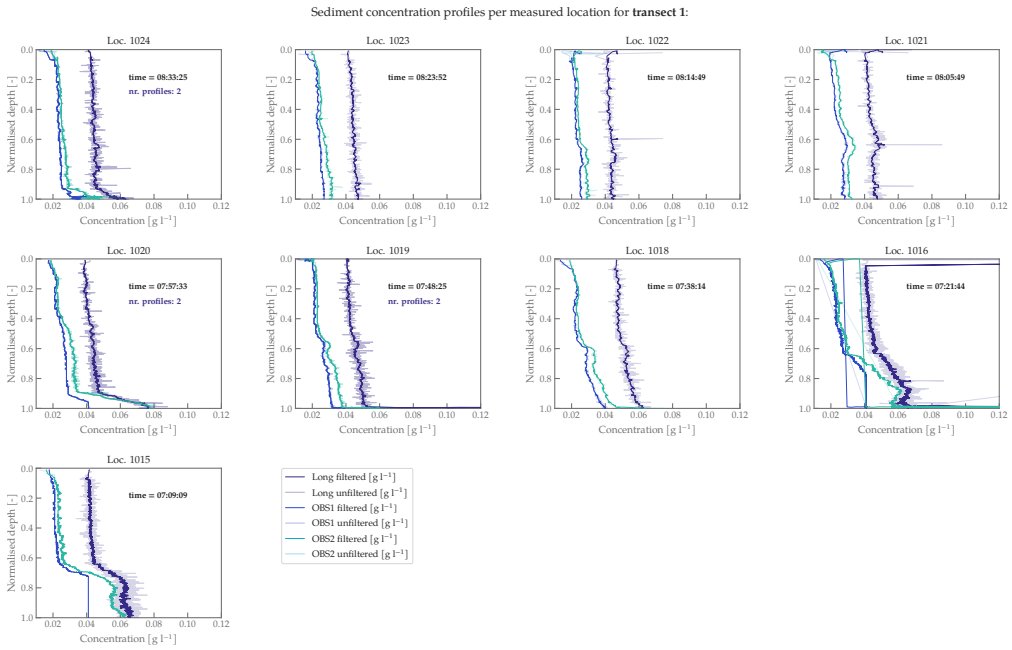

Figure C.5: Measured Siltprofiler profiles for the three turbidity sensors during the first transect. Indicated are the measurements from the three different sensors, giving values that are filtered using a 10 by 10 uniform filter (normal lines) and unfiltered values (opaque lines).

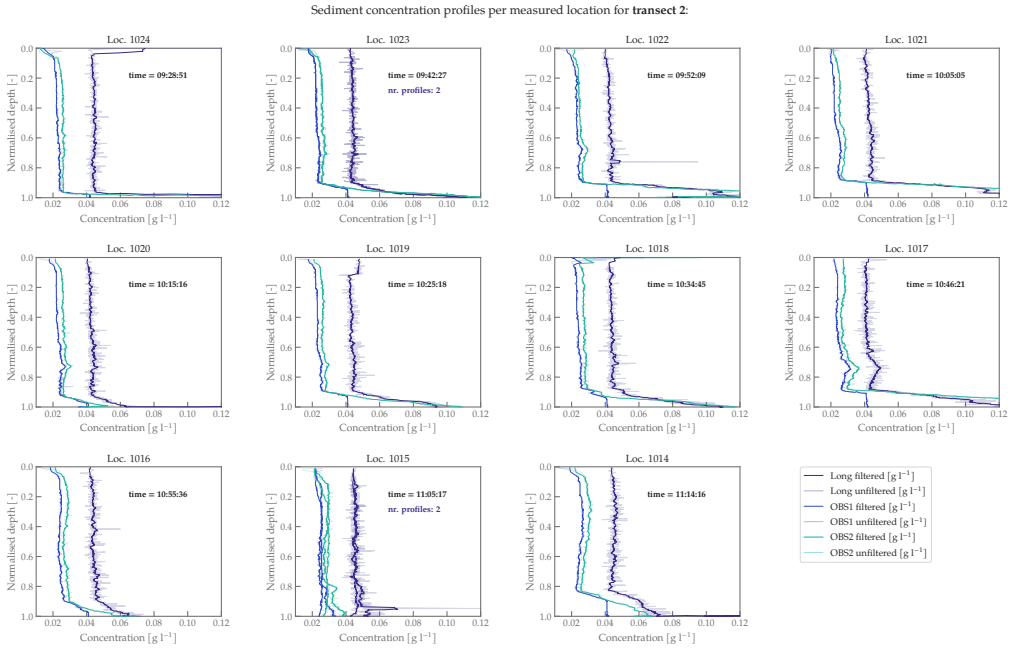

Figure C.6: Measured Siltprofiler profiles for the three turbidity sensors during the second transect. Indicated are the measurements from the three different sensors, giving values that are filtered using a 10 by 10 uniform filter (normal lines) and unfiltered values (opaque lines).

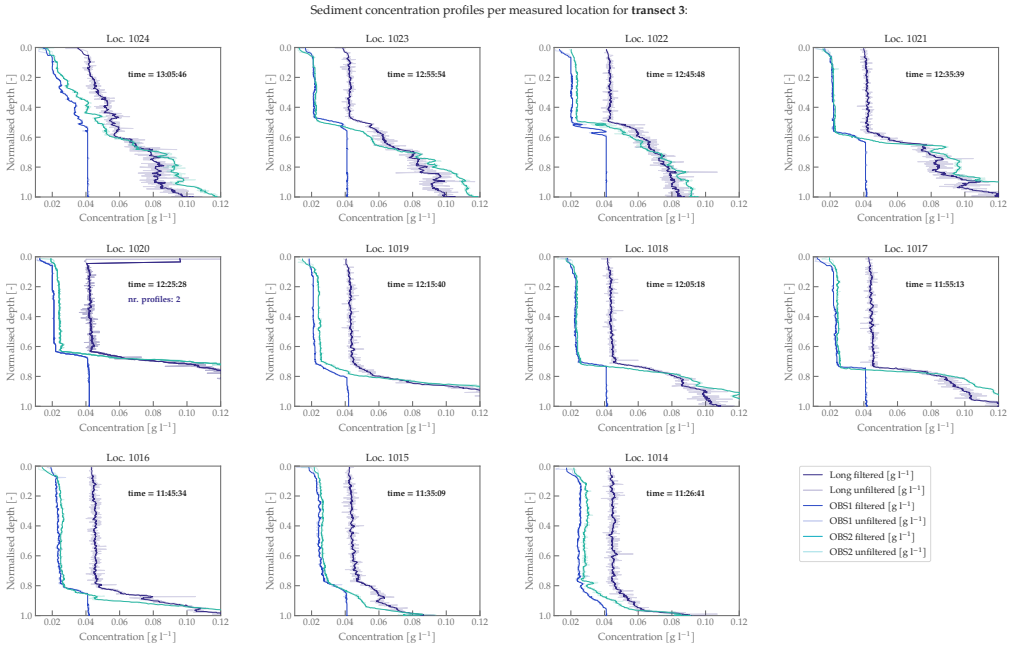

Figure C.7: Measured Siltprofiler profiles for the three turbidity sensors during the third transect. Indicated are the measurements from the three different sensors, giving values that are filtered using a 10 by 10 uniform filter (normal lines) and unfiltered values (opaque lines).

Appendix D

Mathematical background

D.1 Reynolds-averaged Navier-Stokes equations

When we want to model or resolve fluid motion at the smallest scales of motion, a practical problem arises. With the current computational power, it is impossible to resolve fluctuations on all scales in a numerical model. In order to be able to describe non-hydrostatic fluid flow, we decompose the instantaneous quantities in the Navier-Stokes equations into a mean (time-averaged) and fluctuating part. This method is called *Reynolds decomposition*, and application of this method to the Navier-Stokes equations leads to the *Reynolds-averaged Navier-Stokes equations* (RANS equations) (Pietrzak, 2015). This system of equations is composed of six total equations: the continuity equation, three momentum equations (for u, v and w respectively) and two transport equations for salinity (S) and temperature (T).

The Reynolds-averaged momentum equations read:

$$\frac{\partial u}{\partial t} + \frac{\partial uu}{\partial x} + \frac{\partial uv}{\partial y} + \frac{\partial uw}{\partial z} - fv + \frac{1}{\rho_0}\frac{\partial p}{\partial x} - F_x - \frac{\partial}{\partial z}\left(\nu_T \frac{\partial u}{\partial z}\right) = 0 \tag{D.1}$$

$$\frac{\partial v}{\partial t} + \frac{\partial uv}{\partial x} + \frac{\partial vv}{\partial y} + \frac{\partial vw}{\partial z} + fu + \frac{1}{\rho_0}\frac{\partial p}{\partial y} - F_y - \frac{\partial}{\partial z}\left(\nu_T \frac{\partial v}{\partial z}\right) = 0 \tag{D.2}$$

$$\frac{\partial w}{\partial t} + \frac{\partial uw}{\partial x} + \frac{\partial wv}{\partial y} + \frac{\partial ww}{\partial z} + \frac{1}{\rho}\frac{\partial p}{\partial z} + g - F_y - \frac{\partial}{\partial z}\left(\nu_T \frac{\partial w}{\partial z}\right) = 0 \tag{D.3}$$

In these equations ν_T is the vertical eddy viscosity, D_T is the vertical turbulent eddy diffusivity coefficient. Furthermore, F_x and F_y are given by:

$$F_x = \frac{\partial}{\partial x}\left(2\nu_H \frac{\partial u}{\partial x}\right) + \frac{\partial}{\partial y}\left(\nu_H\left(\frac{\partial u}{\partial y} + \frac{\partial v}{\partial x}\right)\right) \tag{D.4}$$

$$F_y = \frac{\partial}{\partial x}\left(2\nu_H \frac{\partial v}{\partial y}\right) + \frac{\partial}{\partial x}\left(\nu_H\left(\frac{\partial u}{\partial y} + \frac{\partial v}{\partial x}\right)\right) \tag{D.5}$$

with ν_H being the horizontal turbulent eddy viscosity. The continuity equation, as a result of the assumption of an incompressible fluid, is given by:

$$\frac{\partial u}{\partial x} + \frac{\partial v}{\partial y} + \frac{\partial w}{\partial z} = 0 \tag{D.6}$$

And lastly, the conservation equations for salinity and temperature are written as:

$$\frac{\partial S}{\partial t} + \frac{\partial uS}{\partial x} + \frac{\partial vS}{\partial y} + \frac{\partial wS}{\partial z} - F_s - \frac{\partial}{\partial z}\left(D_T \frac{\partial S}{\partial z}\right) = S_{SS} \tag{D.7}$$

$$\frac{\partial T}{\partial t} + \frac{\partial uT}{\partial x} + \frac{\partial vT}{\partial y} + \frac{\partial wT}{\partial z} - F_T - \frac{\partial}{\partial z}\left(D_T \frac{\partial T}{\partial z}\right) = \frac{1}{\rho}Q_H + S_{SS} \tag{D.8}$$

Here, F_S and F_T are given by:

$$F_S = \frac{\partial}{\partial x}\left(D_H \frac{\partial S}{\partial x}\right) + \frac{\partial}{\partial y}\left(D_H \frac{\partial S}{\partial y}\right) \tag{D.9}$$

$$F_T = \frac{\partial}{\partial x}\left(D_H \frac{\partial T}{\partial x}\right) + \frac{\partial}{\partial y}\left(D_H \frac{\partial T}{\partial y}\right) \tag{D.10}$$

in which D_H is the horizontal eddy diffusivity. Furthermore, S_{SS} refers to the sources and sinks induced by salinity and Q_H refers to the heat exchange (Pietrzak, 2015).

For the derivation of these equations, a couple of assumptions have been made. The *Bousinessq approximation* assumes that the difference in density are small with respect to the density itself, which implies that the effects of density don't affect the horizontal momentum. Application of the Boussinessq assumption leads to constant density terms in the horizontal acceleration terms, taken as a constant reference density ρ_0. Furthermore, the *f-plane approximation* has been applied, in which the Coriolis term is assumed to be constant with latitude. Under this assumption, the Coriolis term becomes:

$$f = 2\Omega \sin \phi \tag{D.11}$$

where ϕ is the latitude and $\Omega = \frac{2\pi}{86164} = 7.29 \times 10^{-5}$ s^{-1} is the rotation of the Earth in rad/s.

D.2 Measures to determine estuarine dynamics

D.2.1 Richardson numbers

In stratified environments, fluids of different densities are layered (partially) on top of each other. Under the influence of forcing, a stratified fluid can be disturbed, through which particles are displaced by their equilibrium state. Gravity and buoyancy forces will subsequently try to bring the fluid particles back into their equilibrium state, which introduces oscillations into the system. The frequency at which these particles start to oscillate is defined as the *Brunt-Väisalä frequency* or *buoyancy frequency*, which is defined as:

$$N^2 = -\frac{g}{\rho_0}\frac{\partial \rho}{\partial z} \tag{D.12}$$

The definition of this frequency can be derived from considering the forces on a particular fluid parcel in a linearly stratified fluid. When the vertical shear in the flow is large enough, and buoyancy cannot restore the equilibrium state anymore, the flow can become unstable. A well-known number to quantify the amount of stratification is the *gradient Richardson number*, which is the square of the Brunt-Väisalä frequency divided by the velocity shear over the vertical squared (Geyer, 1993; Pietrzak, 2015):

$$Ri_g = \frac{N^2}{\left|\frac{\partial u}{\partial z}\right|^2} = -\frac{\frac{g}{\rho_0}\frac{\partial \rho}{\partial z}}{\left|\frac{\partial u}{\partial z}\right|^2} \tag{D.13}$$

Typical values of the gradient Richardson number in estuaries range from 0.5 to 10, which yields reductions in the eddy diffusivity by one or two orders of magnitude (Geyer, 1993). A criterion for flow stability is often defined as $Ri > \frac{1}{4}$. If the Richardson number is smaller than $^1/_4$, the mixing layer is able to continue to grow, whereas if the Richardson number is larger than $^1/_4$, the generation of turbulence is balanced by the damping of turbulence through stratification (Pietrzak, 2015).

The *flux Richardson number*, R_f, is also a measure of dynamic stability. It is defined as:

$$Ri_f = -\frac{g\overline{w'\rho'}}{\rho\overline{u'w'}\frac{\partial u}{\partial z}} \tag{D.14}$$

It is often used in cases where stably stratified turbulence occurs, as a measure for the amount of turbulent kinetic energy that is irreversibly converted to background kinetic energy due to turbulent mixing.

The *bulk Richardson number*, R_b, is also a measure of stability of a stratified water column. Mathematically, it is an approximation of the gradient Richardson number, where local gradients are approximated by finite differences across layers. In case one is looking at the difference across the pycnocline, an expression for the bulk Richardson number may be (de Nijs *et al.*, 2010a):

$$Ri_B = \frac{g}{\rho\left|\frac{\partial \rho}{\partial z}\right|_{\max}}\frac{(\Delta\rho)^2}{(\Delta u)^2} \tag{D.15}$$

in which Δ represents the difference across the thickness of the pycnocline, which is denoted by $\Delta\rho/|(\partial\rho/\partial z)|_{\max}$ with $|(\partial\rho/\partial z)|_{\max}$ indicating the maximum absolute density gradient.

Lastly, the *horizontal Richardson number* is a measure of the relative importance of baroclinic forcing to bottom stress:

$$Ri_x = \frac{\beta g \frac{\partial S}{\partial x} H^2}{u_*^2} \tag{D.16}$$

where u_* is the friction velocity, H is the water depth and β is the saline expansivity (Monismith *et al.*, 2002). Simpson *et al.*'s criterion for the onset of strain-induced periodic stratification is simply stated as $Ri_x < 0.1$. Later research by, amongst others, Monismith *et al.* (2002) states this criterion as:

$$Ri_x < Ri_{crit} \tag{D.17}$$

where Ri_{crit} is a constant of $O(1)$, which is estuary-dependent. From modelling by Monismith *et al.*, Ri_{crit} was found to be $\sim$ 0.3 for the San Francisco Bay, while observations of the same estuary yield values of $\sim$ 0.6. For Ri_x values larger than the critical horizontal Richardson number, the estuary should remain well-mixed throughout the tidal cycle, whereas for significantly larger numbers, the estuary would not be able to reach a well-mixed state before the end of flood (MacCready and Geyer, 2010).

D.2.2 The Simpson number and the unsteadiness parameter

The Simpson number and the unsteadiness parameter are dimensionless numbers that have been shown to be able to determine the basic dynamics in (nonrotational) tidal estuaries (Burchard *et al.*, 2011). The Simpson number, which is also interpreted as the relative buoyancy gradient, is defined as:

$$\mathrm{Si} = \frac{\partial_x b H^2}{U_*^2} \tag{D.18}$$

where $\partial_x b$ is the tidally averaged longitudinal buoyancy gradient, H is the reference water depth, U_* is a scale for the bottom friction velocity and ω is the tidal frequency. In earlier studies, this Simpson number has generally been denoted as the *horizontal Richardson number*.

The unsteadiness parameter has been denoted as the *inverse Strouhal number* in earlier papers, and can be interpreted as the relative tidal frequency. It is defined as:

$$\mathrm{Un} = \frac{\omega H}{U_*} \tag{D.19}$$

with $\omega = 2\pi/T$ being the tidal frequency.

Appendix E

Hydrodynamic model parameters

	Parameter	Harbour model	NSC-Fine model
Grid	Number of domains	1	1
	Horizontal	7 cells wide in NWW	20 cells wide in NWW
	Vertical	1	10 σ-layers (non-equidistant)
Depth	Source	Lodingen PoR	Lodingen PoR
	Position of depths	Corner points	Corner points
	U and V locations	Averaged	Averaged
	Middle of grid cell	Average of corner points	Average of corner points
Processes		Salinity	Salinity
Loc.	Sea	$>$ 30 km offshore	15 à 20 km offshore
open boundaries	Rivers	Lek (Hagestein)	Lek (Krimpen aan de Lek)
		Waal (Tiel)	Beneden Merwede
		Maas (Lith)	Dordtsche Kil (south side)
			Spui (south side)
Roughness	Type	Manning	Manning
	Values	Globally: 0.024 s $m^{-\frac{1}{3}}$	Globally: 0.020 s $m^{-\frac{1}{3}}$
		Sp. varying: 0.014-0.025 s $m^{-\frac{1}{3}}$	Sp. varying: 0.016-0.026 s $m^{-\frac{1}{3}}$
Viscosity ν_T	Horizontal	6.0	1.0
	Vertical	n/a	$k-\epsilon$ turbulence model
Dispersion/	Horizontal	Globally: 50 m^2/s	Sp. varying: 0.01-1.00 m^2/s
diffusion D_T		Sp. varying: 50-1500 m^2/s	Increasing from W-E
		Haringsvliet Sluice: 0.0	
	Vertical	n/a	1.205
Wind	Air density ρ_a	1.205 kg m^{-3}	1.205 kg m^{-3}
	Drag coefficient C_D	0.0026	0.0026
	Wind forcing	Wind at HvH	Wind at HvH
Numerical settings	Time step Δt	30 s	7.5 s
	Iterations continuity	40	40
	Trunc. crit. continuity	-	0.002 m^3
	Iterations momentum	8	20
	Trunc. crit. velocity	0.0005 m/s	0.0002 m/s
	Δt friction update	10 mins	10 mins
	Anti-creep	n/a	off

Table E.1: Overview of model parameter settings for the operational Harbour model and the NSC-Fine model. From Deltares (2015).

Appendix F

Practical Salinity Scale from PSS-78

This appendix elaborates on the Practical Salinity Scale algorithm. Within this thesis, it is used to calculate the salinity time series—used in the phase shift analysis presented in Chapter 8—from temperature and conductivity time series. It is relevant to include this here, because the algorithm has been adapted slightly—extending it with the extension by Hill *et al.* (1986) for the calculation of salinities lower than 2 PSS. To harmonise the results with the methods that Rijkswaterstaat uses, the pressure correction term was manually set to $R_p = 1$.

In oceanography, a well-known method to calculate the salinity of water from conductivity and temperature measurements is by use of the PSS-78 algorithm. This algorithm is based on two sets of measurements of conductivity ratio of standard seawater solutions. Using a reproducible electrical conductivity standard, a *Practical Salinity Scale* (PSS) has been defined (UNESCO, 1981). Using this definition of Practical Salinity Scale, standard seawater will have a salinity of 35 PSS.

The algorithm used for Practical Salinity, is used as the basis of, amongst others, the salinity measurements done in the Rotterdam Waterway and surrounding harbours by Rijkswaterstaat (Ministerie van Infrastructuur en Waterstaat, 2005). It is defined as follows (Perkin and Lewis, 1980; UNESCO, 1981):

$$S = a_0 + a_1 R_t^{1/2} + a_2 R_t + a_3 R_t^{3/2} + a_4 R_t^2 + a_5 R_t^{5/2} + \Delta S \tag{F.1}$$

with salinity correction ΔS [PSS] and the constants a_i with $i = 1, 2, ..., 5$:

$$\begin{aligned} a_0 &= 0.0080 \\ a_1 &= -0.1692 \\ a_2 &= 25.3851 \\ a_3 &= 14.0941 \\ a_5 &= 2.7081 \\ \Sigma a_i &= 35.0000 \end{aligned}$$

where:

$$\Delta S = \frac{T - 15}{1 + k(T - 15)} \left(b_0 + b_1 R_t^{1/2} + b_2 R_t + b_3 R_t^{3/2} + b_4 R_t^2 + b_5 R_t^{5/2} \right) \tag{F.2}$$

in which T [$^\circ$C] is the in-situ water temperature and $k = 0.0162$. Empirical constants b_i with $i = 1, 2, ..., 5$ are:

$$\begin{aligned} b_0 &= 0.0005 \\ b_1 &= -0.0056 \\ b_2 &= -0.0066 \\ b_3 &= -0.0375 \\ b_4 &= 0.0636 \\ b_5 &= 0.0144 \\ \Sigma b_i &= 0.0000 \end{aligned}$$

A shorthand series notation of (F.1) with the expression of (F.2) is thus:

$$S = \sum_{i=0}^{5} \left(a_i + b_i f\left(t\right)\right) R_t^{i/2} \tag{F.3}$$

with:

$$f(t) = \frac{(T-15)}{1 = k\,(T-15)} \tag{F.4}$$

This formulation makes use of the *conductivity ratio* R_t, which is defined as the ratio of the conductivity of seawater at temperature T [° C] to the conductivity of seawater of 35 PSS and a measured air pressure above 1 atmosphere of p [dbar]:

$$R_t = \frac{R}{r_t R_p} \tag{F.5}$$

where r_t is a temperature correction, R_p [-] is the ratio of the in-situ conductivity to the conductivity of the same sample but at $p = 0$, and R [-] is the in-situ conductivity ratio. R can be calculated from measurements of the conductivity by dividing the measured conductivity by the conductivity of 'standard seawater' of 35 PSS at $T = 15°C$. The temperature correction r_t is defined as follows:

$$r_t = c_0 + c_1 T + c_2 T^2 + c_3 T^3 + c_4 T^4 \tag{F.6}$$

with constants:

$$\begin{aligned} c_0 &= 0.6766097 \\ c_1 &= 2.00564 \times 10^{-2} \\ c_2 &= 1.104259 \times 10^{-4} \\ c_3 &= -6.9698 \times 10^{-7} \\ c_4 &= 1.0031 \times 10^{-9} \end{aligned}$$

Lastly, the pressure correction R_p is defined as:

$$R_p = 1 + \frac{p\left(e_1 + e_2 p + e_3 p^2\right)}{1 + d_1 T + d_2 T^2 + \left(d_3 + d_4 T\right) R} \tag{F.7}$$

with constants:

$$\begin{aligned} e_1 &= 2.070 \times 10^{-4} \\ e_2 &= -6.370 \times 10^{-8} \\ e_3 &= 3.989 \times 10{-}12 \\ d_1 &= 3.426 \times 10^{-2} \\ d_2 &= 4.464 \times 10^{-4} \\ d_3 &= 4.215 \times 10^{-1} \end{aligned}$$

Several institutions, amongst which Rijkswaterstaat and the Port of Rotterdam, use an approximate value of $R_p = 1$, since in-situ measurements of the pressure are not always guaranteed (Ministerie van Infrastructuur en Waterstaat, 2005, 2010).

It is important to note that the algorithm specified in UNESCO (1981) only holds for salinities within the range of 2 to 42 PSS. If the algorithm calculates that the salinity is lower than 2 PSS, which is often the case in estuarine environments during part of the tidal cycle, a correction has to be applied. Because this correction is somewhat difficult to implement, certain institutions do not use this algorithm in parts of the estuarine system where salinities might drop below 2 PSS. In this thesis, however, it is necessary to compute these salinities as well, as they provide the basis for a comparison between model output and measurements. The correction is therefore implemented anyway, by use of the programming language Python.

This correction, first presented in Hill *et al.* (1986), is empirical and based on measurements of the mass-determined salinity, electrical conductivity and temperature for salinities between 0 and 2 PSS. This correction is defined as:

$$S_{\text{corr}} = -\frac{a_0}{1 + 1.5x + x^2} - \frac{b_0 f(t)}{1 + y1/2 + y + y^{3/2}} \tag{F.8}$$

where $f(t)$ is still equal to Equation (F.4), $x = 400R_t$ and $y = 100R_t$. This would yield a final value of $S_{\text{calc}} = S + S_{\text{corr}}$.

In this thesis, the exact implementation that has been described in the newest version of the Thermodynamic Equation of Seawater has been used, which was released in 2010 and is named TEOS-10 accordingly. In this implementation, the correction proposed by Hill *et al.* (1986) is only applied when the salinity calculated with the PSS-78 algorithm calculates a salinity that is lower than 2 PSS. It uses one Newton-Raphson iteration of R_t to ensure that the algorithm is continuous at $S_p = 2$ PSS (IOC SCOR, 2010) with the known temperature T. The Hill *et al.* (1986) correction is then evaluated using this value of R_t.

Appendix G

Tidal analysis

A harmonic analysis (Foreman and Henry, 1989; Godin, 1972) of the water level time series at Hoek van Holland and Maassluis was conducted using the UTide MATLAB® (MATLAB, 2019) scripts developed by Codiga (2011). This was done to derive the main constituents from the water level signal and to see which components the model is able to represent well—or not. This appendix first describes the methodology and used computational scripts, after which the outcome of the analysis is presented in tables.

G.1 Methodology

A harmonic analysis resolves the water movements by representing them as the sum of a finite number of harmonic constituents:

$$H(t) = A_0 + \sum_{i=1}^{k} A_i f_i \cos\left(\omega_i t + (V_0 + u)_i - G_i\right) \qquad \text{(G.1)}$$

with $H(t)$ being the instantaneous water level, A_0 being the mean value and A_i the tidal amplitude, f_i the nodal amplitude factor, ω_i the angular velocity, $(V_0 + u)_i$ the astronomical argument and G_i the Greenwich phase lag for component i.

The UTide functions make use of an *iteratively-reweighted least squares* (IRLS), through which the influence of outliers is minimised. It furthermore implements the robust method first presented in Foreman *et al.* (2009), which incorporates exact *in-matrix* formulations for nodal/satellite corrections, the astronomical argument for Greenwich phase calculation and inferences. The UTide script is also able to handle irregularly distributed temporal sampling and two-dimensional input (such as currents).

Constituents are selected by an iterative process. The starting point for this iterative process are more constituents than are expected to capture significant energy (or are expected to be resolved from the other constituent). The values of the astronomical variables and constituent frequencies in this initial set of constituents is based on the power series expansion formulae presented in *"Explanatory supplement to the Astronomical ephemeris and the American ephemeris and nautical almanac"* (Science Research Council (Great Britain) and United States Naval Observatory Nautical Almanac Office, 1961). The starting point of the computation includes 69 constituents, of which 45 are astronomical, while the other 24 are shallow water constituents. Another 77 shallow water constituents could be included if desired.

Table G.1: Shallow water constituents that may mask main constituents. From Foreman and Henry (1989).

Main constituent	Component constituent
Q_1	NK_1
O_1	NK_1 **
TAU_1	MP_1 **
NO_1 *	NO_1 **
P_1	SK_1 **
K_1	MO_1
J_1	MQ_1
SO_1	SO_1
OQ_2	OQ_2 **
EPS_2	MNS_2
$2N_2$	O_2 **
MU_2	$2MS_2$
N_2	KQ_2 **
GAM_2	OP_2 **
M_2	KO_2 **
L_2	$2MN_2$ **
S_2	KP_2
K_2	K_2
MO_3	MO_3 **
M_3	NK_3 **

* Using M_1 as a satellite

** The modulation of the compound constituent is sufficiently different that the pair could be separated if a long enough record

The constituent selection process is based on the *Rayleigh comparison constituent*. Using a Rayleigh comparison constituent with frequency F_1 and a record with time span T, a constituent with frequency F_0 will be included in the analysis if:

$$|F_0 - F_1|T \geq 1.0 \tag{G.2}$$

Where 1.0 is the most commonly used value of the *Rayleigh criterion value*. Frequencies F_0 and F_1 together form a *Rayleigh comparison pair*, and are determined per constituent group (diurnal, semidiurnal, terdiurnal and low frequency). An example of the chosen Rayleigh comparison pairs for the semidiurnal constituent groups, based on a Rayleigh criterion value of 1.0, are given in Table G.2.

If shallow water effects are noticeable, main constituents may be masked or by non-linear higher order constituents if they are close in frequency. This is taken into account in the UTide package by not taking into account the higher-order compound constituent that may mask the main constituent in the standard constituent data package.

Table G.2: Order of semidiurnal constituent selection in accordance with the Rayleigh criterion. Tidal potential amplitude for main constituents is shown within brackets, and lines with arrows denote the links between Rayleigh comparison pairs. From Foreman and Henry (1989).

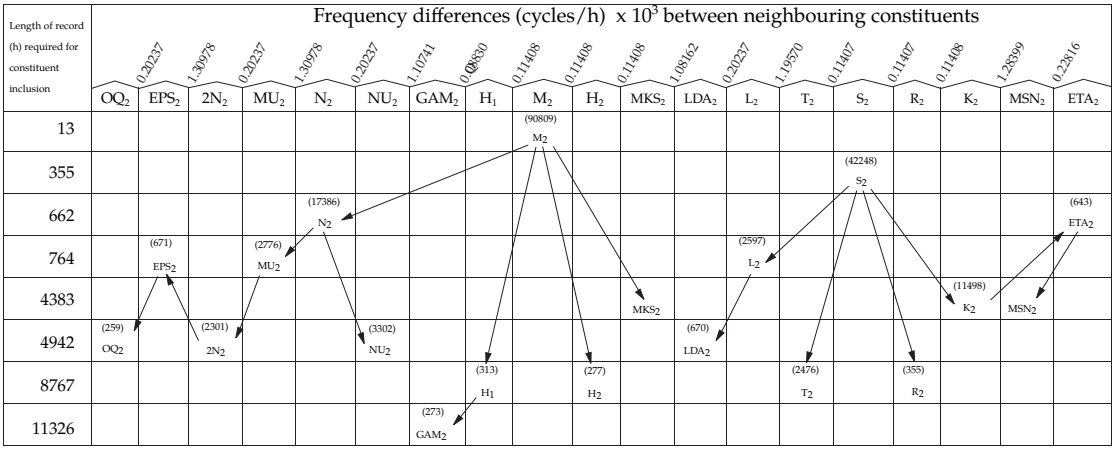

G.2 Tidal analysis of water level records at Hoek van Holland

Component name	Component frequency [s^{-1}]	Percent energy [%]	Amplitude [cm]	Amplitude 95% confidence interval [cm]	Greenwich phase lag [degrees]	Greenwich phase lag 95% confidence interval [cm]
M2	0.080511	81.323183	77.249084	0.594977	9.532289	0.453697
M4	0.161023	5.164931	19.467869	0.893315	8.910202	2.688357
S2	0.083333	3.130054	15.155214	0.607073	158.652944	2.335381
N2	0.078999	2.492225	13.523209	0.554139	96.615488	2.755128
K1	0.041781	1.649396	11.001418	0.365328	12.190125	1.934366
O1	0.038731	1.468752	10.381506	0.445229	114.262228	2.151561
MS4	0.163845	1.169935	9.265462	0.864808	163.347529	5.005989
L2	0.082024	0.785601	7.592542	0.617301	285.922936	5.460537
MN4	0.159511	0.727595	7.306863	0.900590	95.796429	6.370422
MU2	0.077689	0.568938	6.461279	0.562919	43.912644	4.822145
M6	0.241534	0.431666	5.628075	0.570809	263.038474	6.167934
2MS6	0.244356	0.176782	3.601681	0.661128	60.628577	8.575700
Q1	0.037219	0.175766	3.591319	0.354490	181.232446	5.355962
2MN6	0.240022	0.164883	3.478357	0.591907	354.738346	10.449632
M8	0.322046	0.117986	2.942398	0.387029	285.255392	7.634208
NO1	0.040269	0.106864	2.800289	0.333152	329.667742	6.869700
2MK5	0.202804	0.086091	2.513421	0.451703	221.496359	9.567875
MSF	0.002822	0.071501	2.290565	1.677984	51.272964	56.993243
MK3	0.122292	0.041695	1.749157	0.171962	222.405994	5.881599
SN4	0.162333	0.020200	1.217479	0.664887	74.359388	42.156858
MO3	0.119242	0.019688	1.201955	0.199609	6.317956	9.293123
OO1	0.044831	0.017730	1.140620	0.347272	134.507731	16.975702
3MK7	0.283315	0.017659	1.138348	0.164364	139.290249	9.661262
2Q1	0.035706	0.015086	1.052138	0.321819	190.403248	17.957116
EPS2	0.076177	0.013705	1.002815	0.589200	101.543804	37.304654
ETA2	0.085074	0.011985	0.937799	0.597408	120.077866	43.402734
J1	0.043293	0.011446	0.916466	0.401916	9.067569	25.826231
MM	0.001512	0.009680	0.842782	1.409337	188.903641	125.045389
S4	0.166667	0.003685	0.520034	0.775502	357.722523	278.172308
SK3	0.125114	0.002383	0.418157	0.209975	355.503837	35.146839
ALP1	0.034397	0.002058	0.388599	0.344973	36.971959	49.437638
2SM6	0.247178	0.000339	0.157733	0.351500	186.410659	171.646487
2SK5	0.208447	0.000226	0.128717	0.314167	84.038205	158.927852
UPS1	0.046343	0.000224	0.128106	0.268212	215.229274	125.481226
M3	0.120767	0.000061	0.066945	0.143688	104.429834	156.524949

Table G.3: Tidal constituents ranked from most energetic to least energetic from tidal analysis of water level records at Hoek van Holland between 15-07-2019 and 16-08-2019 using the UTide script (Codiga, 2011).

G.3 Tidal analysis of water level SIMONA model outputs (NSC-Fine grid) at Hoek van Holland

Component name	Component frequency [s^{-1}]	Percent energy [%]	Amplitude [cm]	Amplitude 95% confidence interval [cm]	Greenwich phase lag [degrees]	Greenwich phase lag 95% confidence interval [cm]
M2	0.080511	80.874750	77.609740	0.733048	8.652601	0.358357
M4	0.161023	5.054561	19.402223	1.039801	10.085476	2.540279
S2	0.083333	3.421582	15.963320	0.677826	158.332799	2.028706
N2	0.078999	2.588838	13.885522	0.637625	96.266418	2.971993
K1	0.041781	1.629255	11.015502	0.328666	11.716101	1.831281
O1	0.038731	1.497778	10.561692	0.315277	114.179341	1.635205
MS4	0.163845	1.411596	10.253332	0.991761	159.646683	6.411830
MN4	0.159511	0.735938	7.403386	0.969852	94.210002	5.871134
L2	0.082024	0.724542	7.345841	0.665471	284.312964	4.940147
M6	0.241534	0.493232	6.060874	0.510873	272.815862	5.321597
MU2	0.077689	0.477457	5.963167	0.750324	43.291990	6.177406
2MS6	0.244356	0.212668	3.979797	0.476843	72.219552	7.875855
2MN6	0.240022	0.183499	3.696807	0.550578	359.932535	21.676965
Q1	0.037219	0.158726	3.438217	0.259182	181.550806	6.286464
2MK5	0.202804	0.094619	2.654603	0.431896	226.678212	8.604507
M8	0.322046	0.094251	2.649430	0.380701	284.383717	8.526155
NO1	0.040269	0.092761	2.628401	0.341077	327.942948	8.090402
MSF	0.002822	0.059320	2.101891	2.046628	56.864911	65.727839
MK3	0.122292	0.038903	1.702162	0.249062	220.923064	8.069254
SN4	0.162333	0.033426	1.577809	0.853707	65.423546	35.713339
MO3	0.119242	0.019706	1.211459	0.202244	19.673295	11.485890
OO1	0.044831	0.018571	1.176045	0.366924	141.037172	16.578127
ETA2	0.085074	0.017816	1.151891	0.632670	111.255541	33.160360
EPS2	0.076177	0.015843	1.086261	0.674472	98.978012	34.223348
2Q1	0.035706	0.012122	0.950155	0.313549	203.692224	23.472168
J1	0.043293	0.010821	0.897732	0.356819	14.513845	23.256832
3MK7	0.283315	0.009000	0.818730	0.160430	147.984014	10.948821
ALP1	0.034397	0.004743	0.594322	0.359937	59.890130	37.574586
SK3	0.125114	0.004436	0.574772	0.241389	352.517656	30.331075
MM	0.001512	0.003601	0.517859	1.637161	206.523690	163.227653
S4	0.166667	0.002411	0.423723	0.784237	331.967616	162.542968
UPS1	0.046343	0.001576	0.342575	0.296217	235.626218	64.763563
2SM6	0.247178	0.001211	0.300301	0.483140	233.203741	100.512312
M3	0.120767	0.000260	0.139032	0.195022	245.121435	90.592381
2SK5	0.208447	0.000181	0.116049	0.266770	218.308733	131.251480

Table G.4: Tidal constituents ranked from most energetic to least energetic obtained from tidal analysis of water level model output data at Hoek van Holland between 15-07-2019 and 16-08-2019 using the UTide script (Codiga, 2011).